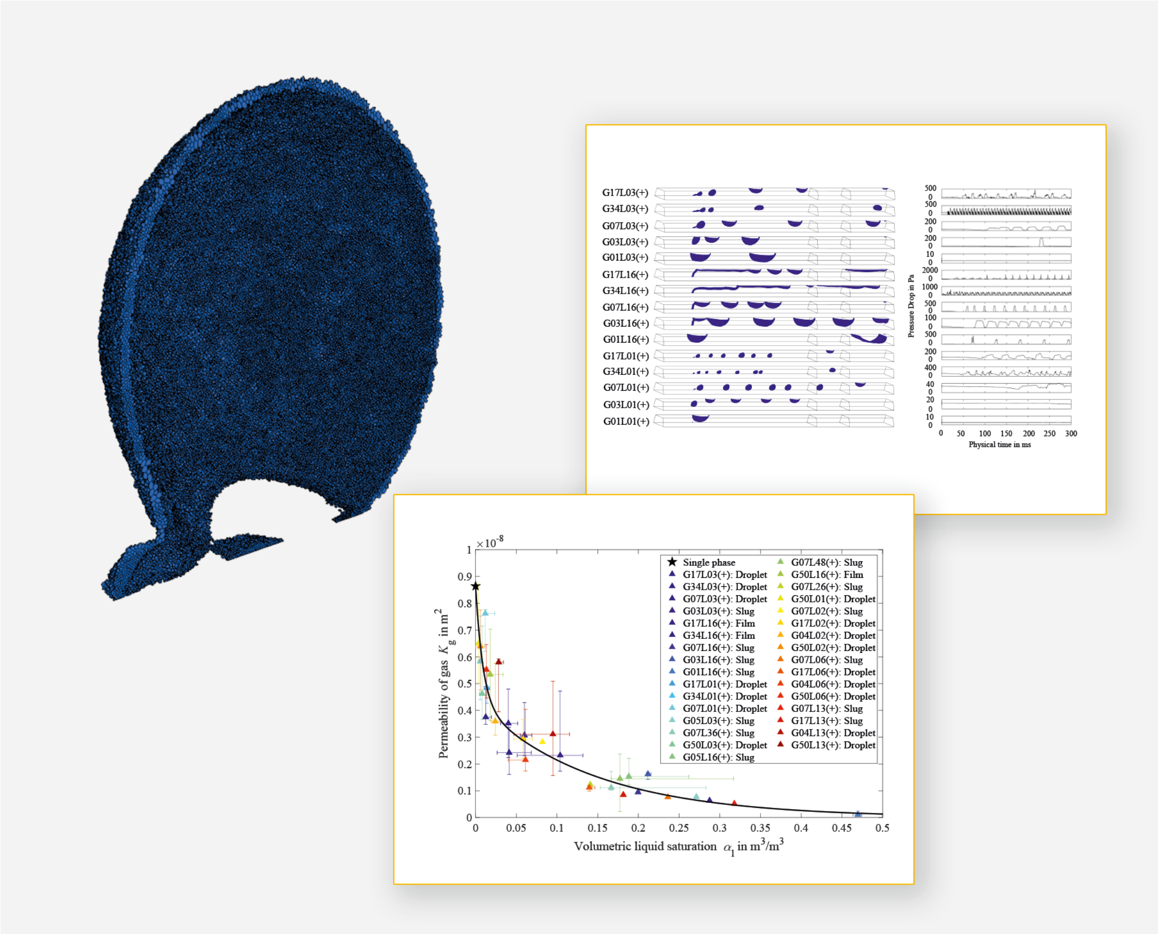

Water Management in Automotive Polymer-Electrolyte-Membrane Fuel Cell Stacks

Savo Asanin

Energie & Umwelt / Energy & Environment
Band / Volume 504
ISBN 978-3-95806-491-1

Mitglied der Helmholtz-Gemeinschaft

JÜLICH
Forschungszentrum

Schriften des Forschungszentrums Jülich
Reihe Energie & Umwelt / Energy & Environment Band / Volume 504

Forschungszentrum Jülich GmbH
Institut für Energie- und Klimaforschung
Elektrochemische Verfahrenstechnik (IEK-14)

Water Management in Automotive Polymer-Electrolyte-Membrane Fuel Cell Stacks

Savo Asanin

Schriften des Forschungszentrums Jülich
Reihe Energie & Umwelt / Energy & Environment Band / Volume 504

ISSN 1866-1793 ISBN 978-3-95806-491-1

Bibliografische Information der Deutschen Nationalbibliothek.
Die Deutsche Nationalbibliothek verzeichnet diese Publikation in der
Deutschen Nationalbibliografie; detaillierte Bibliografische Daten
sind im Internet über http://dnb.d-nb.de abrufbar.

Herausgeber und Vertrieb: Forschungszentrum Jülich GmbH
Zentralbibliothek, Verlag
52425 Jülich
Tel.: +49 2461 61-5368
Fax: +49 2461 61-6103
zb-publikation@fz-juelich.de
www.fz-juelich.de/zb

Umschlaggestaltung: Grafische Medien, Forschungszentrum Jülich GmbH

Druck: Grafische Medien, Forschungszentrum Jülich GmbH

Schriften des Forschungszentrums Jülich
Reihe Energie & Umwelt / Energy & Environment, Band / Volume 504

D 82 (Diss. RWTH Aachen University, 2020)

ISSN 1866-1793
ISBN 978-3-95806-491-1

Acknowledgments

I would like to thank all the people who contributed to this thesis and those who supported me during my time as a doctoral candidate.

First and foremost, I would like to express my sincere gratitude to Dr. Julian Hirschfeld, for his role as technical advisor and mentor. You have been a true inspiration and source of motivation throughout this time.

I would also like to thank my university supervisor Prof. Dr. Werner Lehnert, for all the input and feedback you provided and the trust you put in me despite the distance.

I would like to thank my former students, Benjamin Nefzger-Loders, Fengmin Du, Kunxiong Ling, Naveen Kumar Cheruku and Andres Jurzyk. For all the working hours you put into the project, which greatly contributed to the outcome of this work. I hope you learned as much from me as I did from you.

I would like to express my gratitude and appreciation to all my colleagues at BMW. Dr. Simon Enz for the discussions on CFD simulations of PEMFCs. Dr. Alin Orfanidi for the input regarding electrochemical processes and help with measurements. Dr. Markus Perchthaler and Tim Lochner, for their help regarding experimental validations. Dr. Albert Albert for the help he provided in acquiring necessary simulation parameters. Martin Moser for helping me with the creation of CAD models. Dr.-Ing. Olav Finkenwirth, for always advocating on my behalf when resources in order to realize this project were needed. I enjoyed working with every single one of you.

I want to appreciate the collaboration with STAR-CCM+ regarding the PEMFC model, especially naming Huong Nguyen and Christopher Lueth.

Last but not least, I would like to express my deepest gratitude to the ones closest to me. To my family and friends for their support and encouragement over all these years and to Kate for her unconditional love. None of this would have been possible without you.

Abstract

The detailed simulative investigation of the water management inside automotive PEM fuel cell stacks requires a three-dimensional multiphysics stack model. Due to the lack of appropriate literature approaches, which include the multiphase water transport, in addition to all fluid flow, thermal and electrochemical phenomena a suitable model is developed within the present study. The description is subdivided into two main paths i.e. water transport inside the gas channels of the flow field and within the layers of the MEA. In order to tackle the link between the two, a multi-scale approach is applied. The investigation levels are stack, single cell and single channel. A simplified cell model is derived by using a Darcy-like approach inside the flow fields with a drastic reduction in computational cells. In order to account for two-phase flow effects inside the gas channels, the capability of implementing two-phase pressure drop correlations is integrated. Correlations are obtained through two-phase flow Volume-of-Fluid simulations within single gas channels of anode and cathode respectively. Therefore, a methodology for adaptive mesh refinement (AMR) is derived to effectively investigate the phenomena of two-phase flow in gas channels. During the analysis, effects of dynamic and static contact angles are implemented and compared against each other, showing the necessity of dynamic contact angle models. A speed-up of the simulation process is achieved through a constant coarse mesh refinement (CCMR), using a high resolution interface capturing (HRIC) algorithm. The methodology is validated against detailed AMR results and used for parametric studies, regarding gas and liquid water input velocities. Hereby a study is carried out to investigate the dependency of number and position of liquid water inlet. The results show an independence regarding flow regime and stationary two-phase pressure drop values. Two-phase pressure drop correlations are derived from the filtered and processed result data. Experimental current density and temperature distribution results, as well as detailed simulations are used as a basis for the simplification process and the subsequent validation. The simplified cells are electrically and thermally connected within a 60-cell stack, automatically generated through a developed code. Stack simulations at various operating points are performed and validated against simulative simplified single cell and experimental 60-cell stack data. Very good prediction capabilities of the stack model, regarding stack performance are achieved.

Zusammenfassung

Die detaillierte Untersuchung von automotiven PEMFC Stacks unter Zuhilfenahme von Simulationstools benötigt einen dreidimensionalen Multiphysikansatz. Aufgrund fehlender Ansätze in der Literatur, welche den Mehrphasentransport von Wasser, zusätzlich zur Beschreibung der Fluidströmung, sowie thermischer und elektrochemischer Prozesse inkludiert, wird ein geeigneter Ansatz in der vorliegenden Arbeit entwickelt. Dieser ist unterteilt in zwei Hauptpfade, den Wassertransport in den Gaskanälen des Flussfeldes und innerhalb der einzelnen Schichten der MEA, weshalb auf einen Multiskalenansatz zurückgegriffen worden ist. Stack-, Einzelzell- und Einzelkanalebene sind hierbei untersucht worden. Ein vereinfachtes Einzelzellenmodell ist unter Einbezug des Darcy-Ansatzes hergeleitet worden um die Strömung innerhalb der Flussfelder bei drastischer Reduktion der numerischen Zellzahl untersuchen zu können. Um den Zweiphasendruckverlust in Gaskanälen berücksichtigen zu können, ist das vereinfachte Zellmodell mit einer Schnittstelle für Zweiphasen-Druckverlustkorrelationen aufgesetzt. Diese sind durch Volume-of-Fluid-Simulationen in Einzelkanälen von Anode und Kathode entwickelt worden. Eine Methodologie für einen adaptiven Gitterverfeinerungsalgorithmus ist hergeleitet worden um Zweiphasen-Phänomene in Gaskanälen effektiv untersuchen zu können. Untersuchungen haben hierbei die Bedeutsamkeit eines dynamischen Kontaktmodells aufgezeigt. Zur Optimierung der Simulationenszeiten ist eine grobe, konstante Netzverfeinerung (CCMR), mit Implementierung des High Resolution Interface Capturing (HRIC) Algorithmus, angesetzt und mit detaillierten AMR-Ergebnissen validiert worden. Hierbei ist eine Studie zur Untersuchung des Einflusses von Einlassposition und Anzahl an Flüssigwasserquellen, sowie Gas- und Flüssigkeitsgeschwindigkeiten durchgeführt worden. Die Ergebnisse zeigen eine Unabhängigkeit des stationären Druckverlusts und des sich ausbildenden Strömungsregimes bezüglich dieser Größen. Korrelationen sind aus den Ergebnisdaten hergeleitet worden. Experimentelle Stromdichte- und Temperaturverteilungen, sowie detaillierte Einzelzellsimulationen sind als Basis für den Simplifikationsprozess und die anschließende Validierung verwendet worden. Die vereinfachten Zellen sind elektrisch und thermisch zu einem Stack gekoppelt worden, welcher automatisiert über einen entwickelten Code erstellt wird. Stacksimulationen sind an mehreren Betriebspunkten durchgeführt und gegen Simulationsergebnisse der vereinfachten Einzelzelle, sowie experimentellen 60-Zell-Stacks validiert worden. Eine sehr gute Vorhersagefähigkeit des Modells bezüglich der Stackleistung ist aufgezeigt worden.

Contents

List of Figures

List of Tables

Nomenclature

Latin Symbols

a	Activity	-
b	Width	m
A	Area	$\mathrm{m^2}$
c	Molar concentration	$\mathrm{kmol/m^3}$
c_p	Specific heat	J/(kmol K)
C_1	Fitting parameter	V
C_2	Fitting parameter	$\mathrm{A/cm^2}$
C_3	Fitting parameter	$\mathrm{V(A/cm^2)^{-1}}$
C_4	Fitting parameter	V
C_5	Fitting parameter	$\mathrm{(A/cm^2)^{-1}}$
C_α	Sharpening factor	-
C_θ	Angle factor	-
d	Diameter	m
D	Diffusion coefficient	$\mathrm{m^2/s}$
E_{elec}	Electric energy	J
E_{A}	Activation energy	J
EW	Equivalent weight	kg/kmol
f	General function	-
f_{Blend}	Blending function	-
f_{D}	Darcy-Weisbach friction factor	-
f_{Hoff}	Hoffman correlation	-
$\vec{f}$	General force vector	$\mathrm{N/m^3}$
f_x,f_y,f_z	Volumetric force components	$\mathrm{N/m^3}$
$\vec{f}_\sigma$	Surface tension force vector	$\mathrm{N/m^3}$
F	Faraday constant	C/kmol
F_1,F_2	Forces	N
$\vec{g}$	Gravitational acceleration	$\mathrm{m/s^2}$
G^0	Gibbs free energy	J/kmol
h	Specific enthalpy	J/kmol

H	Height	m
H^0	Reaction enthalpy	J/kmol
I	Electric current	A
j	Current density	A/m^2
$\vec{j}$	Electric current density vector	A/m^2
j_0	Exchange current density	A/m^2
j_0^*	Reference exchange current density	A/m^2
J	Leverett function	-
K_v	Viscous permeability	m^2
K_I	Inertial permeability	1/m
K_0	Intrinsic viscous permeability	m^2
$K_\mathrm{P}, K_\mathrm{I}, K_\mathrm{D}$	Proportionality, integral and derivative factors	-
l	Length	m
L_h	Hydraulic entrance length	m
$\dot{m}$	Mass flow	kg/s
M	Molar mass	kg/kmol
$\dot{n}$	Molar flow	kmol/s
$\vec{n}$	Normal vector	-
n_D	EOD-coefficient	-
n_inner	Number of inner iterations	-
O	Perimeter	m
p	Pressure	Pa
p_c	Capillary pressure	Pa
Δp	Pressure drop	Pa
P	Power density	W/m^2
$\dot{Q}$	Heat flux	W
R	Radius	m
$\mathfrak{R}$	Ideal gas constant	J/(kmol K)
RH	Relative humidity	-
S	Source term position	-
S_mom	Momentum source term	N s/m^3
S_T	Energy source term	J/m^3
S_w	Species source term	1/m^3
S_W	Volume fraction source term	1/s
S_φ	Conservation property source term	-
$\dot{S}_W$	Liquid water source term	m^3/s
t	Time	s
Δt	Time step	s
T	Temperature	K
u	Velocity	m/s

$\vec{u}$	Velocity vector	m/s
$\vec{u}_{12}$	Slip velocity vector	m/s
$\vec{u}_{dr}$	Drift velocity vector	m/s
$\vec{u}$	Velocity vector	m/s
u_x, u_y, u_z	Velocity components in x, y, z direction	m/s
U	Electric potential	V
U_0	Standard potential	V
U_0^{H}	Thermo-neutral potential	V
U_{cell}	Cell voltage	V
U_{stack}	Stack voltage	V
U_{N}	Thermodynamic maximum voltage	V
V	Volume	m^3
$\dot{V}$	Volumetric flow	m^3/s
w	Mass fraction	-
x, y, z	Cartesian coordinates	m
Δx	Cell size	m
y	Molar fraction	-
z	Number of transferred electrons	-

Greek Symbols

α	Volume fraction	-
α_{th}	Heat transfer coefficient	$\mathrm{W/(m^2K)}$
β	Geometric angle	$^\circ$
$\beta_{\mathrm{a}}, \beta_{\mathrm{b}}$	Water absorption and desorption rate	m/s
γ	Geometric angle	$^\circ$
γ_{v}	Viscous resistance	$\mathrm{kg/m^2}$
γ_{I}	Inertial resistance	$^\circ$
$\mathit{\Gamma}$	Diffusion transport coefficient	$\mathrm{kg/(m \cdot s)}$
δ	Difference	-
Δ	Laplace operator	-
ε	Porosity	-
η_{act}	Activation polarization	V
η_{ohm}	Ohmic polarization	V
η_{conc}	Concentration polarization	V
θ	Static surface contact angle	$^\circ$
θ_{a}	Advancing surface contact angle	$^\circ$
θ_{c}	Inner contact angle	$^\circ$

θ_r	Receding surface contact angle	$\circ$
θ_K	Dynamic surface contact angle	$\circ$
κ	Surface curvature	1/m
λ	Membrane water content	-
$\lambda_\mathrm{A}, \lambda_\mathrm{C}$	Stoichiometry factor	-
λ_th	Thermal conductivity	W/(m K)
μ	Dynamic viscosity	Pa s
ν	Kinematic viscosity	m^2/s
ξ	Normalized value of liquid water volume fraction	-
ρ	Density	$\mathrm{kg/m}^3$
σ	Surface tension	N/m
σ_P	Proton conductivity	S/m
τ	Residence time	s
τ_ε	Tortuosity	-
φ	General transport property	-
χ	Charge transfer coefficients	-
χ^eff	Effective charge transfer coefficients	-
Ψ_1, Ψ_2	Reaction order coefficients	-
ω	Geometric angle	$\circ$
Ω	Domain	-

Subscript

avg	Average
A	Anode
BPP	Bipolar plate
c	Numerical cell
check	Evaluation
coarse	Coarse mesh size
cond	Conductive
conv	Convective
cool	Coolant
C	Cathode
crit	Critical
eq	Equilibrium
exp	Eperimental
f	Numeric cell face

fine	Fine mesh size
g	Gas
GC	Gas channel
GDL	Gas diffusion layer
H	Hydraulic
in	Inlet
ID	Investigation domain
IP	In-plane
lq	Liquid water
mark	Marked
max	Maximum
min	Minimum
m	Mixture
mem	Membrane
out	Outlet
PEM	Membrane
ref	Reference state
remesh	Remeshing value
seg	Segment
sup	Superficial
tot	Total
TP	Through-plane
W	Water
x	Cross-section
φ	Conservation property

Dimensionless Numbers

Bo	Bond number
Ca	Capillary number
CFL	Courant number
La	Laplace number
Nu	Nusselt number
Pe	Peclet number
Pr	Prandlt number
Re	Reynolds number
We	Weber number

Abbreviations

AMR	Adaptive mesh refinement
BEV	Battery electric vehicle
BPP	Bipolar plate
CAD	Computer-aided design
CC	Current collector
CH-A,CH-C	Anode/Cathode gas channel region
CCM	Catalyst coated membrane
CCMR	Constant coarse mesh refinement
CFD	Computational fluid dynamics
CFS	Continuum surface force
CICSAM	Compressive Interface Capturing Scheme for Arbitrary Meshes
CL	Catalyst layer
COMP	Compensation region
CV	Control volume
DCA	Dynamic contact angle
DEM	Discrete Element method
DMP	Dispersed Multiphase model
EMP	Eulerian Multiphase model
EOD	Electro-osmotic drag
FF	Flow field
FCEV	Fuel cell electric vehicle
FVM	Finite volume method
GC	Gas channel
GDL	Gas diffusion layer
GHG	Green house gases
HRIC	High resolution interface capturing
HOR	Hydrogen oxidation reaction
HT	High temperature
HX	Heat exchanger
LES	Large eddy simulation
LMP	Lagrangian Multiphase model
LT	Low-temperature
MEA	Membrane electrode assembly
MEM	Membrane
MMP	Mixture multiphase model
MPL	Micro-porous layer
NMR	Nuclear magnetic resonance

OCV	Open cell voltage
ORR	Oxygen reduction reaction
PCI	Phase-change induced
PDE	Partial differential equation
PEM	Polymer electrolyte/Proton exchange membrane
PEMFC	Proton-exchange membrane fuel cell
PFSA	Perfluorosulfonic acid
PLIC	Piecewise Linear Interface Construction
PTFE	Polytetrafluoroethylene (Teflon)
RAM	Random access memory
RANS	Reynolds-averaged Navier-Stokes
SCA	Static contact angle
SLIC	Simple Line Interface Calculation
SOFC	Solid oxide fuel cell
VOF	Volume-of-Fluid
WALE	Wall-Adapting Local Eddy-Viscosity

1 Introduction

In 2014, the European Council stipulated a reduction in greenhouse gases (GHGs) of 40 % by 2030 (compared to 1990) within the members of the European Union. Contributing to almost a quarter of the total GHG emissions, the transportation sector requires further measures, such as an increase in electrification of aviation, road and maritime transportation in order to achieve the set target. A considerable part of road transportation is thereby covered by conventional combustion engine vehicles. [1]

Fuel cell electric vehicles (FCEVs) are a promising addition to battery electric vehicles (BEVs) in substituting conventional propulsion systems [2]. State-of-the-art BEVs still suffer to fulfill customer needs regarding driving ranges and charging times, while being affordable for the vast majority [3, 4]. With additional demands towards advancing digitalization and transformation to autonomous driving, leading to further shortenings in driving range [5], the necessity of a high energy density vehicle increases. The short refueling times (< 5 mins) [6] in combination with high energy densities, leading to long driving ranges (> 500 km), ensures an ongoing driving experience with FCEVs, which is already realizable nowadays [7].

FCEVs run on low temperature polymer electrolyte fuel cells (LT-PEMFCs), producing on-board electricity through the conversion of hydrogen and oxygen into water. In order to increase the power output of around 300 W for a single cell to more than 100 kW, multiple cells are connected in series to a fuel cell stack. While LT-PEMFC stacks have high power outputs, their performance is strongly dependent on the water management of each cell. The membrane demands a humid environment to retain proper conductivity, whereas an excess of water leads to mass transport losses and therefore cutbacks in cell performance. This contradictory process of water demand and removal requires an efficient operating strategy of the fuel cell stack. Either experimental or simulative techniques can be used for this purpose. High costs, in combination with low temporal resolution [8] of experimental state-of-the-art measurement techniques make them economically unfeasible for industrial application. Simulative techniques, on the other hand, are cost efficient and are able to cover all investigation scales [9]. With their ability of resolving the water management in detail on multiple scales, computational fluid dynamics (CFD) simulations are a viable approach for an investigation of the underlying processes inside a fuel cell, which can be used to develop efficient operation strategies.

2 Goal and Outline

The goal of the present work is the development of a three-dimensional stack model with explicit single cell modeling. The model shall be of multiphysics nature, including mass, energy, multiphase and species transport and therefore be able to resolve the water management inside the various layers of each cell. A deep dive into the investigations of the two-phase flow phenomena inside PEMFC gas channels shall be provided in addition. The various two-phase phenomena with their characteristic pressure drop profiles are supposed to be studied. The results shall be used for the derivation of a pressure drop correlation, which is able to predict the pressure drop in gas channels for a given set of gas velocity and liquid water saturation values. The correlation is supposed to be set up in a way, that it can be implemented into the stack model.

An introduction on the theoretical principles of PEMFCs with a focus on water management and simulations of PEMFC stacks is given in chapter 3. Chapter 4 contains a summary of the numerical models used for Volume-of-Fluid (VOF), as well as PEMFC simulations. Investigations of two-phase flows in single gas channels are presented in chapter 5, including studies via adaptive mesh refinement (AMR) and constant coarse mesh refinement (CCMR). Paramteric studies, based on the CCMR method, are given in addition to a two-phase flow permeability correlation derivation. In chapter 6, detailed single cell investigations, which are used as reference results for the subsequent stack modeling, are performed and validated against experimental single cell data. The stack modeling creation is addressed in chapter 7. A validation of the modeling is provided on a single cell basis against simulative detailed cell data. The validated simplified single cell is combined into a 60-cell stack. The simulative investigation of the stack results is elaborated in chapter 8. The final chapter gives a summary of the present work and an outlook.

3 Theoretical Background and Literature Review

3.1 Proton Exchange Membrane Fuel Cells (PEMFCs)

The following section gives an introduction into low temperature polymer electrolyte membrane fuel cells (PEMFCs), as well as the underlying physical processes. Due to the orientation of the thesis, a focus shall be placed on the water management and transport phenomena within the functional layers. As for the application area, the use within the automotive sector is target area of all investigations.

3.1.1 Reactions and Polarization Curve

A low temperature PEMFC is an electrochemical conversion device, used for the production of usable current through the reaction of hydrogen and oxygen. Figure 3.1 shows a schematic section of a single PEMFC under operation. Hydrogen gas is thereby supplied via anode flow field gas channels, being formed by the bipolar plate (BPP), (ideally) uniformly distributed within the gas diffusion layer (GDL) and directed into the anode catalyst layer ($\mathrm{CL_A}$). During a catalytic oxidation reaction of hydrogen (HOR) on a Pt-based catalyst, hydrogen molecules are converted to protons and electrons according to reaction (R1).

$$\mathrm{H_2} \rightarrow \mathrm{2H^+} + \mathrm{2e^-}. \tag{R1}$$

Due to the electrically insulating membrane, electrons have to pass the domain via an external circuit, generating usable current. Despite the presence of a counter directed electric potential, the generated protons are able to move within the ionomer phase of the $\mathrm{CL_A}$, through the polymer electrolyte membrane (PEM) into the ionomer of the cathode catalyst layer ($\mathrm{CL_C}$). Oxygen gas, usually in the form of air, is supplied to the cell via the cathodic flow field channels formed by the cathode BPP. Subsequent to a diffusion through the cathodic GDL, a reduction of oxygen molecules (ORR) with protons and electrons on the $\mathrm{CL_C}$ surface, according to

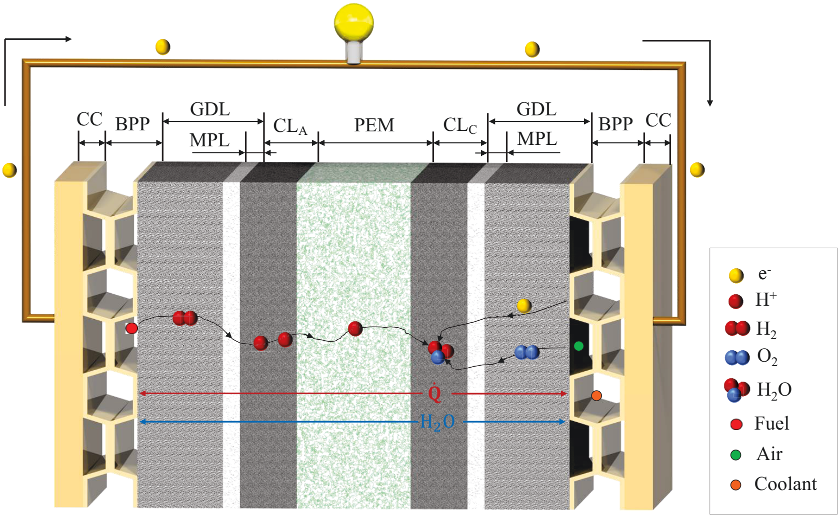

Figure 3.1: Schematic cut-plane through a low temperature PEMFC single cell

reaction (R2), leads to the production of water. While the HOR can be regarded as energetically neutral, the ORR is exothermal, resulting in a release of excess heat during the water production.

$$2H^+ + \frac{1}{2}O_2 + 2e^- \rightarrow H_2O \tag{R2}$$

The combination of both partial reactions (R1) and (R2) gives the total reaction (R3).

$$H_2 + \frac{1}{2}O_2 \rightarrow H_2O\,. \tag{R3}$$

The thermodynamic maximum work output of reaction (R3) can be described as the reaction's change in Gibbs free-energy ΔG_0. The relationship between ΔG_0 and standard potential U_0 is defined in equation (3.1), using z, corresponding to the amount of transferred electrons, as well as the Faraday constant F. The subscript 0 refers to standard conditions.

$$U_0 = -\frac{\Delta G^0}{zF} \tag{3.1}$$

Using $\Delta G^0 = -228.6\,\mathrm{kJ/mol}$ (water production in gas form), $F = 96485\,\mathrm{C/mol}$ and $z = 2$, this leads to a value of 1.19 V for U_0. The thermo-neutral potential U_0^{H}, using the total reaction enthalpy ΔH^0, including entropic losses, can be calculated according to equation (3.2).

$$U_0^{\mathrm{H}} = -\frac{\Delta H^0}{zF} \tag{3.2}$$

With ΔH^0 = –241.8 kJ/mol, this gives a value of U_0^{H} = 1.25 V. The theoretical maximum efficiency of a PEMFC η_{th} is given as the fraction of usable to chemically stored energy (see equation (3.3)).

$$\eta_{\mathrm{th}} = \frac{\Delta G^0}{\Delta H^0} \tag{3.3}$$

Using the values of free gibbs enthalpy ΔG^0 and reaction enthalpy ΔH^0, a maximum theoretical efficiency value of 94.6% can be determined. When using the values for a production of water in liquid state, this value is reduced to 82.9%.
A relationship between the produced current within a cell I and the molar flow of reaction gases that are consumed or produced $\dot{n}_i$ is given by Faraday's law (see equation (3.4)).

$$\dot{n}_{\mathrm{i}} = \frac{I}{zF} \tag{3.4}$$

The value of the the maximum achievable potential U_0 is further lowered due to gas concentration dependencies, hydrogen-crossover, mixed potentials of PtO or H_2O_2 and deviations from the standard conditions. [10] The dependence of the electrode potential regarding gas concentrations is given by the application of the Nernst equation on reaction (R3) (see equation (3.5)). The other mentioned contributions are summed in U_{contr}.

$$U_{\mathrm{N}} = U_0 - \frac{\Re T}{zF} \ln \frac{a_{\mathrm{H_2O}}}{a_{\mathrm{H_2}}\, a_{\mathrm{O_2}}^{1/2}} + U_{\mathrm{contr}} \tag{3.5}$$

U_{N} gives the thermodynamic maximum potential of a cell, reduced by kinetic losses included in U_{contr}, using the standard potential U^0 (1.19 V), the ideal gas constant $\Re$ (8.314 J/(mol · K)), the absolute temperature T, the number of transported electrons (z = 2 for the PEMFC) as well as activities of species a_i of reaction (R3). The activities are defined as the ratio of partial pressure p_i to reference pressure p^0 shown in equation (3.6).

$$a_i = p_i/p^0 \qquad i = \mathrm{H_2}, \mathrm{O_2}, \mathrm{H_2O} \tag{3.6}$$

Figure 3.2 shows a typical polarization and the corresponding power density curve with all aforementioned potential values, as well as irreversible losses.
The real cell voltage U_{cell} differs from the reversible potential U_{N} due to irreversible losses η_i (see equation (3.7). As shown in figure 3.2, three main contributions can be identified, that increase with higher current. With increasing current drawn from the cell, ohmic losses η_{ohm} increase in significance, being a result of irreversible losses during the transport of protons and electrons through the various layer. Thereby a proportionality between current and voltage drop is present, which can be observed as a linear fall of the polarization curve.

$$U_{\mathrm{cell}} = U_{\mathrm{N}} - \eta_{\mathrm{act}} - \eta_{\mathrm{ohm}} - \eta_{\mathrm{conc}} \tag{3.7}$$

In the low current region, activation losses η_{act} are predominant, occurring due to finite reaction rates on the electrode surfaces. A strong initial drop of the polarization curve is observed.

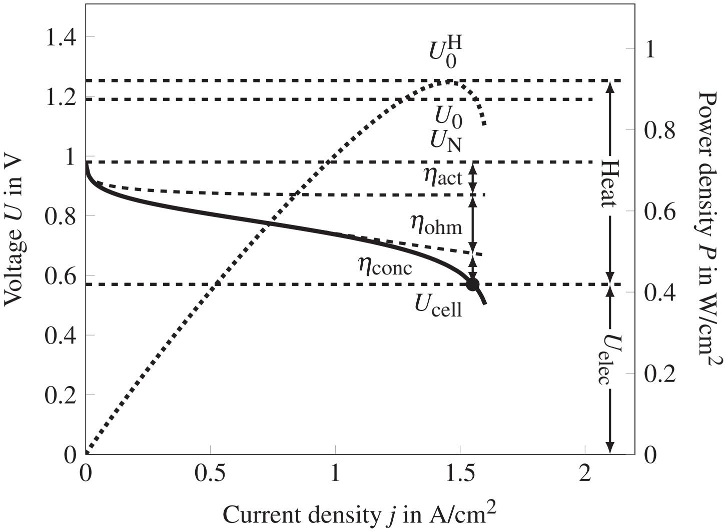

Figure 3.2: General polarization (solid) and power density curve (dotted) of a single PEMFC.

For higher current densities, the losses are mainly dominated by concentration losses η_{conc}, leading to an enhanced drop in voltage. Experimentally determined polarization curves are fitted using empirical approaches. Equation (3.8) shows a typical regression function, which is also applied on the experimental data obtained in the present study. [11]

$$U_{\mathrm{Cell}} = U_{\mathrm{N}} - C_1 \log\left(\frac{j + C_2}{C_2}\right) - C_3 j - C_4 \left[\exp\left(C_5 j\right) - 1\right] \tag{3.8}$$

Variables C_1 to C_5 are fitting parameters.
In the following, the functional layers of a PEM fuel cell are described.

3.1.2 Functional Layers of PEMFCs

All components of a PEMFC are described in respect to the cell design used throughout the thesis. Figure 3.3 shows a sketch of a membrane-electrode-assembly (MEA) in-between two bipolar plates (BPP).
A PEM is incorporated in between anodic and cathodic catalyst layers, forming the catalyst coated membrane (CCM). The CCM is laminated into a subframe and GDLs are attached on both sides of the catalyst layers, giving the membrane electrode assembly (MEA). The main function of the subgasket is an electric insulation of the bipolar plates towards each other. At the same time, an overflow of gases inside distributor and collector gas channels of anode and cathode is prevented. The combination of one MEA in-between two bipolar plates gives a PEM fuel cell.

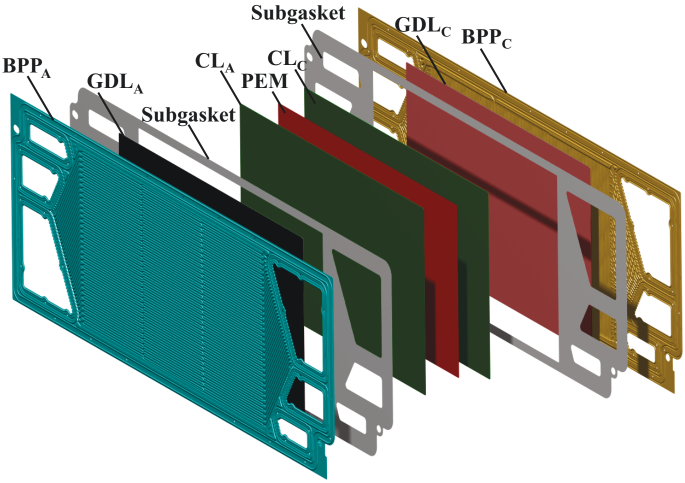

Figure 3.3: PEM fuel cell functional layers

In the following, the functional layers of a PEMFC shall be introduced in detail.

Polymer Electrolyte Membrane (PEM)

The main purpose of polymer electrolyte membranes is the prevention of direct H_2/O_2-contact via spatial separation of anode and cathode compartment while conducting protons and being electrically insulating. At the same time, membranes provide a mechanical stability to the adjacent catalyst layers of anode and cathode. The share of electrons that is directly transported through the membrane, referred to as cross-current, is contributing to the priory discussed drop in voltage from U_0 to U_N. Proton conductivity is a strong function of membrane humidification, whereas increasing membrane water contents λ result in an enhancement of proton conduction. The relationship between water content λ and the water concentration c_{H_2O} is defined in equation (3.9).

$$\lambda = \frac{EW}{\rho_{PEM}} c_{H_2O} \tag{3.9}$$

EW denotes the equivalent weight, ρ_{PEM} the membrane density and c_{H_2O} the water concentration. The equivalent weight *EW* is defined as the ratio of dry ionomer mass to moles of sulfon acid groups (SO_3^-).

As for the composition, perfluorosulfonic acid ionomer membranes are the state-of-the-art material, with Nafion© being the most prominent representative. Thereby a construct of hydrophobic polytetrafluoroethylene (PTFE) backbone with hydrophilic sulfonic groups as side chains is present. A comprehensive study on PEMs is given by *Zhang et al.* [12]

Gas Diffusion Layer (GDL)

The main function of the gas diffusion layer is the uniform distribution of gases and effective removal of water to the gas channels (GCs), as well as conduction of electrons and removal of heat through the GC/GDL land area. In addition, it provides mechanical stability to the adjacent functional layers. State-of-the-art gas diffusion layers (GDLs) are carbon based multi-layered materials, consisting of a macro-porous substrate with pore sizes of 1-100 µm and a micro-porous layer (MPL) with pore sizes of a few hundred nm. Usual substrate materials are carbon cloth or non-woven carbon, which are hydrophobically treated with agents e.g. PTFE, in order to adjust the wettability of the surfaces. [14]

The MPL is fabricated through the deposition of an ink, consisting of carbon black powder in combination with a hydrophobic agent (typically PTFE), on one side of the substrate. Since the MPL ink penetrates into the substrate during the formation process, a meso-porous transition region is created, rather than a sharp joint between the two layers. The integration of a MPL enhances the performance of the cell through an improvement of the water management, whereas the exact mechanisms responsible are still under debate [15]. Various studies claim an optimized water transport in the functional layers through an adjustment of PTFE content within the MPL [16]. An enhanced removal during flooding conditions, as well as an improved water retainment during dry conditions is postulated as the root cause. Another possible reason is the improvement of thermal and electrical contact to between CL and substrate. An additional benefit is the mechanical stability it provides, therefore decreasing the likelihood of a puncturing of the membrane through GDL fibers.

A comprehensive study of recent developments on GDLs for PEMFC applications is given by *Park et al.* [17].

Catalyst Layer (CL)

PEMFC catalyst layers are usually carbon supported catalysts with ionomer layer coverage. The catalyst is typically composed of Pt-alloy-based nanoparticles, being dispersed on a high surface area carbon black support. Ionomer material consists of a perfluorinated polymer backbone with sulfonic acid terminated side-chains. [19]

Protons and electrons, which are produced on the anodic catalyst surface via HOR, have to be transferred to the cathode catalyst surface. The carbon support of the catalyst provides transport paths for electrons through electric conduction, while the ionomer allows an effective transport of protons.

Electrodes of cathode and anode mainly differ in the amount of Pt-loading and alloy components used. State-of-the-art anodic catalyst layers go as low as $0.05\,\mathrm{mg_{Pt}/cm^2}$, whereas, due to the nature of the slow ORR, cathodic catalyst still exist in the order of $0.1\,\mathrm{mg_{Pt}/cm^2}$. Pore sizes of catalyst layers vary from 20-100 nm. [20]

Bipolar Plate (BPP)

The MEA is compressed in-between two bipolar plates, giving one fuel cell. The bipolar plate's main purposes are the uniform supply of reactant gases, while effectively removing water, separating the reactant gases from the coolant and the collection of electric current. Both reaction gases, as well as the coolant are supplied to the cell via flow field channels, being formed by the bipolar plate. Various types of flow field design exist, which can immensely alter the amount of diffusive and convective transport between channels and bipolar plate, therefore influencing the performance of the cell. The focus of further explanations is exclusively focused on the flow field designs used in the present work. A comprehensive study of various flow field designs and their influence on the PEMFC performance is given in [21].

The contact area between bipolar plates and GDLs is referred to as the land area, whereas the remaining channel to GDL contact face is the channel area. The contact resistance in the land area, which is a function of the cell compression, has a significant contribution to the overall cell performance, hence has to be reduced to a minimum. [22]

The bipolar plate design used within the present work is shown in Figure 3.4. The cathode flow field distributor, as well as collector, have 34 parallel channels with constant trapezoidal cross-section, being attached to the active area. Every channel is separated into two smaller channels with variable cross-section area, giving 68 channels in total. This variations occurs as alternating conical contractions and expansions i.e. one channel cross-section is conically expanding along the flow direction while the neighboring is contracting. The induced pressure difference between neighboring channels leads to convective under-the-land flow, enhancing the oxygen distribution within the GDL while removing water accumulations in the land area. Additionally, two gas redistribution sections are implemented (see magnified middle section in Figure 3.4a). The interconnection of two channels with different inlet channels ensures the supply of gas in downstream sections in the case of an upstream channel blocking. The last

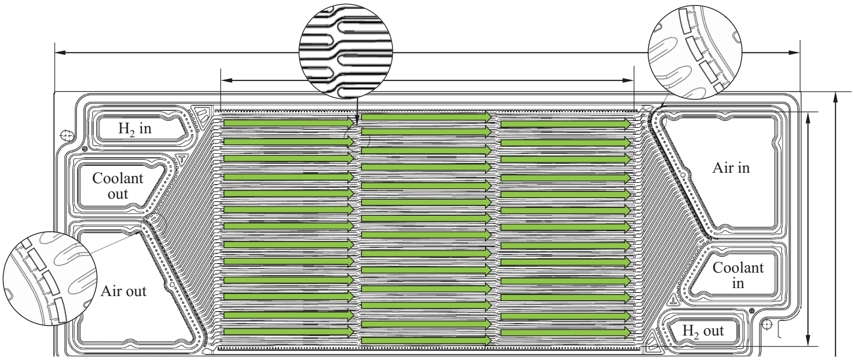

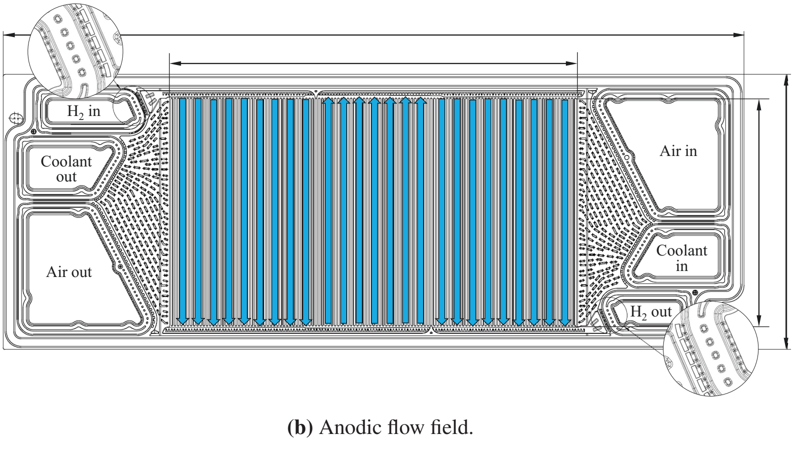

(b) Anodic flow field.

Figure 3.4: Automotive fuel cell flow field with flow direction of gases.

The anode flow field is separated vertically into three sections. The flow field concept is a hybrid between a parallel and serpentine design, whereas inside one section parallel channels with constant trapezoidal cross-section are vertically co-flowing. On the upper and lower end of the plate, collector regions are positioned, collecting and redirecting the mass flows of one section into the subsequent one. In comparison to the cathode side, significantly higher pressure drops can be found (see section 6.5).

The structure of the coolant flow field is comprised of the volume, formed when combining the flow fields of anode and cathode. Coolant enters and exits the domain in co-flow with the cathode flow. The cathodic coolant flow is directly fed from the distributor, while the anode side shows dead-end configurations and is exclusively supplied through the cathodic coolant flow within the active area. In addition, a both-sided bypass coolant flow, connected to the anodic coolant channels, is present.

In order to increase the power output of a PEMFC, multiple cells are connected to a stack in series. The average current within each cell stays constant, while the voltages differ according to local conditions. The difference of thermo-neutral potential to real cell potential is dissipated as heat.

Due to the focus of the following work, a deep-dive into water management inside PEMFCs shall be given in the following.

3.2 Water Management in PEMFCs

The water management of PEMFCs is of high importance for the stable operation under high performance. A balance between water retention and removal has to be ensured in order to keep ohmic losses low by humidify the membrane, while minimizing mass transport losses by preventing water blockage.

Water is found to be present in three phases within the various layers of the PEMFC cell i.e. gaseous, liquid and dissolved. The physical transport phenomena vary, depending on which region and state water is found in. The regions can be divided into three subregions with equivalent water transport mechanisms, namely the PEM (incl. the ionomer phase of the CL) and all miscellaneous porous regions (GDL (incl. MPL) and CL) and the GCs. The transport mechanism within each subregion will be elaborated in the following.

Membrane Water Transport

Water transport between the anode and cathode compartment is possible via prior absorption into the ionomer, followed by a movement through the membrane, as well as a subsequent desorption into the opposite compartment. The transport is driven by two main transport processes, the electro-osmotic-drag (EOD) through migration and (back-) diffusion. The migration results as a consequence of the applied electric field, inducing the transport of protons as hydrated complexes such as H_3O^+, dragging water from the anode to the cathode side. Diffusion occurs, whenever a through-plane concentration gradient of water can be found. As the water production occurs on the cathode, a diffusion driven flux towards the anode is often present, referred to as back-diffusion.

The dominance of either migration or diffusion is strongly determined by the operation point, as well as the design of the cell. High current densities result in a dominance of EOD-driven water transport, often leading to a dry-out of the anode side. Low current densities on the other side, result in a strong dominance of back-diffusion to the anode side. The coexistence of the two processes leads to a complex situation, requiring a sophisticated operation strategy and cell design. A detailed summary of the water transport phenomena in PEMs is given by *Jiao et al.* [13].

Water Transport in Porous Media

The water transport inside porous regions is defined by the coexistence of multiple phenomena. The capillary-driven and phase-change-induced flow (PCI) are herein the most prominent ones. PCI-flow is driven by a gradient in vapor pressure, as a result of local temperature differences, leading to phase change of water. The dominance of a transport process is strongly influenced by the operation point of the fuel cell. Thereby, higher temperatures and higher current densities lead to elevated temperatures and therefore result in a dominance of PCI-flow. Capillary transport on the other hand is favored at lower operating temperatures, and therefore also low current densities.

As a result of smaller pore sizes, Knudsen diffusion becomes one promiment transport mechanisms in MPLs and CLs, whereas stronger effects are found within the CL due to smaller pore sizes. [13]

A comprehensive review on the water transport inside porous media is given by *Andersson et al.* [18].

Water Transport in Gas Channels

The occurance of water under varying local conditions inside gas channels, leads to the formation of various two-phase flow regimes. These are usually subdivided into four main groups, shown in Figure 3.5.

The occurance of a flow regime is thereby accompanied by a characteristic two-phase pressure drop trend. [23] Mist flow, which occurs when liquid water is dispersed into a fine mist of small droplets with negligible influence on the single-phase gas flow shows low, constant pressure drop values that are consistent with single-phase values. Mist flow can be found in configurations with very high gas velocities in combination with low amounts of liquid water.

An increase in liquid water, leads to the built-up of large droplets and the formation of droplet flow, showing an instationary pressure drop trend with a stronger influence on the gas flow. A further increase of liquid water, leads to a transition into film flow accompanied by the formation of a thin film, being prensent along the walls of the channel. Due to channel blockage during the transition of emerging droplets into the continuous film, an instationary pressure drop is observed [23]. Higher amounts of water, as well as lower gas velocities, results in the formation of slug flows. Slug flow is accompanied by a consecutive built-up and release of pressure after a slug has exited the channel, leading to a constant pressure drop with local temporal maxima in pressure.

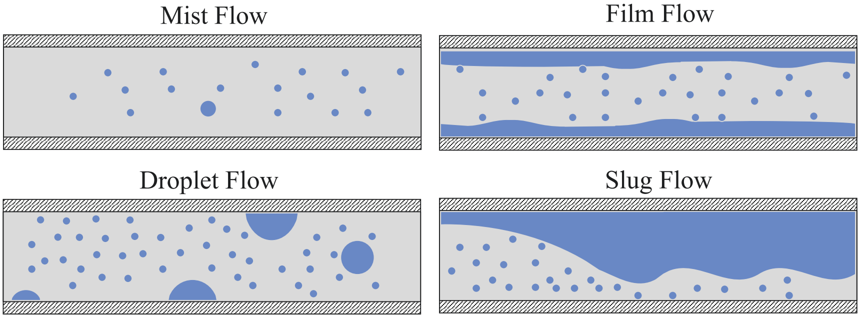

Figure 3.5: Two phase flow regimes inside PEMFC gas channels.

The various flow regimes can be characterized using dimensionless quantities. A summary of the most important dimensionless numbers for the application in two-phase flows is given in Table 3.1.

Table 3.1: Dimensionless numbers for the characterization of two-phase fluid flows.

Name	Definition	In words
Reynolds number	$Re = \frac{\rho\, u\, d_\mathrm{h}}{\mu}$	$\frac{\text{Inertial forces}}{\text{Viscous forces}}$
Capillary number	$Ca = \frac{\mu\, u}{\sigma}$	$\frac{\text{Viscous forces}}{\text{Surface tension}}$
Weber number	$We = \frac{\rho\, u^2\, d}{\sigma}$	$\frac{\text{Inertial forces}}{\text{Surface tension}}$
Bond number	$Bo = \frac{\Delta\rho\, g\, d^2}{\sigma}$	$\frac{\text{Gravitational forces}}{\text{Surface tension}}$
Laplace number	$La = \frac{\Delta\rho\, \sigma\, d}{\mu^2}$	$\frac{\text{Surface tension}}{\text{Internal viscous forces}}$

Thereby, ρ denotes the density, u the velocity, u_{sup} the superficial velocity and μ the dynamic viscosity of the bulk phase. For the application in PEMFC gas channels, the gas is defined as the bulk phase. The characteristic diameter d has to be chosen according to the characterized system of fluids. Variable σ denotes the surface tension, $\Delta\rho$ the density difference between gas and liquid phase and g the gravitational acceleration (9.81 m/s^2). The definition of the hydraulic diameter is given in equation (3.10).

$$d_{\text{h}} = 4\,\frac{A_{\text{x}}}{O_{\text{x}}} \tag{3.10}$$

A_{x} corresponds to the cross-sectional area of the pipe and O_{x} to the respective wetted perimeter. The Reynolds number Re is the most common dimensionless dimensionless quantity in fluid mechanics, defining the transition between laminar and turbulent flows. For pipe flows, a laminar flow criterion is usually given as $Re < 2300$.

The Capillary, Weber and Bond number are putting the effects of viscous, inertial and gravitational forces in perspective to the surface tension. Spherical droplets, which are characterized through a dominance of surface tension are therefore present for low numbers of the latter three. An increase on the other hand, leads to the deformation of the droplet as a result of the present force.

Various experimental, as well as simulative studies have been carried out to investigate these flow regimes and develop correlations to predict the two-phase pressure drop. These are described in the following.

3.3 Investigation of the Water Management in PEMFC Gas Channels

Numerous attempts have been made in literature to investigate the water management inside PEMFCs, using experimental, as well as simulative approaches. An overview of the most common techniques is given in the following.

3.3.1 Experimental Investigation Techniques

In order to optimize the PEMFCs water management, the underlying phenomena have to be fully understood at first. Herefore, various experimental approaches can be found in literature, using in-situ, as well as ex-situ techniques [24, 25]. Numerous studies have been conducted, using transparent bipolar plates to directly visualize the water movement inside gas channels

[26, 27]. Achieving electrical contact to the adjacent GDL, while being transparent and preferably not influencing the operation conditions, makes the construction of the experimental setup rather complicated. The alteration of the bipolar plate material almost always leads to changes in the surface structure (e.g. surface contact angle), which influences the two-phase transport inside the gas channels, leading to questionable results.

Other studies have been carried out, using nuclear magnetic resonance (NMR) imaging for the visualization of liquid water in the cell. One drawback of this technique is the attenuation of the signal in carbon layers, making it unusable for investigation in GDLs. [28]

Another group of visualization techniques are beam interrogation methods, including X-ray tomography, electron microscopy as well as neutron radiography. The only non-invasive, in-situ measuring technique, having been succefully applied to operating PEMFCs are X-ray and neutron radiography measurements [8, 29–31]. Still, both techniques suffer from low temporal, as well as spatial resolution making a capturing of dynamic processes difficult.

A comprehensive review on the various experimental visualization techniques for water inside PEMFCs is given by *Bazylak. et. al.* [24] and *Ji. et. al.* [25].

All priory discussed approaches show difficulties of either being invasive and therefore altering the conditions within the measuring regions or not representing the original setup correctly in the first place. Others show difficulties regarding spatial and temporal resolutions. In order to overcome these issues, simulative investigation techniques can be used. These will be discussed in the following.

3.3.2 Simulative Investigation Techniques

The most prominent group of simulative techniques for the investigation of water phenomena in gas channels are CFD multiphase simulations. Among these, most literature studies rely on an application of the Volume-of-Fluid method, which is able to dynamically resolve the interface between gas and liquid flow. Therefore, detailed analysis of droplet removal, as well as two-phase flow regimes can be performed. Due to the high computational effort associated with multiphase simulations, investigation domains of gas channels are restricted to short section of up to [32–34] 5 mm. The introduction of liquid water into the computational domain in literature studies is realized via patching of already developed droplets [32–34] or introduction of liquid water source terms [35–38]. The source term values vary around 2 µm, corresponding to around two times of the amount of water, expected over the whole length of the channel at 2.5 A/cm^2 (for the present fuel cell geometry). Water introduction through external pipes attached to the GDL-surface of the channel geometry reduces the flexibility of the approaches when it comes to parametric studies. A patching of droplets [32–34] on the other hand neglects the development process of the droplet, hence leading to inaccuracies in detachment times and therefore droplet sizes. The position of water inlet is often chosen to be in the center of the channel, wheras studies [9, 39] have shown an emergence in wall-adjacent regions. The reason is a favorable accumulation of water in the land area of the GDL/BPP-interface as a result of higher GDL compression and proximity to the coolant channels, leading to favorable water condensation. [18]

The adaptive mesh refinement (AMR) approach (discussed in section 5.3) tackles a major part of the prior discussed difficulties.

Due to the extreme computational effort of detailed two-phase simulation models, cell simulations are based on lumped approaches, such as the mixture multiphase (MMP) model. The model is implemented in the present cell and stack simulations and is described in section 4.2.3. In the following, an overview of literature stack modeling approaches is given.

3.4 Modeling of PEMFC Stacks

Various studies on the simulative investigation of PEMFC stacks have been carried out in prior published studies. Figure 3.6 gives an overview of the of the different stack modeling approaches. These are divided into three categories, (1) 0D-stack models, (2) repetition unit averaging models and (3) models with explicit single cell modeling.

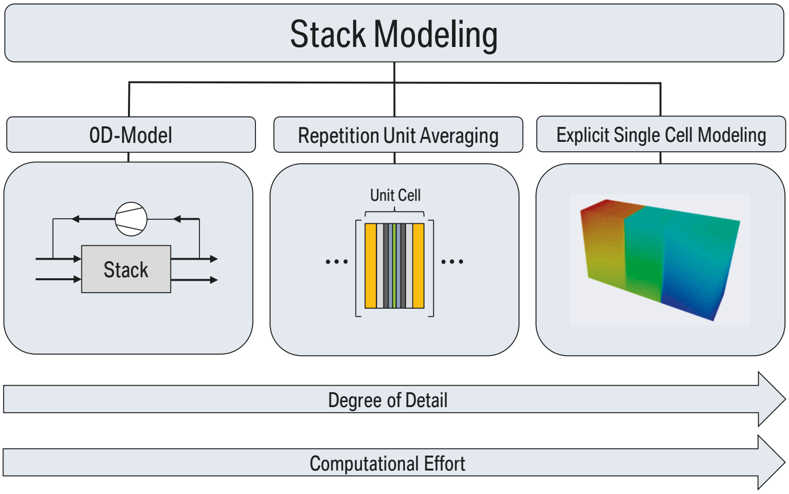

Figure 3.6: Overview of different stack modeling approaches.

0D-approaches have a macroscopic description with no spatial resolution of the stack, which leads to the lowest computational costs [40–43]. Therefore, they are mainly used for the design of fuel cell systems and operation strategies, where transient simulations over large time ranges are performed. Repetition unit approaches show higher degree of detail, while exhibiting increasing computational costs [16]. Thereby, single cells within the stack are modeled as repetition units and coupled in through-plane direction. Models with explicit single cell modeling show the highest detail degree, while also having the highest computational costs [44–49]. The models are set-up, using CFD-based approaches, whereas the majority does not account for liquid water at all (single-phase simplification, HT-PEMFC, or SOFC models) [49] or have limited description.

The present work focuses on the development of a two-phase stack model with explicit cell modeling using a porous-volume approach, coupled with two-phase pressure drop correlations, derived from detailed two-phase single channel simulations.

The following section will provide an overview of the simulation methodology, including a general description of computational fluid dynamics with a focus on two-phase flows, followed by the derivation of the PEMFC model used in the present study.

4 Investigation Methodology

In order to solve problems involving fluid flows via computational fluid dynamics (CFD) approaches, knowledge of the basic governing laws is required. The following section introduces the fundamental conservation equations, including mass, momentum, species and energy equations, as well as necessary spatial and temporal discretization approaches. Subsequently, an overview of the important multiphase approaches, used in the present work, is given, followed by a summary of the PEMFC-specific modeling approaches.

4.1 Computational Fluid Dynamics (CFD)

The investigation of fluid flows requires the description of conservation properties φ as a function of spatial (x,y,z) and temporal changes (t). The Eulerian approach of a spatially-fixed control volume (CV) can be used to describe that relationship. The accumulation of φ inside a CV through convective and diffusive transport, transient changes, as well as other transport terms, can be described through a general, differential form of the conservation equation, shown in equation (4.1).

$$\underbrace{\frac{\partial(\rho\varphi)}{\partial t}}_{\text{Accumulation}} + \underbrace{\mathbf{div}\left(\rho\vec{u}\varphi\right)}_{\text{Convection}} = \underbrace{\mathbf{div}\left(\Gamma\nabla\varphi\right)}_{\text{Diffusion}} + \underbrace{\sum S_{\varphi}}_{\text{Source}} \tag{4.1}$$

Thereby, ρ denotes the density of the fluid, $\vec{u}$ the velocity vector, t the time, Γ a transport coefficient (e.g. diffusion coefficient or thermal conductivity) and S_{φ} a source term including all other sources of the variable φ. The divergence-operator **div** is defined as the sum of spatial derivatives in x-, y- and z-direction of a vector and the Nabla-operator ∇ as the gradient vector of a scalar function.

Momentum Conservation (Navier-Stokes Equation)

Substituting $\varphi = u_i$ within the general conservation form in equation (4.1), leads to the momentum equation for Newtonian fluids in equation (4.13), whereas the right-hand side terms are equivalent to $\sum S_\varphi$.

$$\rho \left(\frac{\partial u_i}{\partial t} + \vec{u} \nabla u_i \right) = -\frac{\partial p}{\partial i} + \mu \, \Delta u_i + \frac{\mu}{3} \frac{\partial}{\partial i} (\mathbf{div}\, \vec{u}) + S_{\mathrm{mom},i} \qquad i = x, y, z. \tag{4.2}$$

Variable p denotes the pressure, u_i the velocity component in i-direction, μ the dynamic viscosity and $S_{\mathrm{mom},i}$ other remaining body forces (e.g. gravitation). The Laplace-operator Δ is defined as the sum of the second spatial derivatives in x-, y- and z-direction of the components of a vector.

Species Conservation

Using $\varphi = w_i$ and $\Gamma = \rho D_i$ on the general conservation form in equation (4.1) leads to the species conservation, shown in equation (4.3).

$$\frac{\partial (\rho w_i)}{\partial t} + \mathbf{div} \left(\rho \, \vec{u} \, w_i \right) = \mathbf{div} \left(\rho \underline{\underline{D_i}} \nabla w_i \right) + S_w \qquad i = x, y, z \tag{4.3}$$

Thereby, w_i denotes the mass fraction of species i, $\underline{\underline{D_i}}$ the anisotropic diffusion coefficient tensor and S_w the species source term.

Energy Conservation

Using $\varphi = \partial h = c_p \, \partial T$ and $\Gamma = \lambda_{\mathrm{th}}/c_p$ on equation (4.1) gives the energy conservation, shown in equation (4.4).

$$\frac{\partial (\rho c_p T)}{\partial t} + \mathbf{div} \left(\rho \, \vec{u} \, c_p \, T \right) = \mathbf{div} \left(\underline{\underline{\lambda_{\mathrm{th}}}} \, \nabla T \right) + S_T \qquad i = x, y, z \tag{4.4}$$

Thereby, c_p denotes the specific heat of the fluid, T the fluid temperature, $\underline{\underline{\lambda_{\mathrm{th}}}}$ the thermal conductivity of the fluid and S_T all further energy contributions.
In order to solve the conservation equations, a spatial (and if applicable temporal) discretization has to be performed. The discretization procedure is elaborated in further detail in the following section.

4.1.1 Spatial and Temporal Discretization

The priory described partial differential equations (PDEs) exhibit no analytic solution and therefore have to be solved in a numeric manner. In order to find an approximate solution for the PDEs, discretization methods are used that lead to a transformation of the PDEs into a system of algebraic equation that can be solved on a computer. The continuum is approximated to finite segments in space and time. The content of the following section arises from *Ferzinger et. al.* [50], who gives a comprehensive overview of the descretization methods.

Commercial CFD codes are almost exclusively based on the Finite Volume method (FVM) for the discretization process. The domain is split into a finite number of non-overlapping control control volumes (CV), creating the numerical grid, also referred to as mesh. The priory defined PDEs are applied on the center of every CV of the domain. An integration over each CV in combination with the application of the Gauss divergence theorem leads to the integral form of the general conservation equation (4.5).

$$\underbrace{\frac{\partial}{\partial t}\int_V \rho\varphi \,\mathrm{d}V}_{\text{Accumulation}} + \underbrace{\oint_{S_V} \rho\varphi\vec{u}\vec{n}\,\mathrm{d}S}_{\text{Convection}} = \underbrace{\oint_{S_V} \Gamma\,\nabla\varphi\vec{n}\,\mathrm{d}S}_{\text{Diffusion}} + \underbrace{\sum\int_V S_\varphi\,\mathrm{d}V}_{\text{Source}} \tag{4.5}$$

Thereby, $\vec{n}$ denotes the normal vector on surface S.

The volume and surface integrals of the general conservation equation have to be approximated subsequently. For the volume integrals, this is realized by using the integrand value of the cell center according to equation (4.6).

$$\int_V \varphi\,\mathrm{d}V \approx \varphi_\mathrm{c}(V)\,V \tag{4.6}$$

Thereby, φ denotes the integrand and $\varphi_\mathrm{c}(V)$ the corresponding center value of the CV. For the approximation of surface integrals, a prior splitting into multiple surface integrals according to equation (4.7) at the respective boundary is performed.

$$\oint_{S_V} \varphi\,\mathrm{d}S = \sum_i \int_{S_i} \varphi\,\mathrm{d}S \tag{4.7}$$

Subsequently, an approximation of the integrals by application of the numerical quadrature is carried out, as shown in equation (4.8).

$$\int_{S_i} \varphi\,\mathrm{d}S \approx \varphi_\mathrm{c}(S_i)\,S_i \tag{4.8}$$

Determining the surface center values $\varphi_\mathrm{c}\,(S_i)$ requires a prior interpolation step. Multiple methods are available, of which the linear interpolation is one of the less complicated. The value is determined through a linear interpolation between CV center values of upwind and downwind

cells. Higher order interpolation schemes, leading to higher interpolation accuracy are also available, however resulting in higher computational efforts.
The discretization steps lead to a transformation of the conservation equations into a system of linear algebraic equations that can be solved using a computer.

For transient simulation, a temporal discretization has to be performed in addition. Herefore, the so called marching methods are applied, which are subdivided into explicit (forward) and implicit (backward) Euler methods, as well as different higher order schemes (e.g. Runge-Kutta).
The explicit Euler method uses the solution of the current time level N in order to approximate the solution at the subsequent time level $N+1$, as shown in equation (4.9).

$$\varphi^{(N+1)} = \varphi^{(N)} + f\left(\varphi^{(N)}, t^{(N)}\right) \Delta t \tag{4.9}$$

Thereby, $\varphi^{(N)}$ denotes the solution of φ at time level N and Δt the time step. All contrubutions from the general conservation besides the accumulation term are summarized in the function f. Within the implicit Euler method, the value of φ is taken at $N+1$ according to equation (4.10).

$$\varphi^{(N+1)} = \varphi^{(N)} + f\left(\varphi^{(N+1)}, t^{(N+1)}\right) \Delta t \tag{4.10}$$

The stability of transient simulations depends on the Courant-Friedrichs-Lewy (*CFL*) number, defined in equation (4.11).

$$CFL = \frac{u \Delta x}{\Delta t} \tag{4.11}$$

The variable u denotes the velocity of the fluid, Δt the time step and Δx the distance between two centers of numerical cells. Due to the nature of both discretization methods, a value of CFL < 1 is required for explicit methods, while $CFL >> 1$ can be used in implicit cases.
The following section gives insight into multiphase models for the application in CFD-simulations.

4.2 Modeling of Multiphase Flows

The following sections places a focus on the numerical implementations and models for the investigation of two-phase flow phenomena. An emphasis is placed on the description of the Volume of Fluid and Mixture Multiphase model, due to the relevance within the present work.
Multiphase modeling approaches are generally separated into two families, the Eulerian-Eulerian and Eulerian-Lagrangian models. The Eulerian-Eulerian models treat the different phases as interpenetrating continua, while recording the volume fraction of each phase. Lagrangian approaches rely on a tracking of the dispersed phase, consisting of parcels of particles (Lagrangian) which move through the computational fluid domain, while interacting with the continuous bulk phase (Eulerian). The two classes are furthermore subdivided into various models, which are summarized in the following [65]:

- **Eulerian-Eulerian Models**
  - Eulerian Multiphase (EMP) Model
  - Mixture Multiphase (MMP) Model
  - Volume-of-Fluid (VOF) Model
  - Film Model
- **Lagrangian-Eulerian Models**
  - Lagrangian Multiphase (LMP) Model
  - Discrete Element Method (DEM)
  - Dispersed Multiphase Model (DMP)

The various models differ in their field of application, whereas the VOF model finds wide application in the investigation of two-phase flows in PEMFC gas channels [33, 35–37, 51]. CFD-based fuel cell models are commonly based on an MMP model to account for multiphase flow effects in porous media and gas channels [52–56], due to the computational efficiency of the approach [57].
As for the relevance of the thesis, both models are explained in more detail in the following.

4.2.1 The Volume of Fluid (VOF) Model

The Volume of Fluid (VOF) model uses a Eulerian-Eulerian modeling approach for the simulation of immiscible fluids with clearly defined interfaces. For an isothermal two-phase flow, a single continuity and Navier-Stokes equation for the mixture is solved, as well as an additional equation for the volume fraction of the primary phase.

A general form of the continuity equation, defined analogously to the single-phase case, is shown in equation (4.12).

$$\frac{\partial \rho_{\mathrm{m}}}{\partial t} + \mathbf{div}(\rho_{\mathrm{m}} \vec{u}_{\mathrm{m}}) = S_{\mathrm{m}} \tag{4.12}$$

Here, ρ_{m} is the mixture density, defined in equation (4.16), and $\vec{u}_{\mathrm{m}}$ the velocity vector of the mixture. As one velocity field is solved, all phases share identical velocities.

The momentum equation (Navier-Stokes equation) is given in equation (4.13)

$$\frac{\partial (\rho_{\mathrm{m}} \vec{u}_{\mathrm{m}})}{\partial t} + \mathbf{div}(\rho_{\mathrm{m}} \vec{u}_{\mathrm{m}} \otimes \vec{u}_{\mathrm{m}}) = -\nabla p + \mathbf{div}\, \underline{\underline{T}} + \rho_{\mathrm{m}} \vec{g} + \vec{f}_{\sigma} \tag{4.13}$$

Thereby, $\otimes$ builds the tensor product of two vectors, p is the pressure shared by both phases, $\vec{g}$ and $\vec{f}_{\sigma}$ denote volumetric gravitational and surface tension forces, respectively.
Tensor $\boldsymbol{T}$ is the viscous tensor which can be expressed as following for Newtonian fluids:

$$\underline{\underline{T}} = \mu_{\mathrm{m}} \left(\nabla \vec{u}_{\mathrm{m}} + (\nabla \vec{u}_{\mathrm{m}})^{\mathrm{T}} \right) \tag{4.14}$$

μ_{m} is the mixture dynamic viscosity, defined in equation (4.17). The superscript $^{\mathrm{T}}$ denotes a transposition of a tensor.

The volume fraction of phase i α_i is solved separately, as shown in equation (4.15).

$$\frac{\partial \alpha_i}{\partial t} + \vec{u}_{\mathrm{m}} \nabla \alpha_i = S_{\alpha} \tag{4.15}$$

Neglecting phase-change processes, the volume fraction source term S_{α} becomes 0.
The mixture density and viscosity are calculated as volume fraction weighted sums of the phase properties (see equation (4.16) and (4.17)).

$$\rho_{\mathrm{m}} = \sum_i \alpha_i \rho_i \tag{4.16}$$

$$\mu_{\mathrm{m}} = \sum_i \alpha_i \mu_i \tag{4.17}$$

With the volume fraction α_i, the surface tension term f_{σ} in equation (4.13) can be calculated, using the continuum surface force (CSF) model [58], defind in equation (4.18).

$$\vec{f}_{\sigma} = -\sigma \kappa \nabla \alpha_i \tag{4.18}$$

The variable σ denotes the surface tension, $\nabla\alpha_\mathrm{i}$ the volume fraction gradient normal to the phase interface and κ the curvature of the interface according to equation (4.19).

$$\kappa = \mathbf{div}\left(\frac{\nabla\alpha_i}{|\nabla\alpha_i|}\right) \tag{4.19}$$

In case of a direct contact between phase interface and a solid surface (wall), the VOF algorithm takes contact angle boundary conditions into consideration. The wall-adjacent normal vectors of interface cells are therefore adjusted according to equation (4.20) [58].

$$\vec{n} = \vec{n}_\mathrm{wall,n} \cdot \cos\theta + \vec{n}_\mathrm{wall,t} \cdot \sin\theta\,. \tag{4.20}$$

Here, $\vec{n}$ is the normal vector of phase interface in the relevant numerical cell. $\vec{n}_\mathrm{wall,n}$ and $\vec{n}_\mathrm{wall,t}$ are unit vectors in wall normal and tangential direction, respectively. θ is the contact angle on the wall. Further details on the definition of the contact angle model, implemented into STAR-CCM+, is given in section A.1.5.

4.2.2 High Resolution Interface Capturing (HRIC) Algorithm

The VOF method exhibits numerical difficulties during discretization of the convective term within the volume fraction conservation equation. During the evolution of the two-phase interface, numerical diffusion, leading to smeared interfaces is observed. On the other hand, a monotonic change in variables has to be ensured during the movement process. [59] Two approaches to solve the aforementioned problems are found in literature i.e. the geometric and high-resolution interface reconstruction method. Common approaches, including a geometric representation of the interface are the Simple Line Interface Calculation (SLIC) [60] or Piecewise Linear Interface Construction (PLIC) [61] method. One major drawback of geometrical reconstruction techniques is that they rely on structured grids, posing a restriction on flexibility. A thorough summary of the various VOF-algorithms is given by *Scardovelli et. al* [62]. Techniques that are not bound to this restrictions are high-resolution schemes. The sharpening of the interface is accomplished by an appropriate discretization scheme rather than a geometric reconstruction. The most prominent approaches are the Compressive Interface Capturing Scheme for Arbitrary Meshes (CICSAM) [63] and the High Resolution Interface Capturing (HRIC) [64] algorithm.

As for the relevance of the present work, the HRIC algorithm is explained in further detail. The description is taken from the STAR-CCM+ documentation [65].

The HRIC scheme is designed to mimic the transport of immiscible fluid components, resulting in a scheme that is suited for tracking sharp interfaces. [65] A bounded solution of the volume fraction cell value $\alpha_\mathrm{lq,c}$ is produced between downwind $\alpha_\mathrm{lq,D}$ and upwind $\alpha_\mathrm{lq,U}$ cells in order to avoid nonphysical oscillation of the solution. Normalized values ξ of the liquid water volume fraction α_{lq} are used and defined in equation (4.21) for face (index f) and cell (index c) values.

$$\xi_{\mathrm{f}} = \frac{\alpha_{\mathrm{lq,f}} - \alpha_{\mathrm{lq,U}}}{\alpha_{\mathrm{lq,D}} - \alpha_{\mathrm{lq,U}}}, \quad \xi_{\mathrm{c}} = \frac{\alpha_{\mathrm{lq,c}} - \alpha_{\mathrm{lq,U}}}{\alpha_{\mathrm{lq,D}} - \alpha_{\mathrm{lq,U}}} \tag{4.21}$$

The normalized face value is calculated in the HRIC scheme, as shown in equation (4.22).

$$\xi_{\mathrm{f}} = \begin{cases} \xi_{\mathrm{c}} & \text{if } \xi_{\mathrm{c}} < 0 \\ 2\xi_{\mathrm{c}} & \text{if } 0 \leqslant \xi_{\mathrm{c}} < 0.5 \\ 1 & \text{if } 0.5 \leqslant \xi_{\mathrm{c}} < 1 \\ \xi_{\mathrm{c}} & \text{if } 1 \leqslant \xi_{\mathrm{c}} \end{cases} \tag{4.22}$$

An additional correction is applied on the face value as a function of the local Courant number (*CFL*), as stability enhancement is observed for cases where the time step is too large to ensure a sharp interface resolution. Larger *CFL* numbers result in stronger interfaces smearing.
The *CFL*-corrected face value ξ_{f}^{*} is further corrected by application of an angle factor C_{θ}, as shown in equation (4.23), to prevent wrinkling, occurring when interface and flow direction are aligned.

$$\xi_{\mathrm{f}}^{**} = \xi_{\mathrm{f}}^{*} (\cos\theta)^{\mathrm{C}_{\theta}} + \xi_{\mathrm{C}} [1 - (\cos\theta)^{\mathrm{C}_{\theta}}] \tag{4.23}$$

Using the *CFL*- and C_{θ}-corrected face value ξ_{f}^{**}, the volume fraction can be expressed as shown in equation (4.24).

$$\alpha_{\mathrm{lq,f}}^{\mathrm{HRIC}} = \xi_{\mathrm{f}}^{**} (\alpha_{\mathrm{lq,D}} - \alpha_{\mathrm{lq,U}}) + \alpha_{\mathrm{lq,U}} \tag{4.24}$$

A further tuning parameter is the sharpening factor C_{α}, defined in equation (4.25), taking up values from 0 to 1.

$$\nabla \cdot \left(\mathrm{C}_{\alpha} |\vec{u}| \frac{\nabla \alpha_{\mathrm{lq}}}{|\nabla \alpha_{\mathrm{lq}}|} \alpha_{\mathrm{lq}} (1 - \alpha_{\mathrm{lq}}) \right) \tag{4.25}$$

The sharpening factor is used to further reduce numerical diffusion, whereas a value of 0 corresponds to no additional reduction and 1 to no numerical diffusion. Increasing the factor unreasonably may lead to non-physical alignment of computational grid lines and two-phase interface.

4.2.3 Eulerian Mixture Multiphase (MMP) Model

The Eulerian Mixture Multiphase (MMP) model represents a simplified Eulerian-Eulerian modeling approach, used for an efficient, while less accurate, investigation of multiphase problems [57]. Instead of solving per-phase momentum equations, a single equation for the two-phase mixture is used. The distinction between phase velocities can be achieved through implementation of slip velocity models, leading to an overall reduction in computational effort.

The mass conservation of the mixture is equivalent to the VOF definition and given in equation (4.26).

$$\frac{\partial \rho_{\mathrm{m}}}{\partial t} + \mathbf{div}(\rho_{\mathrm{m}} \vec{u}_{\mathrm{m}}) = S_{\mathrm{m}} \tag{4.26}$$

The momentum conservation of the mixture, is given in equation (4.27), with the definition of the drift velocity of phase i, $\vec{u}_{\mathrm{dr,i}}$ in equation (4.28).

$$\frac{\partial}{\partial t}\left(\rho_{\mathrm{m}} \vec{u}_{\mathrm{m}}\right) + \mathbf{div}\left(\rho_{\mathrm{m}} \vec{u}_{\mathrm{m}} \otimes \vec{u}_{\mathrm{m}}\right) = -\nabla p + \mathbf{div}\, \underline{\underline{T_{\mathrm{m}}}} + \rho_{\mathrm{m}} \vec{g} + \vec{f} + \mathbf{div}\left(\sum_i \alpha_i \rho_i \vec{u}^{2}_{\mathrm{dr},i}\right) \tag{4.27}$$

$$\vec{u}_{\mathrm{dr},i} = \vec{u}_i - \vec{u}_{\mathrm{m}} \tag{4.28}$$

The variable T_{m} denotes the momentum tensor, p the pressure and $\vec{f}$ miscellaneous forces.
The conservation equations are solved in combination with PEMFC-specific models, which are explained in detail in the following.

4.3 PEMFC Modeling

The PEMFC model, used within this thesis is a multiphysics approach, included in STAR-CCM+. Figure 4.1 gives an overview of the conservation equations, solved for within the model.

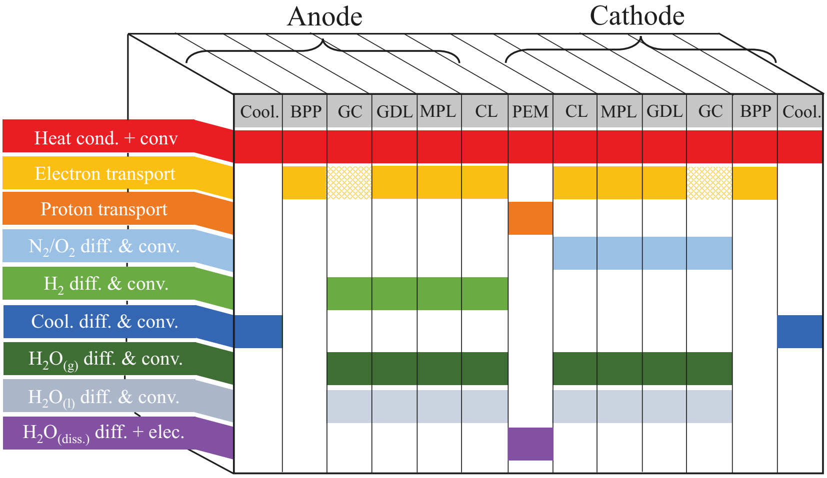

Figure 4.1: Overview of conservation equations in PEMFC model.

Thereby, conservation equations for the transfer of mass, charge and heat are solved in the various functional layers of the PEMFC. Heat transfer via convection and conduction is implemented for all functional layers. The electron transport is exclusively solved for within the porous regions of CL, MPL and GDL, as well as the solid BPPs. During the simplification process of the cell (see section 7.2.3), the electrical contact between bipolar plates and GDLs is interrupted, leading to the implementation of electron transport within gas channels (crosshatched in Figure 4.1). The membrane is assumed to be perfectly insulating, prohibiting voltage losses due to cross currents. Proton transport as a result of proton potential gradients is exclusively solved for in the PEM. Convective and diffusive mass transport for reactant gases and water vapor is accounted for in the respective regions of anode ($H_2/H_2O(g)$) and cathode ($O_2/N_2/H_2O(g)$) for the transport inside the gas channels, as well as the porous regions of GDL, MPL and CL. The PEM is exclusively permeable for water and protons, wherefore an interpenetration of gases, excluding water vapor (through sorption), is prohibited. The transport of absorbed water within the membrane is a result of diffusion processes, as well as electro osmotic drag (EOD). Due to the assumption of a 2-dimensional reaction layer, the optionally implemented porous CL region merely acts as a non-reactive diffusion path. Therefore neither proton nor dissolved water transport transport is considered in this region.

The priory mentioned mixture multiphase model is used within the PEMFC model to account for multiphase effects. All implemented models are discussed in detail in the following.

Multiphase Transport in Porous Media

The mixture momentum equation inside porous media can be derived, using the single-phase momentum equation for porous media for each phase. The phase momentum equations for porous media are defined as shown in equation (4.29).

$$\frac{\partial}{\partial t}\left(\alpha_i \rho_i \vec{u}_i\right) + \mathbf{div}\left[\alpha_i \rho_i \vec{u}_i \otimes \left(\vec{u}_i - \vec{u}_\mathrm{g}\right)\right] = -\alpha_i \nabla p + \alpha_i \rho_i \vec{g} - \alpha_i \gamma_{\mathrm{v},i} \vec{u}_i - \alpha_i \nabla p_{\mathrm{c},i} \tag{4.29}$$

Thereby, α_i denotes the volume fraction of phase i, ρ_i the density of phase i, $\vec{u}_i$ the velocity of phase i, p the pressure, $\vec{g}$ the gravitational acceleration, $\gamma_{\mathrm{v},i}$ the viscous resistance and $p_{\mathrm{c},i}$ the capillary pressure of phase i. With a dominance of viscous terms, the phase momentum equation for each phase i becomes the expression, shown in equation (4.30).

$$0 = -\nabla p - \gamma_{\mathrm{v},i} \vec{u}_i \tag{4.30}$$

Using the definition of the viscous resistance $\gamma_{\mathrm{v},i}$ in equation (4.31), the multiphase Darcy law is obtained (see equation (4.32)), which has to hold true for each phase i.

$$\gamma_{\mathrm{v},i} = \frac{\mu}{K_i \alpha_i^\mathrm{n}} \tag{4.31}$$

$$\nabla p = -\frac{\mu_i}{K_{\mathrm{v},i} \alpha_i^\mathrm{n}} \vec{u}_i \tag{4.32}$$

The definition of the mixture momentum equation for porous media is derived from the phase momentum equations (see equation (4.29)) and shown in equation (4.33).

$$\frac{\partial}{\partial t}\left(\rho_\mathrm{m} \vec{u}_\mathrm{m}\right) + \mathbf{div}\left(\rho_\mathrm{m} \vec{u}_\mathrm{m} \otimes \left(\vec{u}_\mathrm{m} - \vec{u}_\mathrm{g}\right)\right) = -\alpha_\mathrm{m} \nabla P - \sum_i \gamma_{\mathrm{v},i} \vec{u}_i + \rho_\mathrm{m} \vec{g} + \sum_i \vec{f}_i \tag{4.33}$$

Thereby, ρ_m denotes the density of the mixture, $\vec{u}_m$ the velocity of the mixture, $\vec{u}_g$ the gas velocity and $\vec{f}_i$ all miscellaneous forces. With a dominance of viscous terms, the momentum equation, solved for the mixture, gives the expression shown equation (4.34).

$$0 = -\alpha_\mathrm{m} \nabla p - \sum_i \gamma_{\mathrm{v},i} \vec{u}_i + \rho_\mathrm{m} \vec{g} + \sum_i \vec{f}_i \tag{4.34}$$

As only one momentum equation for the mixture is solved within the MMP model (see section 4.2.3), for a binary mixture, velocities of liquid $\vec{u}_{\mathrm{g}}$ and gas phase $\vec{u}_{\mathrm{lq}}$ have to be described in terms of a mixture velocity v_{m} and a slip velocity $\vec{u}_{12}$ (see equation (4.35)).

$$\begin{bmatrix} \vec{u}_{\mathrm{g}} \\ \vec{u}_{\mathrm{lq}} \end{bmatrix} = \begin{bmatrix} 1 & \alpha_{\mathrm{lq}}\,\rho_{\mathrm{lq}} \\ 1 & -\alpha_{\mathrm{g}}\,\rho_{\mathrm{g}} \end{bmatrix} \cdot \begin{bmatrix} \vec{u}_{m} \\ \vec{u}_{12} \end{bmatrix} = \begin{bmatrix} \vec{u}_{m} + \alpha_{\mathrm{lq}}\,\rho_{\mathrm{lq}}\,\vec{u}_{12} \\ \vec{u}_{m} - \alpha_{\mathrm{g}}\,\rho_{\mathrm{g}}\,\vec{u}_{12} \end{bmatrix} \tag{4.35}$$

Using the two-phase velocities on the mixture momentum equation (4.34), leads to an appropriate definition of the viscous porous momentum losses (see equation (4.36)).

$$\begin{aligned} -\sum_{i=1}^{n} \gamma_{\mathrm{v},i}\,\vec{u}_i = -\left(\gamma_{\mathrm{v,g}}\,\vec{u}_{\mathrm{g}} + \gamma_{\mathrm{v,lq}}\,\vec{u}_{\mathrm{lq}}\right) = &-\left(\gamma_{\mathrm{v,g}} + \gamma_{\mathrm{v,lq}}\right)\vec{u}_{m} \\ &-\left(\gamma_{\mathrm{v,g}}\,\alpha_{\mathrm{lq}}\,\rho_{\mathrm{lq}} - \gamma_{\mathrm{v,lq}}\,\alpha_{\mathrm{g}}\,\rho_{\mathrm{g}}\right)\vec{u}_{12} \end{aligned} \tag{4.36}$$

The slip velocity has to be defined in a way, that two-phase velocity definitions in equation (4.35), as well as Darcy's law in equation (4.32) are met. Deviations from Darcy's law occur as a result of gravitational forces, anisotropic inertia and capillary effects. Herefore, equation (4.37) is implemented, whereas influences of capillary forces on the slip velocity are considered exclusively and accounted for via a capillary pressure p_{c}.

$$\vec{u}_{12} = -\left(\frac{\alpha_{\mathrm{g}}}{\gamma_{\mathrm{v,g}}} - \frac{\alpha_{\mathrm{lq}}}{\gamma_{\mathrm{v,lq}}}\right)\gamma_{\mathrm{v,m}}\,\vec{u}_{\mathrm{m}} + \frac{\alpha_{\mathrm{g}}\,\alpha_{\mathrm{lq}}}{\gamma_{\mathrm{v,g}}\,\gamma_{\mathrm{v,lq}}}\gamma_{\mathrm{v,m}}\nabla p_{\mathrm{c}} \tag{4.37}$$

The viscous resistance of the mixture $\gamma_{\mathrm{v,m}}$ is defined in equation (4.38).

$$\gamma_{\mathrm{v,m}} = \rho_{m}\left(\sum_{i=1}^{n}\frac{\alpha_i^2\,\rho_i}{\gamma_{\mathrm{v},i}}\right)^{-1} \tag{4.38}$$

Thereby, the capillary pressure p_{c} is implemented via equation (4.39), using the surface tension of water in air σ, the inner contact angle of the porous medium θ_{c}, the porosity ε, the intrinsic permeability K_0, as well as the Leverett function $J\left(\alpha_{\mathrm{lq}}\right)$.

$$p_{\mathrm{C}} = \sigma\,\cos(\theta_{\mathrm{c}})\sqrt{\frac{\varepsilon}{K_0}}\,\nabla J\left(\alpha_{\mathrm{lq}}\right) \tag{4.39}$$

The Leverett function shown in equation (4.40), initially defined for the drainage and imbibition of air/water in unconsolidated sands [66], is widely used in literature to describe the capillary behavior in porous media of PEMFCs.

$$J\left(\alpha_{\mathrm{lq}}\right) = 1.417\,\alpha_{\mathrm{lq}} - 2.120\,\alpha_{\mathrm{lq}}^2 + 1.263\,\alpha_{\mathrm{lq}}^3 \tag{4.40}$$

Transport in Membrane

The PEM is modeled as a three-dimensional region that exclusively allows the transport of protons and water. Due to the absence of proton concentration gradients within the membrane a diffusion driven transport is neglected. Hence, protons are solely transported as a results of protonic potential gradients. The proton flux can be described by the current density vector $\vec{j}$ via Ohm's law (see equation (4.41)).

$$\mathbf{div}\vec{j} = 0, \quad \vec{j} = -\sigma_{\mathrm{P}} \nabla U \tag{4.41}$$

As mentioned in chapter 3.1.2, the proton conductivity σ_{P} of PEMs is strongly dependent on the degree of humidification, as well as operating temperature. Hence, a dependency on water content λ and temperature T in K is modeled via equation (4.42) according to *Springer et.al.* [67].

$$\sigma_{\mathrm{P}} = \left(0.5139\,\lambda - 0.326\right) \exp\left(1268\left(\frac{1}{303} - \frac{1}{T}\right)\right) \tag{4.42}$$

The membrane water sorption process is modeled as a molar water flux $\dot{n}_{i\mathrm{m,w}}$ according to the boundary-layer-theory, shown in equation (4.43). The process is driven by a deviation in local membrane water content λ from the equilibrium sorption value $\lambda_{i,\mathrm{eq}}$. [68]

$$\dot{n}_{i\mathrm{m,W}} = -\beta_i\, \alpha_{\mathrm{lq}} \frac{\rho_{\mathrm{PEM}}}{EW} \left(\lambda - \lambda_{i,\mathrm{eq}}\right) \qquad i = \mathrm{g, lq} \tag{4.43}$$

Thereby, α_{lq} denotes the liquid water volume fraction. Equilibrium water contents $\lambda_{i,\mathrm{eq}}$ (see equation (4.44)), as well as sorption rates β_i of species i into the membrane are specified for liquid water and water vapor separately.

For water vapor with an activity $a_{\mathrm{W}} \leq 1$, the water content equilibrium value $\lambda_{\mathrm{g,eq}}$ calculation is performed, using a fit (see equation (4.44)) gathered from experimental data. The value of $\lambda_{\mathrm{lq,eq}}$ for an absorption of liquid water ($\alpha_{\mathrm{lq}} > 0$) is described via Henry's law for pure liquid water with a constant equilibrium value of 16.8.

$$\lambda_{i,\mathrm{eq}} = \begin{cases} 0.06929 + 19.38\, a_{\mathrm{W}} - 44.34\, a_{\mathrm{W}}^2 + 39.39\, a_{\mathrm{W}}^3, & \text{for } i = \mathrm{g} \\ 16.8, & \text{for } i = \mathrm{lq} \end{cases} \tag{4.44}$$

The modeling of sorption rates for vapor and liquid water are shown in equation (4.45). Absorption and desorption rates, according to *Wu et. al.* [68] are used.

$$\beta_i = \begin{cases} \beta_{i,\mathrm{a}}, & \text{for } \lambda < \lambda_{i,\mathrm{eq}}\,\text{(absorption)} \\ \beta_{i,\mathrm{d}}, & \text{for } \lambda > \lambda_{i,\mathrm{eq}}\,\text{(desorption)} \end{cases} \tag{4.45}$$

The values of mass transfer coefficients β_i are assumed to $1 \cdot 10^{-5}$ m/s for the absorption $\beta_{i,\mathrm{a}}$ and desorption $\beta_{i,\mathrm{d}}$ process. As for simplicity reasons, values for ab- and desorption are kept equal.
The water transport through the membrane is modeled as a conservation of water concentration, shown in equation (4.46). The two transport mechanisms are water concentration and proton potential gradient driven; diffusion and electroosmotic drag (EOD) respectively.

$$\frac{\partial c_\mathrm{W}}{\partial t} + \mathbf{div}\left(-D_\mathrm{W} \nabla c_\mathrm{W} - \frac{n_\mathrm{d}}{F}\sigma_\mathrm{P} \nabla U\right) = S_\mathrm{W} \tag{4.46}$$

S_W represents the net water flux between membrane and adjacent regions. The EOD coefficient n_d is a water content dependent quantity, described with equation (4.47).

$$n_\mathrm{d} = \frac{2.5}{22}\lambda \tag{4.47}$$

The diffusion coefficent of water inside the membrane is a function of water content and is modeled by equation (4.48). [69]

$$D_\mathrm{W} = 4.1 \cdot 10^{-10} \left(\frac{\lambda}{25}\right)^{0.15} \left[1 + \tanh\left(\frac{\lambda - 2.5}{1.4}\right)\right] \tag{4.48}$$

Diffusion of species through the membrane other than water and protons are not considered, therefore omitting the current drop due to hydrogen cross-over.

Catalyst Layer

The reaction kinetics of anodic and cathodic reaction are describe with a Butler-Volmer approach, giving an expression for the current density j as shown in equation (4.49).

$$j_i = j_{0,i}\, a \left[\exp\left(\chi_\mathrm{a}^\mathrm{eff} \frac{F}{\Re T}\eta\right) - \exp\left(\chi_\mathrm{c}^\mathrm{eff} \frac{F}{\Re T}\eta\right)\right] \qquad i = \mathrm{a,c} \tag{4.49}$$

$$\chi_i^\mathrm{eff} = z\chi_i \tag{4.50}$$

$$\chi_\mathrm{a}^\mathrm{eff} + \chi_\mathrm{c}^\mathrm{eff} = z \tag{4.51}$$

χ_i^eff denotes effective charge transfer coefficients, consisting of the charge transfer coefficients χ_i and the number of transferred electrons z, η the over-potential, F the Faraday constant, $\Re$ the universal gas constant and $j_{0,i}$ the exchange current density. The definition of ξ_i^eff is shown in equations (4.50) and (4.51). The exchange current densities of anode $j_{0,\mathrm{a}}$ and cathode $j_{0,\mathrm{c}}$ are described in equation (4.52) and (4.53) respectively.

$$j_{0,\mathrm{a}} = j^*_{0,\mathrm{a}} \left(\frac{y_{\mathrm{H_2}}}{y_{\mathrm{H_2,ref}}} \right)^{\psi_1} \tag{4.52}$$

$$j_{0,\mathrm{c}} = j^*_{0,\mathrm{c}} \left(\frac{y_{\mathrm{O_2}}}{y_{\mathrm{O_2,ref}}} \right)^{\psi_1} \left(\frac{y_{\mathrm{H_2O}}}{y_{\mathrm{H_2O,ref}}} \right)^{\psi_2} \exp\left(-\frac{E_{\mathrm{A,c}}}{\Re T} \right) \tag{4.53}$$

Molar fractions of the respective species y_i, the activation energy $E_{\mathrm{A},}i$, as well as material specific exchange current density of anode and cathode $j^*_{0,\mathrm{i}}$ are specified. The reaction orders ψ_1 and ψ_2 describe the concentration dependencies of $j_{0,i}$. Values of $\psi_1 = 0.5$ and $\psi_2 = 0.5$ are used for the simulations [65].

The current form of the STAR-CCM+ PEMFC model does not allow a robust implementation of phase change. Therefore, all simulations are run, neglecting phase change processes. Consequently, an occurrence of liquid water within the anode compartment is exclusively possible when desorbed as liquid water from the membrane. As shown in equation (4.44), this is only the case for water contents above 16.8, exclusively observed for extremely humidified cases.

Further information on the PEMFC model can be found within the STAR-CCM+ documentation [65].

5 Two-phase Flow in PEMFC Gas Channels

The following chapter contains simulative investigations on the two-phase flow phenomena inside cathode and anode gas channels. The simulations are carried out, using the Volume-of-Fluid (VOF) method, while applying two-different types of methodologies. In order to perform detailed investigations, an adaptive mesh refinement (AMR) algorithm is developed and used to create reference cases. Longer simulation times are bridged via a constant coarse mesh refinement (CCMR) approach, applying the HRIC algorithm, which is validated against AMR results. The validated CCMR method is used to investigate two-phase flow phenomena and derive two-phase pressure drop correlations through variation of various parameters.

The findings within this section are in preparation to be published [70] and can partially be found in the Master's Thesis of *F. Du* [71], *K. Ling* [72] and *A. Jurzyk* [73], which were created while working under my supervision.

5.1 Computational Domain

The single channel VOF simulations for cathode and anode GCs are performed within trapezoidal channel geometries of constant cross-section, as shown in Figure 5.1. The frontal ($-x$)-surface depicts the channel inlet and the ($+x$)-surface the outlet. The lower surface represents the GDL/GC-interface, whereas all other surfaces represent walls of the bipolar plate.

The geometric parameters for cathode and anode are given in Table 5.1. Channel sections of $l_{\mathrm{GC}} = 12\,\mathrm{mm}$ are created, being equivalent to around 5 % of the total cathode length and around 10 % of the total anode GC length. Six possible sources S_1-S_6 are implemented, whereas source S_1 is used for the flow regime investigation and pressure drop correlations, performed in sections 5.8 and 5.9. All remaining sources are added for the position dependence study, carried out in section 5.8.2. The pressure drop values are evaluated as a function of the local saturation in the investigation domain with a length l_{ID}, confined by two surfaces in the back of the channel. A minimum distance l_4 from the water sources is chosen, to ensure that the emerging droplets are able to form a stable flow regime before evaluation. To avoid numerical instabilities, the first sources are positioned $l_1 = 2.0\,\text{mm}$ from the inlet. A safety distance of the investigation domain from the outlet is implemented in addition.

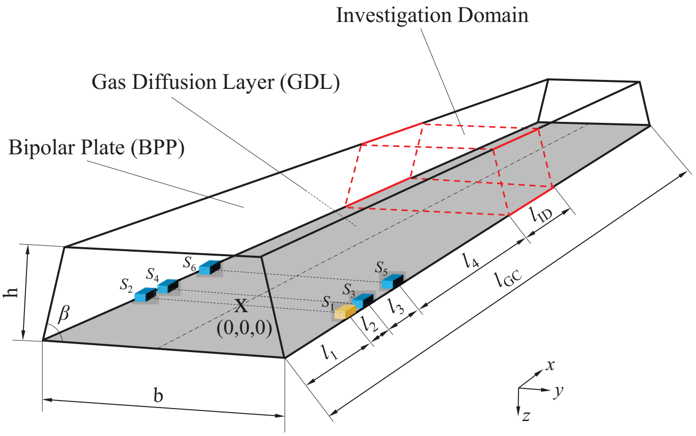

Figure 5.1: Single channel geometry for VOF simulations in cathode and anode GCs with indication of source term positions and investigation domain.

Table 5.1: Parameters for anode and cathode gas single channel geometry.

Parameter	Cathode	Anode
b	0.95 mm	0.90 mm
H	0.38 mm	0.23 mm
β	70°	73°
l_1	2.0 mm	2.0 mm
l_2	0.2 mm	0.2 mm
l_3	0.8 mm	0.8 mm
l_4	5.0 mm	4.0 mm
l_{ID}	1.7 mm	1.57 mm
l_{GC} (AMR/CCMR)	7/12 mm	7/12 mm

In the following, the simulation settings, including geometrical and physical modeling assumption, as well as operating conditions are depicted.

5.2 Simulation Settings

The present section summarizes the assumptions and simplifications, operation conditions and material properties of the models.

5.2.1 Geometrical Simplifications

The modeling assumptions and simplifications can be divided into geometrical and physical quality.

The geometrical modifications within the channel models to simplify the cases are as follows:

1.) Neglection of channel fillet radii:
The fillet radii, which are manufacturing related features, are neglected for both channel geometries, leading to sharp transitions in the bipolar plate corners. Possible effects on the droplet removal process, when including these features, are discussed in the corresponding section.

2.) Simplification of GDL intrusion:
The GDL/GC-interface is represented as a horizontal plane. The intrusion of the GDL into the channels is experimentally determined (according to [74]) for the corresponding compression force of 1.5 MPa and subtracted within the models as a constant horizontal offset from the initial channel cross-section areas adjacent to the GDL.

3.) Channel length shortening:
Due to computational restrictions, simulations with a maximal channel length of l_{GC} = 12 mm are performed for anode and cathode side. The value is chosen as an optimum between feasibility and accuracy, while shortcomings of similar studies are compensated [33, 35–37, 51].

4.) Constant cathode channel cross-section:
The conical contraction and expansion of cathode gas channels, leading to varying cross-sectional areas, are neglected. A full transition from small to large cross-section in the real geometry and vice versa occurs over the length of around 70 mm, corresponding to around 1/3 of the total cathode gas channel length. As a result of computational restrictions, a constant average channel cross-sectional area is chosen for the cathode GC model, as shown in Figure 5.1. Deviations to the real geometry are investigated and summarized in appendix A.1.1 for a single-phase flow.

5.) Simplification of volume source term:
Liquid water favorably accumulates in the land area of the BPP (BPP/GDL-intersection) as a a result of higher GDL compression in combination with low temperatures, caused by the adjacent coolant flow. [9, 18] Inlet positions adjacent to the channel walls are therefore chosen as a result of higher likelihood of droplet emergence. Variations of 1 µl/s, corresponding to the amount of water occuring within one channel of the chosen geometry at 2.5 A/cm^2, are chosen for the value of the water source. The introduction

is implemented by addressing the first layer of geometrically GDL-adjacent numerical cells within a rectangular section inside the gas channels. Although the source term is implemented inside the channel, a negligible influence, resulting from the marginal height of polyhedral cells in the mentioned region, is found. The width of the source terms is chosen to be in the range of average GDL pore diameters. [17] The rectangular shape is restricted by the number and shape of polyhedral cells that approximate it. While the droplets emerge, a spherical shape is formed immediately, justifying the shape of the inlet section. The mathematical implementation of the water source term is explained in detail in section A.1.1.

5.2.2 Physical Assumptions

Regarding physical simplifications, the following assumptions are taken for the simulations:

1.) Constant gas phase molar mass:
With a negligible change in molar mass within cathode gas channels and Mach numbers as low as 0.1, constant density can be assumed for the cathode gas flow. The anode gas flow shows a possibly significant change in molar mass due to replacement of hydrogen with water. Nevertheless, the influence of gas density changes on the two-phase flow will be neglected as a result of computational restrictions. Constant gas densities are therefore assumed for all VOF simulations.

2.) Constant temperature:
Temperature changes of 5-10 °C are expected to occur over the whole length of the cell during typical operating conditions. Changes over the length of the investigation region are therefore assumed to be negligible. Hence, constant temperatures are assumed for all simulations.

3.) Water vapor / liquid water equilibrium:
An equilibrium of water vapor and liquid water is assumed. Therefore, fully saturated gas flows ($RH = 100\,\%$) are used for all simulations. The effect of phase-change might significant influence the amount of liquid water within the gas channel and therefore majorly influence the two-phase pressure drop. [18] Nonetheless, the phase-change models for VOF simulations within STAR-CCM+ are determined to be of insufficient accuracy, which is why phase-change is neglected for all simulations.

4.) Neglection of gravitational forces:
An evaluation of the Bond number for droplets is performed in section A.1.2. A strong

dominance of surface tension forces over gravitational forces is shown. This is in accordance to other literature studies [75].

5.2.3 Operation Conditions and Material Properties

Table 5.2 gives a summary of the boundary conditions used within the VOF simulations. Velocity inlet and pressure outlet boundary condition are applied. All other boundaries are implemented as walls with no-slip boundary conditions. All implemented contact angles are measured via sessile drop technique. [76] As the advancing and receding contact angle of the GDL fall into the measurement tolerance of ±5°, a constant static contact angle of $\theta = 155°$ is applied on the lower boundary. The channel wall contact angle is determined to $\theta = 75°$ with a hysteresis of ± 15°. Regarding turbulence modeling, an LES model is applied. An evaluation of the hydraulic entrance length is carried out (see section A.1.3), showing a dominance of fully developed flow. Therefore, fully developed flow profiles are generated through single-phase flow simulations and implemented as initial states.

Table 5.2: Summary of simulation settings.

Material properties & operating conditions (l_{GC} = 7.0 mm) (Section 5.4 - 5.7)	$T = 75\,°\mathrm{C}$, $p = 1.75\,\mathrm{bar}$, $RH = 100\,\%$ $\rho_C = 1.600\,\mathrm{kg/m^3}$, $\mu_C = 18.60\,\mu\mathrm{Pa{\cdot}s}$ $\rho_W = 974.9\,\mathrm{kg/m^3}$, $\mu_W = 378\,\mu\mathrm{Pa{\cdot}s}$ $\sigma = 63.57\,\mathrm{mN/m}$
Material properties & operating conditions (l_{GC} = 12.0 mm) (Section 5.8 - 5.9)	$T = 85\,°\mathrm{C}$, $p = 2.2\,\mathrm{bar}$, $RH = 100\,\%$ $\rho_C = 1.927\,\mathrm{kg/m^3}$, $\mu_C = 18.73\,\mu\mathrm{Pa{\cdot}s}$ $\rho_A = 0.446\,\mathrm{kg/m^3}$, $\mu_A = 10.59\,\mu\mathrm{Pa{\cdot}s}$ $\rho_W = 968.7\,\mathrm{kg/m^3}$, $\mu_W = 333\,\mu\mathrm{Pa{\cdot}s}$ $\sigma = 61.71\,\mathrm{mN/m}$
Turbulence model	LES (WALE-SGS)
Boundary conditions	$-x$: fully-developed velocity inlet $+x$: Pressure outlet with constant zero $+z$: (GDL-Interface) No-slip, $\theta = 155°$ Others: No-slip, $\theta = 75°$, $\theta_r = 60°$, $\theta_a = 90°$
Initialization	Fully-developed single-phase flow

The next section introduces the AMR methodology in detail.

5.3 Adaptive Mesh Refinement (AMR)

The detailed investigation of two-phase flows in GCs requires an effective methodology, which is able to resolve local phenomena while having sufficient computational efficiency to bridge relevant time spans. An evaluation of the dimensionless numbers in section A.1.2, shows a strong dominance of surface tension inside PEMFC gas channels, depicting the importance of a sufficiently resolved interface. The AMR algorithm uses a locally refined adaptive mesh to resolve the two-phase interface in detail, whereas the bulk phases of both phases are kept coarse to save computational effort. The methodology is introduced in detail in the following.

5.3.1 Methodology of Mesh Refinement

The function of mesh refinement to reduce the cell size in phase interface regions is addressed via a water volume fraction threshold of $0.01 < \alpha_{\mathrm{lq}} < 0.99$. The desired cell size for the remeshing process $\Delta x_{\mathrm{remesh}}$ is defined in equation (5.1).

$$\Delta x_{\mathrm{remesh}} = \begin{cases} \Delta x_{\mathrm{fine}} & \text{if} \quad 0.01 < \alpha_{\mathrm{lq}} < 0.99; \\ \Delta x_{\mathrm{coarse}} & \text{otherwise} \end{cases} \tag{5.1}$$

During remeshing, for cells with a volume fraction between 0.01 and 0.99, size Δx_{fine} is applied, whereas size $\Delta x_{\mathrm{coarse}}$ is used for the bulk of both phases.

The flowchart of the algorithm is shown in Figure 5.2. After initialization, the simulation is run using the implicit solver for transient VOF simulations. The time step is adjusted adaptively in order to ensure an optimum between numerical stability and speed. Further details on the time step settings can be found in appendix A.1.4.

The simulation continues until the “maximum stopping criterion” is satisfied. The criterion examines after each time step, whether there is at least one numerical cell that lies on the phase interface, defined by a threshold of $0.05 < \alpha_{\mathrm{lq}} < 0.95$, and whose volume is larger than the preset threshold of V_{max}.

After the simulation has been stopped, it is automatically checked whether the ending criterion, defined as a maximum amount of time steps or maximum physical time (t_{max}, i.e. 0.1 s), is met. If the conditions of ending the CFD simulation are not met, the remeshing process is started. This includes three main steps:

1.) Extraction of a table containing desired cell sizes $\Delta x_{\mathrm{remesh}}$, defined in equation (5.1);

2.) Initiation of remeshing process by creating a new surface mesh and volume mesh (polyhedral) according to the sizes given within the table;

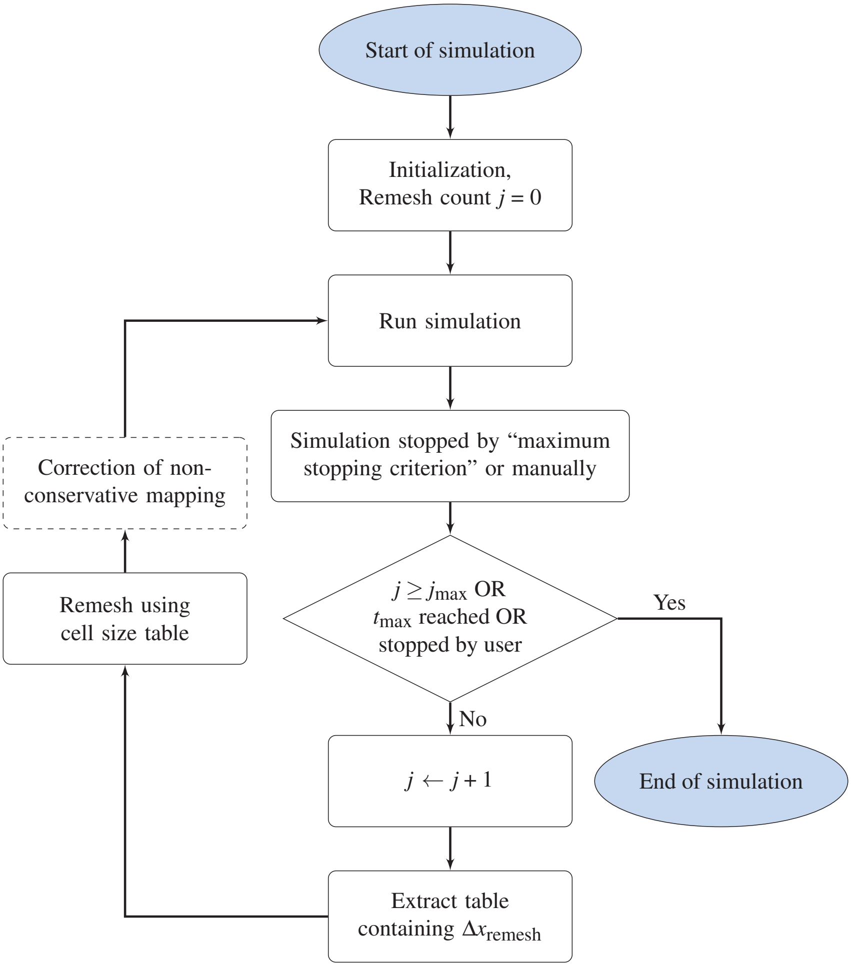

Figure 5.2: Methodology of adaptive mesh refinement. [71]

3.) Correction of non-conservative mapping error (shown as a dashed box in Figure 5.2). The necessity as well as functionality of this process is elaborated in section 5.3.2.

Afterwards, the simulation is resumed on the new mesh and the looping process continues. The parameters during the introduced remeshing and simulation process are summarized in Table 5.3.

Table 5.3: Remeshing parameters and their values used in the exemplary simulation.

Parameter	Description	Value/Interval
Ω_{refine}	Threshold for mesh refinement	$0.01 < \alpha_{\text{lq}} < 0.99$
Δx_{coarse}	Phase bulk (coarse) cell size	$2\,\text{mm}$
Δx_{fine}	Phase interface (fine) cell size	$1.5\,\mu\text{m}$
Ω_{check}	Threshold for maximum cell volume check	$0.05 < \alpha_{\text{lq}} < 0.95$
V_{max}	Maximum interface cell volume criterion	$2 \cdot 10^{-9}\,\text{m}^3$

The parameters and their selection are elaborated in the following:

- Refining region Ω_{refine}, expressed as an interval of the water volume fraction. The lower and upper boundaries of 0.01 and 0.99 are recommended in order to ensure that essentially all interface features are captured by the fine grid.

- The interface and bulk cell sizes, Δx_{fine} and Δx_{coarse}. The selection of the bulk coarse size depends on the physics and geometry of the investigated problem. The fine mesh size should be small enough to favor the interface reconstruction, but is mostly limited by the computational effort.

- Region for maximum cell volume check Ω_{check}, defined as an interval of the water volume fraction. This is defined here by the phase interface with a threshold of $0.05 < \alpha_{\text{lq}} < 0.95$. The interval threshold value has to be smaller than the refining interval, in order to prevent a cell from being coarsened in one remeshing process, yet triggering the next remeshing due to small fluctuations of its volume fraction. For example, if the upper boundaries of both intervals are 0.99, the cells of volume fraction 0.991 may be coarsened in one remeshing process, however, a small fluctuation of the volume fraction (i.e. to 0.989) would trigger the stopping criterion, resulting in a remeshing without purpose.

- Maximum allowed cell volume at interface V_{max}. The value of this threshold volume decides how often a remeshing process is performed. An improperly small value would lead to an unreasonably high amount of remeshing processes, whereas a too large value would mean that the simulation continues even after the phase interface has reached a relatively large cell, thus reducing the accuracy of the simulation. This value should be adjusted based on the individual problem and required frequency of remeshing. A reasonable starting value is gained by approximation of a polyhedral cell as a cube, using the cell size as the space diagonal.

Additionally, a small "growth factor" of the polyhedral volume mesh is advantageous, which leads to a smoother transition between small and large-sized cells, as shown in Figure 5.3.

(a) Cells containing phase interface. **(b)** Cells with small volume.

Figure 5.3: Comparison of phase interface region Ω_{refine} ($0.01 < \alpha < 0.99$, left) to region of small cells (right).

It is evident from Figure 5.3 that the region of small cells is larger than the phase interface region Ω_{refine} with $0.01 < \alpha_{\text{lq}} < 0.99$. This indicates that a transition region between small and large cells is created. This transition is critical as it prevents the phase interface from entering a very coarse cell, which corresponds to strong interface smearing.

5.3.2 Correction of Non-Conservative Mapping

An important issue of the polyhedral remeshing methodology lies in the interpolation of flow variables, the so-called mapping, between the old and new mesh. The interpolation leads to variations in flow variables immediately after the remeshing procedure. Variations of pressure and velocity field, as well as smearing of the phase interface, generally recover automatically after several iterations and time steps. This in particular is important to ensure that the final solution is not affected. However, the non-mass-conservative interpolation leads to changes of the total water volume in the simulation domain, which is apparently a non-physical behavior. It is observed that the water volume is most likely increasing during remeshing, thus accumulating to an intolerable error and being detrimental for the simulation.

It is therefore necessary to derive an algorithm to correct for the nonconservative mapping error. Therefore, the STAR-CCM+ feature "VOF phase replacement" is applied, a method originally designed to eliminate numerical ventilation [65]. Using the VOF replacement, the water volume fraction in certain cells is adjusted to compensate the volume increase during remeshing. Following steps are implemented in the macro introduced in section 5.3.1:

1.) The volume of water before the remeshing process V_{W1} is determined by the volume integral of the total water volume fraction over the whole numerical domain Ω (see equation (5.2)). This step is performed between the decision block and the remeshing block (shown in Figure 5.2).

2.) After remeshing, the volume of water V_{W2} is determined using the same integral (see equation (5.3)).

$$V_{\mathrm{W1}} = \int_{\Omega} \alpha_{\mathrm{lq}} \, \mathrm{d}V \quad \text{(before remeshing)} \tag{5.2}$$

$$V_{\mathrm{W2}} = \int_{\Omega} \alpha_{\mathrm{lq}} \, \mathrm{d}V \quad \text{(after remeshing)} \tag{5.3}$$

3.) The increase in water volume due to remeshing ΔV_{W} is determined via equation (5.4).

$$\Delta V_{\mathrm{W}} = V_{\mathrm{W2}} - V_{\mathrm{W1}} \tag{5.4}$$

4.) This volume difference is compensated by scaling the water volume fraction $\alpha_{\mathrm{lq,o}}$ in certain cells to receive new values $\alpha_{\mathrm{lq,n}}$. Therefore the “replacing VOF phase” function inside STAR-CCM+ is used. The scaling performed for each numerical cell is defined in equation (5.5).

$$\text{Scaling } \alpha_{\mathrm{lq,n}} = \begin{cases} \alpha_{\mathrm{lq,o}} \cdot \left(1 - \dfrac{\Delta V_{\mathrm{W}}}{V_{\mathrm{W,repl}}}\right) & \text{if } \alpha_{\mathrm{lq}} < 0.5 \\ \alpha_{\mathrm{lq,o}} & \text{otherwise} \end{cases} \tag{5.5}$$

The idea is to lower the water volume fraction proportionally in the region of $\alpha_{\mathrm{lq}} < 0.5$, as a compensation for the non-physical volume increase due to non-conservative mapping. Here, $V_{\mathrm{W,repl}}$ denotes the total volume of water in this region. The upper bound 0.5 ensures that the water fraction is lowered only on the air side (where air has a higher volume fraction than water). This treatment numerically increases the gradient of the water fraction which helps improving the interface sharpness.

5.) Scaling of previous volume fractions $\alpha_{\mathrm{lq,o}}$ via “VOF phase replacement” function for exactly one time level to correct the volume difference. After this time level, the replacement is deactivated by setting the value of the deducted water volume $\Delta\alpha_{\mathrm{lq}}$ to uniform zero.

The simulation is regularly continued after these steps (see Figure 5.2).

With the methodology introduced above, the polyhedral mesh can be refined at the phase interface without mass conservation issues. This greatly reduces the mesh count for a fine resolution of the phase interface.

5.4 Droplet Dynamics Investigations via AMR

A detailed droplet investigation inside a cathode gas channel geometry, using the priory introduced AMR methodology, is performed in the following section.

5.4.1 Static vs. Dynamic Contact Angle

The majority of VOF studies [35–37, 51, 77], being carried out inside single channels is performed using static contact angles, rather than dynamic ones, due to simplicity reasons. As studies [33, 78] show, this might lead to misinterpretation of water transport behavior. If the contact angle hysteresis of the material is not negligible this leads to unrealistic results. A hysteresis of the bipolar plate of 15° is determined experimentally, while the contact angle hysteresis of the GDL is within the measurement tolerance. Therefore a separate simulation case is set-up to investigate the effect of static against dynamic contact angle of the bipolar plate.
The cathode channel geometry (see Figure 5.1) is used with a single liquid water source term of $\dot{S}_{\mathrm{W1}} = 1\,\mu\mathrm{L/s}$, corresponding to the total amount of water within a single channel at 2.5 A/cm^2 and a gas velocity of $u_{\mathrm{g}} = 10\,\mathrm{m/s}$. The static contact angle case simulation is performed, using a value of $\theta_{\mathrm{BPP}} = 75\,^{\circ}$, whereas the receding and advancing angles of the dynamic contact angle case can be taken from Table 5.2. All other settings are kept equivalent for both cases and are found in the table as well.
Figure 5.4 shows the simulation results with static (left) and dynamic (right) contact angle implementation at different physical times. A difference in detachment time, as well as water removal phenomena can be observed. The static contact angle (SCA) case shows a droplet detachment after 10 ms, resulting in a droplet removal along the channel side wall. For the dynamic contact angle case (DCA), a vertical water droplet wicking occurs, followed by the

subsequent detachment after 20 ms along the upper channel corner. The difference in detachment time and phenomena can be explained by the total time a droplet is exposed to the gas flow. The transport of momentum from the gas flow, in the case of a droplet with DCA, partially leads to a deformation of the droplet surface. This hindered removal process results in a droplet growth until a contact with the energetically favored channel corner occurs, initiating a wicking process and eventually a droplet detachment.

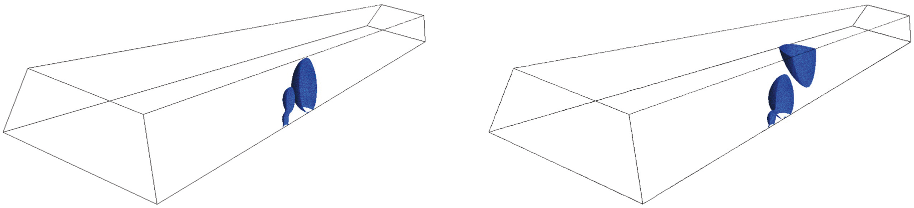

(a) Static contact angle at $t = 10$ ms. **(b)** Dynamic contact angle at $t = 19$ ms.

Figure 5.4: Water volume fraction iso-surface plots of static (left) and dynamic (right) contact angle case.

A surface deformation for SCA droplets is prohibited by definition, as the Young's equation has to be satisfied, leading to a detachment process before a necessary droplet size for the wicking can be achieved. The detached droplet is removed along the channel side wall. As a direct result of detachment time differences, SCA and DCA contact angle case droplets vary in size. With a droplet volume of $1.37 \cdot 10^{-11}\,\mathrm{m}^3$ for the DCA case and a value of $8.95 \cdot 10^{-12}\,\mathrm{m}^3$ for the SCA case, a deviation of 34.7 % is observed.

It becomes apparent that a minimal contact angle hysteresis, leading to an enhanced momentum transfer from gas to liquid, is preferred in order to ensure an optimum in water removal capability within the gas channel.

It can be concluded that an implementation of dynamic contact angle is crucial for a correct description of the detailed water removal process. Therefore all further simulations will be performed with dynamic contact angles for the bipolar plate. As the hysteresis of the GDL is determined to be within the measuring tolerance, a static contact angle is applied for the lower boundary.

The droplet dynamics of the DCA case are elaborated in further detail within the following section.

5.4.2 Droplet Dynamics in PEMFC Cathode Channels

The droplet dynamics of the priory introduced dynamic contact angle case shall be investigated in detail within the present section. The material parameters, as well as operating conditions are summarized in Table 5.2. The resulting water volume fraction iso-plots for an $\alpha_{\mathrm{lq}} = 0.5$ are given in Figure 5.5 for various physical times.

A spherical droplet shape is observed during the initial growth process, which increases in size over time (see Figure 5.5a to 5.5b). The shape is a result of the dominant surface tension forces, as shown in the evaluation of the dimensionless numbers in the appendix in equations (A.4) to (A.6). Low wall-adjacent velocities, associated with low drag forces, are preventing an early drop detachment process.

(a) t = 5.0 ms.

(d) t = 13.7 ms.

(b) t = 12.3 ms.

(e) t = 14.2 ms.

(c) t = 13.3 ms.

(f) t = 19.0 ms.

Figure 5.5: Water volume iso-surface plots at physical times of 5.0, 12.3, 13.3, 13.7, 14.2 and 19 ms. Air flows from left to right.

The growth continues until the point when a first contact with the upper channel corner is initiated and a fast (1-2 ms) wicking of the droplet into the channel corner occurs (see Figure 5.5c to 5.5d). During the wicking process, an initial deformation of three-phase contact line and droplet shape is observed, which transfers into a spherical shape as soon as the transition process is finalized (see Figure 5.5e), once more showing the domination of surface tension. The wicking is initiated by an energetically favored configuration in the upper channel corner (BPP-BPP), in comparison to the lower one (GDL-BPP). It shall be noted, that for the case of channels with radii fillets, a less abrupt but earlier wicking process is likely to be observed.

The detached droplet is removed along the channel corner, while the growth of the next droplet, attached to the source, continues (see Figure 5.5f). Longer simulation times are necessary to investigate the following processes of droplet interaction and removal.

As the prior AMR results serve as validation cases for the simplified CCMR approach, an analytic validation of the former is given in the following.

5.5 Analytic Validation of AMR Results

Due to lack of experimental data, the prior results are validated against an analytic model of a two-dimensional spherical droplet, wetting a wall. Therefore, contact angles of the wetted walls θ_1 and θ_2, as well as geometric parameters i.e. the wall angle β and droplet height H, have to be provided as input parameters for the analytic approach. Using these values, a spherical curve with radius R can be defined according to equation (5.6).

$$R = \frac{-H}{\cos(\theta_1+\beta)+\cos\theta_2}\,. \tag{5.6}$$

The center of the arc $P2$ with x- and y-coordinate x_{P2} and y_{P2} is defined according to equation (5.7) and (5.8) respectively. The derivation of the expressions is given in detail in the appendix A.1.6.

$$x_{\mathrm{OX}} = -H\cdot\cot\beta + R\cdot\sin(\beta+\theta_1)\,; \tag{5.7}$$

$$y_{\mathrm{OX}} = H + R\cdot\cos(\beta+\theta_1) \tag{5.8}$$

Using the contact angle of the BPP of $\theta_{\mathrm{BPP}} = 75\,^\circ$ (equivalent to the static contact angle value), as well as the value for the GDL-surface of $\theta_{\mathrm{GDL}} = 155\,^\circ$ with the derived equations, leads to an analytic solution of the two-dimensional droplet cross-section profile. The analytic shape is plotted with simulation results of the volume fractions on the cross-section at 12.3 ms in Figure 5.6.

The CFD results show a spherical droplet shape, as a result of surface tension dominance, being in excellent agreement to the analytic results. Further analysis of the shapes shows minor deviations between the cases on the contact angle of the droplet, facing the BPP-surface, while the GDL-contact angle condition is met perfectly. The reason for the differences can be found in the dynamic contact angle of the BPP. The real contact angle being present has to be in the range between static and dynamic value and therefore deviates from the static values, used to create the analytic curve.

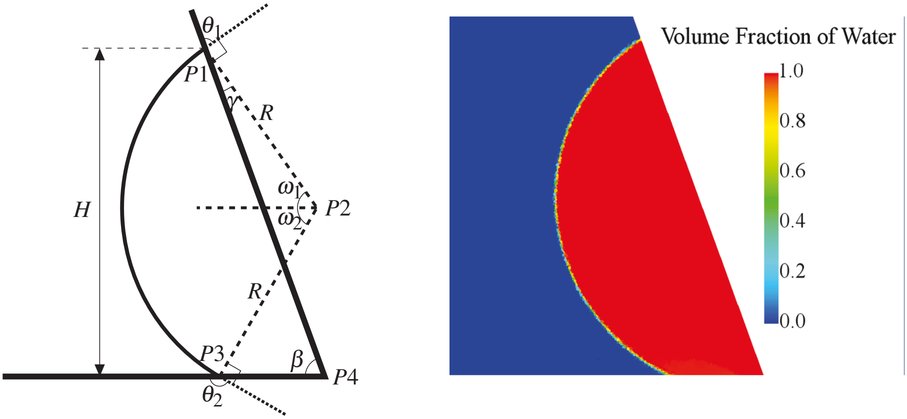

(a) Analytic cross-section shape.

(b) CFD result.

Figure 5.6: Comparison of analytic droplet shape with cross section profile of droplet at 12.3 ms

Using equation (5.9) gives high values for the blending function f_{Blend}, being a result of a slow droplet expansion process in combination with low liquid capillary numbers ($Ca_{\mathrm{lq}} << 1$).

$$f_{\mathrm{Blend}} = \frac{1}{2} + \frac{1}{2} \cdot \cos\left(\frac{Ca_{\mathrm{lq}}}{Ca_{\mathrm{eq}}} \cdot \pi\right) > \frac{1}{2} + \frac{1}{2} \cdot \cos\left(\frac{3 \cdot 10^{-4}}{0.001} \pi\right) = 0.79 \tag{5.9}$$

An evaluation of the present contact angle according to equation (5.10) gives a present contact angle with the BPP-surface of $\theta_{\mathrm{BPP}} = 78\,^{\circ}$ and the dynamic contact angle value θ_{K}. The value is within the estimation tolerance of the experimental contact angle and therefore in good agreement to the static value of $\theta_{\mathrm{BPP}} = 75\,^{\circ}$, explaining the minor deviations between the cases in Figure 5.6.

$$\theta = \theta_{\mathrm{K}} - f_{\mathrm{Blend}} \cdot (\theta_{\mathrm{K}} - \theta_{\mathrm{e}}) < 90^{\circ} - 0.79 \cdot (90^{\circ} - 75^{\circ}) \approx 78^{\circ} \tag{5.10}$$

The comparison shows a validity of the contact angle model, implemented within STAR-CCM+. Further implications cannot be drawn from the present analytic approach, due to the complex nature of the real two-phase flow process. The validated AMR simulation results are used as reference cases for further investigations.

5.6 Constant Coarse Mesh Refinement (CCMR)

The detailed investigations in the previous sections depicted the limitations of the AMR approach regarding total physical times. In order to examine interactions between droplets, as well as other two-phase phenomena, an effective simulation approach is required. Therefore a constant coarse mesh refinement (CCMR) approach is set up, which is explained in further detail in the present section.

By decreasing the resolution of the mesh, while loosening the *CFL* criterion and lowering the number of inner iterations, a drastic speed-up of the simulations can be generated. Instead of using an adaptive mesh refinement in order to keep the interface sharp, the high resolution interface capturing (HRIC) approach is used (see section 4.2.2 for details). The size of numeric cells is kept at a constant and coarse value throughout the whole channel geometry. In order to find a reasonable cell size, single-phase simulations are performed and compared to analytic results. The comparison is shown in appendix A.1.7. A mesh base size of 15 µm is determined as an optimum between accuracy and efficiency and implemented into all CCMR simulations cases.

The HRIC-settings, such as angle factor C_α (see equation (4.23)) and sharpening factor C_θ (see equation (4.25)) are chosen according to recommended values in [65] and modified iteratively to represent the results of the detailed AMR case (see comparison in section 5.7). The unconditional stability of the implicit solver allows values of $CFL > 1$. [79] The *CFL* number is merely a criterion, used for the appropriate setting of the time step. A value of $CFL = 100$ is found to be the optimum value between accuracy and sufficient speed-up. The number of inner iterations, corresponding to the steps within one time steps, is set to $n_{\text{inner}} = 5$. All CCMR-specific settings are summarized in Table 5.4.

Table 5.4: CCMR simulation settings.

Parameter	Description	Value
Δx	Mesh base size of polyhedral cells	15 µm
C_α	Angle factor	0.25
C_θ	Sharpening factor	0.1
$\underline{CFL}$	Lower bound of *CFL*	100
n_{inner}	Number of inner iterations	5

The resulting deviations of the CCMR approach to the detailed AMR methodology are discussed in the following section.

5.7 Validation of CCMR Approach against AMR Results

In order to ensure a proper representation of the two-phase flow for CCMR cases, a validation against AMR results is performed, using the cathode channel two-phase flow results from section 5.4.2. Material and operating conditions are shown in Table 5.2. The droplet dynamics are quantified via iso-surface plots of the volume fraction $\alpha_{\mathrm{lq}} = 0.5$, shown in Figure 5.7 for AMR (left) and CCMR (right) cases.

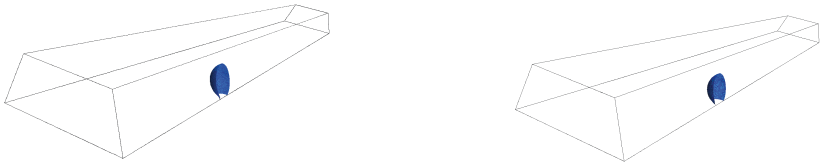

(a) AMR case at t = 5.0 ms.

(e) CCMR case at t = 5.0 ms.

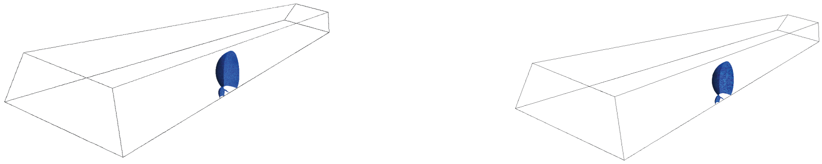

(b) AMR case at t = 10.0 ms.

(f) CCMR case at t = 10.0 ms.

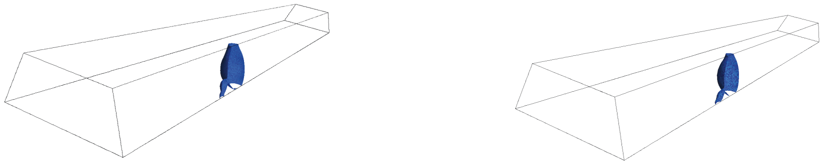

(c) AMR case at t = 13.0 ms.

(g) CCMR case at t = 12.8 ms.

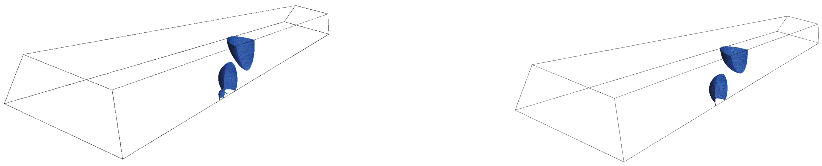

(d) AMR case at t = 18.0 ms.

(h) CCMR case at t = 17.7 ms.

Figure 5.7: Water volume iso-surface plots of AMR and CCMR results at physical times of 5.0, 10.0, 12.8, 13.0, 17.7 and 18.0 ms. Air flows from left to right.

The physical time of the plots is chosen to represent the same physical process and therefore deviates for the last two between the approaches.

A qualitative comparison of the droplet dynamics shows an overall good agreement between the approaches, with the subsequent processes of droplet emergence, built-up, wicking and detachment. The spherical shape of the droplet during growth is resolved well for the CCMR approach, being an indication of sufficient representation of surface tension. Polyhedral cells have the advantage of having a higher number of neighboring cells and therefore superior gradient evaluation, when comparing to conventional hexahedral or tetrahedral cells [80]. This directly effects the evaluation of surface tension positively [81]. Deviations in the droplet shape are negligible up to a physical time of around 10 ms. First noticeable differences can be observed during the wicking process into the channel corner, whereas the process is induced earlier for the CCMR approach (at 12.8 ms). The reason can be found in the larger numerical cell sizes, as the wicking process is initially induced by the first significant presence of liquid water in the channel corner. The physical reasons are found in an energetically favorable configuration of the two upper hydrophilic channel walls. Assuming an approximately equivalent growth velocity between the cases, a numeric cell, geometrically representing the channel corner will experience a detectable volume fraction earlier. The time shift is propagating when comparing the last physical time, whereas the physical processes are equivalent. A transformation back to a spherical droplet shape is observed for the CCMR case at 17 ms, being a result of the dominant surface tension forces (see section A.1.2). An analogous process is expected for the AMR case at a later time. An 11.4 % smaller droplet size is found for the CCMR case with a value of $1.23 \cdot 10^{-11}\,\mathrm{m}^3$, being a result of the earlier detachment. The relatively large numerical cells of the CCMR case lead to a high uncertainty of the droplet volume value due to the undefined division between the phases along the interface.

Analogously to the validation against the analytic droplet shape, a cross-section volume fraction comparison of CCMR to AMR results is performed and shown in Figure 5.8.

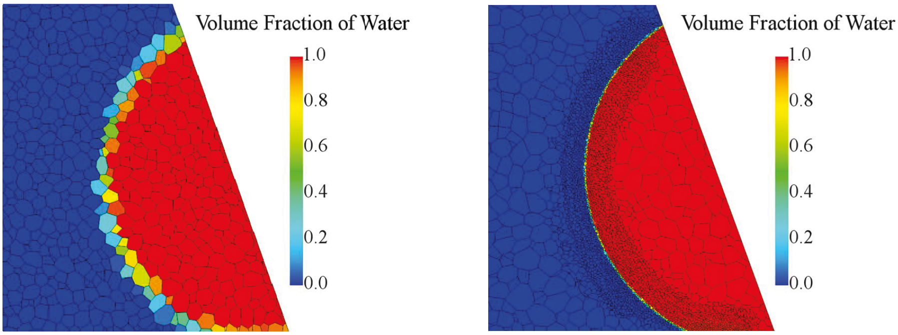

(a) CCMR at t = 12.5 ms.

(b) AMR at t = 12.3 ms.

Figure 5.8: Cross-section plot of volume fraction of CCMR at 12.5 ms (left) and AMR at 12.3 ms (right) simulation results.

The advantage of the HRIC algorithm becomes apparent when looking at the adequately sharp interface with a thickness of 1-2 numerical cells, while having a strong reduction in total mesh count. The droplet shape of the CCMR approach is in very good agreement to the AMR results. Contact angles towards the side wall and GDL are represented sufficiently. The depicted time step for the CCMR approach is slightly prior to wicking induction. With a gap of two numerical cells between droplet and upper channel corner, it becomes clear that a vertical droplet movement is going to be initiated prematurely.

The pressure drop within the investigation regions is used as a further quality criterion and shown in Figure 5.9 for AMR and CCMR case. The pressure spikes of the AMR case a result of the mapping process between two consecutive meshes, leading to initial disturbances of pressure and velocity field. As priory mentioned in section 5.3.2, a fast recovery is observed after a few time steps.

Both approaches show a similar profile for the pressure drop increase, with an absolute offset in the range of 10 up to 18 Pa. While the qualitative process of the droplet dynamics is correctly represented within the profile, a systematic deviation is found between the cases. The initial pressure drop increase of the AMR cases seems to be physically unreasonable. A steady increase would be expected for a negligible amount of water, being present in a region of the channel where inertial gas forces are weaker. The reason might be an initially smeared interface. The initial error is then propagated in time due to the transient nature of the simulation, maintaining an offset between the two approaches.

Regions with strong pressure oscillations of the AMR case indicate a frequent remeshing process. This phenomenon can be observed during the time of the droplet wicking and subsequent detachment, manifested as a local peak in pressure at around 14 ms. A time shift between the cases, as priory shown in Figure 5.7, is observed for the pressure drop.

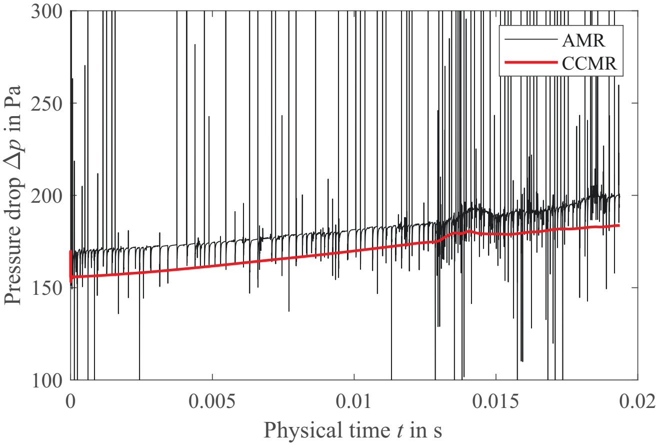

Figure 5.9: Comparison of pressure drop time-series in cathode single channel simulation of AMR and CCMR simulation.

To further investigate the offset in pressure drop, additional AMR and CCMR anode single channel simulations are performed. Equivalent operation conditions, as well as fuel properties shown in Table 5.2 (indicated with an A) are used. The results of the pressure drop curves are shown in Figure 5.10.
Hereby, an excellent match of CCMR and AMR case is observed. As priory mentioned, local fluctuations within the AMR case can be traced back to the data transfer between two consecutive meshes, whereas the anode case is experiencing longer persisting local fluctuations than the cathode case. A steady increase from the single-phase pressure drop values is observed for the AMR case, as also priory expected from the cathode AMR case. Due to the flat shape of the anode channel, lower gas velocities, leading to lower inertial forces, are experienced in the region of liquid water input. Therefore, an initially improper resolution of the interface results in a negligible effect on the pressure drop, being shown through the absence of an initially strong pressure drop (as seen for the cathode cathode).
The flat shape of the anode channel, additionally leads to a change in two-phase flow dynamics. A wicking process of the droplet while still being attached to the source is observed. The detachment of the droplet is rather continuous and therefore does not lead to a noticeable pressure increase, as observed for the cathode channel.

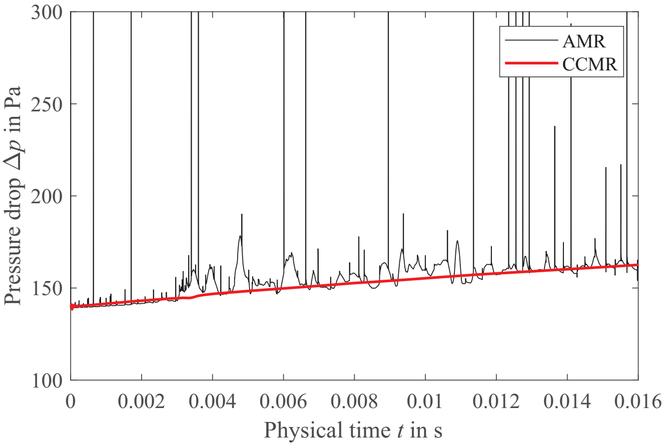

Figure 5.10: Comparison of pressure drop time-series in anode single channel simulation of AMR and CCMR simulation.

It can be assumed, that the CCMR method produces reasonable results regarding droplet dynamics, as well as pressure drop results. Detailed parametric studies of mesh sizes and other CCMR settings might give indications to the source of the deviation within the cathode case. This is assumed to be out of scope for the present work, due to the additional complexity of the investigations.
The use of the CCMR approach leads to an acceleration in computational time of a factor

of around nine, compared to the AMR case, thus giving the possibility of investigating various multi-phase flow regimes with larger time scales. All following VOF investigations are therefore carried out, using the CCMR method.

5.8 Two-phase Flow Regime Investigation

In the present section, the flow inside gas channels is investigated for the developing flow regime, as well as the resulting pressure drops. Herefore, an initial dependence study on the inlet position and number of liquid water inlets is performed, followed by a parametric study of inlet velocities to analyze various flow regimes.

5.8.1 Phase Velocity and Pressure Drop Determination

Phase velocity for gas u_{g} and liquid u_{lq}, as well as the pressure drop Δp within the investigation domain are necessary quantities for the generation of permeability correlations. However, a special evaluation is required, due to lack of slip calculation within the VOF method. Two evaluation approaches are developed and introduced in the following.

The pressure drop within the investigation domain is determined via equation (5.11), as a phase specific force F per channel cross section area A_{GC}. The pressures on inlet p_{in} and outlet p_{out} of the investigation domain are calculated, using the fraction of the cross section α_i that is occupied by the gas phase $A_{2,\mathrm{i}}$, as well as the force $F_{2,\mathrm{i}}$ that acts on it.

$$\Delta p = p_{\mathrm{in}} - p_{\mathrm{out}} = \frac{F_{2,\mathrm{in}}}{A_{2,\mathrm{in}}} - \frac{F_{2,\mathrm{out}}}{A_{2,\mathrm{out}}} = \frac{\alpha_{\mathrm{lq,in}} F}{\alpha_{\mathrm{lq,in}} A_{\mathrm{GC}}} - \frac{\alpha_{\mathrm{lq,out}} F}{\alpha_{\mathrm{lq,out}} A_{\mathrm{GC}}} \tag{5.11}$$

All pressure drop evaluations within the investigation domain are performed via this approach. As shown in section 4.2.1, a single momentum equation is solved for both phases, leading to equal velocities of gas and liquid within the same numerical cell. In order to determine averaged liquid and gas velocities, an averaging method is developed based on the continuity condition shown in equation (5.12).

$$\dot{m} = \dot{m}_{\mathrm{g}} + \dot{m}_{\mathrm{lq}} = \rho_{\mathrm{g}} A_{\mathrm{g}} u_{\mathrm{g}} + \rho_{\mathrm{lq}} A_{\mathrm{lq}} u_{\mathrm{lq}} \tag{5.12}$$

$$u_{\mathrm{g}} = \frac{\dot{m} - \rho_{\mathrm{lq}} A_{\mathrm{lq}} u_{\mathrm{lq}}}{\rho_{\mathrm{g}} A_{\mathrm{g}}} \tag{5.13}$$

The liquid water velocity u_{lq} is assumed to be constant and equivalent to the velocity of the first liquid water volume fraction that enters the investigation domain and exceeds a threshold value of $\alpha = 0.01$. This assumption is found to hold true for the majority of operation cases, especially in the technical relevant superficial velocity intervals of $u_{\mathrm{lq,sup}} = (10^{-4}\,\mathrm{m/s}, 10^{-2}\,\mathrm{m/s})$ and $u_{\mathrm{g,sup}} = (1\,\mathrm{m/s}, 10\,\mathrm{m/s})$. The limits of this assumption are outlined during the creation of the permeability correlation in section 5.9.

Using the calculated liquid water velocities, equation (5.13) is used to determine the averaged gas velocities. In order to increase the accuracy of the calculated values, an averaging is performed according to equation (5.14).

$$u_{\mathrm{g}} = \frac{1}{\tau} \int_{t_{\mathrm{in}}}^{t_{\mathrm{out}}} u_{\mathrm{g}}\, \mathrm{dt} = \frac{1}{t_{\mathrm{out}} - t_{\mathrm{in}}} \sum_{i=1}^{n} u_{\mathrm{g},i}\, \Delta t_i \tag{5.14}$$

Hereby, the averaging process is triggered by the first saturation that enters the investigation domain and exceeds a threshold value of $\alpha_{\mathrm{lq}} = 0.01$. The resulting cross-sectional profile on the inlet face into the domain is used to evaluate the velocity in time fragments, using the time step Δt_i. The number of velocity values available for the averaging procedure is dependent on the velocity of the passing droplet, whereas higher velocities u_{g} result in a lower number of steps n. After exiting the domain, the residence time τ of the droplet in the domain can be estimated.

5.8.2 Position Dependence Study

The previous investigations rely on a single water source term for the analysis of detailed droplet dynamics. With the capability of bridging larger time spans, using the CCMR method, a position and source term number dependence study is performed in the following. Therefore, various positional configurations of source terms and sizes of water volume sources, given in Table 5.5, are implemented.

The total source term flow of 1 µL/s is kept constant for all cases. Configuration 1 defines the baseline case with one introduction position. In addition, the source term is separated into two (configuration 2 – 8) and four (configuration 9 – 11) source terms. The exact source positions are shown in Figure 5.1.

Figure 5.11 depicts the resulting iso-surface plots for a liquid water saturation $\alpha_{\mathrm{lq}} = 0.5$ at $t = 1$ ms (red) and $t = 180$ ms (blue), as well as resulting transient pressure drop signals.

Case 1 shows the baseline configuration with one single source term, resulting in a droplet flow regime (see previous section for detailed description). A division of the source term into two smaller sources (configuration 2 – 5) leads to a droplet flow regime with similar droplet sizes. In addition to variations in detachment times and pressure drops, differences regarding the transition time into the channel corners of the upper wall can be observed. Configuration 2 shows no transition process for the simulated time range.

Table 5.5: Water source configurations for position dependency study with a constant total flow rate of the water source of 1 µL/s.

Configuration	Source positions	Source term in µL/s
1	S1	1
2	S1, S5	0.5, 0.5
3	S1, S3	0.5, 0.5
4	S1, S5	0.25, 0.75
5	S1, S5	0.75, 0.25
6	S1, S2	0.5, 0.5
7	S1, S2	0.25, 0.75
8	S1, S2	0.75, 0.25
9	S1, S2, S5, S6	0.25, 0.25, 0.25, 0.25
10	S1, S2, S3, S4	0.25, 0.25, 0.25, 0.25
11	S1, S2, S3, S6	0.25, 0.25, 0.25, 0.25

The observed droplet sizes are in the range of the channel height. Therefore, small variations in droplet sizes will determine whether a transition to the upper corner occurs or not. Unequal source terms lead to an asynchronous droplet detachment as well as droplet velocity, which eventually results in a recombination of two droplets. The resulting droplet is sufficient in size to perform a position transition to the upper corner (see configuration 4 and 5). The same effect can be observed for cases with source terms that show a similar geometrical position (see configuration 3). Having two geometrically separated source terms equal in size, leads to a droplet removal with approximately constant velocity. A combination of two droplets is not possible for this case (see configuration 2). This results in smaller droplets and therefore absence of a transition process.

An introduction of liquid water on both sides of the channel (configuration 6 – 11) shows a droplet regime flow with variations in droplet sizes. Similar configurations to the previous cases can be observed. Due to smaller individual source terms of 0.25 µL/s, a transition is mainly observed for two sources with close inlet positions (see configurations 10 – 11) and much less frequently for separated source terms (see configuration 9). In general, fluctuations for cases 6 – 11 are assumed to be stronger due to the higher number of droplets that affect the streamline of the gas flow, as well as the stronger cross-sectional channel contraction. These can lead to a diagonal movement of droplets along the side walls of the gas channel, enabling a transition of droplets to the upper corner without the need of large sized droplet diameters (see configurations 7 – 8). A closer look on the respective pressure drop profiles shows reoccurring spikes during the movement of droplets through the measurement section. All profiles show local variations within similar pressure drop ranges.

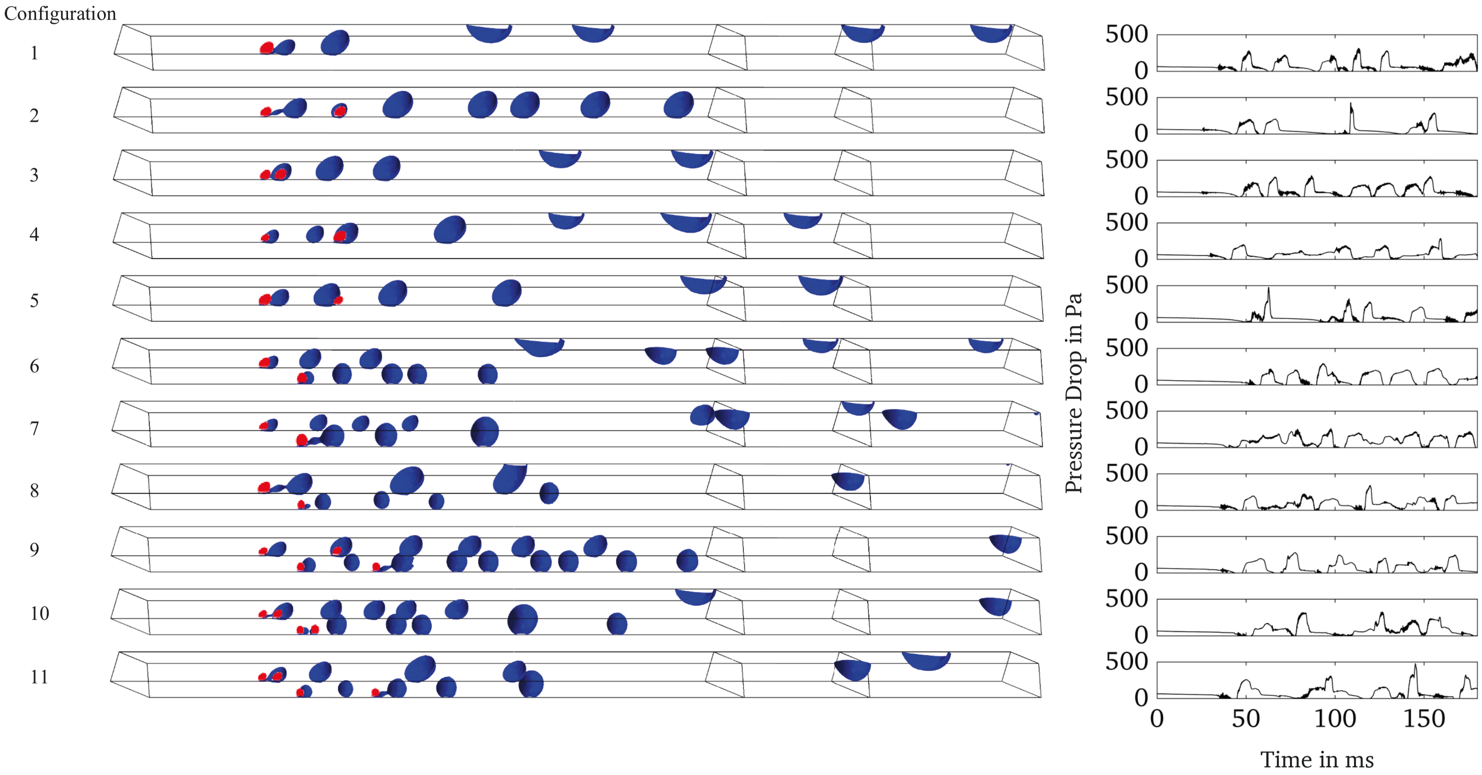

Figure 5.11: Results of position dependency investigation of liquid water source term injection in cathode gas channels. Results show iso-surface plots with $\alpha_{lq} = 0.5$ (left) at t = 1 ms (red) and t = 180 ms (blue), as well as transient pressure drop signals (right).

Hereby, a clear trend regarding pressure drop and position or number of sources cannot be identified, as all cases show deviations. Case 7 and 8 act as an indicator for the numerical errors within the cases, due to the symmetry of both problems. The differences in pressure drops profiles can be seen as the systematic numerical error. Although local variations are present, the pressure drops span over a similar range of 0 to 300 Pa. As the averaged pressure drop is of main interest for these investigations, an independence of the investigated values is assumed.
It can be concluded that a position variation of liquid water source terms results in local differences regarding detachment times as well as droplet sizes, while maintaining the same flow regime. For the purpose of a steady-state two-phase pressure drop correlation, these deviations can be neglected during temporal averaging. It shall be noted, that a position dependence might have a bigger influence for other combinations of superficial velocities i.e. other flow regime. Due to the immense computational effort that would arise for a study with different combinations, this effect shall be disregarded. For all further simulations, a single introduction location equivalent to source term position S_1 in Figure 5.1 is chosen.

5.8.3 Parametric Study

The priory shown independence on inlet position and number of inlets is used as an assumption for further cases. An investigation of flow regimes is performed via variations of gas and liquid mass flows, as shown in Table 5.6 for the cathode cases.

Table 5.6: Overview of two-phase simulation cases in cathode gas channels. The cases are named accoring to GXXLYY where XX corresponds to the superficial gas velocity and YY to the superficial liquid velocity in m/s.

		Gas mass flow $\dot{m}_\mathrm{g}$ in mg/s						
		0.431	2.01	2.278	4.307	10.05	20.62	30.61
Source term $\dot{S}_\mathrm{W}$ in µL/s	15				G07L48	G17L48		G50L48
	11				G07L36	G17L36		G50L36
	8				G07L26	G17L26		G50L26
	5	G01L16	G03L16	G04L16	G13L16	G17L16	G34L16	G50L16
	4			G04L13	G07L13	G17L13		G50L13
	2			G04L06	G07L06	G17L06		G50L06
	1	G01L03	G03L03	G04L03	G07L03	G17L03	G34L03	G50L03
	0.6			G04L02	G07L02	G17L02		G50L02
	0.2	G01L01	G03L01	G04L01	G07L01	G17L01	G34L01	G50L01

The anode case settings are summarized in the appendix in Table A.4. A single liquid water source is used for all stated simulations at the inlet position of S_1 in Figure 5.1. Investigations are carried out for anode and cathode gas channels separately, using the geometry described in Figure 5.1.

The results are visualized as iso-surface plots with $\alpha_{\mathrm{lq}} = 0.5$ for $t = 300\,\mathrm{ms}$. Transient pressure drop signals are provided in addition. Cases 1 – 15 for the cathode gas channels are exemplary shown in Figure 5.12. All further cases can be found in Figures A.6 to A.10.

Analyzing the cases in Figure 5.12, three different flow regimes are found to be present. As previously described in chapter 3.2, two-phase flow regimes of droplet, film and slug flow with characteristic pressure drop profiles are observed. Mist flow is not observed for any configuration.

An exemplary case of a droplet flow regime is given in G17L03. Characteristic for the droplet regime is a periodic formation of droplets, which either results in combination during the removal process, forming larger droplets, or an isolated removal. A periodic built-up and detachment of droplets leads to an alternating sequence of pressure spikes. The volume source term of water, as well as the gas velocity are influencing the detachment process and therefore the size of droplets. Comparing cases G07L01 and G34L01, it becomes apparent that higher gas velocities lead to an earlier detachment and therefore a formation of smaller droplets. At the same time, a comparison of cases G17L01 with G17L03 shows, that lower liquid velocities lead to the same effect.

When gas velocities are further lowered and liquid water velocities are further increased, a transition towards the slug regime is observed, as shown in case G01L16. The a major part of the flow channel cross-section is blocked by liquid water, leading to a strong pressure increase followed by a decrease to the single-phase value after slug removal. The lower the gas velocities and the higher the liquid water source terms, the more severe the slug formation (compare G01L03 to G01L16). The slug flow regime is characterized by an increasing importance of gravitational forces over surface tension, as well as larger characteristic diameters, resulting in higher values of *Bo* and *We*. This might lead to instabilities and therefore deviations from the spherical droplet shape after passing a certain threshold (see section A.1.2). Nevertheless, most slug cases are observed to have fairly spherical shapes.

A strong increase in both velocities leads to a transition into film flow, where a strongly transient liquid water film is removed along the upper channel wall. An example is given with case G34L16. A transition from droplet into film flow is shown in case G17L16, where the combination of droplets in the upper channel corner results in a film formation. With the underlying assumption of constant liquid velocity, the first entering liquid water saturation detected in the evaluation section, is kept constant throughout the analysis. This assumption is found to be unreasonable for the majority of cases in the strongly transient regime of film flows, producing nonphysical pressure drop data. The quantitative pressure drop information is therefore discarded for the affected cases, whereas qualitative data is still used. This shows strongly transient pressure drop data throughout the entirety of the removal process.

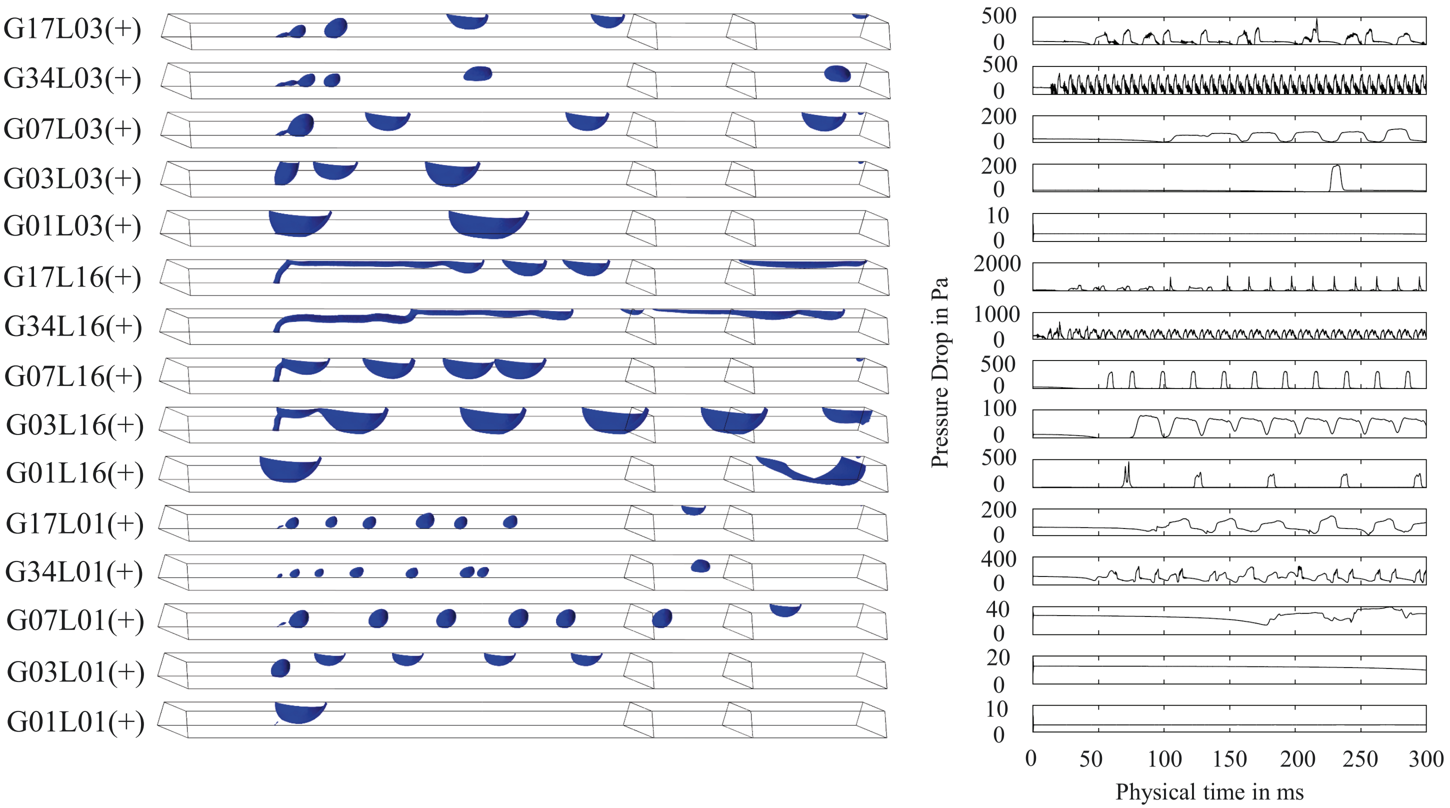

Figure 5.12: Results of inlet gas and liquid water velocities variations for cases 1-15 in cathode gas channels. Results show iso-surface plots with $\alpha_{lq} = 0.5$ (left) for t = 300 ms, as well as corresponding transient pressure drop signals (right).

The anode data shows similar results with stronger facilitation of films and slugs. A stronger influence of surface tension is expected for anode cases, due to the lower viscosity and density of hydrogen gas. In addition, the geometrically lower channel height has to be taken into account. A favored combination of droplets is observed as a result of geographical proximity, transforming into larger configurations of films or slugs.

All cases are subsequently divided into flow regimes of droplet, film or slug flow. The classification is performed through visual iso-surface data and pressure drop information. Flow maps for anode and cathode channels as a function of gas and liquid water superficial velocities are created with transition lines between the regions, as shown in Figure 5.13. The region coloring indicates which cases are used for the subsequent two-phase permeability creation (discussed in section 5.9). Yellow and red cases are neglected, whereas green cases are used. The reasons will be elaborated in the following section.

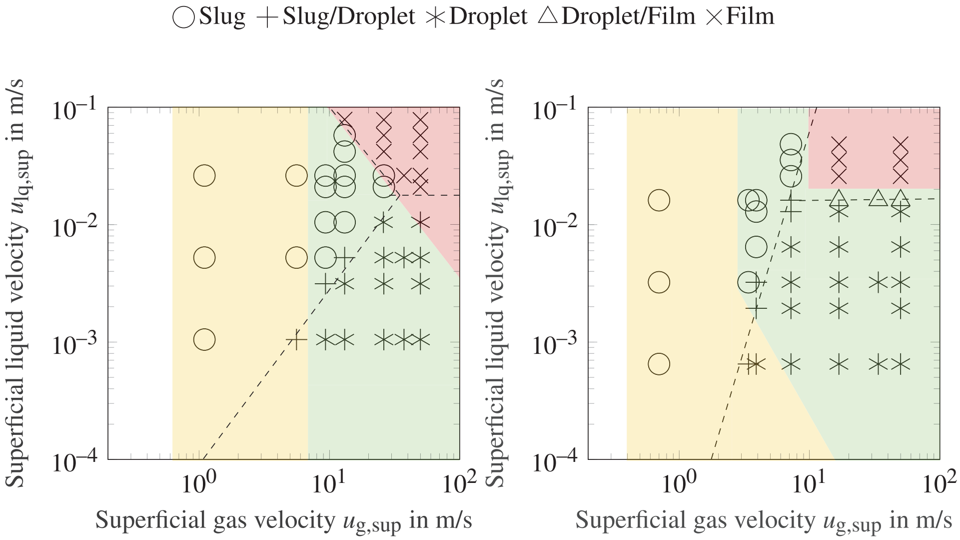

(a) Anode GC flow map.

(b) Cathode GC flow map.

Figure 5.13: Two-phase flow map of VOF simulations in single channels for anode (left) and cathode (right) with indication of nonphysical data (red), unused data (yellow) and correlation data (green).

5.9 Two-phase Pressure Drop Correlations

The pressure drop data, generated from the VOF simulations within selected single channel cases is used to derive two-phase permeability correlations. Darcy's law is used to transform recorded pressure drop values into permeabilities. The correlations can be used to predict two-phase pressure drops in flow field channels, using gas composition and velocity, as well as liquid water saturation values.

The regression data requires previous filtering before it can be used within the correlation. Cases that produced no data within the measuring time of 300 ms, e.g. G01L01 or G03L01, are colored yellow in Figure 5.13 and are not taken into further consideration. As priory mentioned, the majority of film flow pressure drop data is corrupted as a result of highly varying liquid velocities. Hence, the film flow cases are almost entirely excluded from the regression data, with exception of three anode gas channel cases. Additional cases, experiencing a similar transient behavior are not taken into account as well. All cases excluded as a result of nonphysical permeabilities are colored red in Figure 5.13. The remaining cases, shown with green coloring in Figure 5.13, are used to create correlations for anode and cathode side gas channels. The gas permeabilities are calculated according to equation (5.15), using pressure drops, as well as averaged velocities for gas and liquid water according to the approaches discussed in section 5.8.1. Various permeability correlations can be found in literature [82–84], showing a minimum threshold saturation for relative permeability values in two-phase flows that goes as far as 90 %. *Corey et al.* [85] show threshold values of around 80 % for the application in gas and oil two-phase flows. Permeability correlations are used within porous media, as well as channels. According to the trend of the present data, a threshold value of 80 % is assumed and incorporated into the regression process. This assumption is necessary, as saturation values above 50 % could not be reproduced in any of the cases.

$$K_{\mathrm{v,g}}(\alpha_{\mathrm{lq}}) = \begin{cases} \frac{\mu_{\mathrm{g}}\, u_{\mathrm{g}}\, l_{\mathrm{ID}}}{\Delta p_{g}(\alpha_{\mathrm{lq}})}, & \text{for } \alpha_{\mathrm{lq}} < 0.8 \\ 0, & \text{for } \alpha_{\mathrm{lq}} \geq 0.8 \end{cases} \tag{5.15}$$

The relative permeability of liquid water cannot be determined with the present approach. Due to the negligible permeability of liquid water at small liquid water saturation values a threshold for liquid water of 20 % is applied analogously. Hence, the relative permeability of liquid water is assumed to be 0. The focus of the present studies are stationary, technically relevant conditions which are usually found to be low liquid water saturation values within flow field channels, justifying this assumption. The dependency for higher liquid saturation values $X(\alpha_{\mathrm{g}})$ is not further investigated.

$$K_{\mathrm{v,lq}}(\alpha_{\mathrm{lq}}) = \begin{cases} 0, & \text{for } \alpha_{\mathrm{lq}} < 0.2 \\ X(\alpha_{\mathrm{lq}}), & \text{for } \alpha_{\mathrm{lq}} \geq 0.2 \end{cases} \tag{5.16}$$

The exported raw data from selected cases is given in the Appendix in Figures A.11 and A.12. As a result of different liquid water velocities between the cases and therefore differences in number of droplets or slugs passing the investigation domain, unequal numbers of data points are generated. Therefore, in order to achieve an appropriate weighting during regression, all cases are reduced to single points, using a k-means clustering algorithm in MATLAB [86]. The k-means algorithm is used to find k centers for a set of n data points, in order to minimize the total squared Euclidean distance between each point and the center point. [87, 88] Figure 5.14 shows the application of the k-means algorithm on case G26L21. One center point is generated, indicated by an X-symbol. The three outliers are automatically identified by the method and receive lower weighting while determining the center point. Applying the technique on the simulation results, each VOF case is reduced to a single data point.

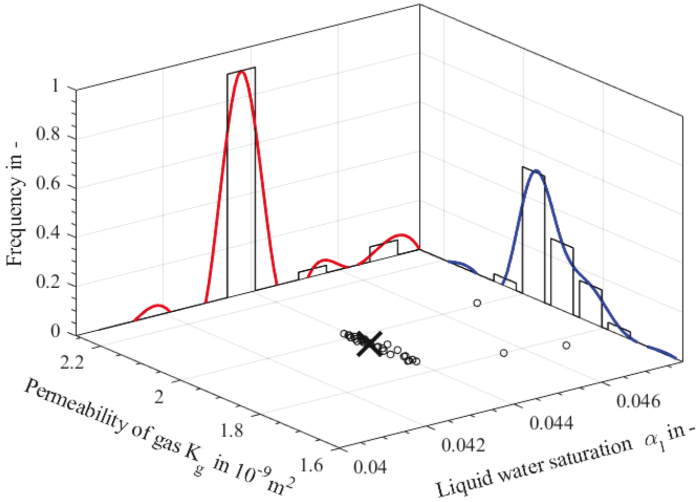

Figure 5.14: Exemplary application of k-means clustering algorithm on case G26L21.

The results of the processed gas permeability data is shown in Figures 5.15 and 5.16 as a function of liquid water saturation for anode and cathode channel, respectively. Error bars are given for each operating point to indicate the maximum spread between data points and center (see Figure 5.14). Performing a regression on the processed data leads to gas permeability correlations, which are given in equation (5.17) and shown in Figures 5.15 and 5.16.

Starting at the single phase permeability of gas for a saturation of $\alpha = 0$, both curves show an exponential drop with increasing saturation values. Higher liquid water values lead to increasing resistances towards the gas flow, reducing the gas permeability and therefore increasing the pressure drop.

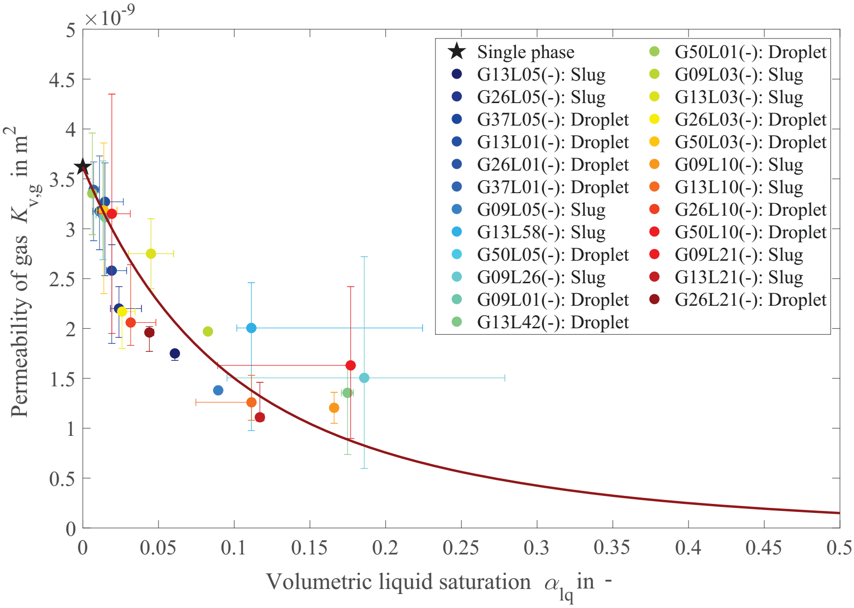

Figure 5.15: Anode gas channel permeability correlation constructed from selected cases with indication of variation bars for the respective case.

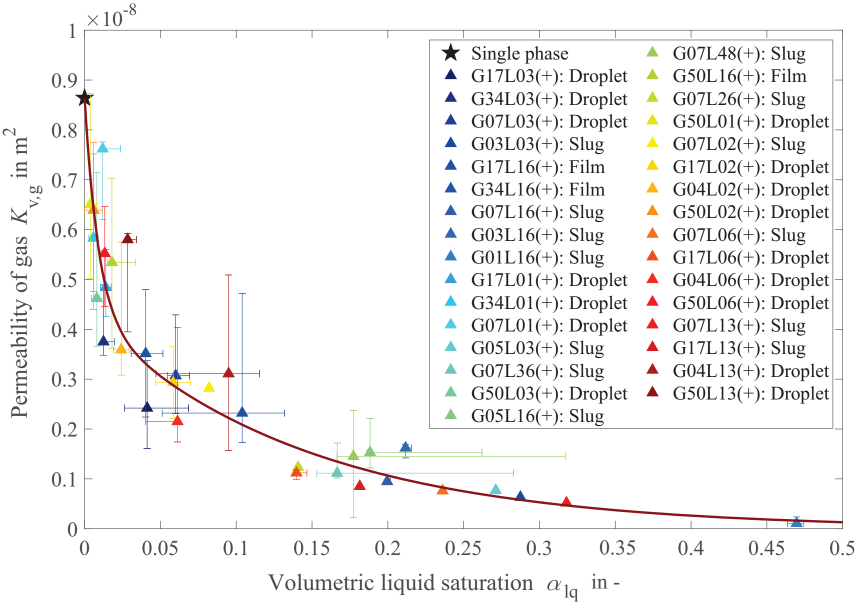

Figure 5.16: Cathode gas channel permeability correlation constructed from selected cases with indication of variation bars for the respective case.

An initially stronger drop is observed inside cathode channels. The reason is found in the stronger presence of droplet cases. The flat cross-sectional shape of anode channels leads to a facilitation of film and slug formation, as priory mentioned, thus resulting in a rather flat regression curve. Additionally, the distance between the core of the flow, exhibiting the highest velocities, and the source position is longer for anode channels. The presence of wall-adjacent liquid water formations therefore poses a weaker resistance to the flow, resulting in a rather flat slope of the permeability curve.

The fluctuations of permeability values within the same operation point, indicated by the vertical error bars, are generally stronger for lower saturation values. On the other hand, liquid water fluctuations within the same point are rather found in slug flow cases with higher saturation values. The horizontal fluctuations have to be set into proportion to the saturation values of the center points itself. Hence, the swings are, relatively observed, not varying significantly when comparing different regimes. Additionally, droplet cases produce more signals, wherefore a higher spread of data points is expected in general.

With determination coefficients of $R_\mathrm{A}^2 = 0.7357$ and $R_\mathrm{C}^2 = 0.8639$ for anode and cathode respectively, the regression functions are found to represent the data reasonably.

$$K_{\mathrm{v,g},i}(\alpha_\mathrm{g}) = \begin{cases} 1.81 \cdot 10^{-9}\mathrm{m}^2 \left(\mathrm{e}^{-15\,\alpha_\mathrm{g}} + \mathrm{e}^{-5\,\alpha_\mathrm{g}}\right), & \text{for } i = \mathrm{a} \\ 4.32 \cdot 10^{-9}\mathrm{m}^2 \left(\mathrm{e}^{-110\,\alpha_\mathrm{g}} + \mathrm{e}^{-7\,\alpha_\mathrm{g}}\right), & \text{for } i = \mathrm{c} \end{cases} \tag{5.17}$$

A comparison with literature models, summarized by *Cho et al.* [89], is given in Figure 5.17. Normalized permeability values are chosen, whereas a normalized relative gas permeability value of $K_\mathrm{v,g}(\alpha)/K_\mathrm{v,g}(\alpha = 0) = 1$ represents the single-phase state of pure gas and $K_\mathrm{v,g}(\alpha)/K_\mathrm{v,g}(\alpha = 0) = 0$ of pure liquid water.

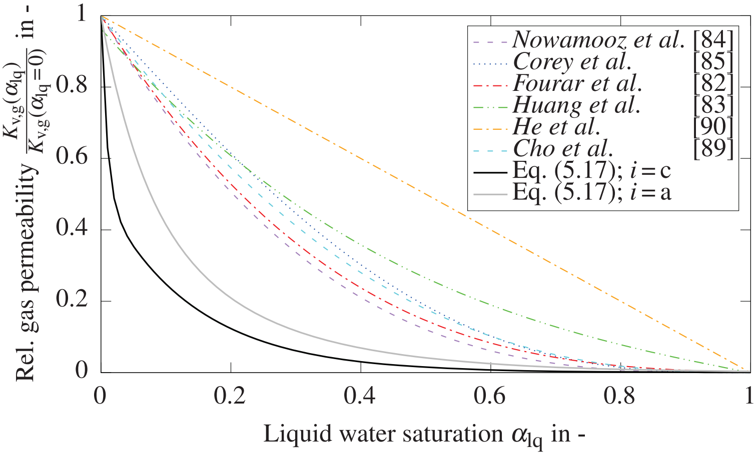

Figure 5.17: Comparison of developed permeability correlations with literature approaches initially summarized by *Cho et al.* [89].

A simple linear dependence on the saturation, reffered to as the X-model [91, 92], is widely used within PEMFC models [90, 93] due to the lack of appropriate data. Further advanced and either experimental [82, 84, 85] or simulation [83] based approaches exist, showing a characteristic shape of the gas permeability function. Whilst all correlations are initially developed for two-phase flow in porous media, *Cho et al.* [89] show a derivation for the application in horizontal micro channels. Separate functions for multiple regimes are generated. The correlation by *Cho et al.* in Figure 5.17 represents the slug-flow results, which are in good agreement with the remaining porous media approaches. A comparison with the present work shows a similar shape with a significantly stronger drop in the region of low saturation values for the developed functions. As previously shown, anode and cathode correlation from equation (5.17) are exhibiting strong difference regarding their corresponding permeability function slopes as a result of channel shape. Differences to the literature correlations are expected to be even higher, as the systems differ strongly in channel geometry, flowing fluid, as well as investigated regimes. While *Cho et al.* showed an agreement to porous media for a particular setup, a generalization in regards to absolute values should not be assumed. Due to the strong interconnections between pores in porous layers, a rather low influence on the pressure is expected for low saturation values. Channels are directly, locally contracted even when low amounts of liquid water are present, representing a resistance for the gas flow. On the other hand, the goal of the present study is to derive a single, numerically stable correlation that represents all regimes within PEMFC gas channels and can be implemented into a simplified channel model. The combination of various regimes leads to deviations in the nature of the function when comparing to literature studies, which mainly focus on a single regime.

In summary, plausible correlations are generated, whereas a final validation via experimental measurements is needed in order to ensure the proper predictability of two-phase pressure drops. The stack model, introduced in the present work is set up in a way that the developed two-phase permeability correlations can be incorporated into the channel regions of the active area of anode and cathode.

In the following, the single cell geometry is simulatively investigated in detail.

6 Detailed PEMFC Single Cell Simulations

The creation of a stack model with explicit single cell modeling requires prior detailed knowledge of the processes within a PEMFC single cell. A PEMFC single cell is therefore investigated and elaborated in the present chapter. Detailed CFD-simulations on a single cell basis are performed, using the STAR-CCM+ PEMFC model. The results are validated against experimental pressure drop, as well as local current density and temperature measurements generated on a single cell setup.
Parts of the results within this chapter can be found in the Master's Thesis of *N. K. Cheruku* [94] and *A. Jurzyk* [73], which were created while working under my supervision.

6.1 Computational Domain

Detailed single cell simulations are performed using the geometry depicted in Figure 6.1.
An MEA with an active area of 263 cm^2, including all functional layers shown in Figure 3.3 is placed as indicated by the measurements.
The anode active area flow field is vertically divided into three regions (as shown in section 3.1.2). Hydrogen gas is introduced into the domain through 4 inlet channels, leading into a single collector region. The flow is vertically redirected into 46 trapezoidal channels with constant cross-section within the active area (Region 2). Following two additional steps of collection and redirection into the subsequent regions (Region 3 with 36 channels and Region 4 with 46 channels), the gas is collected again and exits the anode flow field through 4 channels.
The cathode active area flow field is horizontally divided into three regions (as shown in section 3.1.2). Oxygen is introduced through 30 inlet channels. After passing through 34 trapezoidal distributor channels with constant cross-sectional area (Region 5), the flow is introduced into 68 vertical active area channels (Region 4). The geometric configuration of the channels within the three active area section (Regions 4 - 2) is characterized through vertically alternating contracting and expanding channel cross-sections. The connections between the three main regions is showed in detail in Figure 3.4. Leaving region 2, the gas is directed into 34 collector

channels (equivalent to the channels in Region 5) and exits through 34 outlet channels.
The coolant flow is introduced through 12 inlet channels into a complex distributor region. No defined flow channels are present. After introduction into the first active area region (Region 5), the coolant flow is redirected into cathode and anode coolant channels. The number of channels is equivalent to the gas channels of the respective region. The flow is lead out through a complex collector region into 12 outlet channels. A coolant bypass is present additionally, horizontally flowing at the outer boundaries of the active area.

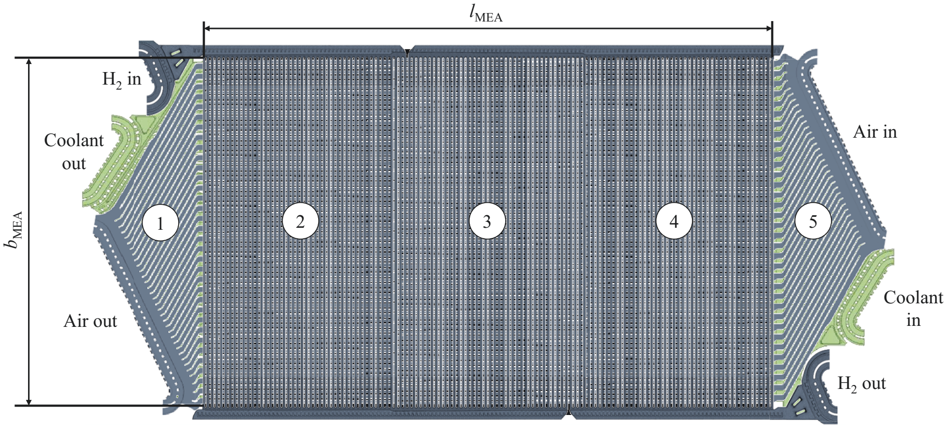

Figure 6.1: Detailed single cell geometry for PEMFC simulations.

A summary of the geometrical measurements of the MEA, including all components, is given in Table 6.1. Anode and cathode values are equivalent.

Table 6.1: Parameters for detailed single cell geometry.

Parameter	Description	Value
l_{MEA}	Length of MEA	217 mm
b_{MEA}	Width of MEA	121.4 mm
A_{MEA}	Geometrical area of MEA	263 cm^2
H_{GDL}	Thickness of GDL	115 µm
H_{MPL}	Thickness of MPL	40 µm
H_{CL}	Thickness of CL	10 µm
H_{PEM}	Thickness of PEM	15 µm

The specifics of the numerical grid are giving in the following.

6.2 Meshing

In order to ensure a proper resolution of local effects while keeping the count of numerical cells at a minimum, a hybrid mesh approach is chosen. Hereby, a maximum total mesh count of 78 million cells is achieved. The upper limit definition is stemming from random access memory (RAM) limitations of 256 GB. The active area is resolved, using a purely conformal mesh, thereby additionally tackling mesh-related numerical challenges. Figure 6.2 shows a fraction of the structured mesh of the detailed cell active area.

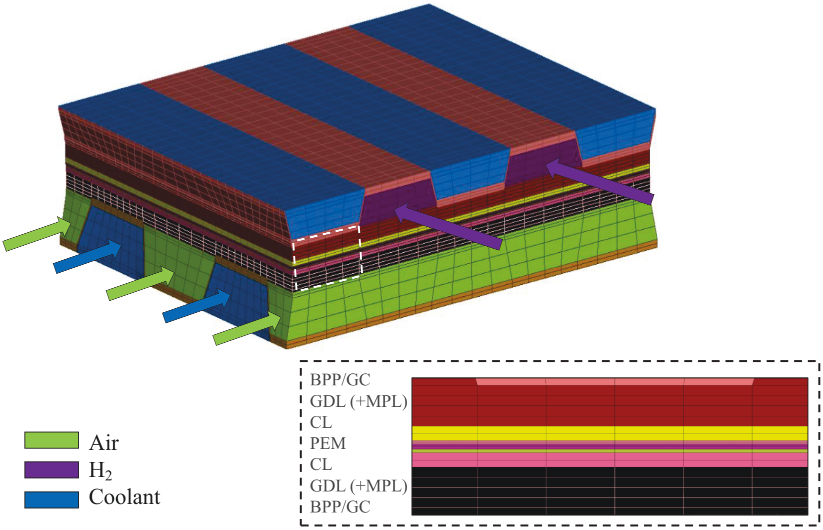

Figure 6.2: Mesh fragment of detailed single cell active area model with indications of fluid inlets.

Due to the dominantly laminar character of the flow inside the channels of the active area (see section A.1.3), a resolution of 5×6 and 5×4 cells in cross-sectional direction is chosen for anode and cathode, respectively. These values are found to be too coarse for the appropriate representations of the flow inside anode flow field collector regions, due to emerging turbulences. In order to estimate deviations of the pressure drop, mesh size and turbulence model, investigations are performed and shown in section A.2.2. Coolant regions inside the active area are resolved with a mesh size equivalent to the anode gas channels. Due to the complexity of the coolant flow field inside the collector and distributor region, a hybrid mesh, consisting of hexa- and tetrahedral cells is chosen. The small thickness of the bipolar plate allows an assumption of thermal equilibrium between cathode gas and coolant within the distributor and collector regions and is therefore neglected (see following section).

Despite the inclusion of a 2-dimensional reaction plane, the CL regions are geometrically represented within the model, with the reactions taking place at the CL-MEM-interfaces. The chosen number of numerical cells in through-plane direction of the MEA (see Figure 6.2) is found to be sufficient for the description of transport processes.

6.3 Simulation Settings

The present section summarizes the assumptions and simplifications, operation conditions and material properties of the models.

6.3.1 Geometrical Simplifications

Modeling assumptions of geometrical and physical nature are made throughout the simulations and summarized in the present section. The geometric simplifications are summarized as follows:

1.) Neglection of channel fillet radii:
Analogously to the single channel simulations in chapter 5, channel fillet radii, which are manufacturing related features, are neglected for all detailed cell simulations, leading to sharp transitions in the bipolar plate corners. The influence on the pressure drop in comparison to the experimental value is discussed in detailed in section 6.5.

2.) Simplification of GDL intrusion:
The GDL/GC-interface is shifted into the channels in order to account for the GDL-intrusion. The interface is assumed to be a horizontal planar plane, whereas the intrusion value into channels is experimentally determined (according to [74]) for the corresponding compression force of 1.5 MPa and subtracted within the models as a constant horizontal offset from the initial channel cross-section areas adjacent to the GDL.

3.) Neglection of BPP in collector and distributor regions:
Due to the small thickness of the bipolar plate, a thermal equilibrium can be assumed at the inlet to the active area. The cathode gas approximately adopts the coolant temperature, due to large differences in heat capacities of the fluids. With the additional assumption of a negligible transversal electrical conductivity within the bipolar plate, a full decoupling of flow fields of the three media can be performed. Additionally, only small regions of anode collector and distributor are effected by the coolant. The bipolar plate is therefore excluded within all regions except the active area.

4.) Periodic connection of anode and cathode coolant flow field:
The simulation of a single cell setup requires the setting of proper geometric separation of the domain. In the present study, the anode and cathode flow fields are geometrically separated and physically connected through the application of periodic boundary conditions.

5.) Introduction of numerical in- and outlet channels:
Due to arising back flow during simulation, outlet channels are introduced, which extend the distance between outlet boundary condition and parts of the investigation domain, thus increasing numeric stability. The additional pressure drop is deducted for evaluations of the pressure drop.

6.3.2 Physical Assumptions

The following physical assumptions are made for all detailed single cell simulations:

1.) Thermal equilibrium between air and coolant flow:
As a result of the neglection of the bipolar plate inside the distributor and collector regions, the inlet cathode gas temperature is assumed to be equivalent to the coolant temperature. The anode inlet temperature is not affected.

2.) Adiabatic boundary conditions:
As for simplicity reason, the outer walls of the cell are assumed to be adiabatic. The temperature deviations towards the experimental cell is discussed in the respective section.

3.) Electrochemical reactions on CL-MEM interface:
Due to the lack of a three-dimensional PEMFC reaction model within STAR-CCM+ [65], the reactions of ORR and HOR are assumed to be occurring on the CL-MEM interface of cathode and anode respectively. The included regions of the catalyst layer act merely as a mass transport resistance. Occurring consequences resulting for this assumption are discussed in the respective region.

4.) Equal reaction rates for vapor and liquid water production:
The phase in which water is produced is often assumed to be a single one only i.e. vapor or liquid, due to a lack in understanding of the underlying processes. As a result, the present work assumes equal rates for parallel reactions of liquid water and water vapor production on the cathode CL-MEM interface.

5.) Neglection of phase-change:
Stability issues of the present PEMFC model in STAR-CCM+ [65] regarding phase-change processes arise, wherefore phase-change is entirely excluded from all simulations. The only possibility of a liquid water presence in anode compartments therefore is through desorption of liquid water, occurring exclusively for $\lambda > 16.8$ (see equation (4.44)). As all studied cases exhibit smaller values, no liquid water is observed within the sections of the anode. Additional consequences of this assumption are discussed in the respective regions.

6.) Mist flow assumption in flow field channels:
Due to lack of an appropriate two-phase model for the pressure drop inside gas channels within STAR-CCM+, the mist flow assumption is applied. It is assumed that the liquid water is dispersed as fine mist, showing a negligible influence on the single-phase pressure drop.

7.) Implementation of RANS turbulence model:
The occurrence of turbulence inside gas channels is found within the side regions of the anode flow field (see section A.2.2). A coexistence of laminar and turbulent flow has to be explicitly accounted for by solving with appropriate models in the respective region. This requires prior knowledge of the regions in which turbulence occurs, as well as a spatial separation of the affected regions. Due to numeric instabilities during simulation when excluding turbulence models, all simulations are run with a k-ε turbulence model. The description of laminar cases or regions with a turbulence model introduces turbulent viscosity terms which falsify the solution. The introduced error is tolerated due to the priory stated reasons.

6.3.3 Operation Conditions and Material Properties

The operating conditions for all detailed single cell PEMFC simulation cases are summarized in Table 6.2. Mass flow inlet and pressure drop outlet boundary conditions are specified for all fluids, as indicated in Figure 6.1. The mass flows, corresponding to the given values of λ_A and λ_C, are generated via experimental data (see section 6.5). All outer walls are thermally insulated (adiabatic). Due to hardware restrictions, minimum mass flows have to be supplied to the system applicable for the low current density cases of ID3. The minimum mass flow is defined as $\lambda_\mathrm{A}\,(U = 0.757\,\mathrm{V}) = 2.0$ and $\lambda_\mathrm{C}\,(U = 0.757\,\mathrm{V}) = 2.2$.
The cell is simulated in potentiostatic mode, applying constant potential boundary conditions on the cathode and anode BPP terminal, as $U_\mathrm{C} = U_\mathrm{cell}$ and $U_\mathrm{A} = 0\,\mathrm{V}$, respectively. Experimental current density values j_exp are given in addition. All further material parameters are given in Table A.5.

Table 6.2: Summary of detailed single cell simulation parameters.

	ID2	ID3	ID4	ID5	ID6	ID7
U_{cell} in V	0.687	0.979 - 0.614	0.693	0.692	0.695	0.696
j_{exp} in A/cm^2	1.0	0 - 1.5	1.0	1.0	1.0	1.0
λ_{A}			2.0			
$p_{\mathrm{A,out}}$ in bar			1.8			
$T_{\mathrm{A,in}}$ in °C	70	90	80	90	90	90
$RH_{\mathrm{A,in}}$ in %	50	25	50	50	75	100
λ_{C}			2.2			
$p_{\mathrm{C,out}}$ in bar			2.1			
$T_{\mathrm{C,in}}$ in °C	65	85	75	85	85	85
$RH_{\mathrm{C,in}}$ in %	50	25	50	50	75	100
$\dot{V}_{\mathrm{Cool,in}}$ in l/min			1.5			
$T_{\mathrm{Cool,in}}$ in °C	65	85	75	85	85	85

The single cell simulation results are discussed in the following section.

6.4 Detailed PEMFC Single Cell Simulation Results

The detailed investigations are focused on the 0.686 V operation point (corresponding to around 1 A/cm^2) of the ID3 case (see Table 6.2). The cell shall be investigated regarding fluid flow, thermal and electrical effects. A focus is placed on the investigation of the water management. The orientation of all plots is in accordance to the configuration shown in Figure 6.1.

Figure 6.3 shows the gas velocity fields of anode and cathode on a plane-cut through the channels for the investigation case.

The cathode flow field shows velocities of around 7 m/s inside the active area, with maximum values of up to 12.5 m/s at in- and outlet regions of the active area. The velocity over the active area is relatively constant, with lower values around the intersection regions. The inflow into the investigation domain exhibits transitional flow pattern, which have to be resolved via a proper turbulence model. Separate investigations addressing that issue are performed in section A.2.2.

The anode gas channels show higher maximum velocities of up to 38.6 m/s, with relatively constant values for the active area sections of around 4 m/s. An unequal distribution of gas is observed in channels, adjacent to the neighboring regions. The gas inside the last channel of one section skips the regular flow path through convective under-the-land flow through the GDL. A continuous loss in gas, indicated through the deceleration along the channel is observed as a result. This phenomenon is characteristic for meandric flow field designs.

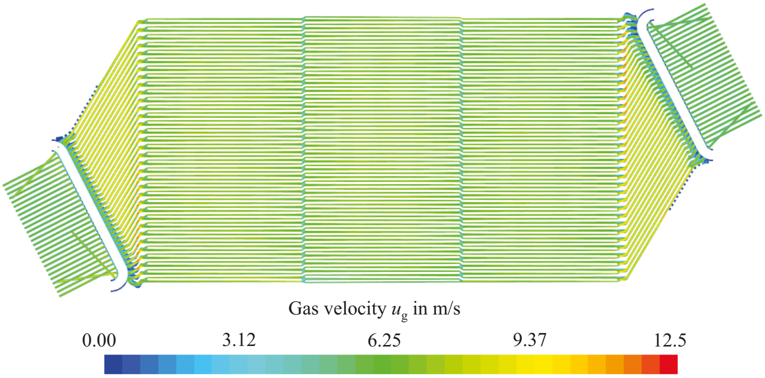

(a) Gas velocity in cathode channels.

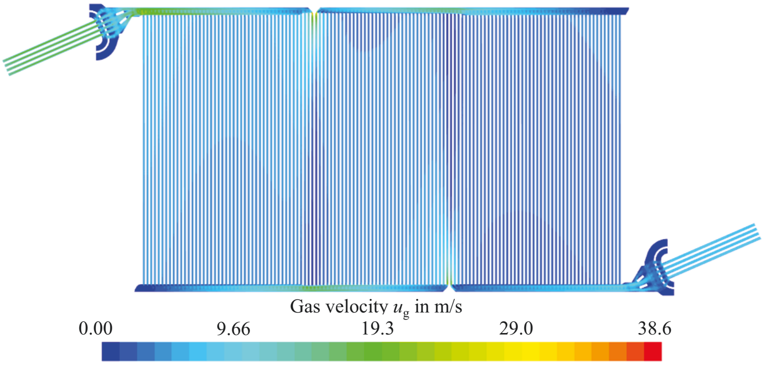

(b) Gas velocity in anode channels.

Figure 6.3: Gas velocity on anode (top) and cathode (bottom) cut plane inside gas channels for ID3 case at 0.686 V.

The highest velocity values are found inside the side regions, due to the combination of the total gas flow inside a single channel. A separate investigation into the proper resolution of turbulence inside the anode flow field can be found in section A.2.2. Both regions show operation conditions inside the active area gas channels, which are in the applicability range of the VOF-based correlation, thus affirming the plausibility of the chosen bounds. Due to the mist assumption in gas channels, no influence through liquid water is observed. Therefore, the presence of liquid water inside the cell is investigated through a plot of the volume fraction on the cathode CL-MEM interface in Figure 6.4.

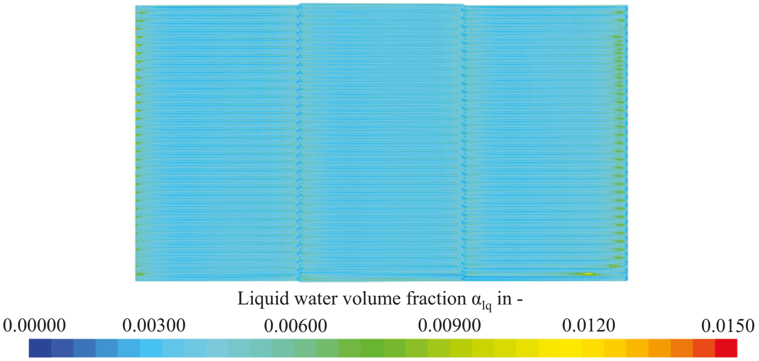

Figure 6.4: Liquid water volume fraction plot on anode CL-MEM interface for ID3 case at 0.686 V.

The plot shows a rather uniform water volume fraction distribution with values between 0.6 % and 1 %. Local maxima of up to 1.5 % are observed, which are assumed to be numeric errors, due to the largely symmetric character of the cell. Local accumulations towards the transition regions, separating the three regions, are found to be present. The profile inside the main regions resembles the shape of the channels. The reason lies in the favored reaction in under-the-channel regions due to limited cross-diffusion of the porous media. Due to the absence of phase-change in combination with low membrane water contents (see Figure 6.5), no liquid water can be found in the compartments of the anode.

The water management inside the cell is further analyzed via means of the membrane water content λ, shown in Figure 6.5 as a plot on the anode CL-MEM interface.

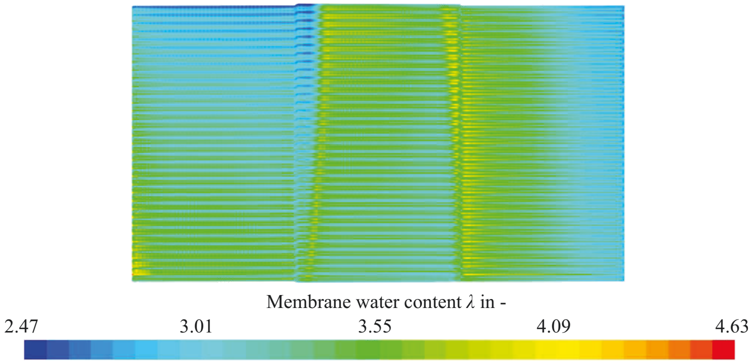

Figure 6.5: Membrane water content plot on anode CL-MEM interface for ID3 case at 0.686 V.

The membrane water content distribution is strongly influenced by the flow field geometries. Two sources of water, leading to a membrane humidification, are coexisting within the fuel cell; cathode product water and water due to inlet gas humidification. For the present operating point, especially product water is dominantly influencing the humidification of the membrane, due to low inlet *RH* in combination with a medium current density. An equilibrium between water retention, removal and absorption into the membrane is present. Region 4 and 3 are showing an increase in water content as a function of cathode flow length, stemming from accumulation in reaction water. The effect is dominated by an influence of the horizontal under-the-land flow of the anode, resulting in a strong local drop in water content in the two affected regions. The horizontal pattern on the water content strongly resemble the cathode channels. Production water on the cathode side is favorably retained in the under-the-land areas within the CL region, as a result of the lower local velocities. Therefore a preferred absorption into the membrane occurs in these regions, leading to higher water contents, while higher local gas velocities lead to a stronger dry out. Faint vertical lines show an analogous but weaker effect of the anode flow channels within the main regions.

The through-plane membrane water content is evaluated at the interfaces between membrane and cathode CL, as well as the four numeric cells in-between as surface average values of in-plane sections. The results are shown in Figure 6.6. Values for the 0.855 V case are included in addition.

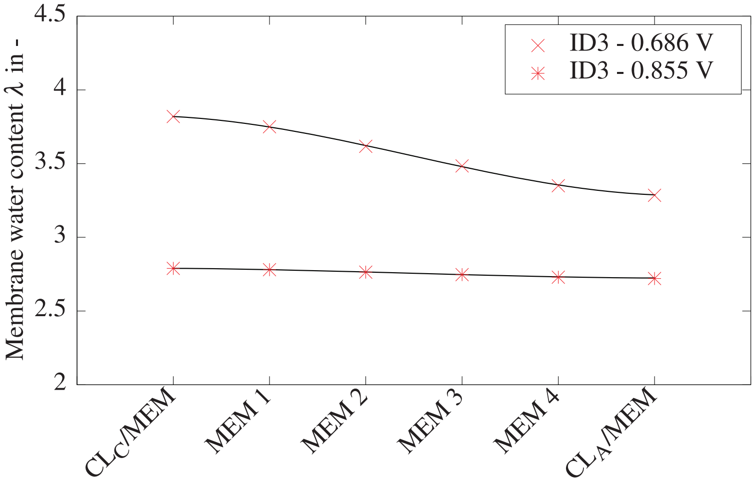

Figure 6.6: Through-plane membrane water content comparison of two ID3 cases at 0.686 and 0.855 V.

The low current point shows a small membrane water content gradient with a maximum value of 2.79 on the cathode side and a minimum of 2.72 on the anode. A low reaction rate leads to the presence of a low water content gradient. The membrane humidification is mainly dominated by the relative humidity of the inlet gases on cathode and anode side.

An increase to a higher current density results in an increase of gradient and absolute membrane water content to values between 3.82 at the cathode CL-MEM interface and 3.29 on the respective anode interface. The increase in anode water content is a result of stronger back-diffusion. A higher reaction rate results in enhanced water production, increasing the concentration gradient between anode and cathode side, leading to a back-diffusion term towards the anode compartment. At the same time, an EOD-driven water flow is present, mainly contributing to a gradient towards the cathode. The ratio of EOD- and back-diffusion-driven flow is shifted towards anode dry-out with increasing current densities. A proper anode gas humidification is crucial for these operating points.

The membrane water content directly affects the current density distribution, which is shown as a surface plot on the anode reaction interface in Figure 6.7.

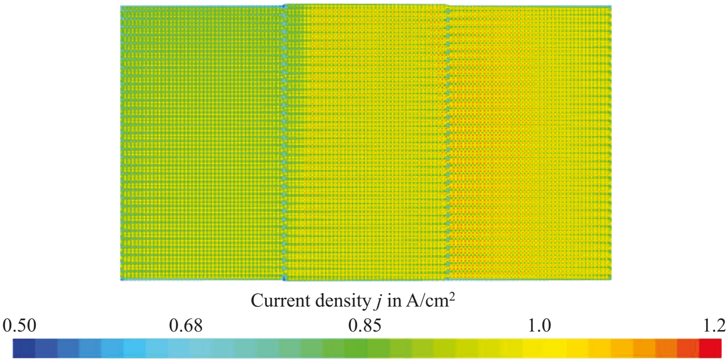

Figure 6.7: Current density plot on anode CL-MEM interface for ID3 case at 0.686 V.

The current density profile strongly resembles the priory discussed water content profile, whereas a higher water content leads to higher current density values. The reason can be found in a decrease in ohmic losses as a result of the enhanced membrane humidification (see section 3.1.1). The strong influence on the membrane water content, gives an indication of a cell operation within the ohmic region. It shall be noted, that for a different operating point with strong liquid water presence, higher gas velocities are crucial for a water removal, therefore leading to lower mass transport losses. This mainly occurs within the concentration region, characterized through higher current densities.

A decrease in current density from cathode in- to outlet is observed in addition, stemming from a reaction induced oxygen depletion. Higher stoichiometries could counteract this effect.

The experimental validation of the detailed single cell PEMFC results is elaborated in the following section.

6.5 Experimental Validation of Detailed PEMFC Simulations

The detailed single cell results are used as reference cases for the subsequent stack model built-up procedure and therefore have to be validated. For this reason, experimental PEMFC single cell investigations are performed and compared to the respective simulation results. The findings are elaborated in the present section.

6.5.1 Experimental Setup and Operating Conditions

Experimental measurements are performed on a single cell PEMFC setup with an integrated current scan shunt device by S++ [95]. The simultaneous in-operation measurement of 544 current and 144 temperature segments is possible. The measurement plate, as well as a single PEM fuel cell are placed inside a cell holder in the configuration shown in Figure 6.8. The gas channels of the bipolar plates enclosing the MEA, are exclusively open on the side which faces the MEA. An additional bipolar plate with closed gas paths is used below the S++ plate to ensure proper tempering. All plates are supplied with coolant. GDLs are placed between the inactive layers to ensure electric contact between the current collector plates and bipolar plates. The configuration is compressed via two pressure cushions in order to ensure a compression force of 31 kN on the cell configuration.

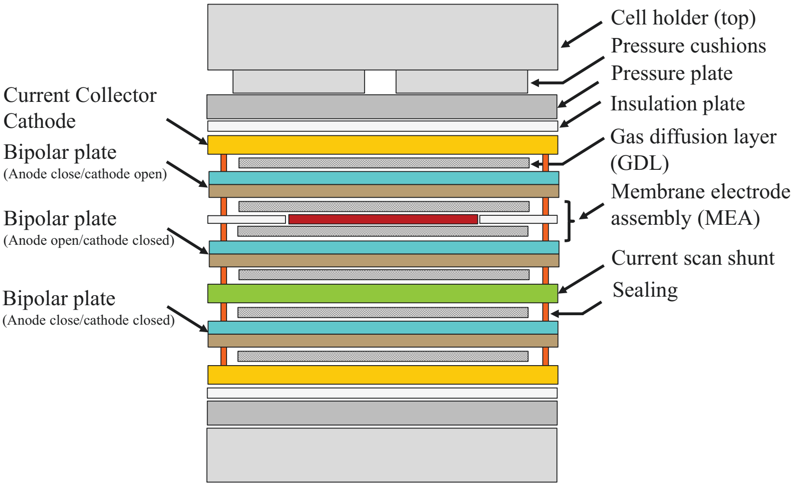

Figure 6.8: Experimental setup for local current (544 segements) and temperature (144 segments) measurement in a single automotive PEM fuel cell according to *Herden et. al* [96].

In order to test the full capability of the PEMFC model, a variation of cell temperature, as well as relative humidities is performed, while recording polarization curves. Herefore, all cases shown in Table 6.2 are used. Before operation, the cell is conditioned, using a defined start-up procedure. The cell temperature is defined as the coolant inlet temperature, as a result of relatively high minimal coolant flow rates. Further details on the experimental setup can be found in [96].

6.5.2 Single Phase Pressure Drop Comparison

Due to the assumption of a mist flow condition inside the flow field channels of the simulation cases, single-phase pressure drop comparisons between experiments and simulations are performed. Herefore, a non-operational, non-humidified experimental setup is operated with pure hydrogen and air on the anode and cathode, respectively. The conditions are given in Table 6.3. The effect of occurring anode turbulence in the redirection sections (see section A.2.2) is included into the analysis by introduction of a high anode stoichiometry $\lambda_A = 4.4$. At the same time, simulations are performed for the corresponding case and compared to the experiments. The results of the comparison are given in Table 6.3.

Table 6.3: Validation of single-phase pressure drop.

Conditions	$T_{A,in} = 90\,^{\circ}C$, $T_{C,in} = T_{Cool,in} = 85\,^{\circ}C$, $RH = 0\,\%$ $j = 2.5\ A/cm^2$, $\lambda_A = 4.4$, $\lambda_C = 2.0$			
	Anode		Cathode	
	Simulation	Experiment	Simulation	Experiment
p_{in} in bar	2.678	2.600	1.940	1.980
p_{out} in bar	2.300	2.300	1.800	1.800
Δp in bar	0.378	0.300	0.140	0.180
Error	26.0%		22.2%	

Pressure drop deviations of 26.0 % and 22.2 % are found for anode and cathode respectively. Separate investigations of the anode flow field in section A.2.2 show, that the source of the anode pressure deviation mainly lies in the lack of adequate resolution of occurring turbulence within the side collector regions. Restrictions regarding computational memory inhibit the increase in numeric mesh count. On the other hand, an implementation of an LES simulation, which showed higher accuracy, requires transient operation, directly resulting in a strong increase in computational time. The numeric cell count is chosen as an optimum between efficiency and accuracy. Due to investigation of a high stoichiometry anode case, regular operating cases are expected to show lower errors.

The values of the cathode are in better agreement, whereas transitional flow behavior is observed in the distributor inflow region.

As priory stated, the description of a laminar flow with RANS models includes additional errors via implementation of turbulent viscosity terms (see section 8.2.2). Anode and cathode channels are affected, contributing to the deviation between experimental and simulative results. Additionally, experimental pressure drop measurement inaccuracies have to be taken into account.

In conclusion, the simulative pressure drop results of anode and cathode are in acceptable agreement to the experimental values.

6.5.3 Comparison of Investigation Case

Experimental and detailed cases shall be compared at three experimental current densities of $j_{\mathrm{exp}} = 0.2$, 0.5 and $1.0\,\mathrm{A/cm^2}$ at conditions of ID3 (see Table 6.2). The comparison mainly focuses on the mid current density case, while the low and high current density results are attached to the appendix in section A.2.3.

The results of the detailed simulation are processed in a developed MATLAB code, interpolating the data onto a mesh with a size corresponding to the measurement segments of current and temperature. The dependency on mesh size elements is removed via area weighting of the values.

The simulated current density data at given potentials is compared to the experimental polarization curve in Figure 6.9.

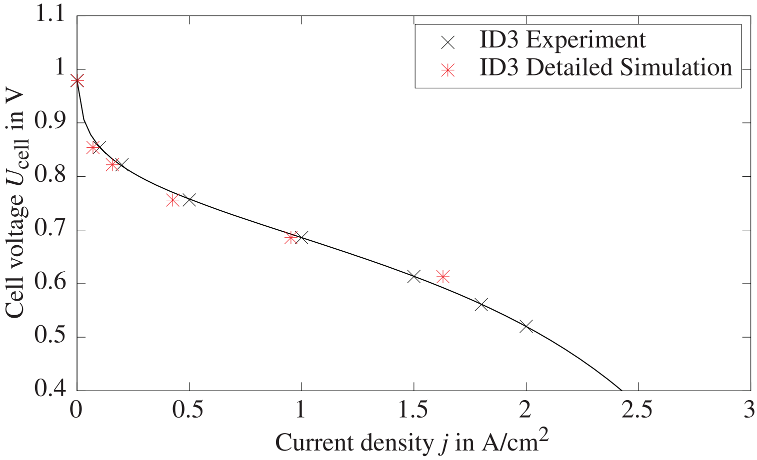

Figure 6.9: Experimental polarization curve with simulative data points at ID3.

Hereby, six simulative cases are shown for voltages from OCV at 0.979 V to 0.614 V. The experimental curve is fitted, using the approach described in section 3.1.1.

Simulative and experimental values are in good agreement with increasing deviations when going towards higher current densities. The reason lies in the lack of an appropriate description of mass transport resistances. An implementation of a more advanced reaction model e.g. agglomerate model [97] might lead to an improved description. Additionally, phase-change has to be included to capture the presence of liquid water appropriately, especially on the anode side.

Current density distributions are given in Figure 6.10 for the experimental results at $j_{\mathrm{exp}} = 1\,\mathrm{A/cm^2}$, as well as the corresponding simulation results.

The experimental measurement hardware shows a connection artifact, visible as two vertical crosses with lower current densities. These can be seen in all current density measurements and shall be disregarded in the comparison.

Both pictures show a decrease of current density along the flow path of the cathode.

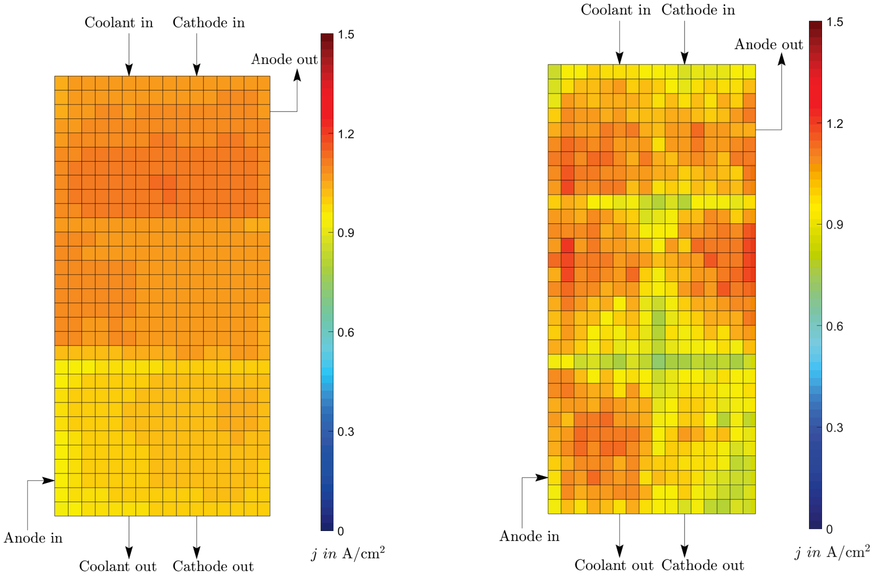

(a) Detailed cell results with $j_{\mathrm{avg}} = 0.97\,\mathrm{A/cm^2}$.

(b) Experimental results with $j_{\mathrm{avg}} = 1.0\,\mathrm{A/cm^2}$.

Figure 6.10: Current density distribution of detailed cell simulation (left) and experimental cell (right) results at 0.686V A/cm^2.

The temperature distributions are compared in Figure 6.11.

Hereby, strong deviations in temperature profiles can be observed. A rather uniform increase of 3 K occurs within the detailed cell simulation with maximum temperatures of 88 °C in the vicinity of the anode inlet. Contrary, the experimental results show a strong temperature maldistribution in cathode and anode flow direction with comparable maximum temperatures, being present over the major part of the cell.

The reason of higher temperatures inside the side channel regions are found to be due to a lower coolant flow, as a result of the by-pass, and a hydrogen inlet temperature of 90 °C. The overheating on the right half of the cell gives indication of a lower coolant flow in these parts of the cell. The reasons can either be found in a non-uniform inflow into the cell or a local over-compression of the bipolar plate, thus posing a higher resistance for the flow. A separate investigation of the inflow conditions is shown not to be the cause (see section A.2.3). It can therefore be concluded, that a local over-compression of the bipolar plate leads to the shown temperature distribution. It cannot be distinguished, whether the effect occurs inside the distributor region or the active area.

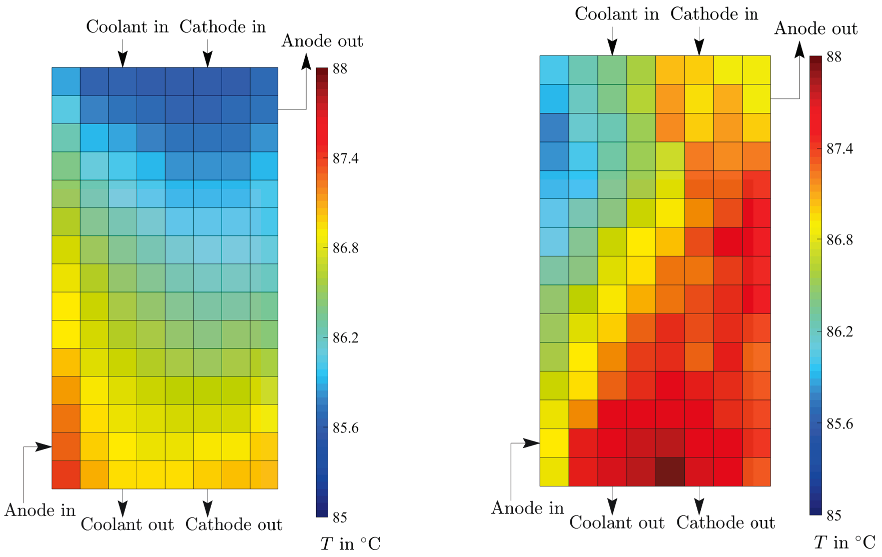

(a) Detailed cell results with $j_{\mathrm{avg}} = 0.97\,\mathrm{A/cm^2}$. **(b)** Experimental results with $j_{\mathrm{avg}} = 1.0\,\mathrm{A/cm^2}$.

Figure 6.11: Temperature distribution of detailed cell simulation (left) and experimental cell (right) results at 0.686V A/cm^2.

In the following, relative humidity variations of the inlet gas flows are investigated.

6.5.4 Relative Humidity Variation

In order to test the capability of the PEMFC model, variations of the inlet relative humidity (*RH*) value of cathode and anode gas are carried out between 25 and 100 %, while keeping the cell temperature at a constant value of 85 °C. Operating conditions of ID3, ID5, ID6 and ID7 are used, given in Table 6.2. The potential boundary condition of the simulative cases is set to match the corresponding experimental configuration. Thus, variations of potential and current density are coexisting between cases of different *RH* values. To allow an in-between comparison of experiments and simulations, as well as in-between cases, operating points with equal current are determined. Assuming equal slopes of experimental and simulative curves inside the ohmic region, the experimental slope between 0.8 and 1.2 A/cm^2 is determined, using the pole curves in section A.2.3, Figure 6.12. Thus, the corresponding voltages to 1 A/cm^2 are determined for all simulative cases. Comparisons of experimental and simulative results are shown in Figure 6.12.

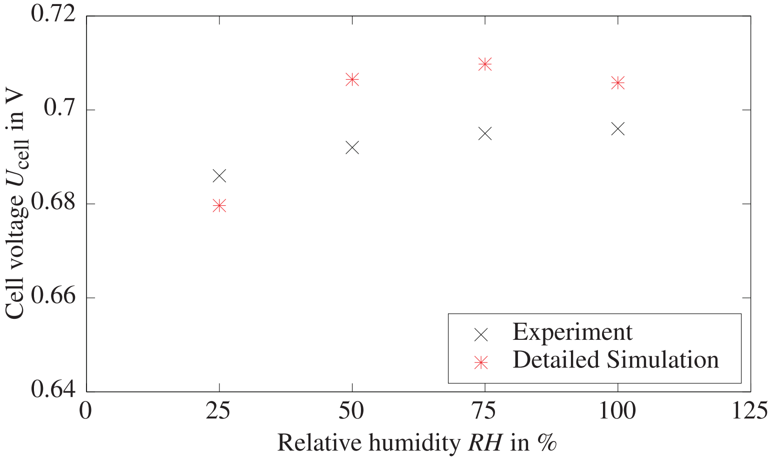

Figure 6.12: Comparison of relative humidity variation between experimental and simulative cases of ID3, ID5, ID6 and ID7 at $j_{exp} = 1.0$ A/cm^2.

An initial increase in voltage until $RH = 75$ % is observed for both approaches, whereas the experimental values show a rather flat progression. An introducing of fully saturated gases shows a voltage drop for the simulative while giving approximately constant values for the experimental case. The initial rise in voltage for both cases can be explained by an enhancement in proton conductivity, leading to lower ohmic losses, as priory shown in Figure 6.7. A flattening of the experimental curve can be explained through the coexistence of multiple effects. On the one hand, excess water is directed to the catalyst layers, leading to a blockage of reaction sites and therefore lowering the reaction rate. At the same time, an operation with higher *RH* values, while maintaining a constant total pressure result in lower oxygen partial pressures, directly decreasing the performance. However, an enhanced humidification of the membrane is achieved, compensating for the prior resistances. All effects, except the mass transport losses as a result of liquid water pore blockage, are also present within the simulations. Higher amounts of liquid water, reducing the reaction rate, are exclusively possible for cases with water content values of $\lambda < 16.8$. Nevertheless, a higher *RH*-value decreases the partial pressure of oxygen which directly results in a voltage drop, being a dominant contribution when operating with fully saturated conditions. It shall be noted, that the shape of the curves is strongly dependent on the chosen cell design, including flow field geometry and all functional layers of the MEA, as well as the operating conditions. An analogous trend of the simulative curve, which shows a stronger sensitivity to humidity, is expected for the experimental cell as well when operating conditions are changed e.g. increase in temperature or λ, as well as extreme current densities. While the temperature and λ increase directly leads to higher amounts of liquid water, as a result of favored condensation and inferior water removal respectively, an operation at extreme current density is not identifiable a priori explicitly. It is not clear whether a low current densities leads to a reduction in mass transport resistances, due to lower amounts of water, or an increase, due to low gas flows. The same applies for for high current densities.

It can be concluded, that a qualitatively physically plausible dependency is observed for the simulative case, while the the absolute values of the performance dependencies lack the inclusion of additional models.

The model shall be investigated regarding the physical correctness of temperature variation effects in the following.

6.5.5 Cell Temperature Variation

An additional variation of cell temperatures is performed to see how well the effects are captured by the PEMFC model. Therefore, the cell temperature is varied in an operation window between 65 and 85 °C at constant cell inlet *RH* values of 25 %, including ID2, ID4 and ID5 from Table 6.2. The potential values, corresponding to 1 A/cm^2 are determined analogously to the *RH*-variation cases. Experimental and simulative results are shown in comparison in Figure 6.13.

A strong deviation between the two approaches is found for a variation of the cell temperature. While the experiments show a weak dependence on the temperature, a strong voltage drop with increasing temperature is observed for the simulations.

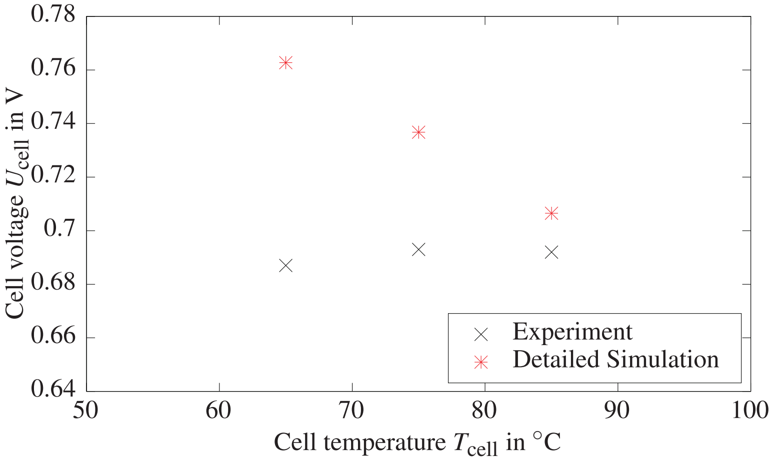

Figure 6.13: Comparison of cell temperature variation between experimental and simulative cases of ID2, ID4 and ID5 at $j_{\mathrm{exp}} = 1.0\ \mathrm{A/cm^2}$.

An increase in temperature, kinetically favors reactions according to the Buttler-Volmer expression (see equation (4.49)), as well as proton conduction according to Springer (see equation (4.42)). Decreasing the temperature too far on the other hand, results in and excess of liquid water due to condensation, leading to mass transport resistances. The coexistence of these effects, describes the voltage difference between the 65 and the 75 °C state. A temperature increase to 85 °C, gives rise to further vaporization of water, resulting in a membrane dry-out, visible as a slight voltage drop.

All mentioned effects, besides phase-change, are included within the simulative model. The strong voltage drop as a function of increasing cell temperature shows an over-prediction of dry-out effects against kinetic and conduction enhancement. The main effect that reduces the voltage when increasing the cell operating temperature can be found in the steeper slope of the vapor pressure curve, leading to earlier membrane dry-out. The neglection of phase change in the model probably additionally leads to an underestimation of the voltage loss at low temperature, especially observed on the anode side (see section A.2.2). Despite a physically present MPL region within the simulation, equivalent GDL properties are specified. The water retaining effect of the MPL is therefore not included in the simulation, directly leading to a dry-out condition and increasing the voltage drop for higher temperatures.

It can be concluded, that the effects during temperature dependence are included within the model. Still, the extent of the dry-out is overestimated in comparison to kinetic and conductivity enhancing effects.

The validated detailed cell simulation results are used as reference cases for the following stack development procedure.

7 PEMFC Stack Modeling

The present chapter describes the stack modeling approach. First, an overview of the stack modeling procedure is given, followed by an in depth description of fluid flow, thermal and electrical simplification on a single cell basis. The PEMFC model is validated against detailed single cell results. In the last part, the modeling algorithm of the stack is described.

Parts of the results within this chapter can be found in the Master's Thesis of *F. Du* [71], *K. Ling* [72], *N. K. Cheruku* [94] and *A. Jurzyk* [73], which were created while working under my supervision.

7.1 Modeling Approach Overview

The creation of a three-dimensional stack model with explicit single cell modeling requires a significant reduction in cell count in order to be computationally feasible.

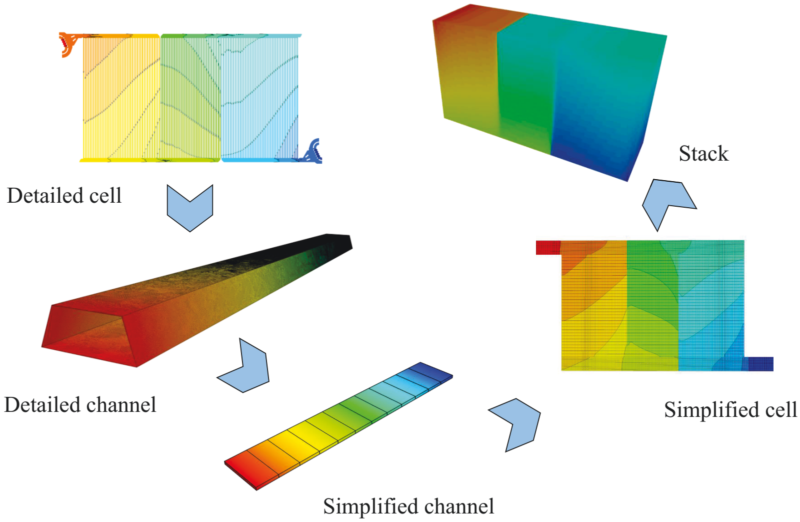

Figure 7.1: Stack model creation procedure.

In the present work, this is mainly realized by the simplification of the detailed flow field structure via a porous volume approach, applying a multi-phase Darcy-like model. The simplification procedure is schematically shown in Figure 7.1.

The *n*-cell stack is built-up of an automated stacking algorithm, combining *n* simplified single cells. The simplification process of the cells is based on detailed single cell PEMFC simulation results. These provide boundary conditions for VOF simulations in detailed flow field channels as previously mentioned in chapter 5. The detailed channel simulations additionally provide input data for the channel simplification process, regarding fluid flow properties. Using these, with additional reference data regarding heat and current transport from the detailed cell simulations, a simplified cell model is built up. The subsequent combination of multiple simplified cells give a multi-physics stack model.

The priory mentioned simplification of the flow field is elaborated in the following section.

7.2 Flow Field Simplification

The simulation of a detailed PEMFC results, as priory shown, in an extremely high computational effort, making even short-stack simulations economically unfeasible. A reduction in computational effort has to be achieved in order to facilitate computational stack investigations. In general, two techniques can be used, being a reduction in numerical cells on one side, as well as a simplified modeling approach on the other. Both are combined in the present work with the major simplification being done within the region of the flow fields of anode, cathode and coolant. A proper representation of thermal, fluid flow and electrical phenomena is crucial.

The present section introduces methods for the simplification of the flow fields, using a Darcy-like porous medium approach. At first, a modeling procedure for pressure and velocity fields in straight and bent channel structures is developed. Subsequently, a heat exchanger model for the thermal representation is introduced, followed by an electrical simplification model.

7.2.1 Single-Phase Simplification

Due to the complexity of their structure, the highest number of numerical cells within a PEMFC mesh can be found within the flow field (see subsection 6.2). The simplification process is therefore focused on a reduction of cells in that particular region. No geometrical simplifications are performed on the regions of the MEA. A fraction of the detailed (left) and simplified (right) cells with cross-sectional plane-cuts are shown in Figure 7.2.

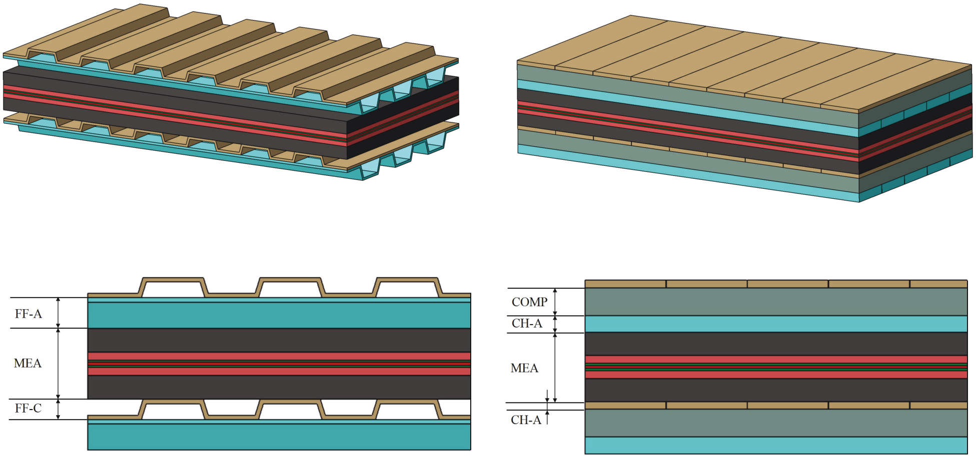

(a) Detailed PEMFC Model

(b) Simplified PEMFC Model

Figure 7.2: Schematic sections of detailed (a) and simplified (b) cell geometry.

The flow field structure (FF), consisting of gas and coolant channels, as well as the bipolar plate separating them, is simplified as a homogeneous region of hexahedral numerical cells. Depending on the flow direction, every column represents one anode (CH-A) and every row two cathode channels (CH-C). This implies, that channels of anode and cathode within the simplified model are resolved by one and "a half" numerical cell in cross-sectional direction, respectively. As a fully-conformal mesh is applied, the along-the-channel mesh resolution is defined by the respective other, leading to a resolution of 128×34 hexahedral cells for the active area of the flow field.

In order to ensure an equivalent representation of the velocity and pressure fields, a transfer criterion of constant cross-sectional area is applied. Due to the coolant channels being modeled through a heat-exchanger approach (see section 7.2.2) and therefore not being geometrically represented within the same layer as the gas channels, a reduction in channel height is necessary to fulfill the preset criterion. Furthermore, the total length of the stack manifolds depends on the total thickness of one cell (referred to as cell pitch), making an additional criterion of equivalent cell pitch necessary. Hence, a channel height reduction is accounted for by introduction of an additional compensation region. Table A.6 gives a summary of the through-plane layer thickness values.

The exchange of mass between channels is prohibited by implementation of inner surfaces that act as walls between neighboring channels, while allowing heat transfer. In addition, their presence results in a defined flow direction, removing the necessity of anisotropic permeability matrices inside the gas channels.

The number of numerical cells within a channel of the simplified flow field does not allow a correct reflection of the flow characteristics by solving the Navier-Stokes equations. Instead a

Darcy-like porous volume approach is applied, which is able to consider geometric features effectively. The following assumptions have to be made:

- Laminar flow
- Stationary
- Incompressible
- Newtonian fluid

With the given assumptions, the single phase pressure drop inside gas channels can be modeled as a function of velocity u_g and viscous and inertial resistance γ_V (in kg/(m^{3}s)) and γ_I (in kg/m^4) as shown in equation (7.1). Due to the presence of a single numeric cell in cross-sectional area, the equations are derived as a one dimensional approach in x-direction.

$$-\frac{\mathrm{d}p}{\mathrm{d}x} = \gamma_\mathrm{V}\, u_\mathrm{g} + \gamma_\mathrm{I}\, u_\mathrm{g}^2 = \frac{\mu_\mathrm{g}}{K_\mathrm{V}}\, u_\mathrm{g} + \frac{\rho_\mathrm{g}}{K_\mathrm{I}}\, u_\mathrm{g}^2 \tag{7.1}$$

The inertial resistance term can be omitted for laminar flows. As for turbulent regions, a non-linear increase of the pressure drop with rising gas velocity is expected, whereas an introduction of a non-zero inertial resistance term is performed.
The cathode flow field is subdivided into three sections shown in Figure 7.3. Air entering through the manifold is directed into 34 continuous, horizontally positioned channels. The number of numeric cells i.e. cathode channels is chosen according to the amount of distributor and collector channels. The subdivision at the transition between distributor, as well as collector, to the active area is not geometrically resolved.
The alternating conical contractions and expansions of cathode channel cross-sections are causing local pressure differences between neighboring channels, which lead to convective exchange of mass through the GDL. The extent of this phenomenon is investigated in detail in section A.1.1. The simplified cell model is set up with constant cross section channels, therefore omitting conical contractions and expansions of gas and coolant channels.
The average cross section area of one real cathode gas channels within the active area is chosen as the transfer criterion for the creation of simplified channels. Velocities within the active area therefore match the average value within the gas channels of the detailed simulations, whereas distributor and collector values are overestimated. As collector and distributor channels merely differ in length, the channel-to-channel distribution is not being affected by the stated deviation. Through simulations of the detailed cell, a single phase pressure drop at specific conditions is obtained. Using equation (7.1), the resistance values can be iteratively adjusted to fit the detailed pressure drop at predefined conditions for regions 1 to 3. Due to geometrical equivalency of collector and distributor, a single value is defined for both regions. The values are summarized in table 7.1.
The anode flow field is subdivided into nine sections shown in Figure 7.3.

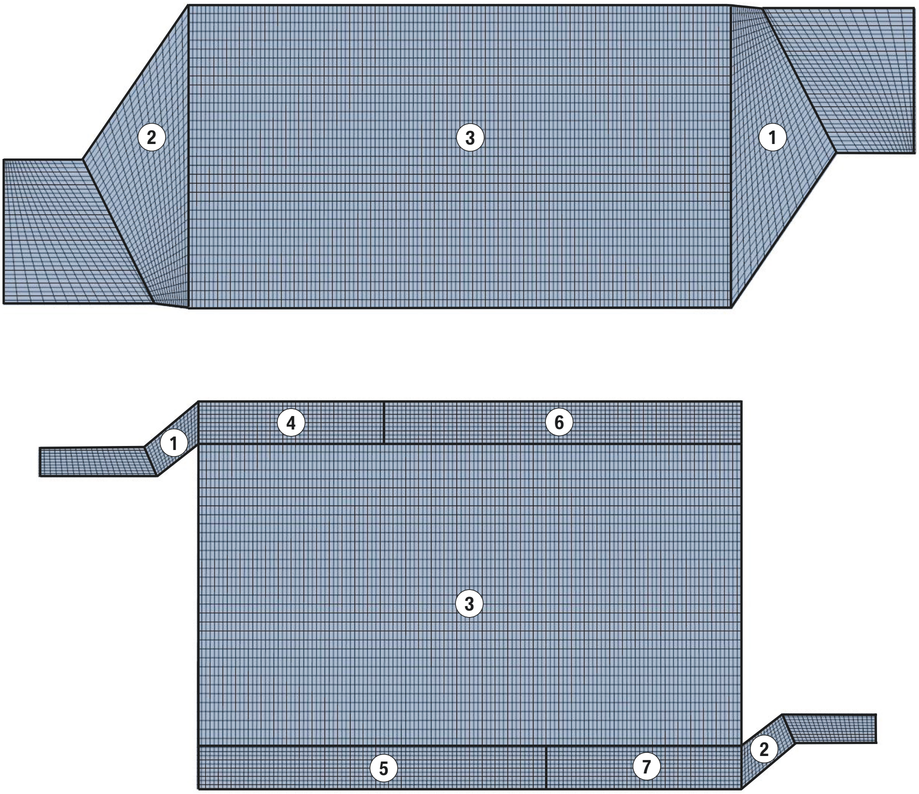

Figure 7.3: Simplified model of cathode (top) and anode (bottom) side gas channel geometries.

Due to geometric equivalence of regions 1/2, 4/7 and 5/6, equal modeling values are used within these regions. Analogous to distributor and collector regions of the cathode flow field, the direction change within regions 1/2 and 4 to 7 leads to a non-linear pressure-velocity relationship that cannot be described via a viscous resistance term exclusively. Therefore, inertial resistance terms are included. Due to the laminar character of the flow inside the active area, an exclusively linear velocity dependency modeling approach via viscous resistances is chosen.

The viscous and inertial permeability values are calculated analogously to the cathode side, using the pressure drop from the detailed flow field simulation results (see chapter 6) and added in Table 7.1.

Table 7.1: Viscous and inertial resistance values for simplified anode and cathode flow fields

		Anode		Cathode	
Region	Description	K_V in m^2	K_I^{-1} in 1/m	K_V in m^2	K_I^{-1} in 1/m
1	Inlet distributor	$1.00 \cdot 10^{-7}$	15	$2.00 \cdot 10^{-8}$	141
2	Outlet collector	$1.00 \cdot 10^{-7}$	15	$2.00 \cdot 10^{-8}$	141
3	Active area	$3.62 \cdot 10^{-9}$	0	$8.64 \cdot 10^{-9}$	0
4	Side collector small	$1.11 \cdot 10^{-8}$	130		
5	Side collector large	$4.00 \cdot 10^{-9}$	250		
6	Side collector large	$4.00 \cdot 10^{-9}$	250		
7	Side collector small	$1.11 \cdot 10^{-8}$	130		

To account for the presence of liquid water inside the flow field channels, equation (7.1) is extended by a second phase dependence, as well as an additional slip velocity dependent term, giving the expression as shown in equation (7.2).

$$-\frac{\mathrm{d}p}{\mathrm{d}x} = -\left(\gamma_\mathrm{v,g} + \gamma_\mathrm{v,lq}\right) u_\mathrm{m} - \gamma_\mathrm{i}\, u_\mathrm{m} - \left(\gamma_\mathrm{v,g}\, \alpha_\mathrm{lq}\, \rho_\mathrm{lq} - \gamma_\mathrm{v,lq}\, \alpha_\mathrm{g}\, \rho_\mathrm{g}\right) u_{12} \tag{7.2}$$

The slip velocity u_{12} definition applied within the gas channel regions is shown in equation (7.3). Neglecting the influence of capillary forces, an analogous approach to the transport in real porous media is achieved (compare to equation (4.37)).

$$u_{12} = -\left(\frac{\alpha_\mathrm{g}}{\gamma_\mathrm{v,g}} - \frac{\alpha_\mathrm{lq}}{\gamma_\mathrm{v,lq}}\right) \gamma_\mathrm{v,m}\, u_\mathrm{m} \tag{7.3}$$

Numerical instabilities in regions 4 to 7 are found to be present when exclusively implementing a porous medium approach. Hence, viscous terms inside porous regions with inertial resistances are implemented additionally, as they are found to be acting as a numerical stabilization on the solution procedure. The local increase in pressure drop has to be counteracted by introduction of a momentum source term equal in value.

In order to approximate the viscous forces inside the momentum equation for a laminar flow, Hagen-Poiseuille's law is used (see equation (7.4)).

$$-\frac{\mathrm{d}p}{\mathrm{d}x} = \frac{32\, \mu_\mathrm{g}\, u_\mathrm{g}}{d_\mathrm{h}^2} = \frac{32\, \mu_\mathrm{g}\, \dot{m}_\mathrm{g}}{A_\mathrm{X}\, d_\mathrm{h}^2} \tag{7.4}$$

The mass flow $\dot{m}$ at each position x is assumed to linearly increase over length of the respective section L and is therefore expressed as a function of the total mass flow $\dot{m}_\mathrm{g,tot}$ in equation (7.5).

This assumption is equivalent to an equal distribution of mass over the section and only applies to the derivation of the correction term.

$$\dot{m}_\mathrm{g} = \dot{m}_\mathrm{g,tot}\,\frac{x}{L} \tag{7.5}$$

Furthermore, the simplification of the cross-sectional area of gas channels with one numerical cell generates an additional deviation from the analytic pressure drop, which is taken into account by a correction factor.

For the estimation of the correction factor, a fully-developed laminar gap-flow (height significantly smaller than other dimensions) is considered. Neglecting boundary effects (2-D), the Navier-Stokes equation simplifies to the expression shown in equation (7.6), with u_g being the velocity in x-direction.

$$-\mu_\mathrm{g}\,\frac{\partial^2 u_\mathrm{g}}{\partial y^2} = \frac{\partial p}{\partial x} \tag{7.6}$$

Considering the boundary conditions at $y = 0$ and $y = H$ (channel height), equation (7.6) can be analytically solved, leading to:

$$u_\mathrm{g}(y) = -\frac{1}{2\mu_\mathrm{g}}\,\frac{\partial p}{\partial x}\,y\,(y-H) \tag{7.7}$$

An evaluation for the maximum velocity $u_\mathrm{g,max}$ at $y = H/2$ (parabolic flow profile) gives:

$$u_\mathrm{g,max} = u_\mathrm{g}\left(y = \frac{H}{2}\right) = \frac{1}{2\mu_\mathrm{g}}\,\frac{\partial p}{\partial x}\,\frac{H^2}{4} \tag{7.8}$$

The wall shear rate leads to the following value:

$$\left.\frac{\partial u_\mathrm{g}}{\partial y}\right|_{y=0} = \frac{H}{2\mu_\mathrm{g}}\,\frac{\partial p}{\partial x} \tag{7.9}$$

Determination of the wall shear rate value for the simplified calculation with one numerical cell in cross-sectional area gives:

$$\frac{\Delta u_\mathrm{g}}{\Delta y} = \frac{u_\mathrm{g,max}}{H/2} = \frac{H}{4\mu_\mathrm{g}}\,\frac{\partial p}{\partial x} \tag{7.10}$$

Comparison of the both shear rate values, indicate a deviation of 50 %. Using equation (7.5), as well as the correction factor, equation (7.4) can be reformulated as a momentum correction term S_mom as follows:

$$S_\mathrm{mom} = \frac{16\,\mu_\mathrm{g}\,\dot{m}_\mathrm{g,tot}}{A_\mathrm{X}\,d_\mathrm{h}^2\,\rho_\mathrm{g}}\,\frac{x}{L} \quad \text{in Pa/m} \tag{7.11}$$

The momentum correction S_{mom} is included as a source term in region 4 to 7 in the anode flow field.
In the subsequent section, the thermal simplification procedure shall be presented.

7.2.2 Heat Exchanger Model

During the simplification procedure of anode and cathode flow fields, a disconnection to the neighboring coolant channels occurs. In order to account for heat exchange between coolant and gas, as well as coolant and GDLs, separate geometrically disconnected coolant regions are created explicitly. Cathode and anode coolant regions are modeled as identical representations of the corresponding simplified gas flow field structures, restricted to the active area. Both coolant subregions are explicitly connected, whereas the coolant is introduced through the cathode coolant inlet. The heat transfer in collector and distributor regions is assumed to be ideal, therefore fully omitting the regions. This is in accordance to the assumptions taken for the detailed cell.
The flow inside the channels is modeled via a single-phase Darcy approach. Due to incompressibility of the coolant fluid, all fluid parameters are assumed to be constant over the application range. The viscous resistance is chosen to be $K_{\mathrm{v}} = 8.3 \cdot 10^{-8}\,\mathrm{m}^2$. Baffle interfaces are chosen for channel-to-channel separations, restricting the exchange of mass while allowing heat transfer.
The thermal interactions between the regions within the detailed and simplified cell are shown in Figure 7.4.
The convective and diffusive transport of hydrogen and air (process (1) and (6)) is explicitly calculated within the simplified model. Through the implementation of a compensation region between anode and cathode gas channels within the simplified model, the convective and conductive exchange between the gases through the bipolar plate (process (3)) is accounted for explicitly. Due to negligible influence of the conductive part, a thermal equilibrium is assumed throughout the compensation region, by implementation of an "infinite" conduction coefficient.
All remaining processes are implemented within the numeric cells inside all regions of the active area as convective and conductive local volumetric source terms $\dot{Q}_{\mathrm{conv}}$ and $\dot{Q}_{\mathrm{cond}}$ (see equation (7.12))

$$S_{\mathrm{th}} = \dot{Q}_{\mathrm{conv}} + \dot{Q}_{\mathrm{cond}} \tag{7.12}$$

The transition of heat between coolant and gas (process (1) and (6)) is a subsequent chain of thermal conduction of the fluids to the bipolar plate, followed by a through-plane conduction process. Due to the small thickness of the plate in combination with the high thermal conductivity, the conduction process is omitted. The convective transport heat source and sink terms are therefore calculated via Newton's law of cooling, shown in equation (7.13).

$$\dot{Q}_{\mathrm{conv}} = \alpha_{\mathrm{th}} A_{\mathrm{seg}} \left(T_{\mathrm{gas}} - T_{\mathrm{cool}}\right) \tag{7.13}$$

The variable α_{th} denotes the heat transfer coefficient, A_{seg} the respective heat exchange area, T_{gas} the local gas temperature and T_{cool} the local coolant temperature. The exchange between coolant and GDL (process (4) and (7)) is dominanted by conduction. Exchange source terms are therefore calculated using Fourier's law, shown in equation (7.14).

$$\dot{Q}_{\mathrm{cond}} = \lambda_{\mathrm{th}} A_{\mathrm{seg}} \frac{\left(T_{\mathrm{GDL}} - T_{\mathrm{cool}}\right)}{\Delta x} \tag{7.14}$$

The variable λ_{th} denotes the thermal conductivity, T_{GDL} the local GDL temperature and Δx the respective thickness of the conducting material. In order to properly account for the surfaces, participating in the heat transfer, the detailed bipolar plate is segmented into sections according to the mesh size resolution within the active area of the simplified model. The area within each cell A_{seg} of the subdivision is therefore evaluated for each of the aforementioned phenomena separately and implemented into the simplified model.

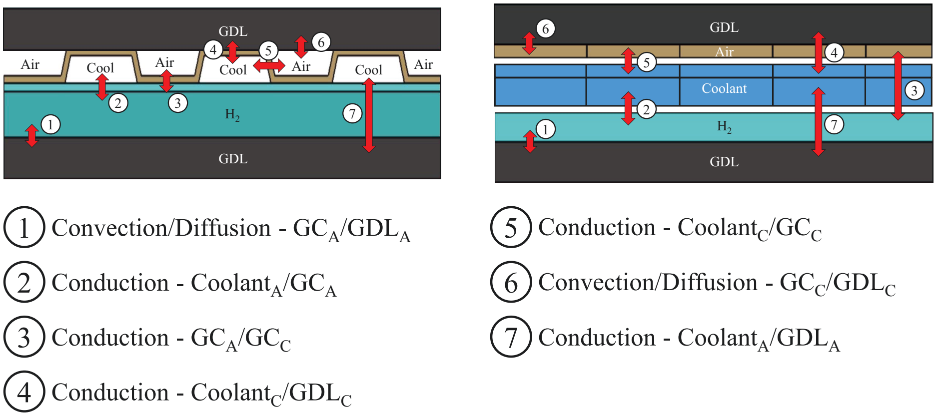

Figure 7.4: Heat exchange in detailed (left) and simplified (right) cell with indication of transfer phenomena.

The local heat transfer coefficient α_{th} is dependent on fluid flow attributes and therefore modeled as a function of local properties, as shown in equation (7.15).

$$\alpha_{\mathrm{th}} = \frac{Nu \cdot \lambda_{\mathrm{th,fluid}}}{d_{\mathrm{h}}} \tag{7.15}$$

The local Nusselt number can be evaluated, using an expression, derived for heat exchanger pipes [98]. With the assumption of constant wall temperature and laminar flow conditions, equation (7.16).

$$Nu = \frac{3.657}{\tanh\left(2.264 \cdot X^{+1/3} + 1.7 \cdot X^{+2/3}\right)} + \frac{0.0499}{X^{+}} \tanh X^{+} \tag{7.16}$$

The dimensionless coordinate X^{+} is defined in equation (7.17).

$$X^{+} = \frac{L}{d_{\mathrm{h}} \cdot Pe} \tag{7.17}$$

The Peclet number Pe is defined in equation (7.18).

$$Pe = Re \cdot Pr \tag{7.18}$$

During every iteration, an update of the source terms is performed and applied on the respective regions.
The electrical simplification is explained in the following.

7.2.3 Electrical Simplification

The simplification of the flow field leads to an electrical disconnection of the anode and cathode terminal. In order to ensure a flow of electrons, the porous regions are assumed to be electrically conducting. This is realized through the introduction of an anisotropic electrical conductivity in the porous channel region, while setting the porosity to $\varepsilon = 0.99$ to keep the influences on the flow negligible. Therefore, the through-plane value is set to "infinity" while keeping the in-plane values low to avoid diffusive effects on the current profiles. Analogously, the compensation region is specified to be perfectly electric conducting in through plane direction, while blocking diffusive in-plane conductivity. Contact resistances are uniformly applied over the active area and specified on the compensation-GC-interface. The values are scaled accordingly to resemble the detailed simulation values.
In the following, the simulative validation of the simplified model, using the detailed single cell simulation results, is performed.

7.3 Simulative Validation of Simplified PEMFC Model

The present section provides a validity investigation of the simplified results by comparison to the experimentally validated detailed cell results. Operating points at low, mid and high current density are chosen to compare the two.

7.3.1 Single-Phase Flow Validation

The simplified model validation is performed at ID3 conditions of the detailed single cell simulations, shown in Table 6.2. In order to prevent the occurrence of liquid water, a voltage of 0.979 V is applied. The detailed simulation results are used as a reference for all further validations.

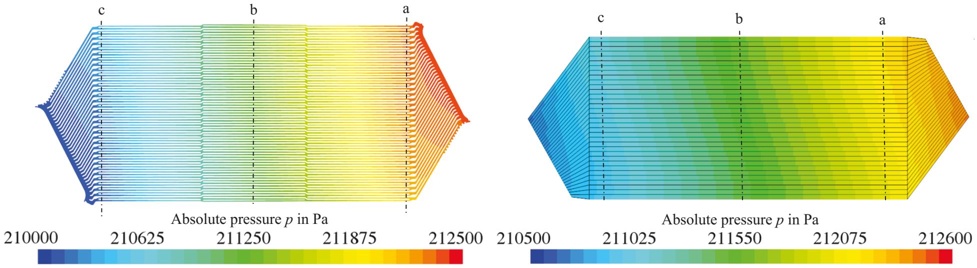

(a) Detailed cathode flow field.

(c) Detailed anode flow field.

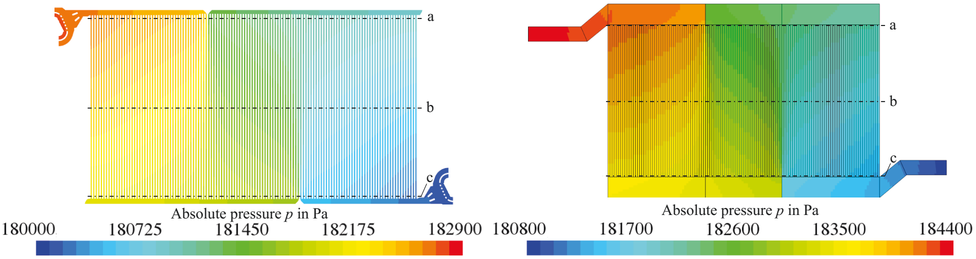

(b) Simplified cathode flow field.

(d) Simplified anode flow field.

Figure 7.5: Comparison of detailed (left) and simplified (right) anode (bottom) and cathode (top) pressure distributions in flow flow field channels with indication of cuts for mass flow distribution evaluation.

Figure 7.5 shows the pressure distribution of detailed simulations (left) to simplified simulations (right) of cathode (top) and anode (bottom) with additional cut-plane locations a to c, which are used for evaluations of mass flow distributions. The specified plot ranges are chosen individually for detailed and simplified cells, due to the presence of numeric inlets of different lengths.

With a total pressure drop of 0.025 bar for the detailed cathode flow field and 0.021 bar for the simplified geometry, a deviation of around 16.0 % is found. The error of the anode simplification is estimated to around 19.4 % with a detailed pressure drop of 0.029 bar and a value for the simplified model of 0.036 bar. As for the pressure distribution profiles, an excellent representation of the profiles on both flow fields is achieved. Minor deviations on the cathode side pressure distribution can be observed, resulting from the rather rudimentary simplification process, using only two viscous resistance parameters. A summary of the pressure values for simplified cell (SC) and detailed cell (DC) simulations is given in Table 7.2.

Table 7.2: Validation of single-phase pressure drop of simplified cell.

Conditions	$T_{\text{A,in}} = 90\,°\text{C}$, $T_{\text{C,in}} = T_{\text{Cool,in}} = 85\,°\text{C}$, $RH_{\text{A,in}} = RH_{\text{C,in}} = 25\,\%$ $U_{\text{cell}} = 0.979\,\text{V}$, $\lambda_{\text{A}}\,(U_{\text{cell}} = 0.757\,V) = 2.0$, $\lambda_{\text{C}}\,(U_{\text{cell}} = 0.757\,V) = 2.2$			
	Anode		Cathode	
	SC simulation	DC simulation	SC simulation	DC simulation
p_{in} in bar	1.844	1.829	2.121	2.125
p_{out} in bar	1.808	1.800	2.100	2.100
Δp in bar	0.036	0.029	0.021	0.025
Error	19.4%		16.0%	

In addition to the pressure, the distribution of mass flows over the active area shall be evaluated. Figure 7.6 and 7.7 show the mass flow distribution of cathode and anode as a function of channel index, respectively. Values are evaluated at the center, as well as in- and outlet of the respective active area labeled with a to c in Figure 7.5. In order to be able to compare the cathode side of detailed and simplified cell, 34 channel index values are chosen. For this purpose, neighboring detailed channels are summed up.

The simplified cell shows a very uniform parabolic profile of mass flow distribution over the channels with a maximum between channels 15 and 20. Channels 5 to 30 for the detailed cell show a similar profile with matching values, whereas the side regions experience deviations. Cut-plane c, representing the inlet into the active area, shows the smallest deviations, which are increasing towards the exit. The separate analysis of the conical contraction and expansion regions in section A.1.1 shows an exchange of mass between neighboring channels over the course of one section. An investigation of a low current density case, showed an almost entirely reversible mass-exchange process after every investigation plane, which is expected to occur analogously for the present case at OCV. However, the effect cannot be seen as the values of channel pairs is added to be comparable to the simplified results. The reason for the differences is expected to be found in the disturbance of the pattern due to deviations in connections of the side channels. At the same time, a single permeability values is chosen for the entirety of the active area of the simplified cell, introducing deviations.

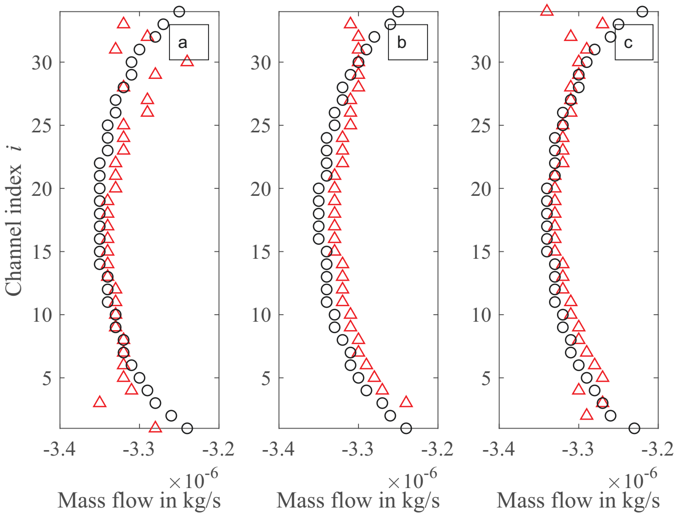

Figure 7.6: Mass flow comparison between detailed (red triangle) and simplified cell (black circle) for cathode flow field, evaluated on plane a (right), b (middle) and c (left).

A good agreement between anode flow distributions in the three meander sections can be observed over all cut sections. The highest deviations can be found in the regions of redirection, which are also the regions of turbulence occurrence (see section A.2.2). The turbulence is approximated via inclusion of a quadratic velocity dependency through an inertial resistance term. Even though good agreement of pressure drop values is found, residual local differences cannot be fully avoided.

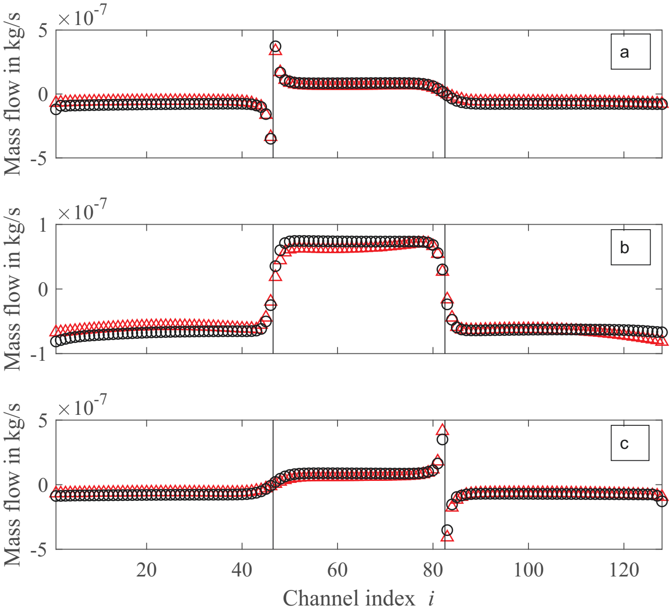

Figure 7.7: Mass flow comparison between detailed (red triangle) and simplified model (black circle) for anode flow field, evaluated on plane cut a (top), b (middle) and c (bottom).

Despite minor local differences between simplified and detailed results, a good overall agreement is found. In the following, the approaches are compared on various operational points.

7.3.2 Comparison of Investigation Case

The validity of the simplified approach is analyzed, using operating conditions of ID3 in the range of $U_{\text{cell}} = 0.979$ to 0.614 V. The results are validated against respective detailed simulation results. Figure 7.8 shows the results of simplified and detailed operating points with additional indication of the experimental pole curve.
An excellent agreement is achieved for low current density cases within the activation region with an increasing deviation for higher current densities. Simplified cell cases are generally found to produce higher current densities at a given potential. The reason is found in the underestimation of mass transport resistances through neglection of the land areas within the simplified approach. As previously shown in Figure 6.7, the finite in-plane diffusion of reactant

gases leads to an under-supply of CL-regions below land areas in comparison to under-the-channel regions. A possible modification of the diffusion coefficient or the in-plane permeability value of the porous regions of the simplified model can be used to counteract this effect.

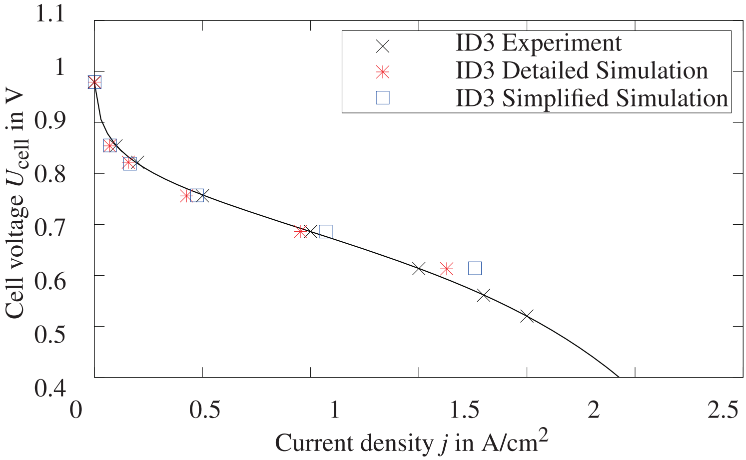

Figure 7.8: Polarization curves for simulation and experimental validation at ID3

Analogously to the comparisons in section 6.5.3, a reduction process through interpolation of detailed cell data is performed in order to compare the simplified and detailed plots. In the present case, the resolution of the simplified cell of 34 x 128 numeric cells is applied. The interpolation error is evaluated after the interpolation process of the detailed cell data, comparing the deviation between the initial average current density and the post interpolation value. The difference is uniformly added to the geometry to maintain a consistent j_{avg}.

The comparison of current density distributions in the active area for a potential of 0.686 V is given in Figure 7.9 for simplified (left) and detailed (right) simulations results.

The characteristic threefold division of the profile is also obtained for the simplified cell. Additionally, the decrease in current density over the course of the cathode flow, as a result of oxygen depletion, is achieved. At the same time, a similar shape of the intersections is observed, indicating a representation of the under-the-land overflow phenomenon. The priory mentioned overestimation of the current densities due to underestimation of mass transport resistances leads to an overall increase of the current density for the simplified case. The effect is particularly seen in the inlet regions of the cathode to the active area. The entirety of these effects leads to average current density values of $j_{\text{avg}} = 1.06$ A/cm^2 for the simplified approach, which are slightly higher then the detailed cell value of 0.97 A/cm^2.

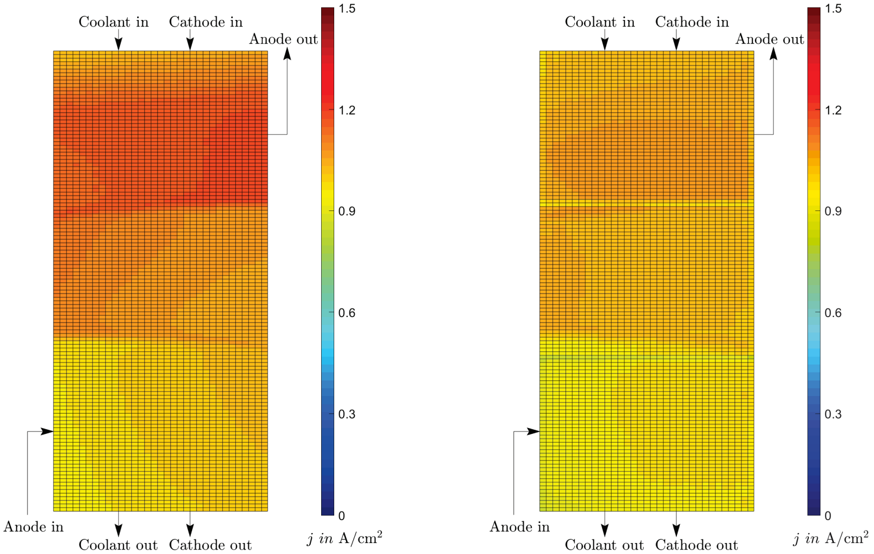

(a) Simplified cell results with $j_{\mathrm{avg}} = 1.06\,\mathrm{A/cm^2}$.

(b) Detailed cell results with $j_{\mathrm{avg}} = 0.97\,\mathrm{A/cm^2}$.

Figure 7.9: Current density distribution of simplified (left) and detailed (right) cell simulation at 0.686V.

In addition, Figure 7.10 gives the temperature profiles of simplified (left) and detailed (right) cell simulations.

The simplified cell exhibits a one-dimensional temperature increase from cathode in- to outlet with negligible horizontal gradients. Herein, a temperature increase of 3 K with a maximum temperature of 88 °C can be observed. An equivalently high maximum temperature inside the detailed cell is mainly found in the vicinity of the bypass regions, particularly at the anode inlet. Due to the assumption of a constant permeability over the active area for the coolant region, in combination with a uniform mass inlet and absence of distributor, collector and coolant by-pass regions an even distribution of coolant is achieved. With negligible temperature gradients along the anode channels, an approximately one-dimensional increase in temperature from cathode in- to outlet is observed. This leads to an overestimation of the temperature within the cathode outlet region. As a result, membrane dry-out is found in this region, compensating the overall increase in current due to mass transport resistance underestimation. The result is a better match of current densities between the approaches in the cathode outlet region, as seen in Figure 7.9. The higher inlet temperature of hydrogen, in comparison to air and coolant, does not appear to have a noticeable effect on the temperature profile for the simplified cell. Due to lower overall temperatures in the outlet region of the detailed cell, the inlet hydrogen flow visibly increases the local coolant temperature.

A fairly reasonable approximation of the coolant flow is achieved through the simplified approach, which would strongly benefit from an implementation of a parabolic inlet flow profile, as well as the inclusion of distributor and collector regions.

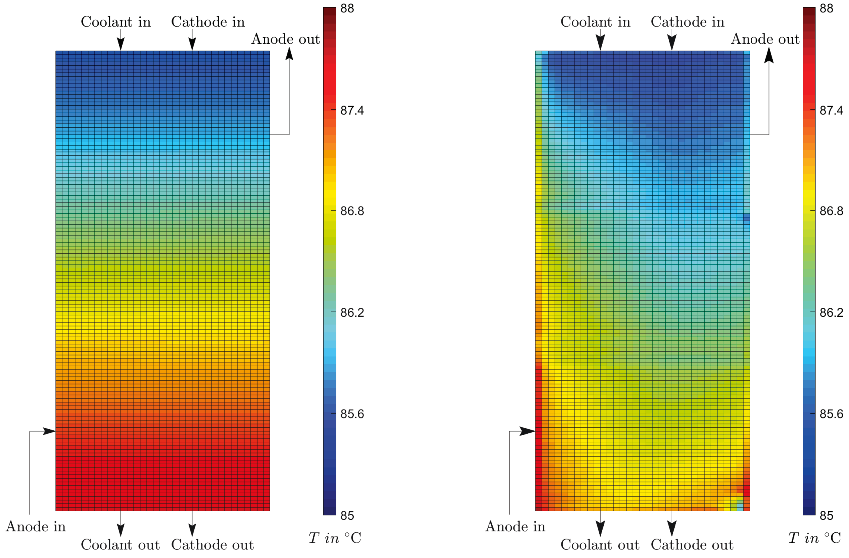

(a) Simplified cell results with $j_{\mathrm{avg}} = 1.06\,\mathrm{A/cm^2}$.　**(b)** Detailed cell results with $j_{\mathrm{avg}} = 0.97\,\mathrm{A/cm^2}$.

Figure 7.10: Temperature distribution of simplified (left) and detailed (right) cell simulation at 0.686V.

The water content on the anode CL-MEM interface is given in Figure 7.11 for simplified (left) and detailed (right) simulation.

Analogously to the current density profile, a threefold split of the active area is observed, with well matching profiles for SC and DC results. Inlet regions of cathode and anode show relatively low water content values between 2.5 and 3. The rest of the upper section as well as the mid section exhibit the highest humidification with values up to 4 for the simplified and 3.8 for the DC results.

As priory described for the detailed geometry, two sources of membrane water humidification are found, being the cathode product water and inlet gas humidity. Therefore, the water production, as well as the gas flow distribution inside the flow field structure have to be properly included to adequately represent the membrane water content distribution of the detailed cell. The relatively low water content values at the inlet regions of cathode and anode can be traced back to a humidification, mainly arising from the inlet humidity. A comparison of these to the low current density case in Figure 6.6, representing a low water production case, supports this argument. The subsequent downstream accumulation of product water inside both compartments results in a continuous increase in membrane water content. This effect is strongly observed in the anode outlet region. Due to the priory mentioned occurrence of higher temperatures in the bottom section, a membrane dry-out is observed in these regions. The effect is more prominent within the simplified cell, as a result of temperature overestimation. The overflow on the intersections of the three anode compartments is represented well inside the simplified model, leading to a shift of the profile. The humidification on the anode outlet is slightly overestimated by the SC approach.

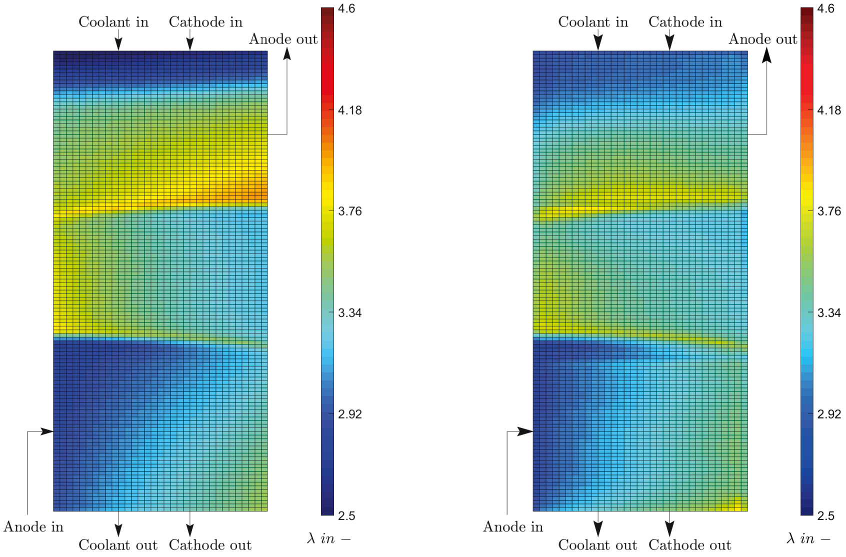

(a) Simplified cell results with $j_{\mathrm{avg}} = 1.06\,\mathrm{A/cm^2}$. **(b)** Detailed cell results with $j_{\mathrm{avg}} = 0.97\,\mathrm{A/cm^2}$.

Figure 7.11: Membrane water content distribution of simplified (left) and detailed (right) cell simulation on anode CL-MEM interface for ID3 at 0.686V.

In addition, the through-plane water gradient inside the membrane is investigated for the SC and DC cases. For this reason, a plot of the surface averaged membrane water contents on CL/MEM-interfaces of cathode and anode, as well as the four numeric cells of the membrane in through-plane direction are given in Figure 7.12.

Matching profiles are obtained with maximum membrane water contents of 3.87 and 3.82 for simplified and detailed cell simulation, respectively. When moving towards the anode compartment, the deviation between the approaches decreases. The minimum values, found on the anode CL/MEM-interface, are found to be 3.30 for the simplified and 3.29 for the detailed model.

It is apparent, that back-diffusion- and EOD-driven water transport are adequately represented within the simplified cell model. As for the deviation of the curves, the overall higher current density of the simplified cell leads to an enhanced water production on the cathode reaction interface. Hence, a stronger water absorption into the membrane is present, leading to higher water content values on the cathode CL/MEM-interface. This increase in water content, in turn, causes an increase in water diffusion towards the anode. As the difference in current is not significant, a correspondingly small deviation between the curves is found.

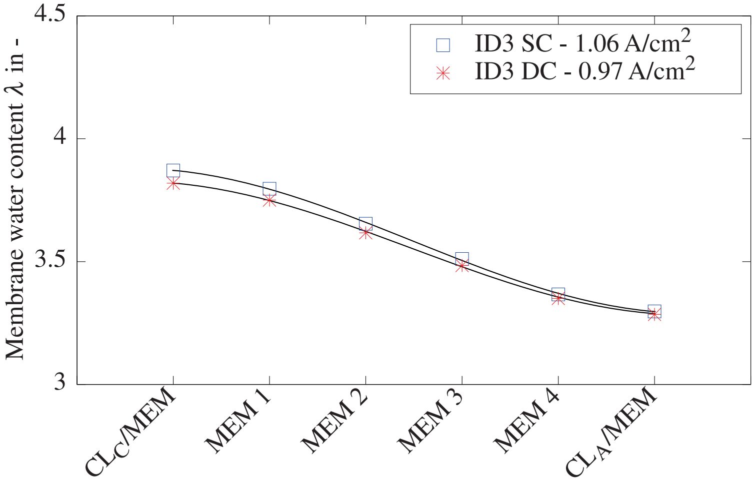

Figure 7.12: Through-plane membrane water content λ comparison of simplified (blue square) and detailed (red star) case for ID3 at 0.686 V.

The liquid water fraction distribution inside the cathode gas channels is plotted in addition in Figure 7.13. Due to neglection of phase-change and membrane water contents below the liquid water desorption threshold of 16.8, a investigation of the anode channels is excluded.

Very low liquid water amounts with similar trends are observed within the cathode channels for both approaches. An increase of liquid water along the cathode flow direction occurs in both simulations, starting from a single-phase flow entering the domain via the distributor and accumulating to maximum values of 0.015 %. Noticeable amounts of liquid water approximately start occurring from the middle of the active area. Distributors and collectors show constant values. While the simplified cell appears to have higher amounts of liquid water, it has to be considered that the land areas are not plotted, therefore making the simplified cell appear flooded. The increase in cathode flow direction is a result of reaction water accumulation, continuously being ejected into the gas channels within the active area. Hence, due to the additional neglection of phase-change, distributors and collectors show constant liquid water values. For a future implementation, a regular two-phase pipe flow correlation might be applicable here.

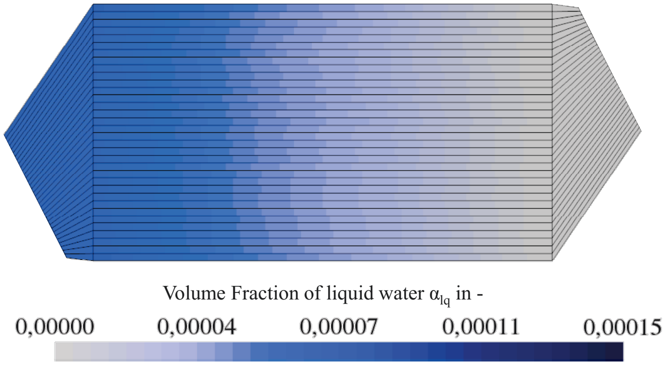

(**a**) Simplified cell results with $j_{avg} = 1.06\,\mathrm{A/cm^2}$.

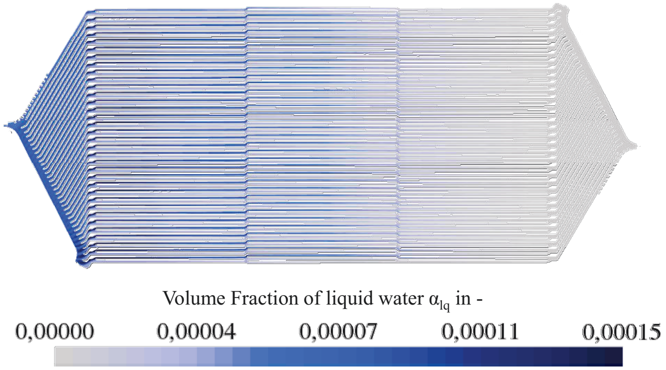

(**b**) Detailed cell results with $j_{avg} = 0.97\,\mathrm{A/cm^2}$.

Figure 7.13: Liquid water volume fraction distribution in cathode gas channels of simplified (top) and detailed (bottom) cell simulation for ID3 at 0.686V.

As for the generally low amounts of liquid water, the absence of an appropriate resistance model is found to be the cause. This leads to an underestimation of the interdependent resistances between the phases, resulting in a higher slip velocity and therefore stronger retention of liquid water inside the channels. First simulations with implementation of a simple linear resistance model show an increase in water content for equivalent settings.

In summary, a very good agreement between simplified and detail model is found, while both approaches lack a proper description of two-phase gas channel phenomena. Models such as the permeability model developed in section 5.9 can help to improve the quality of the prediction. However, a numerically stable implementation of the model is not given currently, which is why the inclusion is not part of the present study.

The simulatively validated simplified cell model is used in the following to create a stack model.

7.4 Automated Stack Algorithm

The combination of multiple simplified single cells leads to the creation of the stack model. For this reason, an automated stacking algorithm is created using a JAVA-based macro. An exemplary geometry of a 400-cell stack is shown in Figure 7.14.

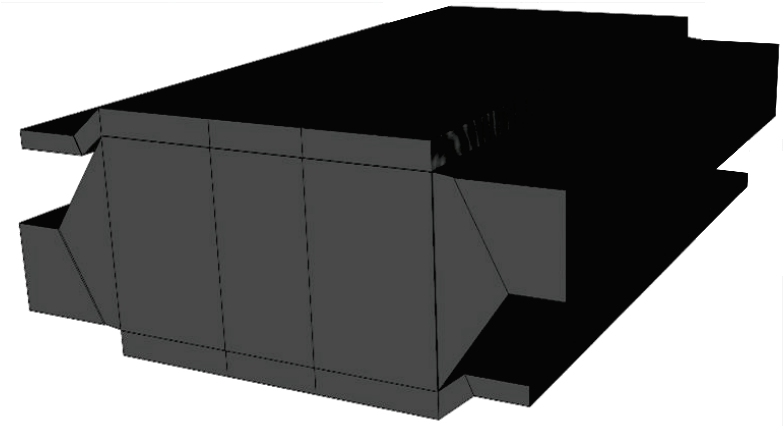

Figure 7.14: 400-cell PEMFC stack geometry.

The steps of the stacking process are as following:

1.) Creation of stack CAD geometry:
A stack CAD geometry is created by combination of *n* simplified single cells. The cells are connected, using compensation regions. In addition, current collectors as well as pressure end plates are implemented. An inclusion of manifolds is possible.

2.) Structured meshing:
The priory created CAD geometry is meshed, using an automated, fully structured hexahedral mesh.

3.) Adjusting boundary conditions:
Depending on the specified number of cells, boundary conditions, such as potentials, in- and outlets or thermal boundaries of the geometry have to be adjusted.

4.) Region specific initialization:
The convergence of the stack model requires a proper initialization in order to be numerically stable. Especially the potential through the various cells has to be initially

approximated accordingly. For this reason, a cell-dependent step-wise initialization of the voltage is introduced.

In order to keep computational power requirements low, the validity of the stack model is analyzed against experimental data on a 60-cell PEMFC stack basis exclusively.

8 PEMFC Stack Simulations

Within the following chapter, the priory developed stack model is applied on a 60-cell PEMFC stack geometry to evaulate its applicability. A focus is placed on the investigation of the water management within the stack. For this purpose, simulations are performed and subsequently validated against experimental results.

8.1 Computational Domain

60-cell stack simulations are performed using the geometry depicted in Figure 8.1. The stack is created through the geometrical combination of 60 equivalent simplified single cells.

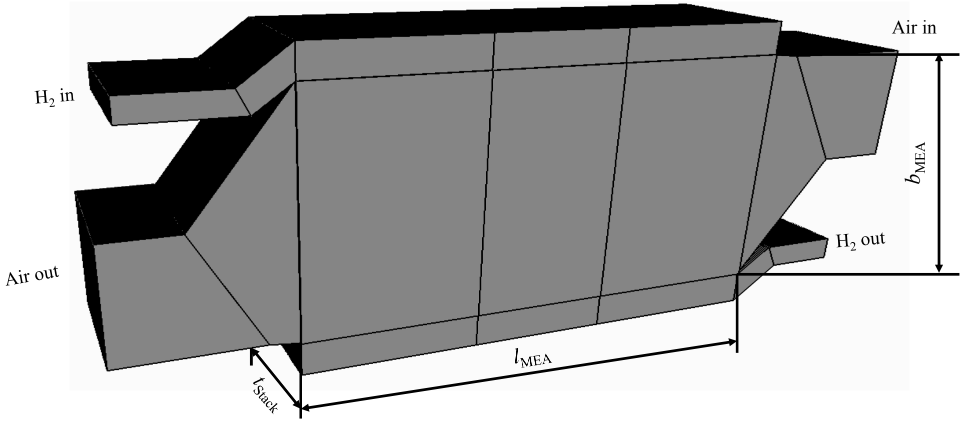

Figure 8.1: Detailed single cell geometry for PEMFC simulations.

A summary of the geometrical measurements of the stack is given in Table 6.1.

Table 8.1: Parameters for 60-cell stack geometry.

Parameter	Description	Value
l_{MEA}	Length of MEA	217 mm
b_{MEA}	Width of MEA	121.4 mm
A_{MEA}	Geometrical area of MEA	$263\,\mathrm{cm}^2$
H_{Stack}	Thickness of Stack	67.1 mm
n_{cells}	Number of fuel cells	60

In the following, the simulation settings are introduced.

8.2 Simulation Settings

The present section summarizes the assumptions and simplifications, as well as operating conditions used of the simulations.

8.2.1 Geometrical Simplifications

In addition to the simplifications performed on a single cell basis, geometrical adjustment are performed, which can be summarized as follows:

1.) Exclusion of stack manifold:
In order to decrease the numeric complexity, a decoupling of mass exchange between cells is performed through exclusion of the manifold. Instead, manifold sections of the single cells are used to introduce separate mass flows for each cell.

2.) Implementation of numerical in- and outlets:
Analogously to the single cell simulations, numerical in- and outlets are introduced to prevent a presence of numeric instabilities in regions of interest e.g. back flow. The respective manifolds are extruded for that matter. The modification is not shown in Figure 8.1.

8.2.2 Physical Assumptions

In addition to the modeling performed throughout the previous chapter, physical assumptions are made as follows:

1.) Adiabatic boundary conditions:
As for simplicity reason, the outer walls of the stack are assumed to be adiabatic. The temperature deviations towards the experimental stack is discussed in the respective section. An investigation of thermal side effects due to non-adiabatic scenarios are not in the scope of the present work.

2.) Decoupling of mass interaction:
As a result of the prior exclusion of the manifold, mass exchange between fuel cells is neglected. This assumption has to be made due to the present remaining instability of the model.

3.) Uniform distribution of mass inlets:
The presence of manifolds, leads to a cell-to-cell maldistribution of stack mass inlet flows. Experimental investigations shows a negligible cell-to-cell variation due to the moderate size of the stack, as well as presence of dummy cells, thus justifying the assumption. With increasing stack sizes e.g. 400 cells, this assumption has to be dropped. In these cases, the manifold has to be implemented explicitly.

4.) Conservation of charge:
A conservation of electric charge is ensured throughout all regions of the stack geometry. This results in the flow of equivalent total charge in every cell.

8.2.3 Operation Conditions and Material Properties

To ensure a comparability to the single cell results, operation conditions of the stack are set to the ID3 settings of the single cell. A summary of the stack parameters is given in Table 8.2. Material properties of the simplified single cell are applied to the respective region.

Table 8.2: Summary of 60-cell stack simulation parameters.

U_C in V	49.1	41.1	36.8
j_{exp} in A/cm^2	0.2	1.0	1.5
λ_A		2.0	
$p_{A,out}$ in bar		1.8	
$T_{A,in}$ in °C		90	
$RH_{A,in}$ in %		25	
λ_C		2.2	
$p_{C,out}$ in bar		2.1	
$T_{C,in}$ in °C		85	
$RH_{C,in}$ in %		25	
$\dot{V}_{Cool,in}/n_{Cells}$ in Nl/min		1.5	
$T_{Cool,in}$ in °C		85	

The simulation results are elaborated in the following section.

8.3 60-cell PEMFC Stack Simulation Results

The stack investigations are focused on the 41.2 V operation point (corresponding to the 0.686 V single cell case). Analogously to the single cell results, a comparison regarding fluid flow, thermal and electrical effects is made. A focus is placed on the investigation of the water management inside the stack. The orientation of all plots is in accordance to the configuration shown in Figure 8.1. Due to an assumption of equal cell inlet mass flows for all media, major differences in-between cells of the stack are expected to be small. The evaluation is therefore focused on a comparison to single cell data.

Figure 8.2 shows the pressure profiles in anode and cathode gas channels. The pressure drop profiles are identical to the respective single cell case. Mass-exchange within the manifolds of distributor and collector is excluded, whereas accordance to the single cell is to be expected. The qualitative and quantitative consistency of results is merely an indication for a converged solution.

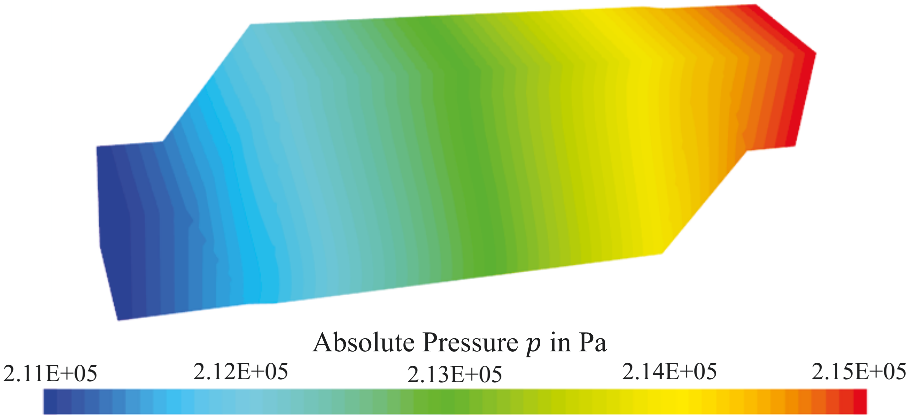

(a) Cathode pressure distribution.

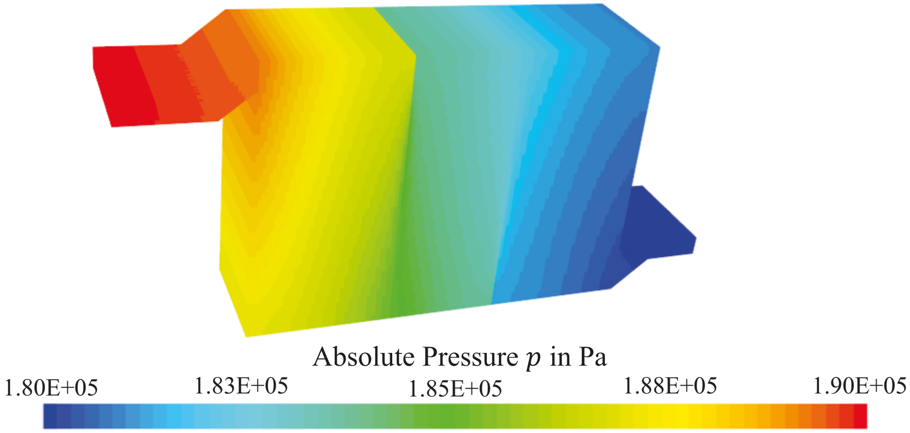

(b) Anode pressure distribution.

Figure 8.2: Cathode and anode pressure distribution in flow field channels of 60-cell stack for ID3 case, corresponding to a voltage of 41.2 V.

A distribution of the temperatures inside the coolant flow is shown in Figure 8.3. A continuous increase in temperature from an initial value of 85 °C to 88 °C is observed from in- to outlet of the active area. Edge cells of the stack show a slower increase along the cathode flow direction compared to those located in the center, resulting in local differences of up to 1 K. Center cells

within the stack experience a production of heat within the cell, as well as inside neighboring cells. Edge cells in contrast, lack one heat source on the outer sides of the stack, while being equivalently cooled, which therefore results in a lower temperature gradient.
A comparison with the temperature results of the simplified single cell, shown in Figure 7.10, indicates even lower values than the edge cells of the stack regarding temperature gradient and cathode outlet value. The reason can be found in the thermal boundary conditions of the single cell setup, which is assumed to be adiabatic to the surroundings. At the same time, a single heat source without neighboring cells within the cell is present, while being equivalently cooled on anode and cathode side, therefore resulting in a lower temperature increase. This effect is enhanced when operating at higher current densities, as shown in Figure A.28. The lack of an additional heat source on the outer sides of the stack therefore leads to a higher discrepancy of up to 2 K between edge and center cells.
It shall be noted, that the neglection of natural convection due to imperfect thermal insulation leads to an underestimation of the edge cell cooling. Even lower cell temperatures are therefore to be expected on edge cells of the stack, further shifting the through-plane stack temperature distribution.

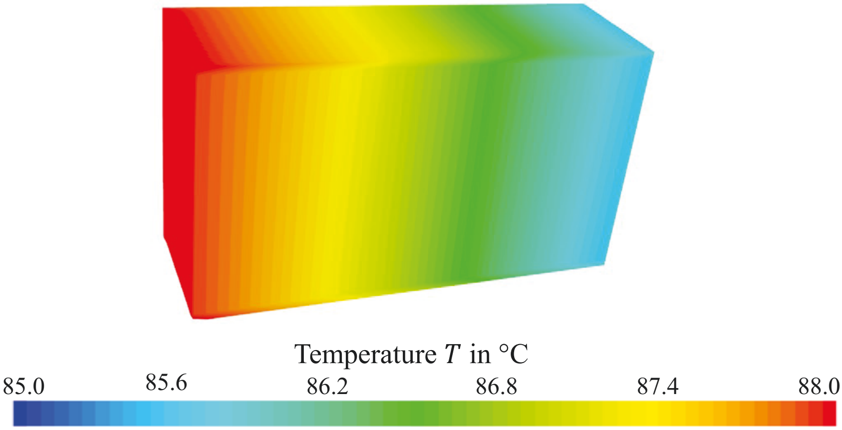

Figure 8.3: Temperature distribution in anode and cathode coolant regions of 60-cell stack for ID3 case, corresponding to a voltage of 41.1 V.

Figure 8.4 shows the current density distribution on the CL-MEM interface of anode and cathode of all cells inside the stack. A threefold division as a result of the redirection regions is present within the profile. Qualitative and quantitative results are in accordance to single cell results, with exception of a mismatch inside the middle region, where slightly higher current densities can be observed. The reason is most likely located in errors due to the highly challenging numeric setup.

The unequal temperature distribution, as a result of dissimilar thermal boundary conditions does not show a noticeable effect on the present current profile. However, a stronger impact is observed for higher current densities, as shown in Figure A.29. The stronger increase in temperature results in an acceleration of reaction kinetics and therefore slightly higher current densities in center cells in comparison to edge cells. It shall be noted, that this effect might be reversed, when high temperatures lead to dry-out conditions of cells, increasing ohmic potential losses. Overly cooled edge cells on the other hand can lead to flooding states, as a result of enhanced water condensation. An individual analysis of the respective operating point is necessary in order to be able to evaluate the criticality of the case.

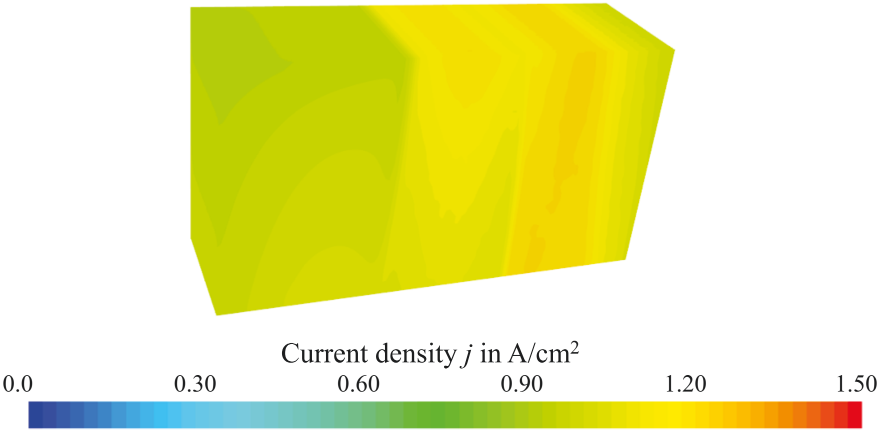

Figure 8.4: Current density distribution on reaction planes of 60-cell stack for ID3 case, corresponding to a voltage of 41.2 V.

In order to be able to analyse the water management inside the stack, the membrane water content on the anode CL-MEM interface is shown in Figure 8.5.

Accordance of membrane water content is achieved with small local deviations, resulting in a shift of the membrane water content maximum. The impact of this effect is in accordance to the current density profiles. As priory mentioned, the source of the deviation is most likely to be found in numeric errors. The main characteristics of the distribution, e.g. the three fold separation, as well as the dry-out zone on the cathode inlet are properly represented. As priory observed for the current distribution, a slightly noticeable imbalance between edge and center cells is found to be present at higher current densities (see Figure A.30), while the effect is negligible for the present case. The main contributor for the imbalance is found to be the current density maldistribution, whereas higher current densities lead to an enhanced water production and therefore humidification of edge cells in comparison to neighboring ones.

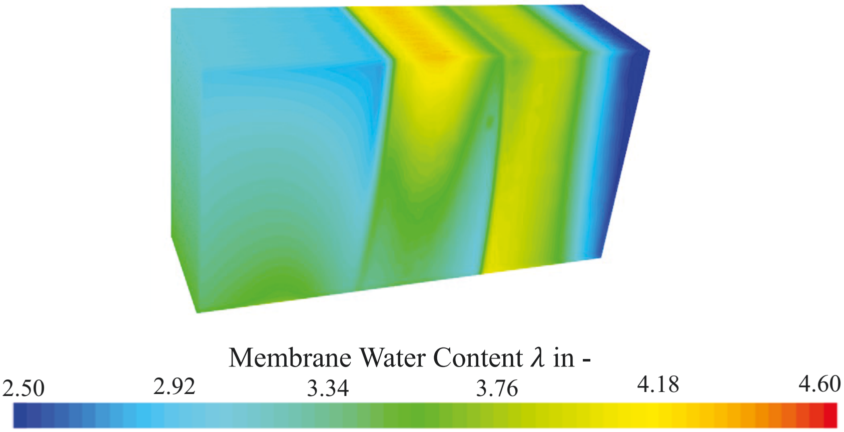

Figure 8.5: Membrane water content distribution on anode CL-MEM interface of 60-cell stack for ID3 case, corresponding to a voltage of 41.2 V.

Due to the absence of an appropriate two-phase resistance model, a significant change in water saturation distribution is not expected (see Figure 7.13). Therefore, mass flow distributions of water vapor inside anode and cathode gas channels are consulted (see Figure 8.6) to further investigate the water management of the stack.

An increase in water vapor mass flow from in- to outlet in along-the-channel direction on the cathode is observed, with the increase being a result of product water accumulation. This can be affirmed by the lower absolute concentrations values at the lower current density case (see Figure A.27) and higher values at higher current densities (see Figure A.31). The anode side shows significantly lower, rather constant mass flow values with an exception of maxima on the boarder of the threefold regions. The lower values are a result of water being produced and therefore also mainly removed on the cathode side. The maximum amounts in water are a result of under the channel flow stemming from pressure gradients between adjacent channels, which is in accordance to the mass distribution shown in Figure 7.7.

An evaluation of the relative humidity on the outlet surfaces of cathode and anode shows an increase to 59.7 % and 48.1 %, respectively. For the present case, a neglection of phase-change effects on a global scale would be justified. It shall be noted, that local over-saturation can be present, leading to a shift in liquid volume fraction.

Despite small deviations to the single cell setup, good qualitative and quantitative agreement of the results is found. The main advantage of the model in its present state in comparison to the majority of literature approaches is the resolution of local effects with inclusion of edge cell effects.

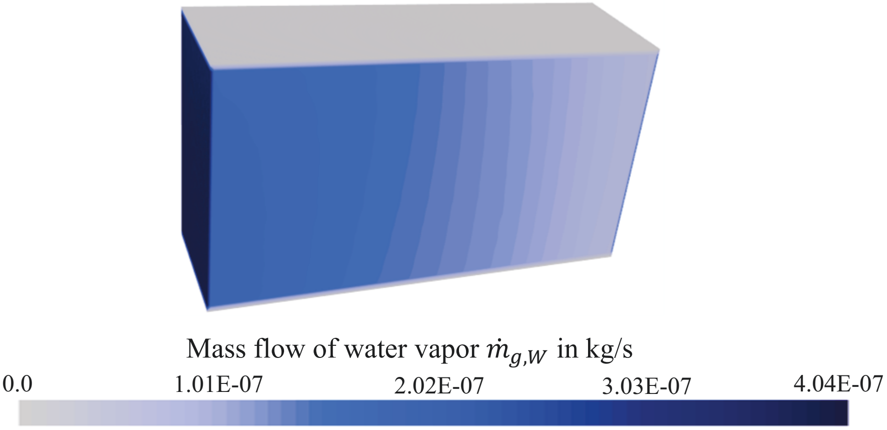

(a) Cathode gas channels.

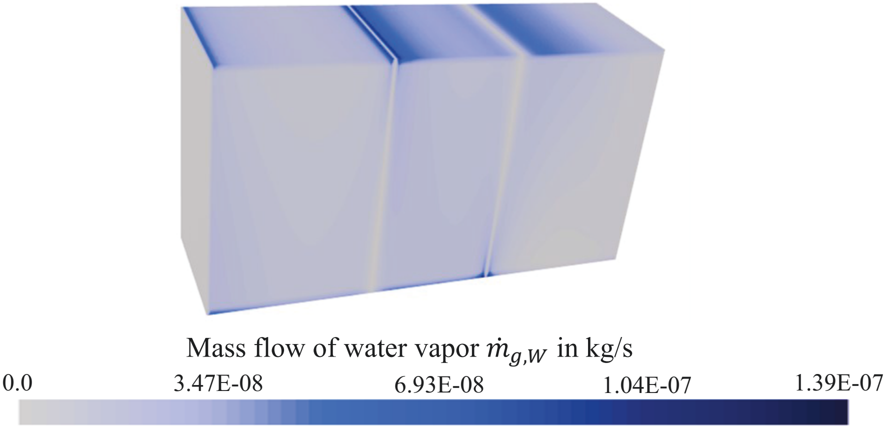

(b) Anode gas channels.

Figure 8.6: Mass flow distribution of water vapor in cathode and anode gas channels of 60-cell stack for ID3 case, corresponding to a voltage of 41.2 V.

The entirety of cells inside the stack at stationary operation conditions is found to not be properly represented by a single cell setup or decoupled approaches with appropriate boundary conditions, as the impact of edge cell effects has to be implemented explicitly. In the case of a maldistribution on the cell inlets of the stack, a fully coupled model has to be investigated to properly capture the resulting effects. The present approach is able to capture these through specification of varying mass inlets or the explicit modeling of the manifold geometry.
After simulative validation, a comparison to experimental 60-cell results is performed in the following section.

8.4 Experimental Validation of 60-cell PEMFC Stack Simulations

In order to validate the results of the stack model, a comparison to experimental 60-cell measurements is performed. The results of the investigations are elaborated in the following.

8.4.1 Experimental Setup and Operating Conditions

Experimental 60-cell stack measurements are performed, using the short stack box shown in Figure 8.7.

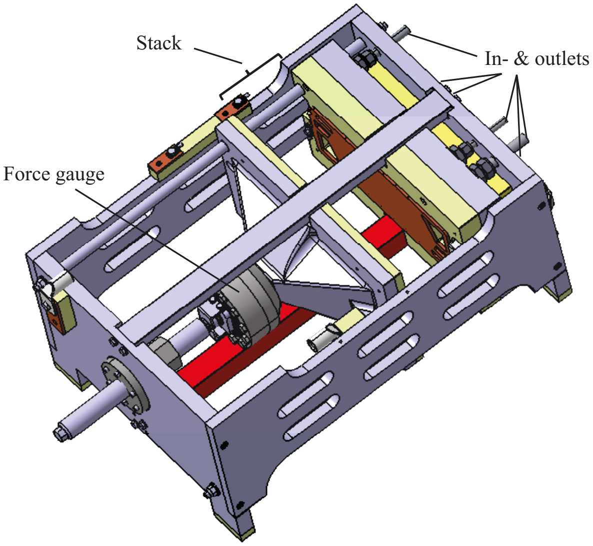

Figure 8.7: Experimental setup for 60-cell measurements.

A cell voltage monitoring is connected to the stack, allowing an in-operation cell voltage measuring. A compression force of 31 kN is used, corresponding to the single cell setup value. The value is ensured via a force gauge. Two dummy cells are used on each side of the setup, thus providing five additional inlets for the coolant flow, two for the air flow and none for the hydrogen flow. The excessive coolant flow provides a proper tempering for the side cells, whereas the additional flow paths for the gas ensure an even cell-to-cell distribution.
The experimental operating conditions are summarized in Table 8.3. Parameters differ from the simulative conditions, defined in Table 8.3, due to sensitivity of the experimental setup, as well as safety restrictions of the test stand.

Table 8.3: Summary of 60-cell stack parameter variation settings.

	Variation	UI-curve
j_{exp} in A/cm^2	0-2.5	0-2.5
λ_{A}	1.2-1.7	1.7
$p_{\text{A,out}}$ in bar	1.8-2.3	1.7
$RH_{\text{A,in}}$ in %	25-70	33
λ_{C}	1.8-2.4	2.2
$p_{\text{C,out}}$ in bar	1.7-2.3	2.1
$RH_{\text{C,in}}$ in %	16/33/49	33
$\dot{V}_{\text{Cool,in}}$ in Nl/min	10-42	10-42
$T_{\text{Cool,in}}$ in °C	50-70	65

The obtained data is compared to the priory discussed 60-cell stack simulation results in the following section.

8.5 Comparison of Investigation Case

In order to be able to compare the stack simulation results with experimental investigations, sensitivity analysis of RH, p_{out} and λ-values, as well as cell temperature of anode and cathode are performed. The resulting effect on the cell voltage is given in Figures A.32 to A.38.
The average cell performance is found to be relatively independent of all investigated parameters, besides the stack temperature. The minimum voltage cell (cell 24) shows systematically lower voltages than the average cells with additional sensitivity regarding all investigated values. The cells with the highest voltage (varying between cell 6 and 13) exhibits a slightly more stable trend than the average cell in all tested parameters with the highest voltage values.

The minimum voltage cell shows poor performance as a result of flooding, which is clearly evident from the dependency on stoichiometry, relative humidity and cell temperature. Higher stoichiometry values lead to an enhanced water removal, unblocking the porous system, while higher temperatures accelerate water unblocking through phase change and subsequent removal as vapor. An increase in relative humidity values, on the contrary, result in an increase in water, leading to an enhanced blockage state. Due to the position of the minimum voltage cell inside the stack, in combination with surrounding cells not showing anomalies, an initially faulty cell is assumed to be present, which cannot be represented by the simulation model. Nevertheless, it shows the severity a water flooding might have on the stack performance. Maximum and average voltage cells are relatively independent on the tested values over the whole range with exception of the cell temperature.

The simulative parameters of relative humidity RH-, and pressure values p_{out} are within the investigation range. While the cathode stoichiometry λ_C is within the investigation region, the anode value λ_A is slightly higher than the maximum experimental value. All mentioned values can therefore be assumed to have a negligible effect on the stack performance. The dependence on the stack temperature on the other hand in combination with differing values for experiment (65 °C) and simulation (85 °C) has to be taken into account in further investigations. The following validation is therefore performed in consideration of this difference.

Figure 8.8 shows the experimentally determined polarization curve with additional indication of the three simulative points. The curve fitting is performed analogously to the single cell results, using equation (3.8).

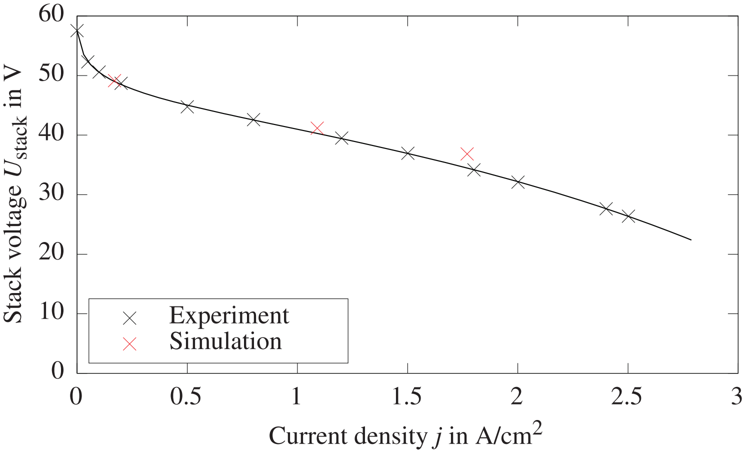

Figure 8.8: Experimental polarization curve of 60-cell stack with inclusion of simulative results.

The low current density operating point at 0.17 A/cm^2 is in good agreement with experimental data. The increase in current density to 1.09 A/cm^2 and further to 1.77 A/cm^2 shows a growing deviation with a stronger potential drop of the experimental curve.

As priory shown for the experimental single cell validation (see section 7.3.2), a proper agreement of the model at low current densities is achieved. The slight deviation in the concentration region of the polarization curve can be lead back to two effects. On one hand, the concentration losses are underestimated due to the lack of an appropriate description in the present STAR-CCM+ PEMFC model (see section 4.3). On the other hand, the operation of the experimental stack is performed at lower temperatures (65 °C compared to 85 °C). This leads to significantly stronger condensation of water and subsequently to a blocking of pores and channels, visible as an exponential drop of the polarization curve. An additional indication are given by the relative humidity sensors on the outlet of anode and cathode. These show fully saturated flows at all operating points of the pole curve. The simulation results in contrary, show outlet humidity values of 59.7% on cathode and 48.1% on anode at 41.2 V, being far below the dew point. Although concentration losses are present, the results show an enhanced stability in performance inside the stack in comparison to a single cell configuration. This is typical due to the superior thermal conditioning of a stack. While a single cell is strongly influenced by environmental conditions within the cell holder geometry, a stack is fairly insulated and tempered through the presence of neighboring cells. This counteracts the effect of lower temperatures and results in a smaller deviation towards simulation results, when comparing to the single cell validation. Due to the absence of a proper representation of concentration losses within the model, a linear drop is expected for further increase in current, leading to a growth in deviation between the two approaches. An operation within these regions is not of technical relevance for automotive applications.

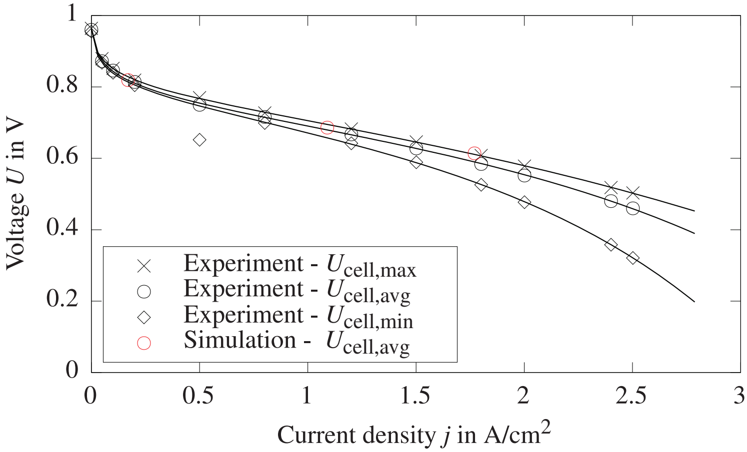

Figure 8.9: Experimental polarization curve of single cells in 60-cell stack with U_{max}, U_{avg} and U_{min}.

Since the stack voltage is a combination of all single cell voltages, which also include flooded cells, an additional evaluation on single cell basis shall be performed. Therefore, single cell polarization curves of the minimum, maximum and average voltage cells of the experimental setup are shown in Figure 8.9. Simulation results for the three operation points of cell 30 are given in addition.

The simulation results are located in-between the experimental average and maximum voltage cell results for all three operating points. The minimum voltage cell shows a strong voltage drop with increasing current densities, with an outlier at 0.5 A/cm^2.

The priory mentioned drop in voltage due to cell flooding is clearly visible for the minimum voltage cell at increasing current densities. Under-performing cells like these contribute to a noticeable decrease in stack voltage, explaining the priory shown deviation. The simulation results are in excellent agreement to the experimental data when comparing to average and maximum voltage cells. The reason can be found in the already mentioned superior thermal connection of the cells when comparing to a single cell setup. While in this state, the stack is properly humidified to a degree where ohmic resistances are low while mass transport resistances due to water blockage are low as well.

Disregarding the malfunctioning cell inside the stack, an excellent agreement between results of experiment and simulation could be achieved. The present model therefore allows the prediction of stack performances, including local phenomena and side effects. It shall be noted, that if the stack is operated at a state with higher flooding risk (e.g. lower λ- or higher RH-values) an increasing deviation towards simulation results is expected. An incorporation of a proper description of concentration losses and two-phase flows is necessary in order to properly reproduce these effects.

9 Summary and Outlook

A model for the feasible simulation of three-dimensional PEMFC stacks with explicit single cell modeling was developed in the present thesis. The model is of multiphysics nature, including mass, energy, species and multiphase transport and is therefore able to resolve the water management inside the stack. The creation of the stack model required detailed single cell data, which were collected via detailed single cell PEMFC simulations. The latter were priory validated against experimental results. Using the reference data allowed a simplification of the flow field region, crucial for the necessary reduction in numeric cells. An automated algorithm for the creation of n-cell stack models was successfully created. A deep dive into the two-phase flow phenomena inside gas channels was performed in addition, using a Volume-of-Fluid (VOF) based approach. The evaluation of parametric studies allowed the creation of two-phase permeability correlations which were derived to be compatible for an implementation within the stack model.

Detailed two-phase investigations in single channels of the flow field, using the Volume-of-Fluid (VOF) method, were performed which require highly resolved meshes. The fine mesh resolution leads to low time steps in order to be numerically stable and therefore limits the physical time spans that can be resolved. The necessary acceleration was achieved through the development of an adaptive mesh refinement (AMR) simulation approach, allowing the detailed investigation of two-phase phenomena in gas channels. During the investigation, a comparison between static and dynamic wall contact angles was performed, which resulted in strong differences in the droplet removal process. Using the dynamic contact angle formulation in combination with the AMR method, detailed investigations of the two-phase flow in cathode gas channels were carried out. In order to validate the AMR approach, a two-dimensional analytic arc function was developed and compared to the cross-section of the simulative results, showing an excellent agreement.

The development of a two-phase pressure drop correlation required a strong acceleration in computational time. As a result, a constant coarse mesh refinement (CCMR) approach, based on the high resolution interface capturing (HRIC) method, was used to carry out additional cathode gas channel simulations. The results were compared to the detailed AMR simulations, which showed a good accordance regarding the two-phase flow phenomenology. While the cathode geometry produced an offset in pressure drop values, additional anode simulations showed a good agreement between the two approaches.

The validated CCMR approach was used to conduct parametric studies of the liquid water inlet position to investigate a dependence on the location and number of inlets. Using a single set of specified inlet conditions of gas and liquid water volume flow, a presence of droplet regimes with comparable pressure drop values could be shown exclusively, thus giving indications for an independence. A relationship could not be investigated for further flow regimes, due to the immense related computational effort. As a result, a single volumetric source term was used for further simulations.

The CCMR approach was used subsequently to analyze the effects of gas and liquid water velocities on the flow regime and resulting pressure drops for cathode and anode gas channels. The results of the simulations were used to create two-phase pressure drop maps, showing the presence of three main two-phase flow regimes; namely slug, droplet and film flow. The cases were filtered for unphysical data and processed, using a k-means algorithm, to create gas permeability correlations for anode and cathode gas channels. A comparison with literature studies showed a good agreement regarding curve shapes. However, a significantly stronger influence on low saturation values, leading to strong resistances and therefore pressure drops, was found to exist for the present simulation results.

Detailed single cell simulations on a highly structured mesh were carried out with inclusion of multiphysics to validate the STAR-CCM+ PEMFC model and create reference results, which were used in the subsequent simplification process for the stack model creation. An evaluation of the single-phase pressure drop values inside the flow field channels against experimental single cell data showed a deviation of 26.0 and 22.2 % for anode and cathode, respectively.

An increasing deviation of average current densities was found when decreasing the applied potential, whereas the detailed results lead to higher current density values. The lack of an appropriate inclusion of mass transport resistances within the PEMFC model of STAR-CCM+ was found to be the cause. The profiles of current density distributions inside the active area were in accordance to the experiments. The corresponding temperature distributions were found to strongly deviate, resulting from a local compression of the experimental setup, leading to a non-ideal coolant distribution. This could not be represented within the simulative model. While the effect of inlet gas humidification on cell performance could be reproduced well, an increase of cell temperatures resulted in an overestimated drop in cell voltage.

The validated simulative results of the single cell were used as reference results for the creation of a simplified cell model, which was subsequently combined to form a stack. The simulative description of large stacks required a strong reduction in computational cells which was mainly achieved through a simplification of the flow field geometries of anode, cathode and coolant. To ensure a proper description of pressure and velocity distributions inside the simplified regions, a Darcy-like modeling approach was utilized. Areas of the flow field with identical flow behavior were combined into common regions with equal inertial and viscous resistance values. The bipolar plate was fully omitted during the modeling process, therefore disconnecting the terminals electrically. This problem was overcome by definition of a perfect electrical through-plane conductivity inside the gas channels, while restraining an in-plane propagation. A compensation layer with perfect electric and thermal through-plane conductivity is included in-between anode and cathode gas channels to guarantee a correct cell pitch. The thermal equivalence was ensured by inclusion of a heat exchanger model, which handles the heat transport between gas channels and coolant, as well as GDLs and coolant. Volumetric source terms, accounting for conductive and convective heat transfer, are used in the respective regions.

A validation of the simplified model was performed on a single cell basis against detailed single cell simulation results. Comparing the single-phase pressure drop values of the anode and cathode gas flow fields, showed a deviation of 19.4 and 16.0 % to detailed results, respectively. The distribution of mass flows and pressures were shown to be represented well within the simplified model. Additional investigations of operational cases demonstrated a good agreement of the values up to higher current densities of 1.5 A/cm^2, while a further increase resulted in a higher deviation. The analysis of the water transport showed a good accordance between simplified and detailed simulation results when comparing membrane water contents, as well as saturation plots inside cathode gas channels.

The validated simplified single cell model was used within an automated stacking algorithm to set up a 60-cell stack simulation. Independent inlet section for the single cell were assumed with equally distributed mass flows, therefore omitting the manifold geometry. Good agreement to simplified single cell results was found. Due to the thermal boundary conditions of the stack setup, temperature gradient differences between center and edge stack cells occurred. Lower gradients on edge cells were observed for all operating points, resulting from a lack of one neighboring heat source, while being equally cooled. An increase in current density showed an enhancement of the deviation with local differences of up to 2 K between cells. The resulting effects on current density and membrane water content distribution were slightly visible for the higher current density case. An enhancement of reaction kinetics is found for stronger temperature increases, thus giving higher current densities and therefore higher membrane water contents. The mass flow of water vapor within the gas channels is found to be increasing in along-the-channel direction of the cathode, while showing relatively constant amounts on the anode. An evaluation of outlet RH-values showed non-saturated gases for all cases.

A subsequent comparison to experimental 60-cell stack data was performed. Good prediction capability of the stack performance in the three investigation cases was achieved. Slightly increasing deviation were observed for higher current densities, which were linked to mass transport resistances. The STAR-CCM+ PEMFC model in its present state was not able to properly account for theses losses, leading to an overestimation in performance. In summary, the stack model was able to predict the stack performance at the three investigated operating points, while resolving local distributions inside each cell.

In order to further improve the present modeling approach, guidelines are given as follows:

- **VOF simulations in single channels**
  - Experimental validation of two-phase pressure drop results:
    An experimental validation of the two-phase pressure drop data is pending. The quantitative estimation of accurate values is remaining difficult to date, as most state-of-the-art techniques are of invasive character (see section 3.3.1). Nonetheless, an experimental validation is crucial.
- **Detailed PEMFC single cell simulations**
  - Inclusion of phase-change:
    The present formulation of the STAR-CCM+ PEMFC model did not allow a stable implementation of phase-change phenomena, thus limiting the presence of liquid water within the anode compartment. The presence of liquid water is especially important in order to capture mass transport losses within the catalyst layers. In order to predict these states, an implementation of phase-change is necessary.
  - Inclusion of mass transport resistances in CL:
    Mass transport resistances inside the CL regions were omitted in the current PEMFC model by STAR-CCM. An implementation, e.g. in form of an agglomerate model, would strongly benefit the prediction capabilities at higher current densities. A direct implementation on cell level is possible for the current model, while changes regarding the stack model are not necessary.
- **Stack simulations**
  - Consideration of natural convection:
    Real stacks are exposed to natural convection, as a result of non-ideal thermal insulation, thus influencing the state and production of water inside side cells. The implementation of non-adiabatic boundary conditions could help with an investigation of these effects.
  - Inclusion of stack manifolds:
    The coupling of mass flows via the manifolds was excluded in the present work. An inclusion would account for cell-to-cell variations and therefore bring out the full prediction capabilities of an explicit single cell approach.

- Implementation of two-phase permeability correlation:
  The implementation of the developed gas permeability correlations into the simplified cell model is yet to be done. A numerical stable implementation is necessary for the investigation of the whole operation span of low to high current densities. In combination with the manifold implementation, cell-to-cell distribution changes as a result of liquid water presence could be analyzed.

A Appendix

A.1 Two-Phase Flow in Gas Channels

The present chapter gives additional information on assumptions and derivations regarding VOF simulations in PEMFC gas channels.

A.1.1 Geometric Simplification of Cathode Gas Channels

The deviations due to neglection of conical expansions and constrictions within the cathode gas channels are investigated within this section. A 4-repetition unit model, according to the mesh shown in Figure 6.2, is used to investigate the amount of mass transfer between neighboring channels. The PEMFC model without reaction, as well as sorption processes is used. The investigation geometry is shown in Figure A.1.

Figure A.1: 4-repetition unit geometry of cathode gas channels with investigation planes 1 - 6.

In order to check for maximum and minimum mass transfer, two cases with mass flows, adjusted to represent cathode stoichiometry-values of 0.5 and current densities of 2.5 A/cm^2, were implemented. Results are evaluated on sections 1 to 6 and shown in Figure A.2 and A.3 respectively. The triangle markers, represent the top channel, starting with a wide cross-sectional area and the circle markers the bottom channel with smaller area. Total mass flows in the respective plane are given, as well as the corresponding average mass flow, representing the constant channel cross-section area cases, shown in Figure 5.1.

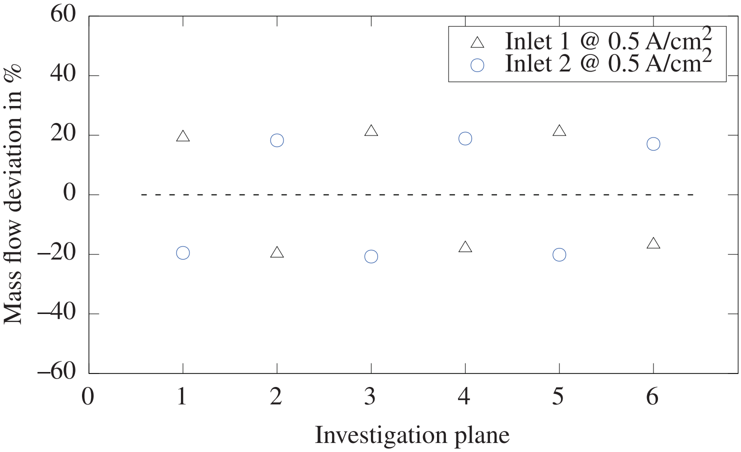

Figure A.2: Exchange mass flow rate from 4-repetition unit simulation of cathode gas channels at 0.5 A/cm^2.

The 0.5 A/cm^2-case shows an approximately constant, alternating deviation of around ± 20 % between neighboring channels.

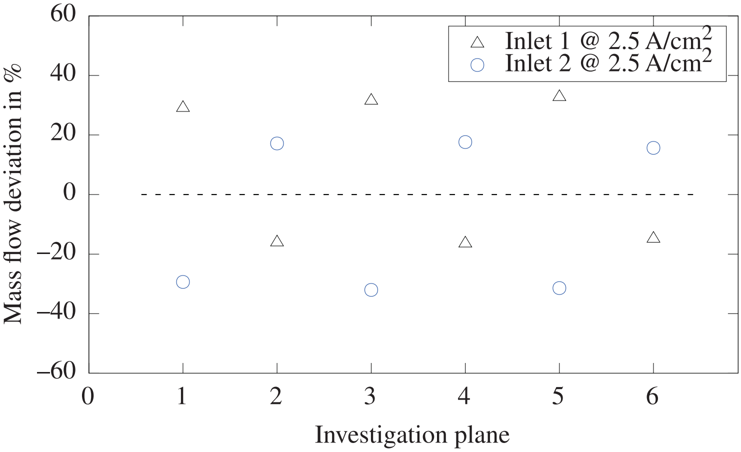

Figure A.3: Exchange mass flow rate from 4-repetition unit simulation of cathode gas channels at 2.5 A/cm^2.

Local pressure gradients between adjacent channels, as a result of differences in cross-sectional area, lead to a convective under-the-land flow. The differences in mass flow between plane 1/2, as well as 3/4 and 5/6 are a result of that effect. When reaching the exchange regions between planes 2/3 and 4/5, mass flows are redistributed, approximately resetting the initial states. An increase in mass flow (see 2.5 A/cm^2-case) results in stronger pressure gradients between adjacent channels, and therefore initially higher deviations from the average mass flow value of around 30 %. An increase in velocities, while keeping a constant channel length, results in the effect that longer flow path would be necessary to flip the values (compare planes 1 and 2).

In summary, mass flow deviations of about 20 to 30 % from the average values, when using constant cross-sectional areas, are found. As the initial states are recovered within the exchange regions between 2/3 and 4/5, the built-up of a simplified model with constant cross-section channels is valid. Effects on the two-phase flow investigations can be more severe, as an under-the-land flow can facilitate the removal of liquid water into the channel. A narrowing of the channel cross-section can lead to combination of liquid water emerging from both channel sides. Due to computational restrictions, the stated effects are not considered in further simulations.

Introduction of Water Source Term

In order to generate a two-phase flow inside a gas channel simulations, water has to be introduced into the channel, in addition to the gas inlet boundary conditions. The majority of literature studies solve the problem of water introduction either via initial patches of droplets [32–34] or implementation of geometrically present pipes [35–37, 51]. Both suffer from problems regarding proper physical representation of the two-phase phenomena during built-up or flexibility regarding inlet position variations. Therefore, a volumetric source term approach is used in the present study.

The water source term is implemented within the first layer of geometrically, GDL-adjacent numerical cells inside the channel model. The addressing function f_1 is exemplary shown on source term position S_1 within the cathode channel geometry in equation (A.1).

$$f_1 = \begin{cases} 1 & \text{if } 1.4\,\text{mm} < x < 1.5\,\text{mm and } y > 0.46\,\text{mm and } z > -4\,\mu\text{m}; \\ 0 & \text{else} \end{cases} \tag{A.1}$$

The orientation of coordinates x, y, z is shown in Figure 5.1.
A definition of the implemented source term is shown in equation (A.2), as the ratio of desired volume source term V_{W} and sum of geometrical volume of the numerical cells V_{mark,f_1} addressed via f_1.

$$\dot{S}_{\mathrm{W1}} = \frac{\dot{V}_{\mathrm{W1}}}{\sum V_{\mathrm{mark},f_1}} \tag{A.2}$$

For the case of an AMR simulation, numerical cells might be altered during meshing process, hence changing the volumetric source term. In order to solve this problem, a second function f_2 is used, defined in equation (A.3).

$$f_2 = f_1 \frac{\dot{V}_{\mathrm{W1}}}{\int_{\mathrm{V}} f_1 \,\mathrm{d}V} \tag{A.3}$$

The water source introduction approach is used analogously for all source terms during VOF investigations.

A.1.2 Evaluation of Dimensionless Quantities

A characterization of the two-phase flow inside anode and cathode gas channel is performed, using dimensionless quantities mentioned in section 3.2. The necessary material and geometrical parameters are given in Table A.1.

Table A.1: Summary of material and geometrical parameters for evaluation of dimensionless numbers.

Parameter	Description	Value		Unit
		Anode	Cathode	
ρ_{g}	Gas density	0.446	1.93	kg/m^3
ρ_{lq}	Liquid water density	969		kg/m^3
μ_{g}	Dyn. viscosity gas	10.6	18.7	µPa s
μ_{lq}	Dyn. viscosity liquid	333		µPa s
σ	Surface tension	0.0636		N/m
A_{x}	Channel cross-sectional area	0.191	0.310	mm^2
d_{h}	Channel hydraulic diameter	0.357	0.508	mm

An evaluation of the two-phase flow dimensionless quantities, shown in Table 3.1 requires the definition of appropriate reference phases. The inertial and viscous forces for the evaluation of Capillary and Weber number are defined for the gas phase, as shown in equation (A.4) and (A.5).

$$Ca = \frac{\mu_{\mathrm{g}}\, u_{\mathrm{g}}}{\sigma} \tag{A.4}$$

$$We = \frac{\rho_{\mathrm{g}}\, u_{\mathrm{g}}^2\, d}{\sigma} \tag{A.5}$$

The Bond number is defined in equation (A.6), whereas the characteristic diameter is the hydraulic channel diameter d_{h}.

$$Bo = \frac{(\rho_{\mathrm{lq}} - \rho_{\mathrm{g}})\, g\, d_{\mathrm{h}}^2}{\sigma} \tag{A.6}$$

In comparison to the Capillary number, which uses the viscous force of the gas, the Laplace number is incorporating the liquid viscous forces through the liquid water viscosity μ_{lq}. The characteristic diameter is the hydraulic diameter of the channel d_{h}. The definition of La is shown in equation (A.7).

$$La = \frac{(\rho_{\mathrm{lq}} - \rho_{\mathrm{g}})\, \sigma\, d_{\mathrm{h}}}{\mu_{\mathrm{lq}}^2} \tag{A.7}$$

The calculation of above mentioned dimensionless quantities is performed, assuming a droplet diameter equivalent to 50% of the hydraulic diameter of the respective channel geometry. The Capillary number is calculated with a gas velocity of $u_{\mathrm{g}} = 50\,\mathrm{m/s}$, corresponding to the maximum value within the parametric study in section 5.8.3. In addition to the maximum velocity case, an additional evaluation of minimum anode and cathode velocities of $u_{\mathrm{g}} = 1.12\,\mathrm{m/s}$ $u_{\mathrm{g}} = 0.722\,\mathrm{m/s}$ is performed to determine Weber number values. The results are summarized in Table A.2 for anode and cathode two-phase gas channel flows. The inverse value of the Laplace number La^{-1} is given to facilitate the evaluation.

Table A.2: Results of dimensionless number evaluation in cathode and anode gas channels.

Parameter	Value	
	Anode	Cathode
$Ca\,(u_{\mathrm{g,max}})$	$8.33 \cdot 10^{-3}$	$1.47 \cdot 10^{-2}$
$We\,(u_{\mathrm{g,min}})$	$1.58 \cdot 10^{-3}$	$4.02 \cdot 10^{-3}$
$We\,(u_{\mathrm{g,max}})$	3.13	19.3
Bo	$4.76 \cdot 10^{-3}$	$9.64 \cdot 10^{-3}$
La^{-1}	$1.01 \cdot 10^{-5}$	$7.10 \cdot 10^{-6}$

The low values of Bo, La^{-1} and Ca show the dominance of surface tension forces to gravitational, internal viscous and inertial forces respectively. The Weber number for low u_{g} is in accordance, whereas an increase in gas velocity results in a rising relevance of viscous forces, indicated by higher values of *We*. Various experimental studies [99–101] identify a critical Weber number of $We_{\mathrm{crit}} \approx 11$ for the breakup of droplets, thus indicating the boundary up to which a droplet will maintain its spherical shape. Therefore, an unstable state is expected for the cathode maximum velocity case.

It should be noted, that the prior investigations are performed for droplets of a fixed size exclusively. Naturally, other flow regimes will show a stronger influence of the mentioned forces in comparison to surface tension and will therefore lead to strong deviations towards the evaluated values. As these phenomena are highly dynamic and very complex in shape, an analytical investigation can not be performed.

A.1.3 Turbulence and Hydraulic Entrance Length

The hydraulic entrance length L_{h} of a channel with constant cross-section can be approximated using equation (A.8) with the definition of the hydraulic diameter, shown in equation (3.10). The definition of *Re* is given in Table 3.1.

$$L_{\mathrm{h}} \approx 0.056\, Re\, d_{\mathrm{h}} \tag{A.8}$$

The gas flow values of the parametric study of cathode and anode are used to evaluate the corresponding hydraulic entrance length values. The results with corresponding conditions are summarized in Table A.3.

All cases, with exception of the cathode case of 50 m/s, are found to be of exclusively laminar nature with $Re < 2300$. The LES model is applied for all VOF cases, due to turbulence which arises as a result of the two-phase flow. Hence, a proper description is ensured, even for the extreme velocity case of the cathode channel. The proper representation via Darcy's law within the simplified model is analyzed in section 7.2. The assumption of fully developed single-phase conditions as an initial solution for all VOF simulations is found to hold true for all anode cases. With a total length of 121.4 mm for the active area anode channels, the majority of regions are expected to exhibit a fully developed profile.

Table A.3: Turbulence and hydraulic entrance length evaluation for single-phase parameter variation cases.

Anode				Cathode			
$\dot{m}_\mathrm{g}$ in mg/s	u_g in m/s	Re in -	L_h in mm	$\dot{m}_\mathrm{g}$ in mg/s	u_g in m/s	Re in -	L_h in mm
0.096	1.122	17	0.34	0.431	0.722	38	1.082
0.478	5.609	84	1.678	2.01	3.368	176	5.01
0.796	9.345	140	2.797	2.278	5.293	277	7.885
1.115	13.09	197	3.935	4.307	7.217	377	10.731
2.23	26.18	394	7.87	10.05	16.84	881	25.077
3.186	37.39	562	11.226	20.62	33.68	1761	50.127
4.26	50	752	15.021	30.61	50	2615	74.435

The redistribution regions within cathode channels (see Figure A.1) lead to a disturbance of the profile. Hence, the hydraulic entrance length has to be evaluated using a length of 70 mm, representing one channel section. High velocity cases are found to show values of >50 mm, therefore indicating a continuous change in velocity profile over the major part of the channel. In addition, the conically alternating channel profiles are neglected, which are likely to result in even stronger disturbance. A profound approximation of the entrance length in cathode channels is therefore not possible by the present means.

The assumption of a fully developed, laminar flow is applied on all VOF cases.

A.1.4 Time-Step Control

An implicit temporal discretization is used within all VOF simulations, which is unconditionally numerically stable. Hence, a CFL-stability criterion is not defined. Nevertheless, a CFL-based time-step control is implemented in order to prevent smeared interfaces, which lead to unphysical behavior as a result of inappropriately large time steps. Time-step controls are defined for AMR and CCMR methodologies separately and explained in the following.

AMR

The CFL-based time-step control function for the AMR approach, shown in equation (A.9), is evaluated at the two-phase interface Ω, whereas a constant time-step of 10^{-7} s is applied for the first 10 time levels to ensure minimal phase interface smearing.

$$\Delta t^{(N)} = \begin{cases} \Delta t^{(N-1)} \cdot 1.1 & \text{if } CFL_{\Omega,\max} < \underline{CFL}; \\ \Delta t^{(N-1)} & \text{if } \underline{CFL} \leq CFL_{\Omega,\max} \leq \overline{CFL}; \\ \Delta t^{(N-1)} \cdot 0.1 & \text{if } CFL_{\Omega,\max} > \overline{CFL}. \end{cases} \tag{A.9}$$

The variables $\Delta t^{(N)}$ and $\Delta t^{(N-1)}$ denote the time steps of level N and $N-1$, $CFL_{\Omega,\max}$ the maximum Courant number at the phase interface and $\underline{CFL}$ and $\overline{CFL}$ the lower and upper bounds of the Courant number specification, defined as 0.45 and 0.5, respectively. The slow increase of the time-step, in combination with a fast decrease, ensures a numerically stable algorithm.

CCMR

The time-step control within the CCMR approach is optimized using an adaptive approach based on a Proportional-Integral-Derivative (PID) controller applied in a specified domain Ω. The domain is defined as the two-phase interface with a criterion of $\Omega = \{\alpha | 0.01 < \alpha < 0.99\}$. Herefore, the difference between targeted CFL number $CFL^*_\Omega = 0.5$ and maximum courant number within the domain at the present time step $CFL_{\Omega,\max}$ is evaluated continuously, as shown in equation (A.10).

$$e(t) = CFL^*_\Omega - CFL_{\Omega,\max}. \tag{A.10}$$

The deviation $e(t)$ is then used within the PID-controller as shown in equation (A.11) to evaluate the controller function $u(t)$.

$$u(t) = K_\mathrm{P}\, e(t) + K_\mathrm{I} \int_0^t e(\tau)\,\mathrm{d}\tau + K_\mathrm{D} \frac{\mathrm{d}e(t)}{\mathrm{d}t}. \tag{A.11}$$

The variables K_P, K_I and K_D denote the factors of the proportionality, integral and derivative part of the controller respectively. A manual optimization of the parameters leads to values of $K_\mathrm{P} = 1$, $K_\mathrm{I} = 2 \cdot 10^{-4}$ 1/s and $K_\mathrm{D} = 10^{-8}$ s. The controller function is finally used with an exponential expression to adjust the next temporal time step $\Delta t^{(N)}$ (see equation (A.12)).

$$\Delta t^{(N)} = \Delta t^{(N-1)} \cdot \exp(u(t)). \tag{A.12}$$

A.1.5 Dynamic Contact Angle Implementation

The implementation of the dynamic contact angle model into STAR-CCM+ is described in further detailed in [65]. A summary is shown in the following.
In order to account for dynamic contact angle effects, the Kistler correlation [102], shown in equation (A.13), is implemented in STAR-CCM+. Advancing θ_a or receding θ_r contact angles are applied, depending on the sign of the Capillary number value, as well as the Hoffman correlation f_Hoff (see equation (A.14)). Therefore, the Kistler contact angle θ_K is applied.

$$\theta_\mathrm{K} = f_\mathrm{Hoff}\left(Ca + \frac{1}{f_\mathrm{Hoff}(\theta_\mathrm{a/r})}\right) \tag{A.13}$$

$$f_\mathrm{Hoff}(\theta_\mathrm{a/r}) = \arccos\left(1 - 2\tanh\left(5.16\left(\frac{\theta_\mathrm{a/r}}{1 + 1.31\,\theta_\mathrm{a/r}^{0.99}}\right)^{0.706}\right)\right) \tag{A.14}$$

The definition of the Capillary number Ca is given in Table 3.1. A range of the equilibrium Capillary number Ca_eq is defined to enhance the stability of the implementation. Herein, the dynamic contact angle θ_K is blended with the equilibrium contact angle θ_e, specified as the corresponding static contact angle θ_s, as a weighted average (see equation (A.15)). The equilibrium Capillary number is kept at a default value of $Ca_\mathrm{eq} = 10^{-3}$.

$$\theta = \begin{cases} f_\mathrm{Blend}\,\theta_\mathrm{e} + (1 - f_\mathrm{Blend})\,\theta_\mathrm{K} & \text{if } -Ca_\mathrm{eq} < Ca < Ca_\mathrm{eq}; \\ \theta_\mathrm{K} & \text{else}. \end{cases} \tag{A.15}$$

The definition of the blending function f_Blend is given in equation (A.16).

$$f_\mathrm{Blend} = \frac{1}{2} + \frac{1}{2}\cos\left(\frac{Ca}{Ca_\mathrm{eq}}\pi\right). \tag{A.16}$$

A.1.6 Analytic Droplet Shape Derivation

An analytic cross-sectional droplet shape is developed to validated the computational VOF results. Therefore, the following assumptions have to be made:

- Spherical droplet:
  For dominant surface tension forces over inertia, viscous and gravitational forces, a spherical shape is generated (see section A.1.2).

- Wetted wall angle:
  The presence of a wetted wall angle is confirmed via evaluation of the Concus-Finn condition. [103]

Figure A.4 shows a 2D-Sketch of the channel corner with present droplet.

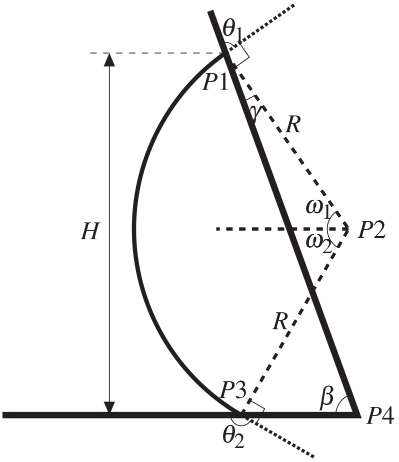

Figure A.4: 2D-Sketch of a spherical droplet inside a channel corner, for the derivation of an analytical solution.

The geometrical relations of the auxiliary angles γ, ω_1 and ω_2 are defined in equations (A.17) to (A.19), as a function of contact angles θ_i and geometric channel corner angle β.

$$\gamma = \frac{\pi}{2} - \theta_1 \tag{A.17}$$

$$\omega_1 = \beta - \gamma = \beta + \theta_1 - \frac{\pi}{2} \tag{A.18}$$

$$\omega_2 = \frac{\pi}{2} - (\pi - \theta_2) = \theta_2 - \frac{\pi}{2} \tag{A.19}$$

A relationship between the droplet height H and the radius R is given in equation (A.20).

$$H = R \cdot \sin\omega_1 + R \cdot \sin\omega_2 \tag{A.20}$$

A combination of prior equations leads to an expression for the radius R, shown in equation (A.21).

$$R = \frac{H}{\sin\omega_1 + \sin\omega_2} = \frac{-H}{\cos(\theta_1 + \beta) + \cos\theta_2} \tag{A.21}$$

Based on the position of the wall corner $P4$, a definition for points $P1$, $P2$ and $P3$ in Figure A.4 can be derived. The Cartesian coordinates of points $I = P1, P2, P3, P4$ are given in vector notation as $\vec{I} = (x_I, y_I)$ in equations (A.22) to (A.24).

$$(x_{P1}, y_{P1}) = (x_{P4}, y_{P4}) + H \cdot (-\cot\beta, 1) \tag{A.22}$$

$$(x_{P2}, y_{P2}) = (x_{P1}, y_{P1}) + R \cdot (\cos\omega_1, -\sin\omega_1) \tag{A.23}$$

$$(x_{P3}, y_{P3}) = (x_{P2}, y_{P2}) - R \cdot (\cos\omega_2, \sin\omega_2) \tag{A.24}$$

Therefore the two-phase interface can be expressed as shown in equation (A.25)

$$\begin{cases} x = & x_{P2} + R \cdot \cos\gamma \\ y = & y_{P2} + R \cdot \sin\gamma \end{cases} \quad \text{with} \quad \pi - \omega_1 < \gamma < \pi + \omega_2 \tag{A.25}$$

A.1.7 Mesh Independence Study

In order to determine the appropriate constant base size for the polyhedral mesh of the CCMR approach, an independence study is performed. Therefore, five polyhedral meshes with different base sizes are used to determine the simulative single-phase pressure drop inside the anode gas channel at various velocities. Combining the expression of Darcy-Weisbach in equation (A.26) with the expression for the Darcy-Weisbach friction factor f_D in equation (A.27) gives an expression to determine an analytic solution of the single-phase pressure drop in laminar pipe flows, as shown in equation (A.28).

$$\frac{\Delta p}{\Delta L} = f_\mathrm{D} \frac{\rho_\mathrm{g}}{2} \frac{u_\mathrm{g}^2}{d_\mathrm{h}} \tag{A.26}$$

$$f_\mathrm{D} = \frac{64}{Re} = \frac{64\,\mu_\mathrm{g}}{\rho_\mathrm{g}\, u_\mathrm{g}\, d_\mathrm{h}} \tag{A.27}$$

$$\Delta p = \frac{32\,\mu_\mathrm{g}}{d_\mathrm{h}^2} u_\mathrm{g}. \tag{A.28}$$

Equation (A.28) is used to generate analytic reference results of the single pressure drop. The simulation results are compared against these and plotted in Figure A.5 as a function of mesh base size and gas velocity.

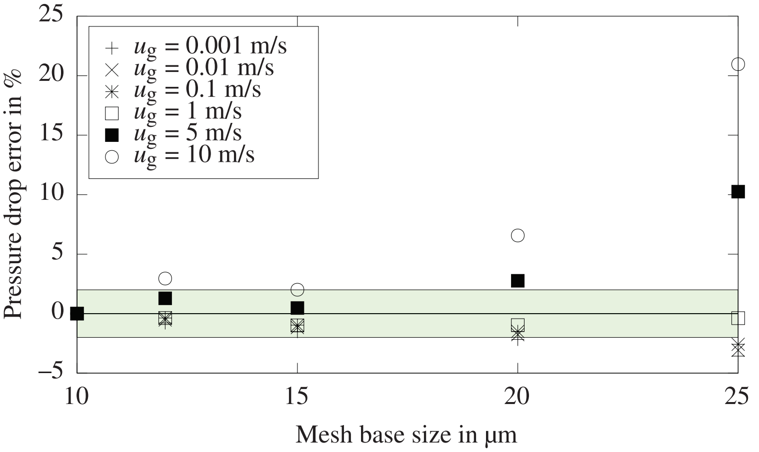

Figure A.5: Mesh independence study for single-phase flow inside anode gas channel.

Disregarding the results for a mesh base size of 12 µm, an increase in pressure drop error, as a function of increasing base sizes can be observed. At the same time, an increase in gas velocities leads to higher errors in pressure drop prediction. The trends are justified through an inferior spatial discretization, giving higher errors, which are overproportionally increasing with higher pressure drops. A deviation of 2 %, indicated by the green region in Figure A.5, is chosen to be of sufficient accuracy, while maintaining an optimal efficiency for the simulations. Therefore, a constant mesh base size of 15 µm is chosen for all CCMR simulations.

A.1.8 Two-phase Pressure Drop Correlation Data

Table A.4: Overview of two-phase simulation cases in anode gas channels. The cases are named accoring to GXXLYY where XX corresponds to the superficial gas velocity and YY to the superficial liquid velocity in m/s.

Source term $\dot{V}_{\mathrm{H_2O}}$ in µL/s	Gas mass flow $\dot{m}_\mathrm{g}$ in mg/s						
	0.096	0.478	0.796	1.115	2.230	3.186	4.260
15				G13L79	G26L79		G50L79
11				G13L58	G26L58		G50L58
8				G13L42	G26L42		G50L42
5	G01L26	G06L26	G09L26	G13L26	G26L26	G37L26	G50L26
4			G09L21	G13L21	G26L21		G50L21
2			G09L10	G13L10	G26L10		G50L10
1	G01L05	G06L05	G09L05	G13L05	G26L05	G37L05	G50L05
0.6			G09L03	G13L03	G26L03		G50L03
0.2	G01L01	G06L01	G09L01	G13L01	G26L01	G37L01	G50L01

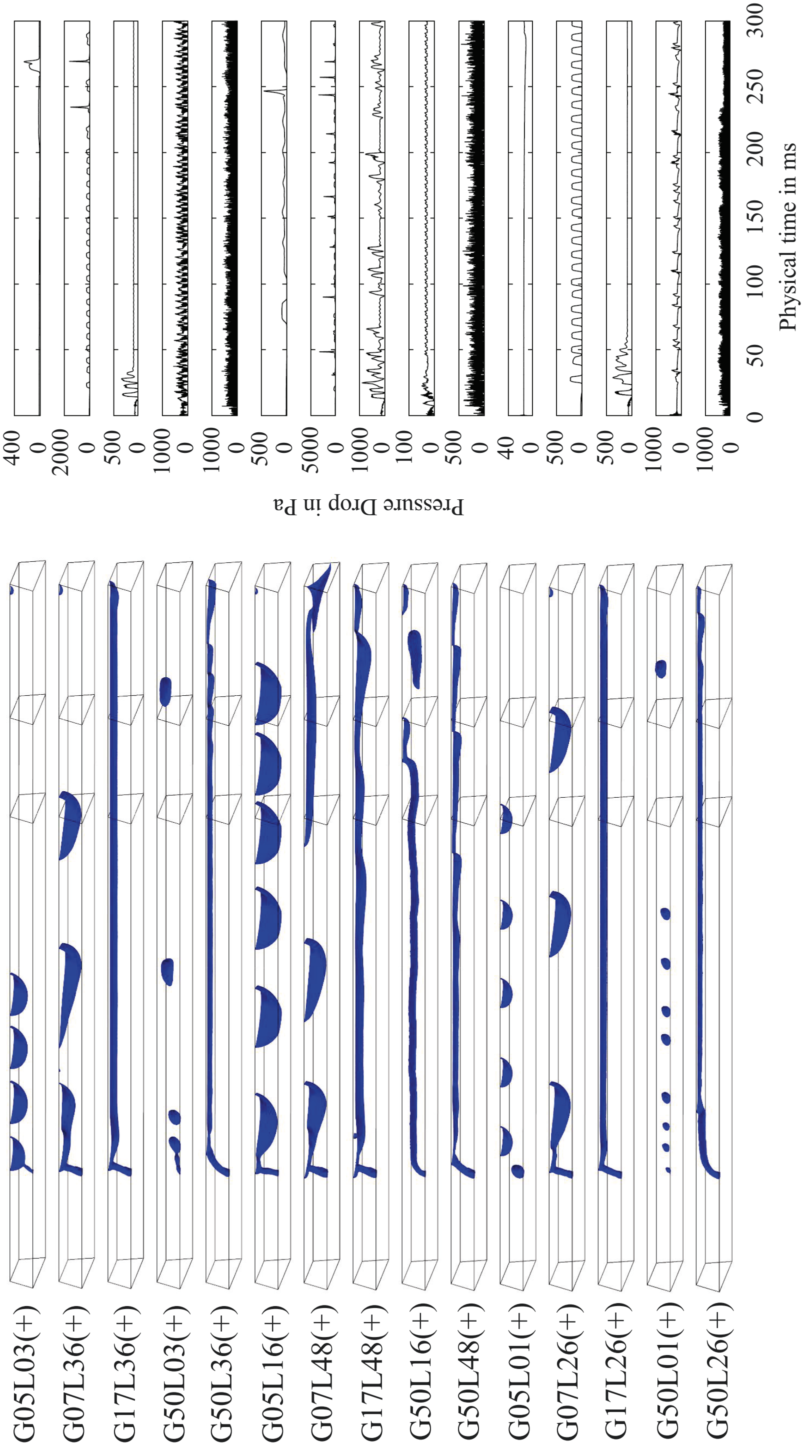

Figure A.6: Results of inlet gas and liquid water velocities variations for cases 16-30 in cathode gas channels. Results show iso-surface plots with $\alpha_{\mathrm{lq}} = 0.5$ (left) for $t = 300\,\mathrm{ms}$, as well as corresponding transient pressure drop signals (right).

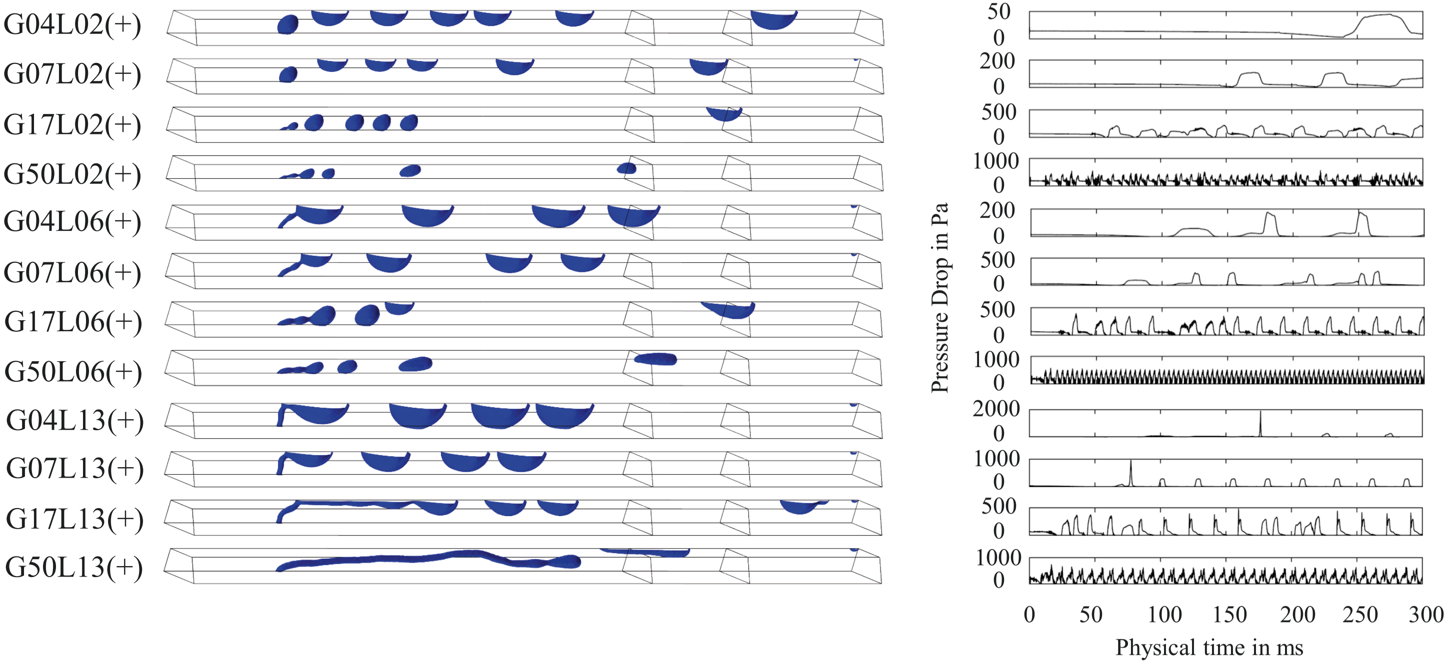

Figure A.7: Results of inlet gas and liquid water velocities variations for cases 31-42 in cathode gas channels. Results show iso-surface plots with $\alpha_{\mathrm{lq}} = 0.5$ (left) for $t = 300\,\mathrm{ms}$, as well as corresponding transient pressure drop signals (right).

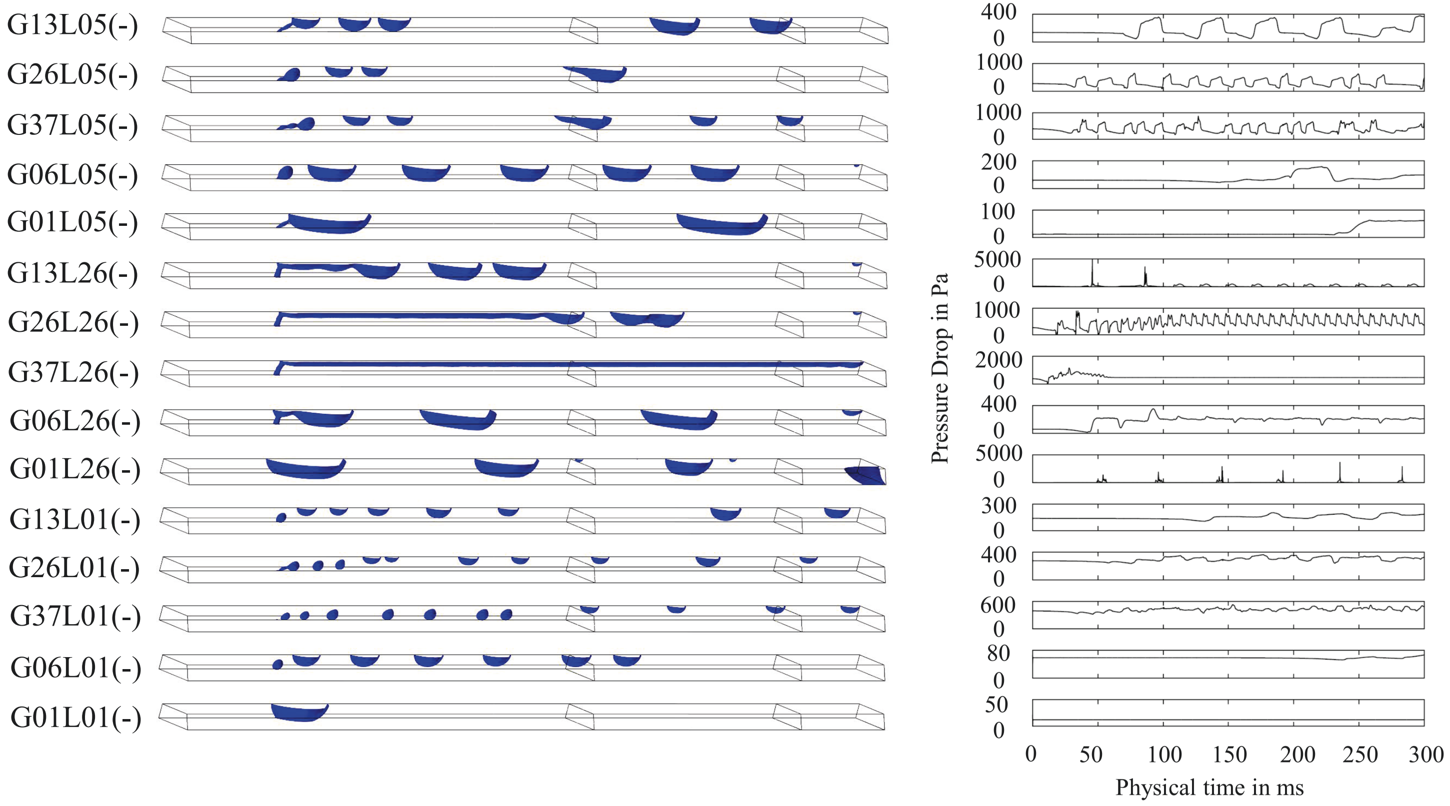

Figure A.8: Results of inlet gas and liquid water velocities variations for cases 1-15 in anode gas channels. Results show iso-surface plots with $\alpha_{\mathrm{lq}} = 0.5$ (left) for $t = 300\,\mathrm{ms}$, as well as corresponding transient pressure drop signals (right).

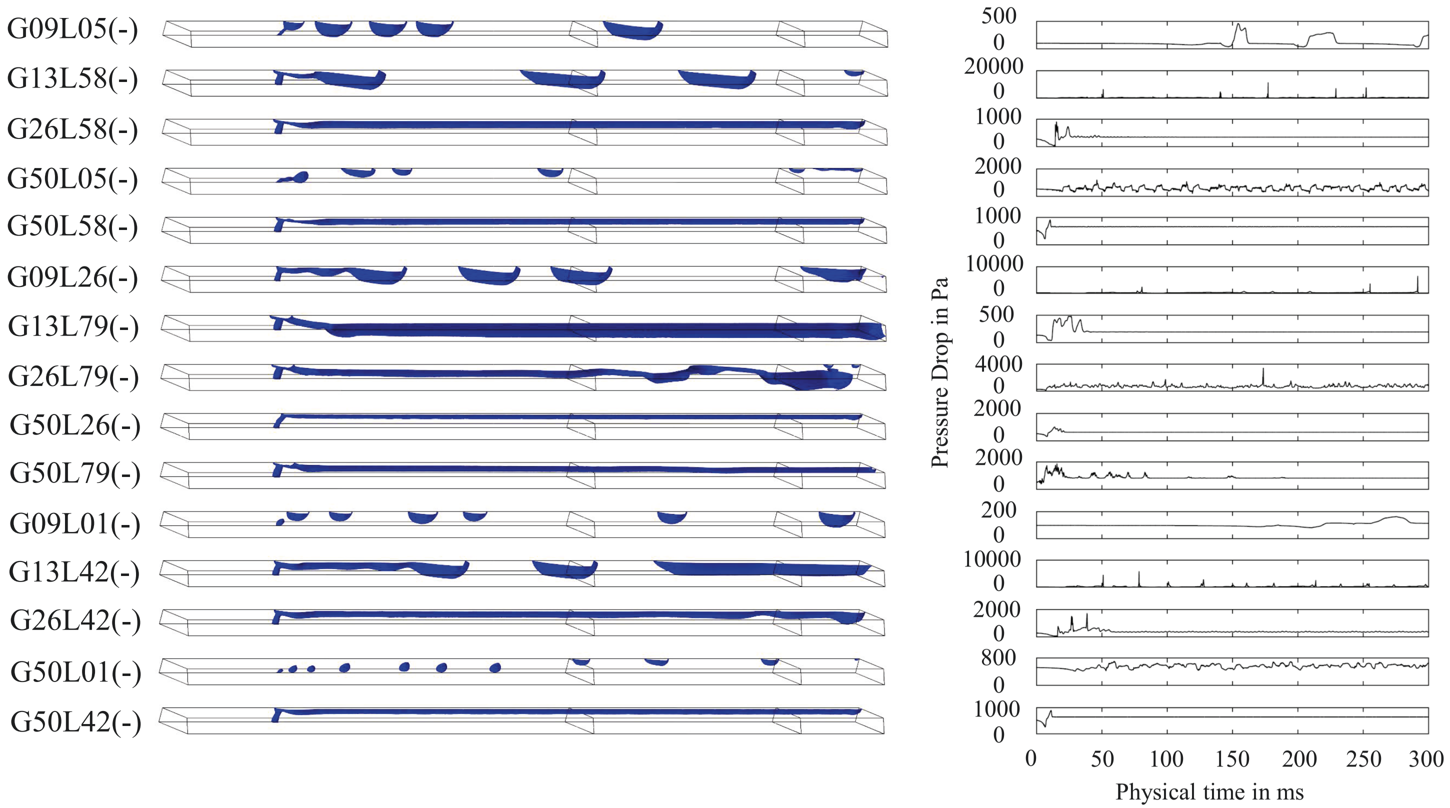

Figure A.9: Results of inlet gas and liquid water velocities variations for cases 16-30 in anode gas channels. Results show iso-surface plots with $\alpha_{\mathrm{lq}} = 0.5$ (left) for $t = 300\,\mathrm{ms}$, as well as corresponding transient pressure drop signals (right).

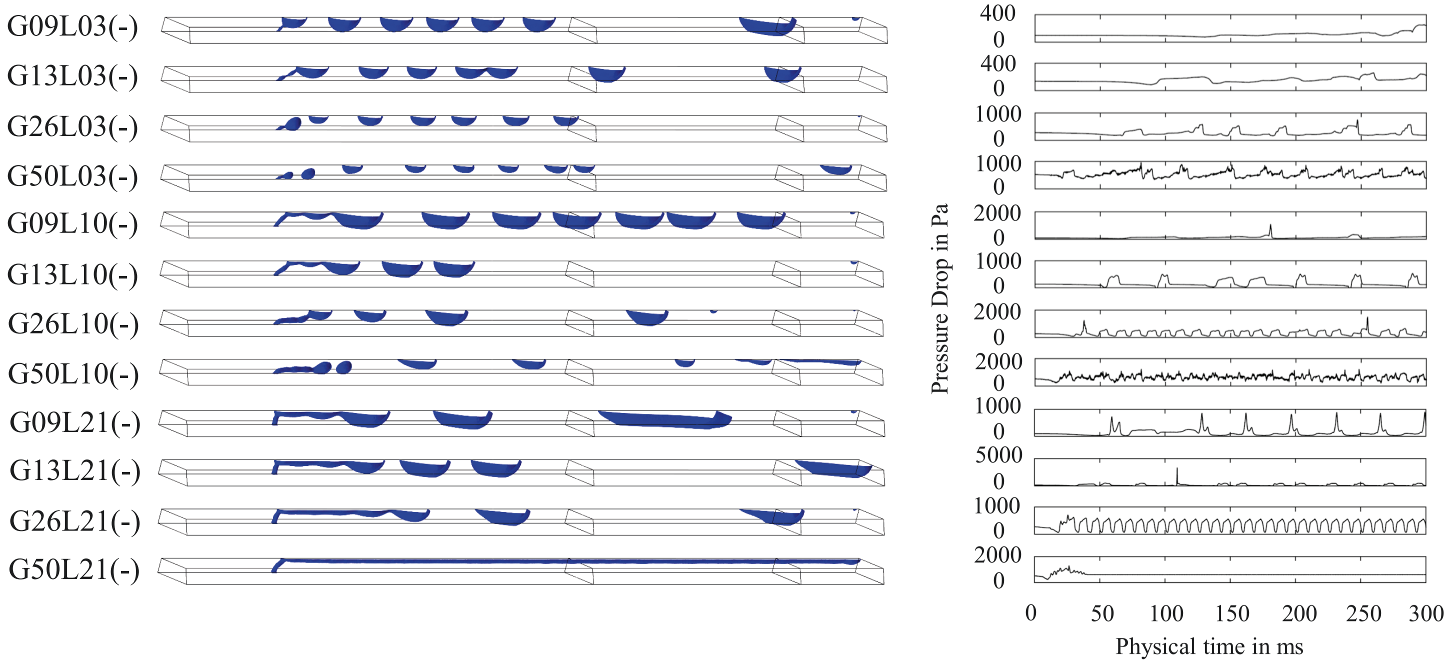

Figure A.10: Results of inlet gas and liquid water velocities variations for cases 31-42 in anode gas channels. Results show iso-surface plots with $\alpha_{\mathrm{lq}} = 0.5$ (left) for $t = 300\,\mathrm{ms}$, as well as corresponding transient pressure drop signals (right).

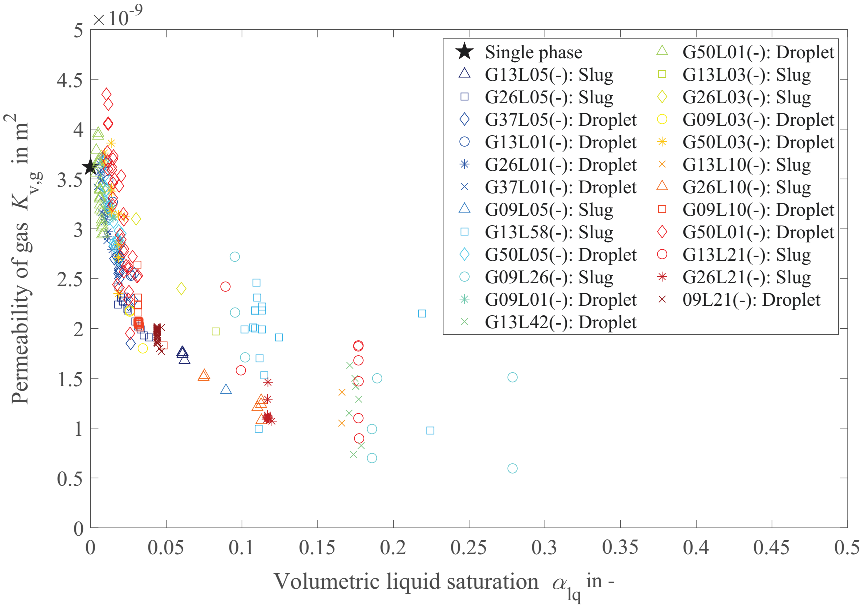

Figure A.11: Raw data of anode gas channel permeabilities from selected cases.

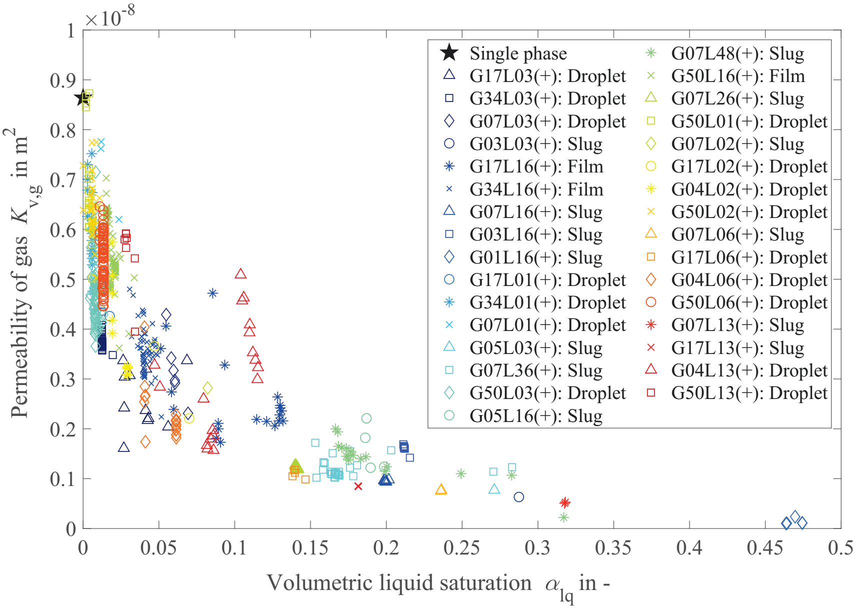

Figure A.12: Raw data of cathode gas channel permeabilities from selected cases.

A.2 Single Cell Simulations and Experiments

The present chapter gives additional information on PEMFC single cell simulations and experiments, including the acquisition of experimental parameters, model and mesh independency investigations, as well as various results.

A.2.1 Simulation Parameters

The major part of the necessary material and transport parameters is obtained via simulations inside reconstructed domains of substrate and MPL. [104] A substrate reconstruction based on μ-CT measurements is performed, leading to a representative volume (RV) of $0.2\times0.6\times10\,\mathrm{mm}^3$ with a voxel size of $2.28\,\mu\mathrm{m}$ (see left red cuboid in Figure A.13). As for the MPL, a reconstruction using FIB/SEM-tomographie scans is carried out leading to a RV of $4\times5\times1\cdot10^{-3}\mathrm{mm}^3$ and a voxel size of approximately 8.5 nm (see right red cuboid in Figure A.13). The reconstructions are performed in a binary matter, distinguishing between void pore space and bulk material under respective resolution.

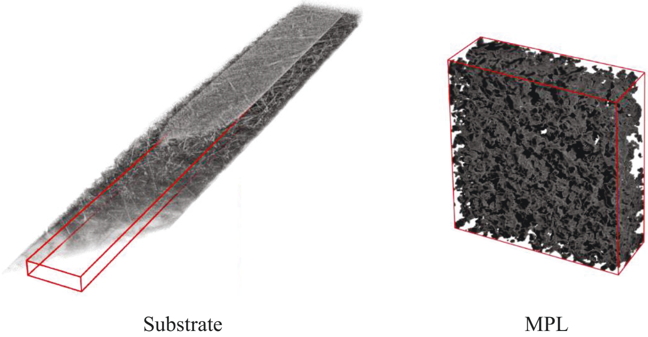

Figure A.13: Representative Volumes (RV) of substrate and MPL, produced via µ-CT and FIB/SEM-tomographie scan reconstructions.

Hereby the following parameters are obtained:

- Porosity ε
- Gas permeability K_i
- Diffusion coefficient D_i
- Electrical conduction coefficient σ_i

- Thermal conduction coefficient λ_i
- Leverett function $J(\alpha)$

Due to limited capabilities of the multi-phase mixture model, regarding anisotropic permeability values, isotropic values are chosen for all porous media. All parameters are summarized in Table A.5. As for the membrane and CL parameters, either experimental values are used or the values were adjusted iteratively.

Table A.5: Summary of material parameters used in PEMFC simulations.

Parameter	Description	Value
GDL		
ε	Porosity	0.688
τ_ε	Tortuosity	1
$K_{\mathrm{v,IP/TP}}$	Viscous permeability (in-plane/through-plane)	$1 \cdot 10^{-11}\,\mathrm{m}^2$
$\sigma_{\mathrm{e,IP/TP}}$	Electrical conductivity (in-plane/through plane)	2000 S/m
$\lambda_{\mathrm{th,IP}}$	Thermal conductivity (in-plane)	9.4 W/(m K)
$\lambda_{\mathrm{th,TP}}$	Thermal conductivity (through-plane)	5.7 W/(m K)
PEM		
EW	Equivalent weight	872 kg/kmol
$\rho_{\mathrm{th,PEM}}$	Density	$2027\,\mathrm{kg/m}^3$
c_{p}	Specific heat	903 J/(kg K)
$\lambda_{\mathrm{th,PEM}}$	Thermal conductivity	0.445 W/(m K)
$\beta_{i,\mathrm{a}}$	Liquid water/Water vapor absorption rate	$1 \cdot 10^{-5}\,\mathrm{m/s}$
$\beta_{i,\mathrm{d}}$	Liquid water/Water vapor desorption rate	$1 \cdot 10^{-5}\,\mathrm{m/s}$
CL		
χ_{a}	Transfer coefficient of anodic reaction	0.5
χ_{c}	Transfer coefficient of cathodic reaction	0.5
$j^*_{0,\mathrm{a}}$	Anode reference exchange current density	$19080\,\mathrm{A/m}^2$
$j^*_{0,\mathrm{c}}$	Cathode reference exchange current density	$300\,\mathrm{A/m}^2$
$j^*_{0,\mathrm{c,lq}}$	Cathode reference exchange current density liquid	$300\,\mathrm{A/m}^2$
BPP		
ρ_{BPP}	Density	$8055\,\mathrm{kg/m}^3$
$c_{\mathrm{p,BPP}}$	Specific heat	480 J/(kg K)
$\lambda_{\mathrm{th,BPP}}$	Thermal conductivity	15.1 W/(m K)
$\sigma_{\mathrm{e,BPP}}$	Electrical conductivity	$3.87 \cdot 10^7\,\mathrm{S/m}$

A.2.2 Turbulence Investigation in Flow Field Gas Channels

In order to investigate the turbulence inside anode and cathode flow field gas channels, single-phase flow field simulations are carried out. Two meshes with different turbulence models are used. The LES simulations are carried out with a polyhedral mesh of 50 µm base size, while the k-ε turbulence model is applied in combination with the mostly structured mesh, introduced in section 6.2. The flow field channels are exclusively activated in both approaches. Operating conditions, corresponding to a λ_i of 4 at a current density of 2.5 A/cm^2 are applied, representing an extreme case.

Figure A.14 shows the velocity profile of a cathode flow field cut-section plane, simulated, using the LES approach with unstructured polyhedral cells. Results in section A for a simulation with the k-ε approach and the structured mesh are given in addition.

The cathode gas channels exhibit lower velocities with values as high as 47.1 m/s, found in the vicinity of the inlet regions. While gas velocities are not sufficient to exceed the critical Reynolds number for a turbulent flow, a transitional behavior is still observed as a result of a complex inlet region.

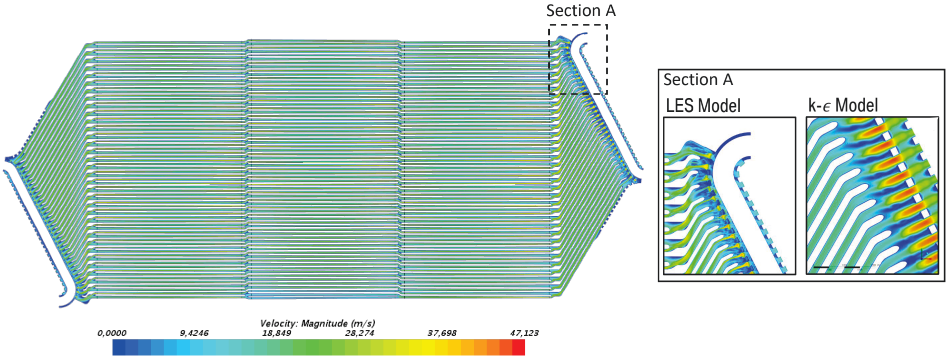

Figure A.14: Velocity profile of cathode flow field cut section plane with indication of turbulence, using an LES and $k-\varepsilon$ approach with inlet air mass flows, corresponding to $\lambda_C = 4$ at $j_{avg} = 2.5$ A/cm^2.

The corresponding velocity distribution inside anode gas channels is given in Figure A.15. Maximum gas velocities of 162.3 m/s are found to be present in the redirection regions of the side collectors. The shape of the velocity profile in section A indicates differences when comparing both approaches. The results clearly show the occurrence of turbulence as a result of the total mass flow being recombined inside one side collector channel. The additional redirection leads to the highly anisotropic nature of the turbulence. It becomes apparent, that a RANS approach is not sufficient to resolve these effects properly. As a result, pressure drop values are overestimated as priory shown. The LES approach is found to represent the processes with higher accuracy. Due to the high amount of numerical cells necessary for this approach, as well as the transient nature of the LES approach, a feasible use inside multiphysics PEMFC simulations is not found to be present.

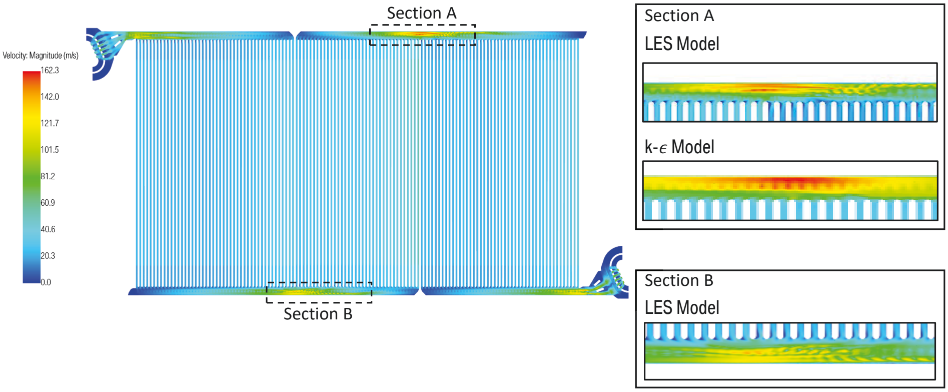

Figure A.15: Velocity profile of anode flow field cut section plane with indication of turbulence, using an LES and k-ε approach with inlet hydrogen mass flows, corresponding to $\lambda_A = 4$ at $j_{avg} = 2.5$ A/cm^2.

As a result of geometric complexity, an additional mesh independence study is performed for the anode flow field, while tracking the pressure drop from in- to outlet. Various meshes and models are used, summarized in Figure A.16.

Mesher	Polyhedral	Hybrid	Hybrid	Hybrid + LMR*	Polyhedral	Hybrid + LMR	Structured	Experiment P_{in} = 2.60 bar P_{out} = 2.30 bar
Base Size in µm	50	400	400	400 + 40	50	400 + 40	-	
Time Solver	Steady	Steady	Implicit Unsteady	Implicit Unsteady	Implicit Unsteady	Implicit Unsteady	Steady	
Equation of State	Constant Density	Constant Density	Constant Density	Constant Density	Constant Density	Ideal Gas	Ideal Gas	
Turbulence Model	RANS (k-epsilon)	RANS (k-epsilon)	LES (WALE Subgrid)	LES (WALE Subgrid)	LES (WALE Subgrid)	LES (WALE Subgrid)	RANS (k-epsilon)	
Error (ΔP)	52.8%	17.3%	25.9%	6.7%	6.0%	7.9%	26.0%	

Figure A.16: Mesh independence study for anode flow field single phase pressure drop.

A polyhedral mesh with a base size of 50 µm, in combination with a $k-\varepsilon$ turbulence approach and assumption of constant density leads to insufficient accuracy. Hence, hybrid approaches are chosen, using structured meshes for the straight channels inside the active area, which lead to an improvement in accuracy while retaining a lower cell count. In general, an LES approach leads to a superior representation of turbulence, resulting in a further increase in accuracy. The constant polyhedral mesh with a LES approach, shows the lowest error in comparison to the experimental results with 6.0%. Due to the high computational effort accompanied with unstructured meshes, a structured mesh is chosen for the detailed cell (see Figure 6.2). The structured cell simulation leads to pressure drop deviation of 26% in comparison to the experimental results.

A.2.3 Detailed and Experimental Single Cell Results

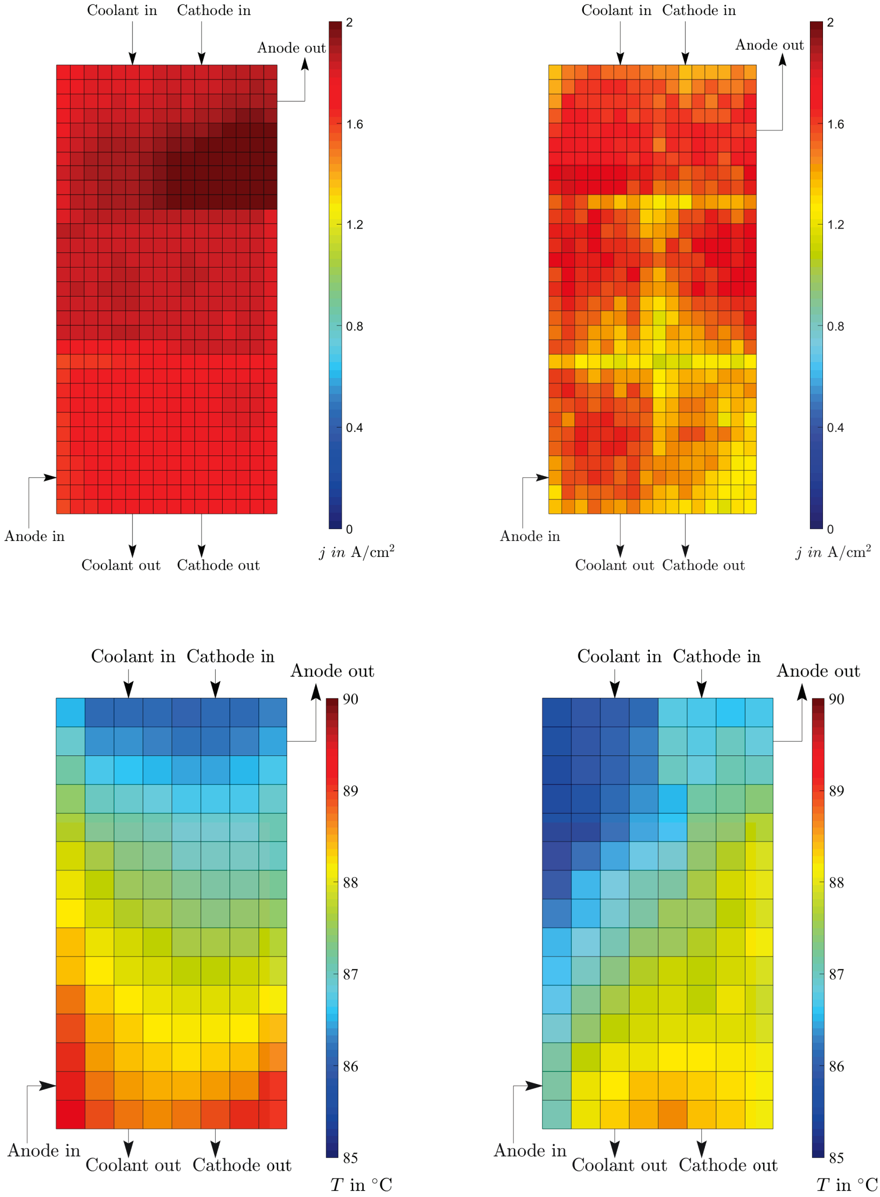

(a) Detailed cell results with $j_{\text{avg}} = 1.67\,\text{A/cm}^2$.

(b) Experimental results with $j_{\text{avg}} = 1.5\,\text{A/cm}^2$.

Figure A.17: Current density (top) and temperature (bottom) distribution of detailed cell simulation (left) and experimental cell (right) results of ID3 at 0.614 V.

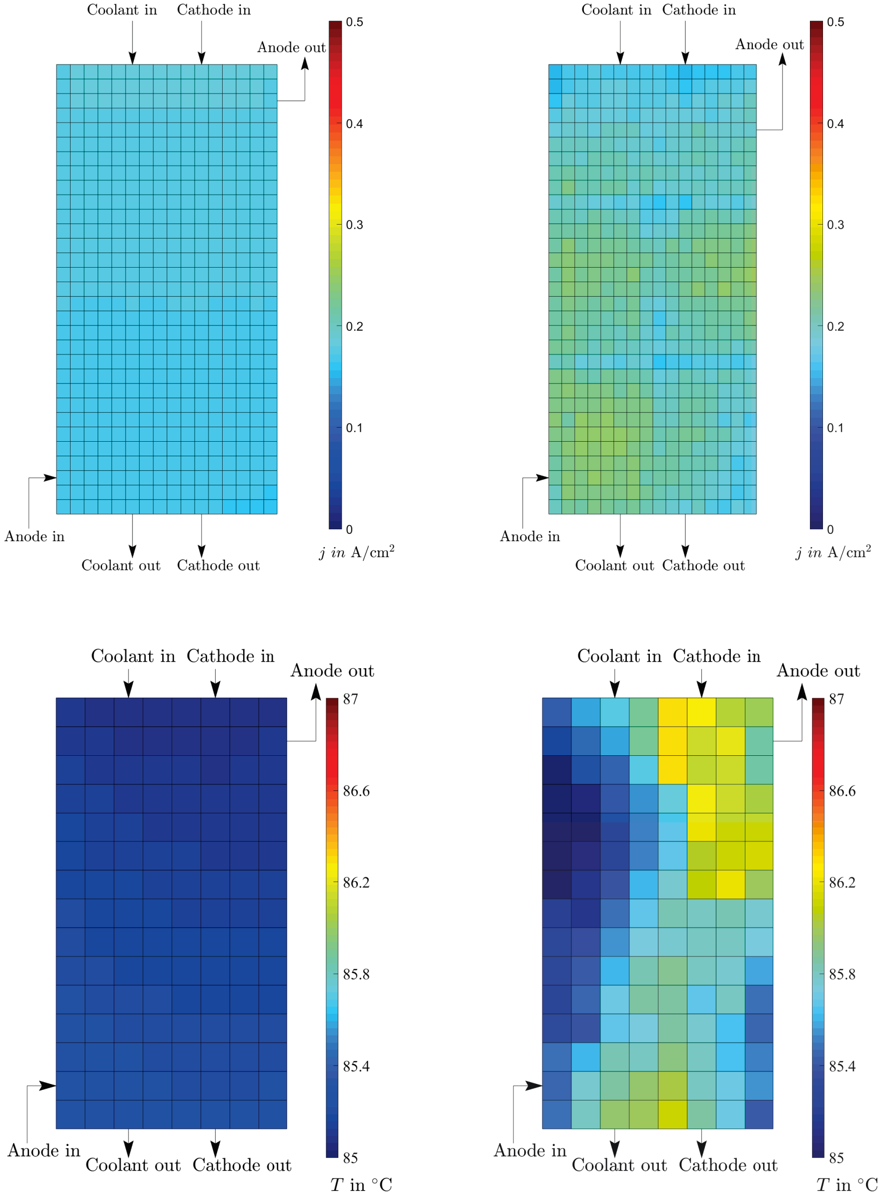

(a) Detailed cell results with $j_{\text{avg}} = 0.16\,\text{A/cm}^2$.

(b) Experimental results with $j_{\text{avg}} = 0.2\,\text{A/cm}^2$.

Figure A.18: Current density (top) and temperature (bottom) distribution of detailed cell simulation (left) and experimental cell (right) results of ID3 at 0.819 V.

Investigation of Uneven Coolant Inflow

The uneven coolant inflow is investigated, using the detailed single cell PEMFC case of ID3 at 0.686 V. An extreme maldistribution is analyzed via an introduction of the majority of the inlet mass flow through two channels. The resulting temperature distribution is shown in Figure A.19. A well distributed temperature profile with an increase of around 3 °C is observed. Due to the interconnection of channels inside the distributor of the coolant flow field uneven inflow conditions can be counter be compensated. It becomes evident, that an uneven inflow cannot explain the malidistribution in temperature, as seen within all experiments.

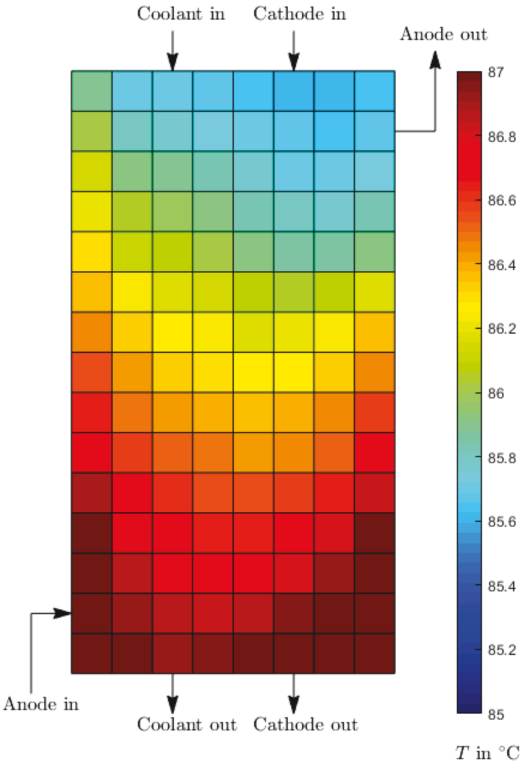

Figure A.19: Temperature profile of uneven coolant introduction simulation of ID3 at 0.686 V.

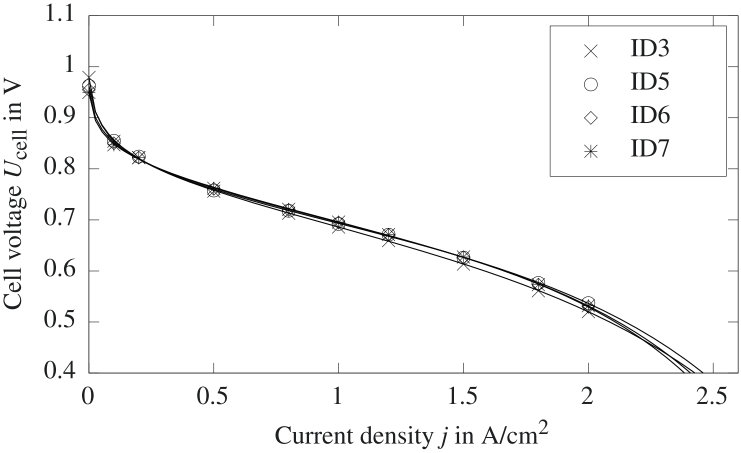

Figure A.20: Experimental polarization curves for relative humidity variation at ID3, ID5, ID6 and ID7.

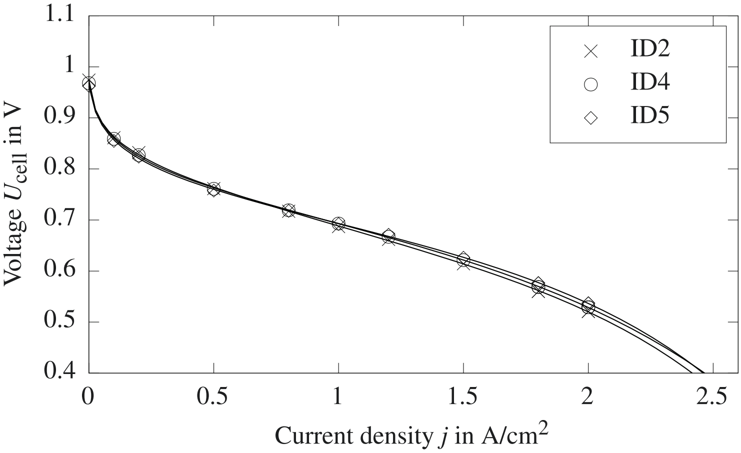

Figure A.21: Experimental polarization curves for temperature variation at ID2, ID4 and ID5.

A.3 Single Cell Simplification

The present chapter gives additional information on PEMFC single cell simplification, including modeling settings, as well as additional results.

A.3.1 Simplification Settings

Table A.6: Through-plane layer thicknesses.

<table>
<tr><th>Layer</th><th>Detailed cell
Thickness in mm</th><th>Simplified cell
Thickness in mm</th></tr>
<tr><td>Cathode BPP</td><td>0.065</td><td>-</td></tr>
<tr><td>Cathode GC</td><td>0.38</td><td>0.173</td></tr>
<tr><td>Cathode GDL Intrusion</td><td>0.02</td><td>-</td></tr>
<tr><td>Cathode GDL (excl. MPL)</td><td colspan="2">0.115</td></tr>
<tr><td>Cathode MPL</td><td colspan="2">0.04</td></tr>
<tr><td>Cathode CL</td><td colspan="2">0.01</td></tr>
<tr><td>PEM</td><td colspan="2">0.015</td></tr>
<tr><td>Anode CL</td><td colspan="2">0.01</td></tr>
<tr><td>Anode MPL</td><td colspan="2">0.04</td></tr>
<tr><td>Anode GDL (excl. MPL)</td><td colspan="2">0.115</td></tr>
<tr><td>Anode GDL Intrusion</td><td>0.02</td><td>-</td></tr>
<tr><td>Anode GC</td><td>0.23</td><td>0.113</td></tr>
<tr><td>Anode BPP</td><td>0.065</td><td>-</td></tr>
<tr><td>Compensation</td><td>-</td><td>0.494</td></tr>
<tr><td>Cell pitch</td><td colspan="2">1.125</td></tr>
</table>

A.3.2 Detailed and Simplified Single Cell Results

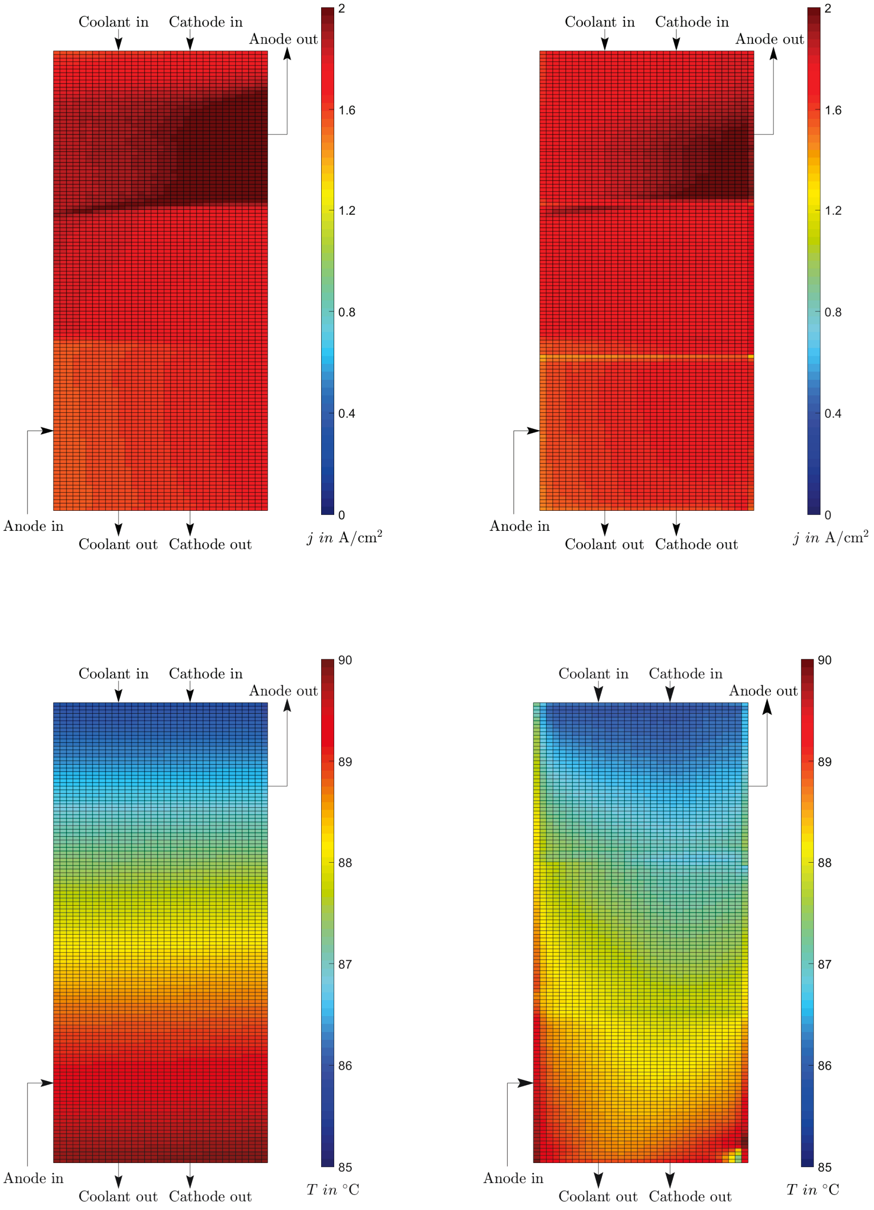

(a) Simplified cell simulation.

(b) Detailed cell results with $j_{\mathrm{avg}} = 1.67\,\mathrm{A/cm^2}$.

Figure A.22: Current density (top) and temperature (bottom) distribution of simplified (left) and detailed cell simulation (right) results of ID3 at 0.614 V.

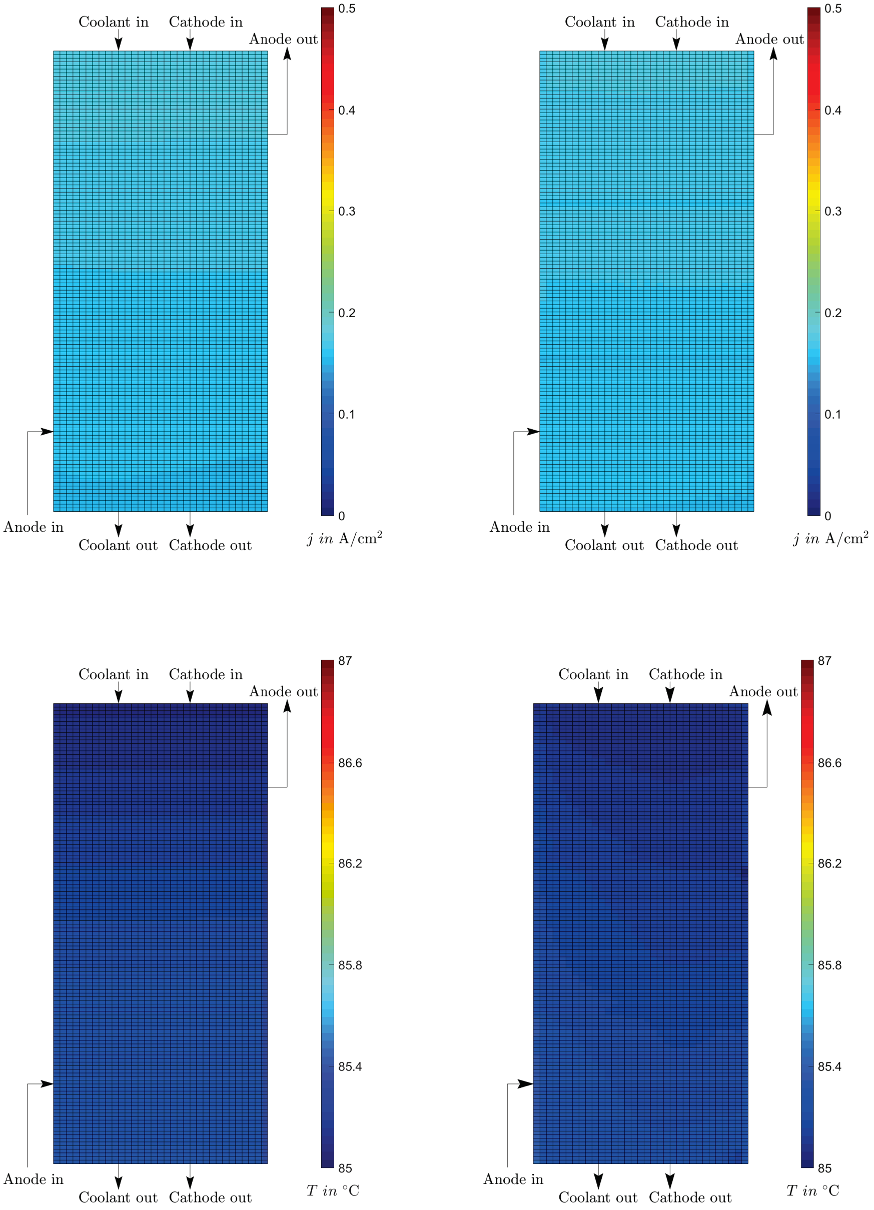

(a) Simplified cell simulation. **(b)** Detailed cell results with $j_{\text{avg}} = 0.16\,\text{A/cm}^2$.

Figure A.23: Current density (top) and temperature (bottom) distribution of simplified (left) and detailed cell simulation (right) results of ID3 at 0.819 V.

A.4 60-cell Stack Simulations and Experiments

The following section provides additional results on 60-cell stack simulation and experiments.

A.4.1 60-cell Stack Simulation Results

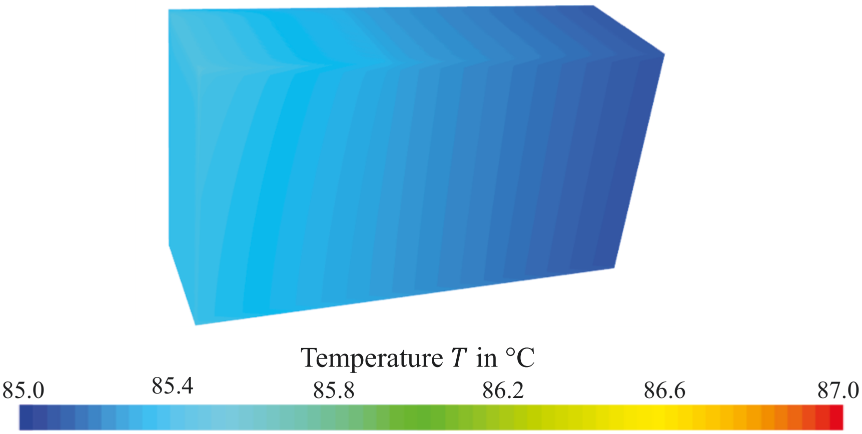

Figure A.24: Temperature distribution in coolant regions of 60-cell stack for ID3, corresponding to a voltage of 49.1 V.

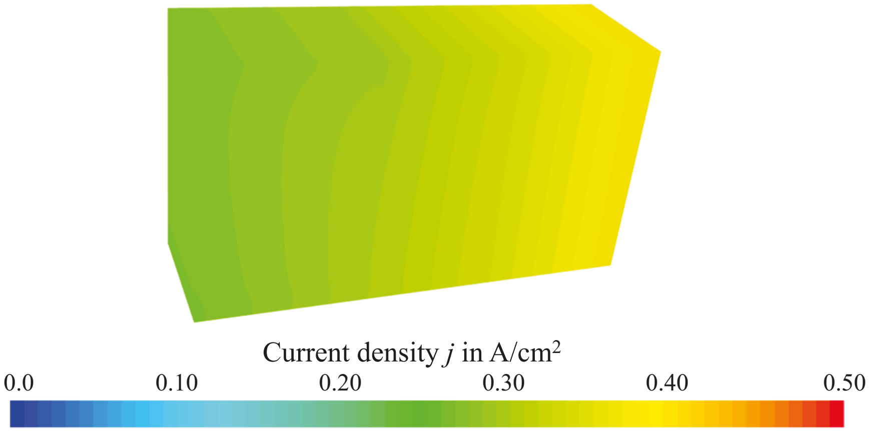

Figure A.25: Current density distribution on anode and cathode reaction planes of 60-cell stack for ID3, corresponding to a voltage of 49.1 V.

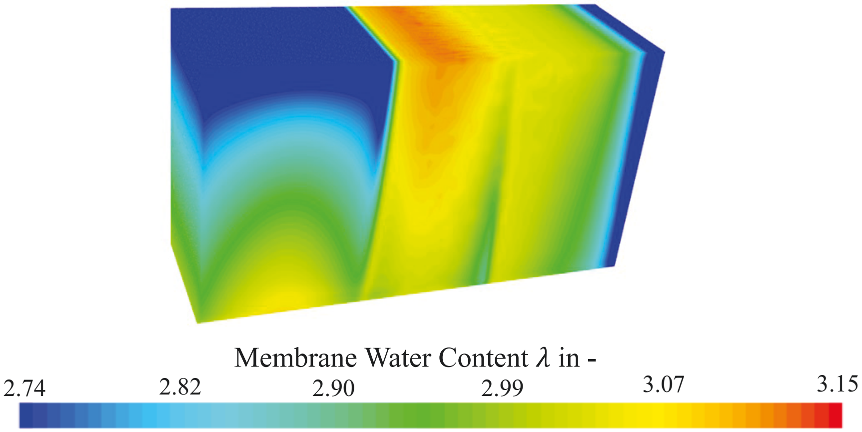

Figure A.26: Membrane water content distribution on anode CL-MEM interface of 60-cell stack for ID3 case, corresponding to a voltage of 49.1 V.

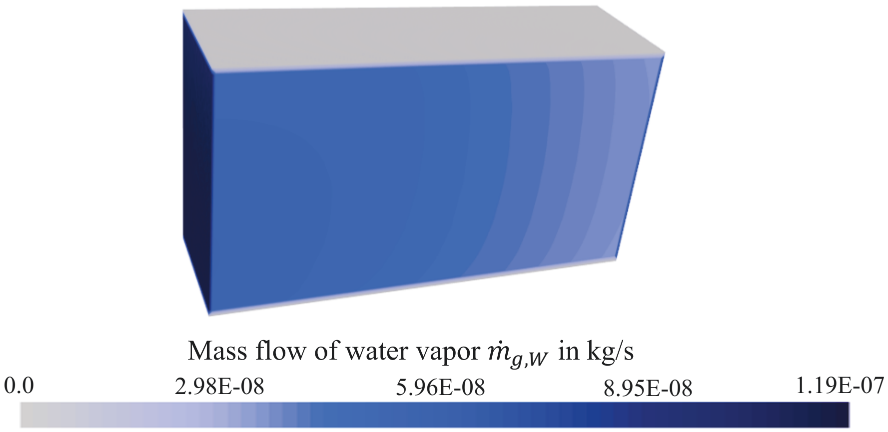

(a) Cathode gas channels.

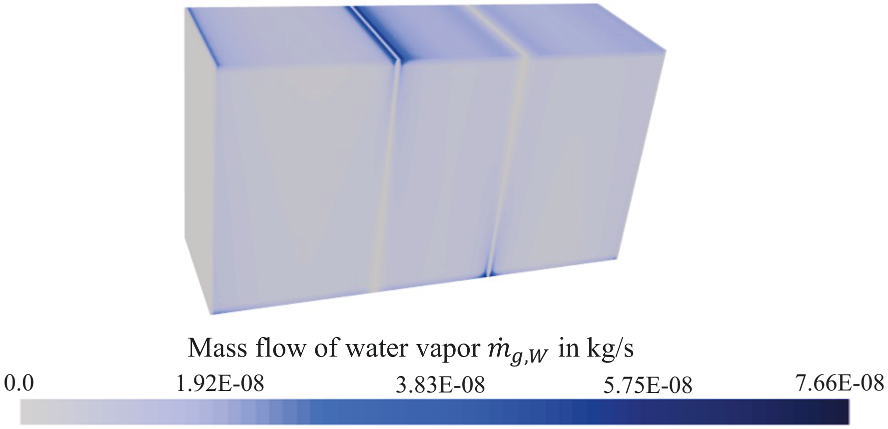

(b) Anode gas channels.

Figure A.27: Mass flow distribution of water vapor in cathode and anode gas channels of 60-cell stack for ID3 case, corresponding to a voltage of 49.1 V.

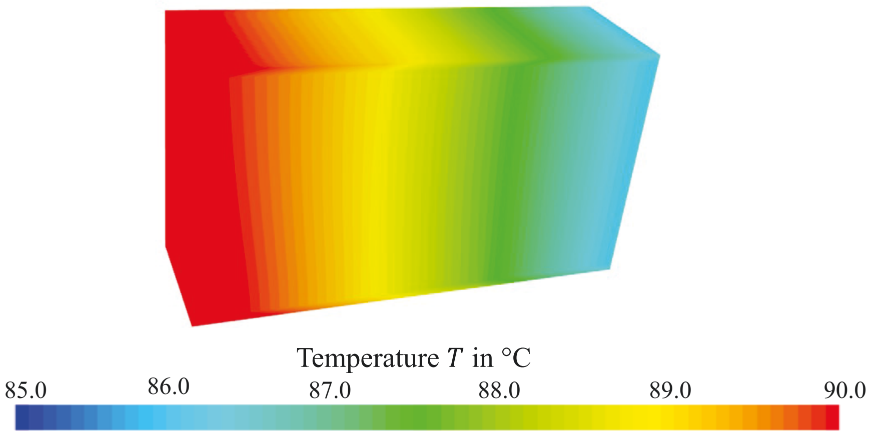

Figure A.28: Temperature distribution in coolant regions of 60-cell stack for ID3, corresponding to a voltage of 36.8 V.

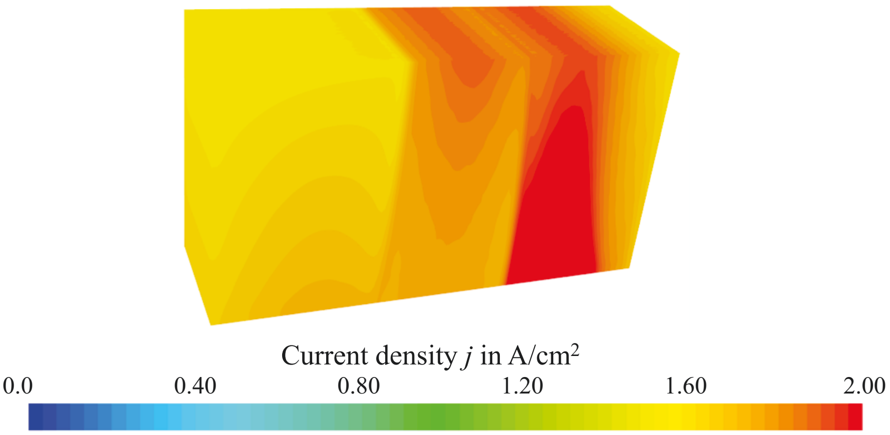

Figure A.29: Current density distribution on anode and cathode reaction planes of 60-cell stack for ID3, corresponding to a voltage of 36.8 V.

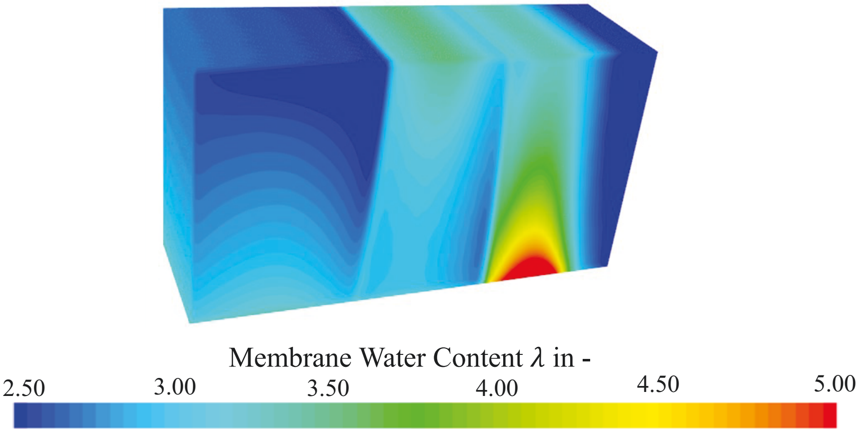

Figure A.30: Membrane water content distribution on anode CL-MEM interface of 60-cell stack for ID3 case, corresponding to a voltage of 36.8 V.

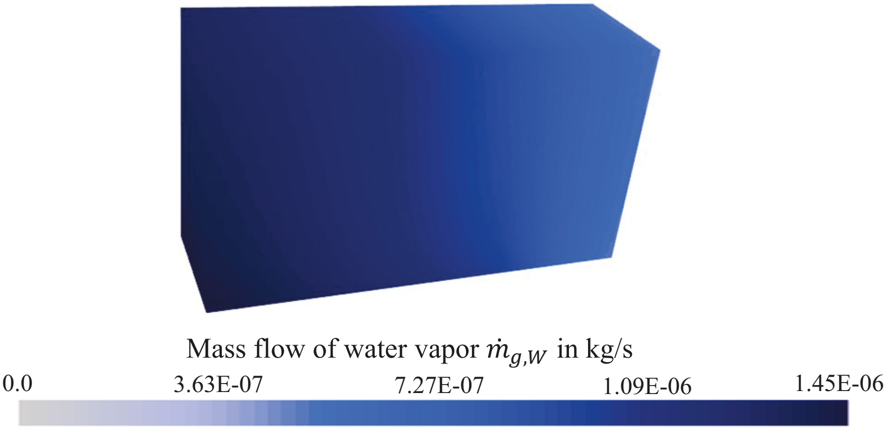

(a) Cathode gas channels.

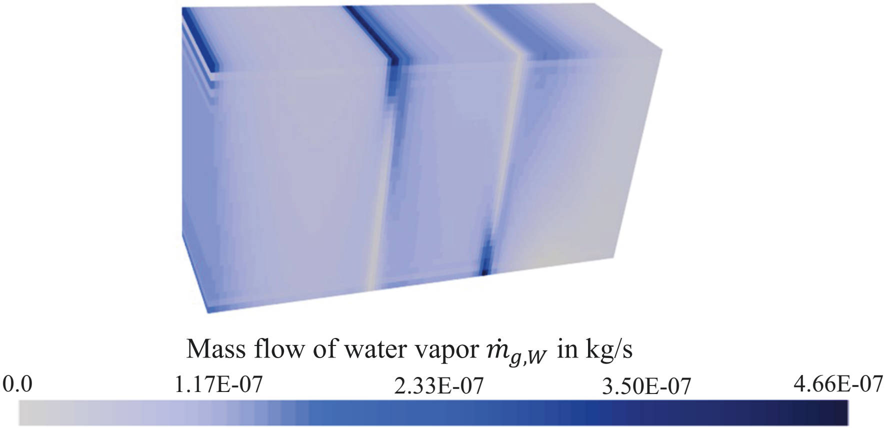

(b) Anode gas channels.

Figure A.31: Mass flow distribution of water vapor in cathode and anode gas channels of 60-cell stack for ID3 case, corresponding to a voltage of 36.8 V.

A.4.2 60-cell Stack Experimental Results

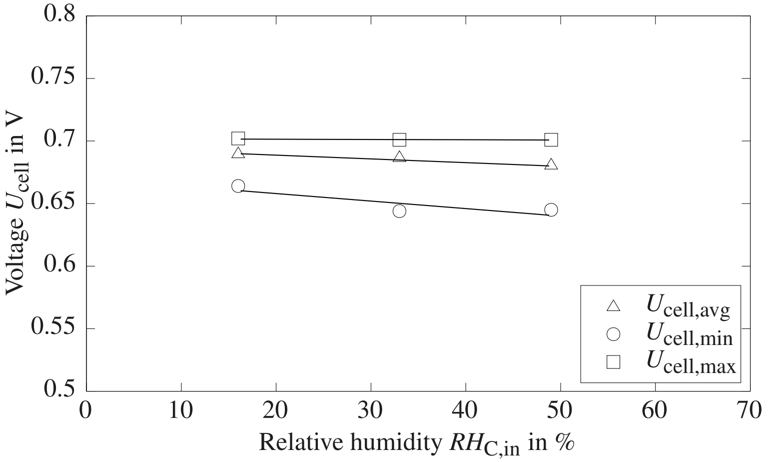

Figure A.32: Minimal, maximal and average cell voltages of 60-cell stack for cathode inlet *RH* variation.

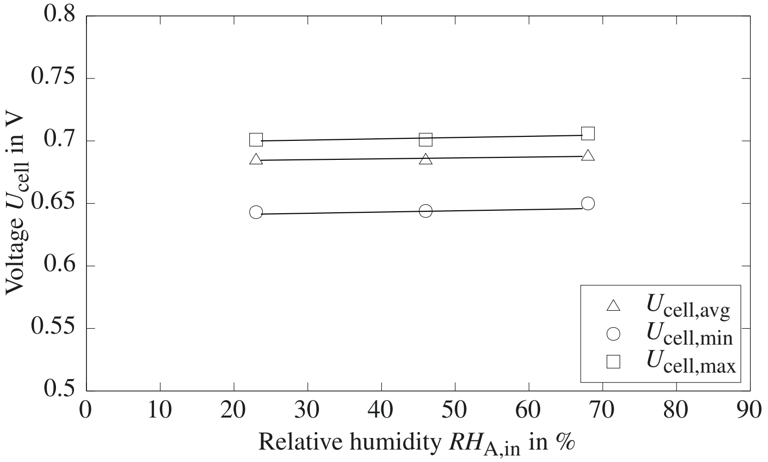

Figure A.33: Minimal, maximal and average cell voltages of 60-cell stack for anode inlet *RH* variation.

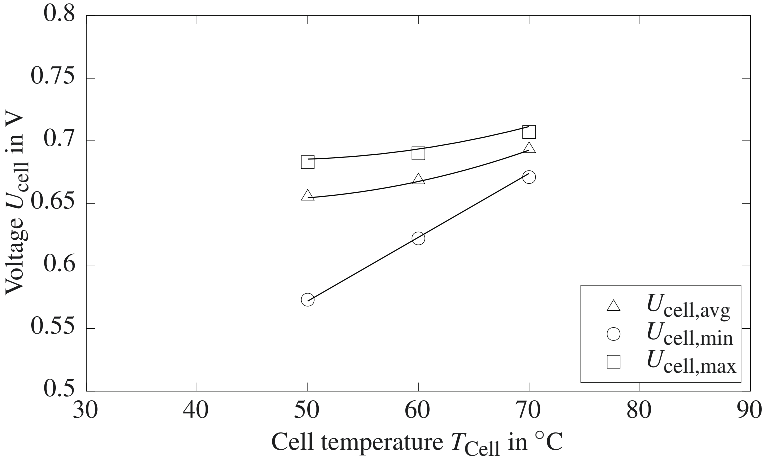

Figure A.34: Minimal, maximal and average cell voltages of 60-cell stack for cell temperature variation.

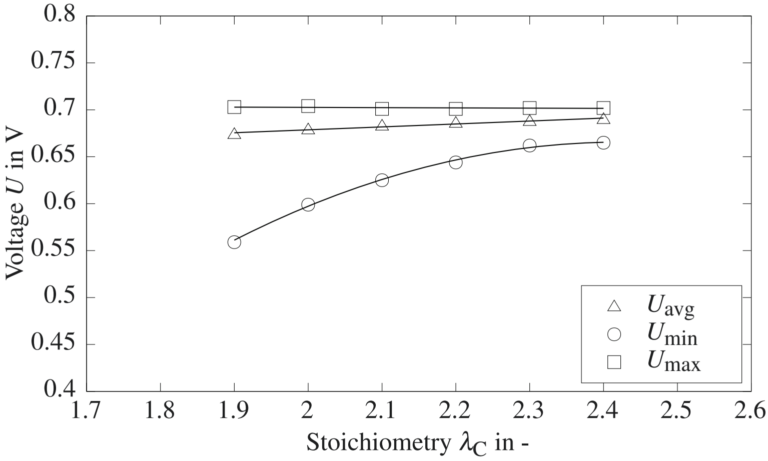

Figure A.35: Minimal, maximal and average cell voltages of 60-cell stack for cathode stoichiometry variation.

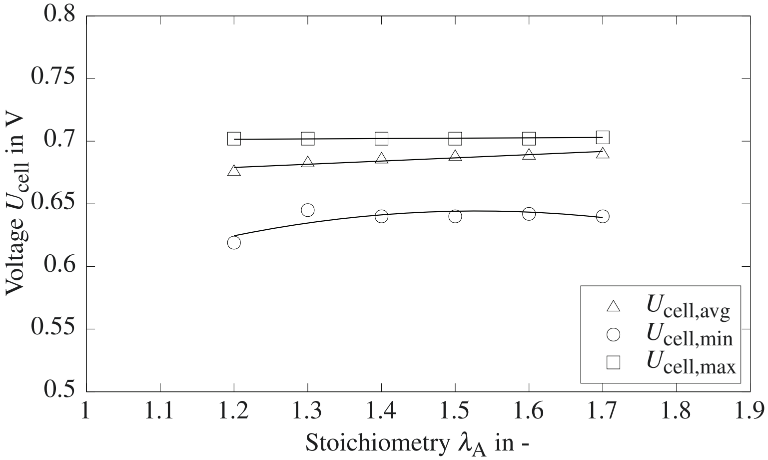

Figure A.36: Minimal, maximal and average cell voltages of 60-cell stack for anode stoichiometry variation.

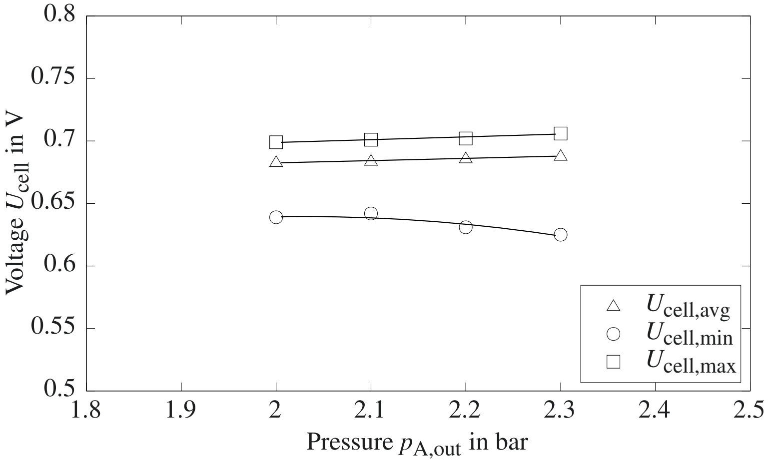

Figure A.37: Minimal, maximal and average cell voltages of 60-cell stack for cathode outlet pressure variation.

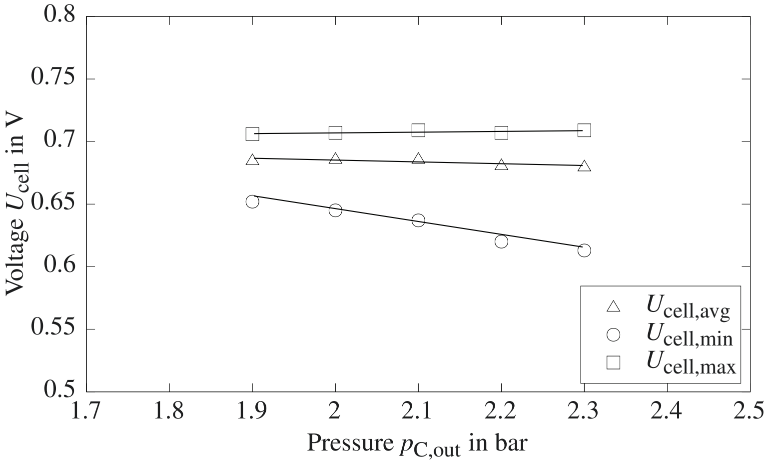

Figure A.38: Minimal, maximal and average cell voltages of 60-cell stack for anode outlet pressure variation.

B Bibliography

[1] European Parliament and Council, Regulation (EU) 2018/842, **2018**.

[2] M. Robinius, J. Linßen, T. Grube, M. Reuß, P. Stenzel, K. Syranidis, P. Kuckertz, D. Stolten, *Comparative Analysis of Infrastructures: Hydrogen Fueling and Electric Charging of Vehicles*, Forschungszentrum Jülich GmbH Zentralbibliothek, Verlag, Jülich, **2018**, VII, 108 pp.

[3] O. Egbue, S. Long, *Energy Policy* **2012**, *48*, 717–729.

[4] T. Franke, J. F. Krems, *Transport Policy* **2013**, *30*, 56 –62.

[5] S.-C. Lin, Y. Zhang, C.-H. Hsu, M. Skach, M. E. Haque, L. Tang, J. Mars in Proceedings of the Twenty-Third International Conference on Architectural Support for Programming Languages and Operating Systems, ACM, Williamsburg, VA, USA, **2018**, pp. 751–766.

[6] R. Álvarez Fernández, F. B. Cilleruelo, I. V. Martínez, *International Journal of Hydrogen Energy* **2016**, *41*, 4808 –4819.

[7] K. Reddi, A. Elgowainy, N. Rustagi, E. Gupta, *International Journal of Hydrogen Energy* **2017**, *42*, 16675 –16685.

[8] H. Murakawa, K. Sugimoto, N. Kitamura, M. Sawada, H. Asano, N. Takenaka, Y. Saito, *Physics Procedia* **2015**, *69*, Proceedings of the 10th World Conference on Neutron Radiography (WCNR-10) Grindelwald, Switzerland October 5–10, 2014, 607 –611.

[9] A. Z. Weber, R. L. Borup, R. M. Darling, P. K. Das, T. J. Dursch, W. Gu, D. Harvey, A. Kusoglu, S. Litster, M. M. Mench, R. Mukundan, J. P. Owejan, J. G. Pharoah, M. Secanell, I. V. Zenyuk, *Journal of The Electrochemical Society* **2014**, *161*, F1254–F1299.

[10] J. Zhang, Y. Tang, C. Song, J. Zhang, H. Wang, *PEM fuel cell open circuit voltage (OCV) in the temperature range of 23°C to 120°C*, *Vol. 163*, **2006**, pp. 532–537.

[11] D. Hao, J. Shen, Y. Hou, Y. Zhou, H. Wang, *International Journal of Chemical Engineering* **2016**, *2016*, 1–10.

[12] H. Zhang, P. K. Shen, *Chemical Reviews* **2012**, *112*, PMID: 22339373, 2780–2832.

[13] K. Jiao, X. Li, *Progress in Energy and Combustion Science* **2011**, *37*, 221–291.

[14] L. Cindrella, A. Kannan, J. Lin, K. Saminathan, Y. Ho, C. Lin, J. Wertz, *Journal of Power Sources* **2009**, *194*, XIth Polish Conference on Fast Ionic Conductors 2008, 146 –160.

[15] H. K. Atiyeh, K. Karan, B. Peppley, A. Phoenix, E. Halliop, J. Pharoah, *Journal of Power Sources* **2007**, *170*, 111 –121.

[16] S. Park, J.-W. Lee, B. N. Popov, *Journal of Power Sources* **2008**, *177*, 457 –463.

[17] S. Park, J.-W. Lee, B. N. Popov, *International Journal of Hydrogen Energy* **2012**, *37*, XII International Symposium on Polymer Electrolytes: New Materials for Application in Proton Exchange Membrane Fuel Cells, 5850 –5865.

[18] M. Andersson, S. B. Beale, M. Espinoza, Z. Wu, W. Lehnert, *Applied Energy* **2016**, *180*, 757 –778.

[19] Y. Liu, C. Ji, W. Gu, J. Jorne, H. A. Gasteiger, *Journal of The Electrochemical Society* **2011**, *158*, B614–B621.

[20] A. Rabis, P. Rodriguez, T. J. Schmidt, *ACS Catal.* **2012**, *2*, 864–890.

[21] A. P. Manso, F. F. Marzo, J. Barranco, X. Garikano, M. G. Mujika, *International Journal of Hydrogen Energy* **2012**, *37*, The 2011 Asian Bio-Hydrogen and Biorefinery Symposium (2011ABBS), 15256 –15287.

[22] L. G. Pătularu, D. M. Schitea, A. Crăciunescu in 2013 8TH INTERNATIONAL SYMPOSIUM ON ADVANCED TOPICS IN ELECTRICAL ENGINEERING (ATEE), **2013**, pp. 1–4.

[23] M. Grimm, E. J. See, S. G. Kandlikar, *International Journal of Hydrogen Energy* **2012**, *37*, 12th CHEC, 12489 –12503.

[24] A. Bazylak, *International Journal of Hydrogen Energy* **2009**, *34*, 3845 –3857.

[25] M. Ji, Z. Wei, *Energies* **2009**, *2*, DOI `10.3390/en20401057`.

[26] H.-S. Kim, K. Min, *Journal of Mechanical Science and Technology* **2008**, *22*, 2274–2285.

[27] A. Bozorgnezhad, M. Shams, H. Kanani, M. Hasheminasab, G. Ahmadi, *International Journal of Hydrogen Energy* **2015**, *40*, 2808 –2832.

[28] K. W. Feindel, S. H. Bergens, R. E. Wasylishen, *Phys. Chem.* **2007**, *9*, 1850–1857.

[29] P. Boillat, D. Kramer, B. C. Seyfang, G. Frei, E. Lehmann, G. G. Scherer, A. Wokaun, Y. Ichikawa, Y. Tasaki, K. Shinohara, *Electrochemistry Communications* **2008**, *10*, 546 –550.

[30] I. Manke, H. Markötter, T. Arlt, C. Tötzke, M. Klages, J. Haußmann, S. Enz, F. Wieder, J. Scholta, N. Kardjilov, A. Hilger, J. Banhart, *Physics Procedia* **2015**, *69*, 619–627.

[31] A. Iranzo, A. Salva, P. Boillat, J. Biesdorf, E. Tapia, F. Rosa, *International Journal of Hydrogen Energy* **2017**, *42*, Special Issue on The 21st World Hydrogen Energy Conference (WHEC 2016), 13-16 June 2016, Zaragoza, Spain, 13839 –13849.

[32] P. Quan, B. Zhou, A. Sobiesiak, Z. Liu, *Journal of Power Sources* **2005**, *152*, 131–145.

[33] C. Fang, C. Hidrovo, F.-m. Wang, J. Eaton, K. Goodson, *International Journal of Multiphase Flow* **2008**, *34*, 690–705.

[34] A. Theodorakakos, T. Ous, M. Gavaises, J. M. Nouri, N. Nikolopoulos, H. Yanagihara, *Journal of Colloid and Interface Science* **2006**, *300*, 673–687.

[35] X. Zhu, P. C. Sui, N. Djilali, *Journal of Power Sources* **2008**, *181*, 101–115.

[36] X. Zhu, Q. Liao, P. C. Sui, N. Djilali, *Journal of Power Sources* **2010**, *195*, 801–812.

[37] Y. Ding, H. T. Bi, D. P. Wilkinson, *Journal of Power Sources* **2010**, *195*, 7278–7288.

[38] C. Qin, S. M. Hassanizadeh, D. Rensink, S. Fell, *Journal of The Electrochemical Society* **2012**, *159*, B737–B745.

[39] M. Hossain, S. Z. Islam, A. Colley-Davies, E. Adom, *Renewable Energy* **2013**, *50*, 763–779.

[40] A. R. Korsgaard, M. P. Nielsen, S. K. Kær, *International Journal of Hydrogen Energy* **2008**, *33*, 1909 –1920.

[41] S. C. Lee, O. Kwon, D. Lee in 2012 7th International Conference on Computer Science Education (ICCSE), **2012**, pp. 974–979.

[42] F. Musio, F. Tacchi, L. Omati, P. G. Stampino, G. Dotelli, S. Limonta, D. Brivio, P. Grassini, *International Journal of Hydrogen Energy* **2011**, *36*, Hysydays, 8045 –8052.

[43] C. Dépature, L. Boulon, P. Sicard, M. Fournier in 2013 15th European Conference on Power Electronics and Applications (EPE), **2013**, pp. 1–10.

[44] Z. Liu, Z. Mao, C. Wang, W. Zhuge, Y. Zhang, *Journal of Power Sources* **2006**, *160*, Special issue including selected papers presented at the International Workshop on Molten Carbonate Fuel Cells and Related Science and Technology 2005 together with regular papers, 1111 –1121.

[45] S. Shimpalee, M. Ohashi, J. W. V. Zee, C. Ziegler, C. Stoeckmann, C. Sadeler, C. Hebling, *Electrochimica Acta* **2009**, *54*, 2899 –2911.

[46] A. D. Le, B. Zhou, *Journal of Power Sources* **2010**, *195*, 5278 –5291.

[47] M. Peksen, *International Journal of Hydrogen Energy* **2011**, *36*, 11914–11928.

[48] J. Macedo-Valencia, J. M. Sierra, S. J. Figueroa-Ramírez, S. E. Díaz, M. Meza, *International Journal of Hydrogen Energy* **2016**, *41*, 23425 –23433.

[49] R. Nishida, S. Beale, J. G. Pharoah, L. de Haart, L. Blum, *Journal of Power Sources* **2018**, *373*, 203 –210.

[50] J. H. Ferziger, M. Peric, *Numerische Strömungsmechanik*, Springer-Verlag, **2008**.

[51] C. Qin, D. Rensink, S. M. Hassanizadeh, S. Fell, *Journal of the Electrochemical Society* **2012**, *159*, B434–B443.

[52] C. Y. Wang, P. Cheng, J. P. Hartnett, T. F. Irvine, Jr., Y. I. Cho, G. A. Greene in *Advances in Heat Transfer*, *Vol. 30*, Elsevier, **1997**, pp. 93–196.

[53] Z. H. Wang, C. Y. Wang, K. S. Chen, *Journal of Power Sources* **2001**, *94*, 40–50.

[54] H. Meng, C.-Y. Wang, *Journal of The Electrochemical Society* **2005**, *152*, A1733–A1741.

[55] L. You, H. Liu, *International Journal of Heat and Mass Transfer* **2002**, *45*, 2277–2287.

[56] L. You, H. Liu, *Journal of Power Sources* **2006**, *155*, 219–230.

[57] M. Mikko, T. Veikko, K. Sirpa, *VTT Publications* **1996**.

[58] J. U. Brackbill, D. B. Kothe, C. Zemach, *Journal of Computational Physics* **1992**, *100*, 335–354.

[59] T. Waclawczyk, T. Koronowicz, *Journal of Theoretical and Applied Mechanics* **2008**, *46*, 325–345.

[60] W. F. Noh, P. Woodward in *Proceedings of the Fifth International Conference on Numerical Methods in Fluid Dynamics June 28 – July 2, 1976 Twente University, Enschede*, (Eds.: A. I. van de Vooren, P. J. Zandbergen), Springer Berlin Heidelberg, **1976**, pp. 330–340.

[61] D. L. Youngs, *Numerical methods for fluid dynamics* **1982**.

[62] R. Scardovelli, S. Zaleski, *Annual Review of Fluid Mechanics* **1999**, *31*, 567–603.

[63] O. Ubbink, R. I. Issa, *Journal of Computational Physics* **1999**, *153*, 26–50.

[64] S. Muzaferija, M. Peric, *Numerical Heat Transfer Part B: Fundamentals* **1997**, 369–384.

[65] STAR-CCM+ documentation version 1.06, Siemens, **2019**.

[66] M. C. Leverett, *Transactions of the AIME* **1941**, *142*, 152–169.

[67] T. E. Springer, T. A. Zawodzinski, S. Gottesfeld, *Journal of The Electrochemical Society* **1991**, *138*, 2334–2342.

[68] H. Wu, X. Li, P. Berg, *Electrochimica Acta* **2009**, *54*, 6913 –6927.

[69] A. A. Kulikovsky, *Journal of The Electrochemical Society* **2003**, *150*, A1432–A1439.

[70] S. Asanin, F. Du, A. Jurzyk, K. Ling, J. Hirschfeld, W. Lehnert, *(In preparation)* **2019**.

[71] F. Du, MA thesis, Technische Universität München, **2017**.

[72] K. Ling, MA thesis, Technische Universität Darmstadt, **2018**.

[73] A. Jurzyk, MA thesis, Technische Universität München, **2019**.

[74] S. M. Haase, PhD thesis, Technische Universität München, **2015**.

[75] M. Mortazavi, K. Tajiri, *Renewable and Sustainable Energy Reviews* **2015**, *45*, 296–317.

[76] V. I. Nizhenko, V. N. Eremenko, L. I. Sklyarenko, *Soviet Powder Metallurgy and Metal Ceramics* **1965**, *4*, 463–466.

[77] M. Renardy, Y. Renardy, J. Li, *Journal of Computational Physics* **2001**, *171*, 243–263.

[78] K. S. Chen, *ECS Transactions* **2007**, *11*, 715–724.

[79] D. Dutykh, *Computing Research Respository* **2016**, *abs/1611.09646*.

[80] M. Peric, S. Ferguson, The advantage of polyhedral meshes, tech. rep., CD-adapco, **2005**.

[81] D. Deising, H. Marschall, D. Bothe, *Chemical Engineering Science* **2016**, *139*, 173–195.

[82] M. Fourar, R. Lenormand, A Viscous Coupling Model for Relative Permeabilities in Fractures, New Orleans, Louisiana, **1998**.

[83] H. Huang, Z. Li, S. Liu, X.-y. Lu, *Int. J. Numer. Meth. Fluids* **2009**, *61*, 341–354.

[84] A. Nowamooz, G. Radilla, M. Fourar, *Water Resources Research* **2009**, *45*, DOI `10.1029/2008wr007315`.

[85] A. T. Corey, *Producers Monthly* **1954**.

[86] Statistics and Machine Learing Toolbox: User's Guide (R2018b), Siemens AG, **2017**.

[87] B. Everitt, *Cluster Dissection and Analysis: Theory, Fortran Programs and Examples. by H. Spath*, *Vol. 148*, **1985**, pp. 285–286.

[88] D. Arthur, S. Vassilvitskii, *K-Means++: The Advantages of Careful Seeding*, *Vol. 8*, **2007**, pp. 1027–1035.

[89] S. C. Cho, Y. Wang, *International Journal of Heat and Mass Transfer* **2014**, *70*, 340–352.

[90] W. He, J. S. Yi, T. Van Nguyen, *AIChE Journal* **2000**, *46*, 2053–2064.

[91] P. M. Adler, *Porous media: Geometry and transport*, Butterworth-Heinemann, **1992**.

[92] J. M. B. J. Bear, *Modeling and Applications of Transport Phenomena in Porous Media*, **1991**.

[93] T. Berning, N. Djilali, *Journal of The Electrochemical Society* **2003**, *150*, A1589–A1598.

[94] N. K. Cheruku, MA thesis, Universität Duisburg Essen, **2019**.

[95] S++ Simulation Services, http://www.splusplus.com/measurement/en/csshunt.html.

[96] S. Herden, J. A. Hirschfeld, C. Lohri, M. Perchthaler, S. Haase, *Journal of Power Sources* **2017**, *364*, 449 –457.

[97] F. C. Cetinbas, S. G. Advani, A. K. Prasad, *Journal of The Electrochemical Society* **2013**, *160*, F750–F756.

[98] H. Dieter Baehr, K. Stephan, *Heat and Mass Transfer*, **2011**.

[99] B. E. Gelfand, *Progress in Energy and Combustion Science* **1996**, *22*, 201–265.

[100] W.-H. Chou, G. M. Faeth, *International Journal of Multiphase Flow* **1998**, *24*, 889–912.

[101] Z. Dai, G. M. Faeth, *International Journal of Multiphase Flow* **2001**, *27*, 217–236.

[102] S. F. Kistler in, CRC Press, **1993**, Chapter Hydrodynamics of wetting, pp. 311–420.

[103] P. Concus, R. Finn, *Proceedings of the National Academy of Sciences of the United States of America* **1969**, *63*, 292.

[104] M. Klingele, R. Moroni, S. Vierrath, S. Thiele, *Journal of Electrochemical Energy Conversion and Storage* **2017**, *15*, 014701–014701–7.

Schriften des Forschungszentrums Jülich
Reihe Energie & Umwelt / Energy & Environment

Band / Volume 490
Micromechanical Characterization of Ceramic Solid Electrolytes for Electrochemical Storage Devices
J. F. Nonemacher (2020), xv, 131 pp
ISBN: 978-3-95806-461-4

Band / Volume 491
Nanoscale investigation of high temperature oxidation mechanisms of high-Cr ferritic steels
A. Vayyala (2020), xix, 105 pp
ISBN: 978-3-95806-467-6

Band / Volume 492
Electrolyte development for a SOFC operating at low temperature
J. Zhang (2020), vi, 121 pp
ISBN: 978-3-95806-471-3

Band / Volume 493
Modeling and Simulation of Polymer Electrolyte Fuel Cells
S. Zhang (2020), 4, xii, 214 pp
ISBN: 978-3-95806-472-0

Band / Volume 494
Ab initio perspective on hydrogenated amorphous silicon for thin-film and heterojunction photovoltaics
P. Czaja (2020), 107 pp
ISBN: 978-3-95806-474-4

Band / Volume 495
Measurements of Atmospheric OH and HO_2 Radicals by Laser-Induced Fluorescence on the HALO Aircraft during the OMO-ASIA 2015 Campaign
C. Künstler (2020), 156 pp
ISBN: 978-3-95806-477-5

Band / Volume 496
Tomographic observations of gravity waves with the infrared limb imager GLORIA
I. Krisch (2020), vii, 187 pp
ISBN: 978-3-95806-481-2

Band / Volume 497
Aquisition of temporally and spatially highly resolved data sets of relevant trace substances for model development and model evaluation purposes using a mobile measuring laboratory
D. Klemp, R. Wegener, R. Dubus, U. Javed (2020), 110 pp
ISBN: 978-3-95806-465-2

Schriften des Forschungszentrums Jülich
Reihe Energie & Umwelt / Energy & Environment

Band / Volume 498
Charakterisierung des Werkstoffverhaltens während des Kosinterns einer neuartigen, inert gestützten Festoxidbrennstoffzelle
F. Grimm (2020), ix, 168 pp
ISBN: 978-3-95806-482-9

Band / Volume 499
WEGE FÜR DIE ENERGIEWENDE
Kosteneffiziente und klimagerechte Transformationsstrategien für das deutsche Energiesystem bis zum Jahr 2050
M. Robinius et al (2020), VIII, 141 pp
ISBN: 978-3-95806-483-6

Band / Volume 500
Mechanical Behavior of Solid Electrolyte Materials for Lithium-ion Batteries
G. Yan (2020), x, 139 pp
ISBN: 978-3-95806-484-3

Band / Volume 501
Retrieval of atmospheric quantities from remote sensing measurements of nightglow emissions in the MLT region
Q. Chen (2020), 208 pp
ISBN: 978-3-95806-485-0

Band / Volume 502
Auswirkungen der Energiewende auf das deutsche Gastransportsystem
B. Gillessen (2020), XVII, 186
ISBN: 978-3-95806-487-4

Band / Volume 503
Lagrangian Simulation of Stratospheric Water Vapour: Impact of Large-Scale Circulation and Small-Scale Transport Processes
L. Poshyvailo (2020), 126 pp
ISBN: 978-3-95806-488-1

Band / Volume 504
Water Management in Automotive Polymer-Electrolyte-Membrane Fuel Cell Stacks
S. Asanin (2020), XVIII, 172 pp
ISBN: 978-3-95806-491-1

Weitere ***Schriften des Verlags im Forschungszentrum Jülich*** unter
http://wwwzb1.fz-juelich.de/verlagextern1/index.asp

Energie & Umwelt / Energy & Environment
Band / Volume 504
ISBN 978-3-95806-491-1

Mitglied der Helmholtz-Gemeinschaft

JÜLICH
Forschungszentrum